Micromechanics of Hearing Organs

Anna Vavakou

Cover design: Martina Gounela
Layout: Anna Vavakou
Printing: Optima Grafische Communicatie
ISBN: 978-94-6361-686-7

Micromechanics of Hearing Organs

Micromechanica van gehoororganen

Thesis

to obtain the degree of Doctor from the
Erasmus University Rotterdam
by command of the
rector magnificus

Prof.dr. A.L. Bredenoord

and in accordance with the decision of the Doctorate Board.
The public defence shall be held on

Friday 10 June 2022 at 10.30 hrs

by

Anna Vavakou
born in Athens, Greece.

Erasmus University Rotterdam

Doctoral Committee:

Promotor:	Prof.dr. J.G.G. Borst
Other Members:	Prof.dr. E.S. Olson Prof.dr. P. van Dijk Dr. J.J.M. Pel
Copromotor:	Dr. M.L. van der Heijden

Contents

Abbreviations

AC:	alternating current
AGC:	automatic gain control
AN:	auditory nerve
an-po, ap:	anterior-posterior
BF:	best frequency
BM:	basilar membrane
CA:	crista acoustica
CAP:	sound evoked compound action potential
CC:	cap cell
CF:	characteristic frequency
DC:	direct current, rectified component
do-ve, dv:	dorsal-ventral
DP2s:	second order distortion products
DPOAEs:	distortion product otoacoustic emissions
DV:	direct view
DW:	dorsal wall
EP:	endocochlear potential
FFT:	fast Fourier transform
IHC:	inner hair cells
I/O:	input/output
IP:	intraperitoneal
IV:	intravenous
HS:	hotspot, the OHC/Deiters' cells area
LCM:	local cochlear microphonics
LDV:	laser Doppler vibrometry
MT:	mechanotransducer
MV:	mirror view
OCT:	optical coherence tomography
OHC:	outer hair cells
OoC:	organ of Corti
pDV:	predicted direct view
pr-di, pd:	proximal-distal
RL:	reticular lamina

RWM: round window membrane
SM: scala media
S/N: signal to noise ratio
SP: summating potential
SPL: sound pressure level
ST: scala tympani
SV: scala vestibuli

Chapter 1

General Introduction

Hearing organs receive pressure oscillations in air or water, and transduce them to neural discharges. These are further processed in higher areas of the nervous system to extract pitch, loudness and other perceptual attributes, and to separate, identify and localize sound sources. Across animals, hearing organs are characterized by elaborate anatomy and various anatomical gradients across their length. These facilitate the separation of incoming frequencies and the encoding of different sound intensities. The mammalian cochlea overall is a vulnerable organ, as it is susceptible to damage related to age, anoxia, toxic agents and infection. Inside it, there are few thousands of sensory cells (hair cells) that are necessary for hearing; they do not regenerate throughout life. Mammalian hair cells consist of two subgroups that perform the following tasks: 1) They sense and alter the mechanical responses of the cochlea to sound, facilitating hearing. 2) They provide the output of the cochlea. Dysfunction or death of these sensory cells is the most common cause of hearing loss. According to the WHO, millions of people are affected to different degrees of hearing loss (5.5% of the global population (WHO, 2021)). The cochlea is difficult to access and vulnerable, while the number of sensory cells is small. All these factors hinder the progress of research in the field of cochlear function. For example, it is still unknown how these sensory cells control the mechanical responses of the cochlea to sound. Understanding the mechanisms that underlie the cochlear function is a prerequisite for developing future therapies for hearing loss. The current thesis contributes towards understanding the function of the cochlea, in relation to its anatomy. Furthermore, the insect hearing organ is studied in a comparative manner to the bushcricket hearing organ.

Anatomy of the cochlea

The mammalian hearing system is able to separate and sense sounds across a wide range of frequencies and intensities. For example, humans can hear frequencies from 20 Hz to 20 kHz, whereas some mammals can hear frequencies down to a few hertz, and

others, up to 200 kHz. The ability to hear frequencies above 10 kHz is relatively rare in non-mammalian species. Apart from its specialization to high-frequency hearing, the mammalian hearing system is characterized by a spectacular sensitivity at low sound intensities. At the same time, it is able to cope with intensities that cover a range of 120 dB, that is an enormous 6 orders of magnitude of sound pressure level (SPL). The mammalian cochlea has to first mechanically separate the incoming acoustic energy, ensuring that different frequencies are sensed at different locations of the organ, and additionally, it has to compress the mechanical excitation of the sensory cells prior to transduction, to encode the wide range of intensities.

The impinging sound waves are collected by the outer ear, which is adapted to collect sound waves and channel them into the ear canal. There, eventually, they strike on the ear drum and cause it to vibrate. The middle-ear ossicles transmit these vibrations to the oval window, the input port of the cochlea (Fig. 1.1A). The cochlea is the sensory organ that is responsible for sensing sound; it is unique to the mammalian inner ear. It consists of three fluid filled ducts (scalae) that run in parallel and form a snail shaped structure (scala vestibuli (SV), scala tympani (ST) and scala media (SM), Fig. 1.1A,B), which is where the cochlea takes its name from (*cochlias* is Greek for snail). The sensory epithelium (OoC, Organ of Corti) is found in the scala media. In the OoC, sound-induced mechanical vibrations of the surrounding structures stimulate the inner hair cells (IHCs, mechanosensors inside the cochlea) by deflection of their stereocilia (black lines, apical side of the IHC, Fig. 1.1C). The receptor potential of the IHCs triggers neural discharges of the spiral ganglion cells which encode the acoustic signal. They are conveyed by the auditory nerve (AN) to higher areas of the brain, where they are further processed. The outer hair cells (OHCs) are found close to the IHCs and they also sense sound-induced mechanical displacements with their stereocilia (Fig. 1.1C). They are thought to shape the input to the IHCs by altering the mechanics of the OoC, but the underlying mechanisms are not fully understood until now. Like the IHCs, the OHCs sense mechanical vibrations as their stereocilia deflect. A deflection directed towards the tallest row opens the mechanically gated ion channels on the shorter stereocilia. As a consequence, the inward flow of cations is increased and the cell depolarizes. The depolarized OHC decreases in length, as the voltage-gated protein prestin in the OHC basolateral cell membrane changes its conformation. Conversely, the OHC length increases when the stereocilia are deflected towards the shortest row, and the cell hyperpolarizes. The SM is electrically and ionically insulated from the other scalae, and it contains

endolymph, which maintains a higher potential (80-120 mV) than the perilymph that is found in SV and ST. Endolymph also has a much higher K+ concentration than perilymph. This difference in electrical potential and ion concentration is maintained by an intracochlear structure, the stria vascularis. Its operation is crucial to hearing, as the OHCs rely on this "battery" to function.

Cochlear mechanics research

The anatomy of the cochlea was studied by Helmholtz, Corti, Kolliker and others during the 19^{th} and early 20^{th} century. Helmholtz proposed his theory of hearing in 1885, where he described the cochlea as a set of tuned resonators. This theory was criticized because the microstructures in the cochlea that were proposed to resonate, are coupled. Still, this piece of work set the foundations for a theoretical description of the cochlea. No theory could relate anatomy with function, until Békésy described the travelling wave inside the cochlea in 1928 (von Békésy, 1960). Using stroboscopy, he managed to photograph the propagation of low-frequency mechanical waves inside a human cadaver cochlea. His findings revealed that mechanical vibrations propagate inside the cochlea in the form of a travelling wave, and he also showed that the distance of wave propagation depends on its frequency, a property named tonotopy (Fig. 1.1B). He established the field of cochlear mechanics and was awarded a Nobel prize in 1961 for his contributions.

A recurring challenge in the field of cochlear mechanics is the vulnerability and the inaccessibility of the mammalian cochlea. In his stroboscopy experiments, Békésy presented the human cadaver cochleas with 120-dB-SPL tones up to a few hundred hertz. This stimulus paradigm is sufficient to reveal the passive properties of the dead cochlea, but it does not clarify how the live cochlea works.

In the mid 1960s, Kiang and colleagues exploited advanced electrophysiology techniques and were able to record single fibers from the auditory nerve (AN) (Kiang, 1965). Their results revealed that the nerve fibers were much more sharply tuned than the cadaver cochlea that Békésy had described. This discrepancy between mechanical and neural data was puzzling the field until the 1970s. In 1971, Rhode used the Mössbauer technique to record sound-induced vibrations in squirrel monkey cochleas in vivo (Rhode, 1971). He reported that mechanical responses of the basilar membrane (BM) were somewhat more sharply tuned than those of Békésy sy. (Later recordings by Sellick et al. (1982) showed an even sharper BM tuning, resembling closely the auditory

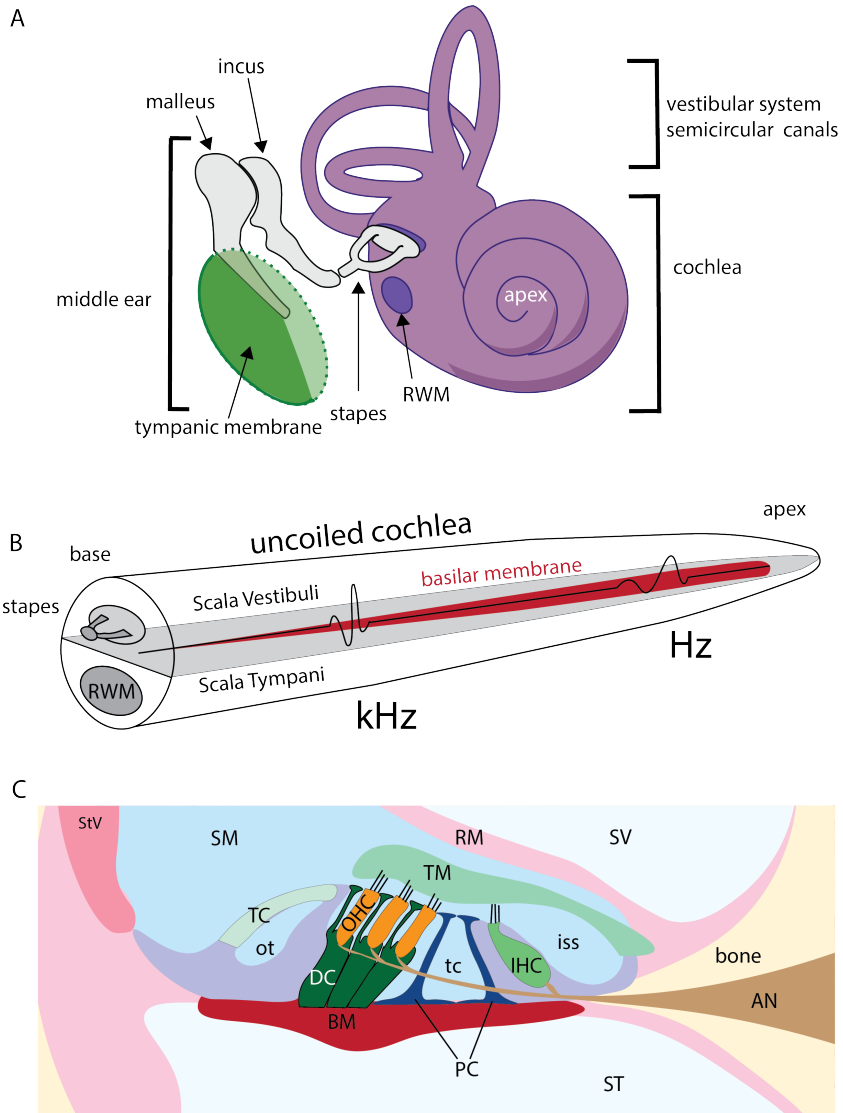

Figure 1.1: Anatomy of the mammalian cochlea. (**A**) Anatomy of the middle and inner ear. (*RWM*: round window membrane, *OWM*: oval window membrane, Adapted from Lars Chittka; Axel Brockmann, CC BY 2.5, via Wikimedia Commons) (**B**) The uncoiled cochlea. Mechanical waves propagate as travelling waves and peak in a frequency dependent position. (**C**) Schematic of a cochlear cross section. (*BM*: basilar membrane, *TM*: tectorial membrane, *RM*: Reissner's membrane, *AN*: auditory nerve, *SV*: scala vestibuli, *ST*: scala tmpani, *SM*: scala media, *ot*: outer tunnel, *tc*: tunnel of corti, *iss*: inner spiral sulcus, *IHC*: inner hair cell, *OHC*: outer hair cell, *TC*: tectal cell *DC*: Deiters' cell, *PC*: pillar cells)

nerve responses; compare Fig. 1.2A). Importantly, Rhode reported that BM vibrations exhibited compression, growing <1 dB/dB in magnitude with stimulus intensity (Fig. 1.2B). Rhode's findings were initially treated with skepticism. Coincidentally, around that time, Kemp used a microphone to record sounds that are emitted by the ears of human subjects during sound simulation, and discovered otoacoustic emissions (Kemp, 1978). Later work confirmed that emissions are generated inside the cochlea, and that travel back to the ear canal where they can be recorded. They are absent in passive cochleas. These two findings, followed by further experimental validation of Rhode's findings using laser Doppler vibrometry (LDV, a more sensitive and less invasive vibrometry technique) convinced the field that the cochlea is an active sensory organ. The mechanisms that underlie this nonlinear, "active," behavior are still unclear.

In 1975, Ryan and colleagues reported that OHC loss leads to reduced hearing sensitivity (Ryan & Dallos, 1975), and that the frequency range of the hearing loss accurately matches the tonotopic regions where OHC are missing. It then became clear that the OHCs play an important role in modifying the local propagation properties of the travelling wave inside the OoC, allowing for sharp tuning and compression. The subsequent discovery of electromotility, electrically driven changes in the length of the OHCs (Brownell, 1983), presented a very strong suggestion of their functional significance. In 2000, the protein underlying electromotility was discovered. Prestin (Zheng et al., 2000), changes its conformation in a voltage gated way (Santos-Sacchi & Dilger, 1988), resulting in length changes in the OHCs. Many studies afterwards described physiological aspects of the OHCs and the protein prestin. Very recently, the conformational changes of prestin molecule that are responsible for its electromotile capacity were identified using cryo-electron microscopy (Bavi et al., 2021).

The mechanical waves are often thought to suffer from friction loss and dissipation as they propagate in the cochlea. Along that line of thinking, the cochlea is commonly viewed as an amplifier that is assumed to compensate for friction losses and dissipation. Bringing all these findings together, the OHCs function both as sensors and actuators. Specifically, they are thought to sense mechanical vibrations and amplify them depending on frequency, by changing their length in a cycle-by-cycle manner. Following this assumption, the OHCs should be driving the BM, and compression is a result of the saturation of the amplifier.

In that scenario, OHC motility should be fast enough to follow ultrasounds (up to 200kHz in some bats), thus enabling high frequency hearing. Mechanical vibrations deflect the stereocilia of the OHCs, altering the receptor current. The membrane

voltage follows changes in the receptor current, but the question that arises is how fast can it follow them. This is because the cell membrane has capacitive properties that low-pass filter the membrane voltage after changes in the receptor current. The functional implication of this low-pass filtering is a limitation on the ability of the OHCs to affect the propagating wave in a cycle-by-cycle manner, known as the RC problem (Housley & Ashmore, 1992). Finally, the signal to noise ratio is a fundamental property of signal detection. Because electromotility is not frequency selective, it is quite possible that amplifying the mechanical displacements in an instantaneous manner would deteriorate the signal to noise ratio, and, as a result, impede hearing sensitivity.

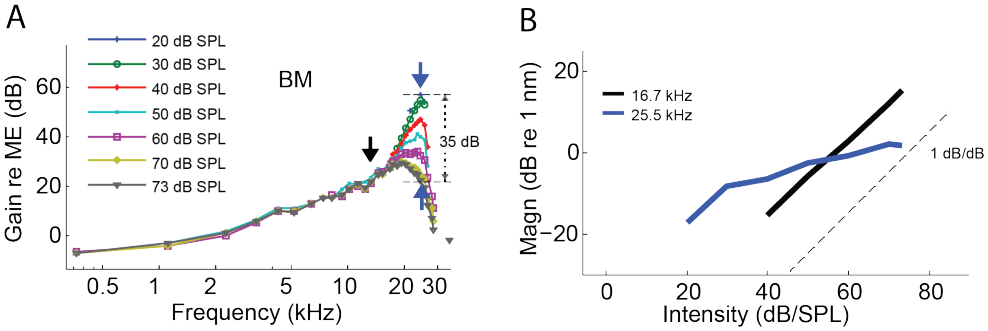

Figure 1.2: Mechanical responses of the gerbil Basilar Membrane following sound stimulation. (**A**) Sharp tuning responses of the BM. Vibration magnitude as a function of frequency, normalized to stapes motion. Sound intensity is indicated in the key, with blue arrows indicating amounts of compression observed at CF (25 kHz) between 20 and 73 dB SPL. (**B**) Compressive displacement responses of the BM. Input–output functions for different frequencies, based on the tuning curves of panel(A). Dashed lines illustrate linear growth for reference. (black: bellow CF frequency, blue: CF frequency. Adapted from Cooper et al. (2018))

Technical advances in cochlear mechanics

Technical challenges have been a limiting factor for advances in the field of cochlear mechanics. The cochlea itself is a physiologically vulnerable structure, and it is susceptible to mechanical and metabolic stress, ototoxicity and anoxia. Additionally, the cochlea is not superficially exposed, and surgery is required in order to measure sound-induced vibrations. Another limitation is the magnitude of the vibrations, which can be in a sub-nanometer range. Moreover, studying high-frequency hearing can be

quite challenging as it requires hardware with high sampling rate, in the range of few hundreds of kilohertz. These factors have made data collection quite challenging, and technical advances quite slow.

From the early 1990s till recent years, laser Doppler vibrometry was the main experimental technique used in the field of cochlear mechanics. Typically, the round window membrane was torn and reflective beads were placed in the scala tympani. The beam of a laser vibrometer is aimed at a reflective bead, and sound-induced vibrations are measured. There are quite a few limitations when using this technique. Primarily, vibrations are measured indirectly, from the reflective bead, and the experimenter has little control over the bead position. Additionally, the bead will land on the surface of a structure, usually the BM, and in-depth vibration measurements are not an option. Moreover, the BM is a confined membrane, that in all likelihood only allows for transverse motion. Because of that, it has not been possible to explore experimentally other directions of motion in the OoC and the surrounding fluid. An exception is fluid pressure measurements in the SV and the SM, performed by Elisabeth Olson and colleagues (Olson, 2001; Kale & Olson, 2015). Finally, the cochlear duct is opened by tearing the round window membrane or by opening the bone, causing changes to the pressure of the cochlear fluids and loss of sensitivity. Due to the anatomy of the cochlea, it has only been possible to perform mechanical measurements of the BM at the base of the cochlea or the TM at the apex of the cochlea.

In 2011 Optical Coherence Tomography (OCT) vibrometry was used for the first time to perform mechanical measurements inside the OoC (Chen et al., 2011). OCT uses low-coherence light to image optically scattering media. It employs the same principles as ultrasound imaging, but because it uses light waves instead of sound waves, it achieves sharper imaging resolution, that can be in the range of few micrometers. A drawback is the low tissue penetration, limiting the image to only 2-3-mm deep. It is widely used in ophthalmology, to image superficial structures and to diagnose pathologies of the retina. In the field of cochlear mechanics, researchers use either custom made hardware, or commercially available hardware. The latter is increasingly more favorable option, since the sampling rates of commercial hardware have increased (100-200 kHz).

For the first time, it has become possible to perform mechanical measurements on cross sections along the cochlea in a non invasive manner. OCT vibrometry provides the field with the experimental tools to investigate the mechanical behavior of OHCs and other structures within the OoC during sound stimulation.

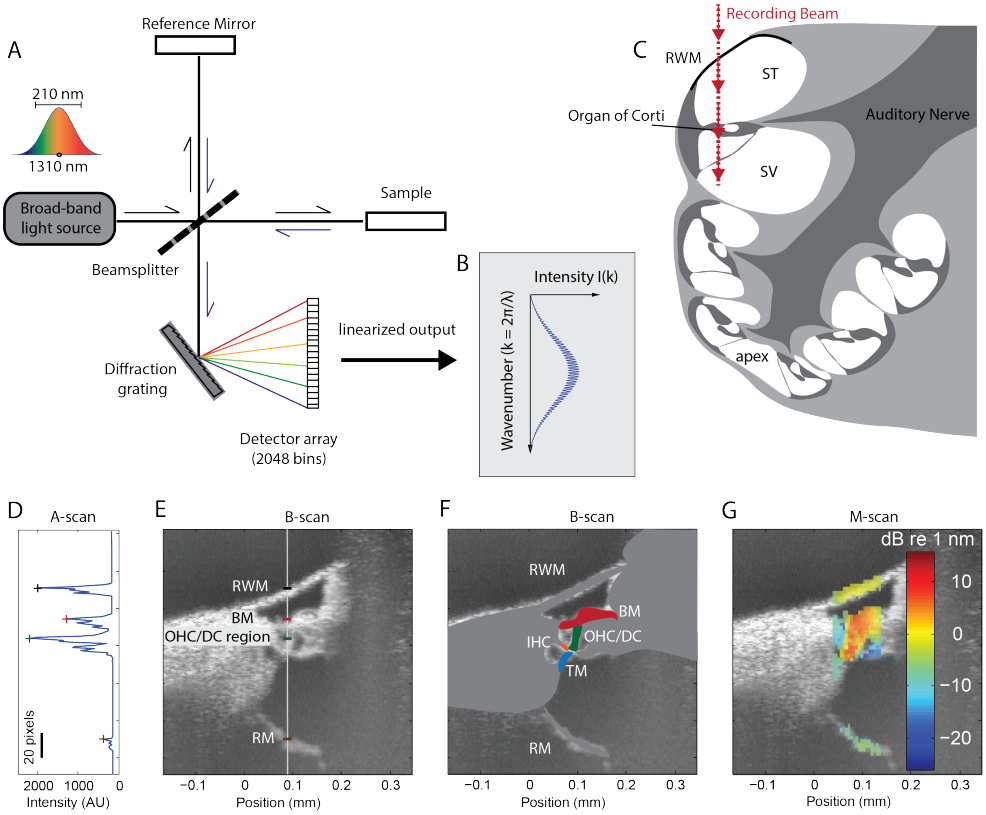

Figure 1.3: OCT vibrometry application in cochlear mechanics. (**A**) Schematic of basic spectral domain OCT system, following the basic concepts of a Michelson interferometer. The broadband light field output is split by a diffraction grating, and the different wavelengths are subsequently detected by a linear detector array. (**B**) Spectral raw data. The linearized light detector output is expressed as light intensity over k-space. (**C**) Schematic of the gerbil cochlea cross section. The recording beam is reaching the Organ of Corti through the intact round window membrane. (RWM: round Window Membrane, ST: scala tympani, SV: scala vestibuli, adapted from Dong & Olson (2013)) (**D**) A depth reflectance profile (A-scan). (**E**) An OCT B-scan is obtained by performing spatially adjacent A-scans. Distinct anatomical structures correspond to reflectivity peaks in the A-scan. (**F**) Underlying anatomical structures (RWM, round window membrane, BM, basilar membrane, IHC, Inner Hair Cell region, OHC/DC: Outer Hair Cells / Deiters' cells region, TM, tectorial membrane) (**G**) OCT vibrometry M-scan cross section.

OCT vibrometry - Method

OCT is an imaging technique based on the principles of interferometry, using light to image optically scattering media. OCT is the optical equivalent of ultrasound imaging. However, as the speed of light is very high, it is not possible to directly measure travel delays (echoes) of light pulses accurately. Instead, the principles of interferometry are used. The basic idea of interferometry is the separation of a single light beam into a reference beam and a sample beam. After reflection from a mirror (reference beam) and the measurement object (sample beam), the two beams are brought together and the resulting interference pattern is measured.

There are three main OCT technical approaches: TD-OCT (time domain), SD-OCT (spectral domain) and SS-OCT (swept source). In TD-OCT, the light source is incoherent and broadband, hence interference between the reference and sample beams only occurs when their optical pathlengths are very nearly equal. To scan in depth, the reference mirror is displaced in a controlled manner, to allow for travelling path adjustment and thus achieve depth resolution. However, the mirror motor limits the sampling frequency to a maximum of $\sim$ 400-Hz. SS-OCT and SD-OCT also use a broadband light source to achieve depth resolution, but the different spectral components of the light are separated, either in the time domain during generation (SS-OCT), or in space by an optical grating prior to photo detection. Thus, in SS-OCT the light is separated into different wavelengths during generation, whereas in SD-OCT, the light is separated at detection. Both these techniques employ spectral interference, and thus resolve depth in a single measurement. The use of rapidly sweeping lasers (SS-OCT) or rapidly sweeping line cameras (SD-OCT) allows for high sampling rates (up to 200 kHz), thus enabling vibration measurements at the high frequencies relevant for hearing. SD-OCT yields superior axial resolution and is inherently phase stable, so it is recommended for vibrometry. SS-OCT vibrometry is also used in the study of hearing organs, and it can often provide deeper measurement depths.

The SD-OCT setup used in the present work incorporates a broadband low coherent infrared light source (central wavelength, 1300 nm). The light is fed to a beamsplitter and subsequently reaches the reference mirror and the sample (Fig. 1.3A). The reflected light from the reference mirror and back-scattered light from the sample are brought together and fed into a high-speed spectrometer (diffraction grating), and captured by 2048 detector array cells (CCD line camera). Thus, the light is separated into different wavelengths prior to detection. The linearized output of the spectrometer

is expressed as intensity over k-space ($k = 2\pi/\lambda$) (Fig. 1.3B). This pattern of intensity as a function of k is called the interferogram. Light scattered from a single depth in the sample causes a periodic ripple in the interferogram, and each depth corresponds to a different ripple periodicity. Depth resolution is achieved by separating the different ripple periods using a fast Fourier transform (FFT). In OCT terminology, a depth profile is called an "A-scan" (Axial profile), following terminology from ultrasound imaging (example: Fig. 1.3D).

Using a commercial Thorlabs Telesto II hardware (Thorlabs Telesto TEL320C1), it was possible to acquire adjacent A-scans with a spatial resolution of few microns. That way, 2D cross sections (B-scans, "Brightness-Scan" in ultrasound terminology) of the Organ of Corti were compiled (Fig. 1.3E). The axial resolution is defined by the spectral bandwidth of the light source (∼210 nm in our setup), whereas the lateral resolution is defined by the chosen application optics (the numerical aperture of the lens, similar to standard microscopy). The high imaging resolution (axial resolution: ∼6 μm, lateral resolution: 13 μm) allowed us to relate the acquired B-scans with the anatomy of the Organ of Corti, identifying key structures (Fig. 1.3F).

Vibrometry measurements are obtained by utilizing the high sampling rate of the setup (140 kHz). The measuring beam is parked in one position, and consecutive A-scans are acquired. The OCT A-scan acquisition is time locked to the sound stimulus. That way, the reflectance of each discreet pixel along the depth profile is followed throughout the stimulus presentation. At high frequencies, sound-induced vibrations in hearing organs are characterized by very low magnitudes, ranging from sub-nanometer values up to several nanometers. This magnitude is way lower than the axial resolution of the system (∼6 μm), and will not be captured in the intensity of the measured pixel over time. However, the change in the phase $\delta\phi$ of a measured pixel across A-scans (which is also acquired by the FFT) is linearly related to the displacement δx:

$$\delta\phi = 2k_{\mathrm{mid}}\delta x,$$

where k_{mid} is middle value of k, and the factor 2 comes from the change in both the forward and backward path of the light. Using phase values over time, it is thus possible to calculate the vibration displacement at sub-pixel depth difference magnitudes (M-scan). Finally, vibration maps are compiled by performing spatially adjacent M-scans (Fig. 1.3G).

The cochlear studies were performed in the mongolian gerbil. In our measurements,

the OCT recording beam reached the Organ of Corti at the base of the cochlea through the round window membrane (RWM) (Fig. 1.3C). The RWM was intact, and the cochlea was exposed by removing the bulla in a minimally invasive manner. The animals were deeply anesthetized by administering a mix of ketamine/xylazine anesthetics through intraperitoneal injections.

The insect crista acoustica

The insect hearing organ, the crista acoustica (CA), supports a travelling wave and is arranged in a tonotopic manner. These are shared functional principles with the mammalian cochlea. For that reason, there can be several comparative and methodological advantages in studying insect hearing. The bushcricket hearing organ utilizes ∼50 sensory units to resolve sounds up to 80 kHz. The sensory tissue, crista acoustica (CA), is found on the tibia of their front legs. The sensory units are surrounded by the two tympana across the anterior-posterior anatomical axis. Along the dorsal axis they are embedded in fluid, and ventrally, they are in contact with an air-filled tube, the trachea (Fig. 1.4). Owing to its superficial position, the mechanics of the tympana and the CA have been studied using LDV in the past (Michelsen & Larsen, 1978). The two tympana move in an antiphasic manner, and in that way they transfer motion to the sensory unit in a lever-resembling scheme. As mentioned above, there is a travelling wave in the CA and the mechanical waves are sensed in a tonotopic manner, but, contrary to the cochlea, there is no dynamic compression or sharp tuning (Palghat Udayashankar et al., 2012). Still, the neural tuning is sharper than the reported mechanical tuning (Hummel et al., 2016). It is still unknown what drives transduction in the CA, and thus the discrepancy among neural and mechanical data remains unexplained.

Research Questions

Hearing organs exhibit a variety of elaborate properties that facilitate the sensing of mechanical vibrations. The mammalian cochlea supports travelling waves, and it is an active, nonlinear sensory organ that exhibits sharp frequency tuning and is capable of compressing the range of its mechanical responses. The bushcricket CA also supports tonotopically arranged travelling waves, and is capable of sensing a wide range of frequencies with only 50 sensory units. The study of the mechanics of hearing organs

has been impeded by technical limitations that mostly restricted the measurement site to superficial structures. It is still unclear how the anatomy of hearing organs relates to function, and that is the main focus of the current thesis. For that purpose, we extensively explored and analyzed the micromechanical responses of the cochlea and the CA to sound stimuli. The research topics elaborated in the next chapters are as follows:

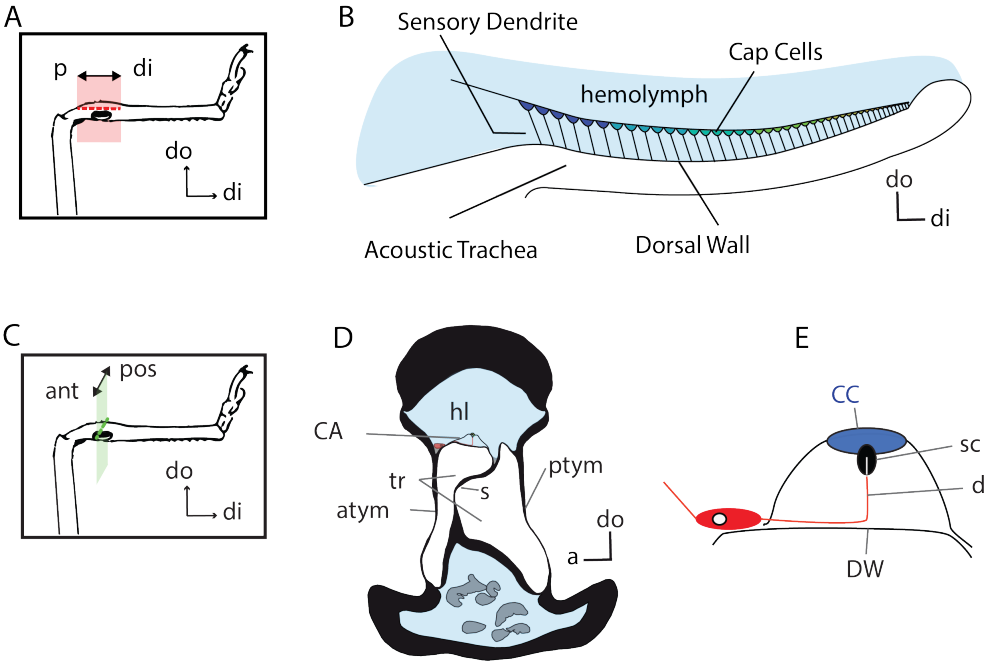

Figure 1.4: Anatomy of the bushcricket crista acoustica. (**A**) Schematic drawing of the foreleg that holds the hearing organ, crista acustica (CA), including a proximal-distal/dorsal-ventral section of the CA. (**B**) Sketch of the CA across the proximal-distal axis. (**C**) An anterior-posterior/dorsal-ventral section of the CA. (**D**) Anatomical sketch of a cross-section of the bushcricket front leg. (*atym*: anterior tympanum, *ptym*: posterior tympanum, *tr*: trachea, *s*: septum, *CA*: crista acustica, *hl*: hemolymph) (**E**) Anatomical sketch of a cross-section of the bushcricket CA. (*CC*: cap cell, *sc*: scolopale cell, *d*: sensory dendrite, *DW*: dorsal wall) (Adapted from Vavakou et al. (2021)

Vibration modes within the mammalian Organ of Corti

In cochlear models, the OHCs are commonly thought to drive the BM motion, in a simple push and pull manner. Along these lines, the OHCs are thought to actively amplify the BM vibrations in a frequency dependent manner, in phase with the travelling wave, thus achieving sharp frequency tuning. Compression is thought to be a result of the saturation of the amplifier. However, this assumption has not been tested extensively, as it was not possible to measure sound-induced vibrations on the OHCs and the BM simultaneously. **Chapter 2** provides a detailed description of the motion profiles of cross sections of the Organ of Corti. The structures of interest are measured at different frequencies and sound intensities. The BM and the OHC vibration modes are compared spatially, spectrally and in terms of their compression profile. Overall, the two structures exhibit different modes of vibrations. A simple push and pull explanation is not sufficient to describe the functional relation of the OHCs and the BM. In the final part of **Chapter 2** we present experimental evidence for longitudinal direction of motion in the region of the OHCs.

Vibration modes within the insect crista acoustica

The hearing organ of the bushcricket *Mecopoda elongata* relies on fewer than 50 sensory neurons to sense a wide range of frequencies. Transduction is thought to take place by stretching of the sensory dendrite, that is found along the dorsal-ventral axis of the sensory unit. However, the sensory dendrite had not been measured along its dorsal-ventral direction. In **Chapter 3**, we present a detailed description of the micromechanical motion of the structures surrounding the sensory dendrite (Dorsal Wall and Cap Cells). The two structures support different modes of vibration along the dorsal-ventral axis, that are spectrally and spatially distinct. The relative motion of the two structures is found to be more sharply tuned than the individual structures. This is a property that resembles the neural tuning of the sensory neurons, and for that reason it is a candidate to drive transduction in the CA.

The tympana that surround the sensory unit are reported to exhibit antiphasic motion, acting as levers that squeeze the sensory epithelium in a frequency dependent manner. Using OCT-vibrometry, we measured the two tympana that surround the sensory units simultaneously for the first time, and also the septum that lies between them (**Chapter 3**). We confirm the antiphasic manner of the two tympana and we report that the tracheal septum follows the anterior tympanum motion. This work on

the bushcricket CA is the first published study of insect hearing that applies OCT vibrometry.

Disentangling different directions of motion

The cochlear mechanics literature has been highly dominated by measurements of the BM motion, which is mainly transverse. Similarly for the insect hearing organ, the most accessible structures have been the two tympana, which are also dominated by transverse motion. This is partially the reason why complex directions of motion have not been discussed extensively when studying and modelling the mechanical responses of hearing organs. However, the above-mentioned hearing organs are filled with fluid that is incompressible and surrounded by stiff walls. Consequently, the fluid that is displaced by the transverse travelling wave is expected to escape towards other directions.

The anatomy of the OoC is highly suggestive of longitudinal and radial motion, as the angle of the OHCs and the Deiters' cells with the BM exhibits a gradient along the length of the cochlea. Radial motion has already been reported experimentally by Lee et al. (2016). In **Chapter 2** we manage to measure the travelling wave both propagating towards and away from the measurement beam. There is a distinct phase reversal across the two measurements that is highly indicative of motion along the longitudinal axis, and combined with the transverse motion this should result in elliptical trajectories. That finding challenges furthermore the idea that the OHCs simply push and pull the BM.

The current vibrometry techniques are only capable of capturing the projection of the overall motion of the measured structure onto the recording beam. The different vibration modes within the Organ of Corti reported in **Chapter 2** may well reflect differences in motion *direction* rather than differences in magnitude and phase of motion in a fixed direction, and in that case their appearance is shaped by a "viewing-angle bias", i.e., the recording beam favoring certain directions of motion over others.

In **Chapter 3**, we report different vibration modes in the structures surrounding the CA sensory dendrite. Following the same line of thinking, we postulate that the tuned vibration modes in the CA can be caused by a frequency dependent interplay of different directions of motion. In order to disentangle different directions of motion, we need to measure the same structure from two different angles. The insect CA is found on the front tibia of the bushcricket, and is easily accessible to OCT. For that reason, it is possible to use a mirror and measure sound induced vibrations on the CA from

two different directions (**Chapter 4**). We report that the structures surrounding the sensory dendrite exhibit elliptical motion, and that the relative motion along the two disentangled directions is sharply tuned. The methodological procedures developed in **Chapter 4** are fundamental for disentangling different directions of motion using OCT vibrometry. Similar techniques can be applied when studying the mammalian cochlea.

The temporal limits of OHC motility

As mentioned in the overview of cochlear mechanics section, the OHCs alter their length following changes in the receptor potential. The question that arises is how fast can the receptor potential follow changes in the receptor current, after it is filtered by the capacitive membrane. In other words, what is the corner frequency of the OHCs? To answer this question, we performed in vivo measurements of OHC motility. We presented the cochlea with sound and measured mechanical vibrations on the OHCs. The mechanical response included also frequencies that were not part of the stimulus. These vibrations were generated by the OHCs, and they follow changes in the membrane voltage. That way, we were able to isolate motility from the mechanical response, and report its temporal properties. The results presented in **Chapter 5**, show that the OHCs have a corner frequency that does not surpass 3-kHz. In summary, the OHC motility is much slower than the frequencies that these cells are often assumed to amplify in a cycle-by-cycle manner. These findings call for a fundamental reconsideration of the role of the OHCs in cochlear function.

What is the function of the OHCs?

In the final chapter of the current thesis, we take a step back to reconsider old and new findings that are important for the function of the OHCs (**Chapter 6**). As mentioned before, the OHCs are commonly viewed as sensors and actuators that amplify mechanical vibrations on a cycle-by-cycle basis. Amplification is thought to be necessary to overcome viscous damping and frictional losses in the mechanical responses of the cochlea, thus enabling high sensitivity to high-frequency sounds.

However, OHCs are rectifying and sluggish. Both these characteristics are not suited for a cochlear amplifier. The former because rectification introduces more distortions that weaken the signal-to-noise ratio, and the latter because the OHCs are reported to be too slow to amplify sound induced vibrations in a cycle-by-cycle

manner (**Chapter 5**). On the other hand, rectification followed by a low-pass filter yields a temporally integrated metric of intensity, and this is precisely what is needed for an automatic gain control (AGC) mechanism. An AGC adjusts the gain after assessing the overall magnitude of the displacement, it is resilient to noise and does not need to be fast.

Another consideration when discussing the cochlear amplifier is whether it is needed at all to overcome losses by viscous damping. In **Chapter 6** we report that low-intensity cochlear travelling waves suffer losses of only a few dB as they propagate to their peak region. At the same time, unless strongly attenuated, high-intensity travelling waves will evoke a destructive displacement amplitude of several hundred nanometers. A saturating amplifier at its best will not contribute to the destructive displacement magnitude. In contrast, an AGC control mechanism that regulates the amount of dissipation can protect the cochlea against vibration magnitude fluctuations that are potentially harmful.

Chapter 2

Vibration hotspots reveal longitudinal funneling of sound-evoked motion in the mammalian cochlea[1]

The micromechanical mechanisms that underpin tuning and dynamic range compression in the mammalian inner ear are fundamental to hearing, but poorly understood. Here, we present new, high-resolution optical measurements that directly map sound-evoked vibrations on to anatomical structures in the intact, living gerbil cochlea. The largest vibrations occur in a tightly delineated hotspot centering near the interface between the Deiters' and outer hair cells. Hotspot vibrations are less sharply tuned, but more nonlinear, than basilar membrane vibrations, and behave non-monotonically (exhibiting hyper-compression) near their characteristic frequency. Amplitude and phase differences between hotspot and basilar membrane responses depend on both frequency and measurement angle, and indicate that hotspot vibrations involve longitudinal motion. We hypothesize that structural coupling between the Deiters' and outer hair cells funnels sound-evoked motion into the hotspot region, under the control of the outer hair cells, to optimize cochlear tuning and compression.

[1] Cooper, N. P., Vavakou, A., and van der Heijden, M. (2018). Vibration hotspots reveal longitudinal funneling of sound-evoked motion in the mammalian cochlea. *Nature communications*, 9(1), 1-12. https://doi.org/10.1038/s41467-018-05483-z

Introduction

Before sound-evoked vibrations are converted into the neural signals that underlie our sense of hearing, the inner ear separates them by frequency and compresses them nonlinearly into a physiologically manageable dynamic range (von Békésy, 1960; Rhode, 1971; Sellick et al., 1982; Robles & Ruggero, 2001; Cooper, 2004). Each location along the length of the spiraling cochlear partition is tuned, in a level-dependent manner, to its own characteristic range of frequencies: high frequencies stimulate the cochlear base, and low frequencies, the apex (von Békésy, 1960). This place-based spectral analysis, or mechanical tonotopy, underlies the brain's ability to distinguish and identify sounds, even when multiple sound sources are present simultaneously. Exactly how the analysis is achieved is not understood, although the mechanical and physiological properties of key anatomical components have been studied in some detail (von Békésy, 1960; Olson & Mountain, 1994; Emadi et al., 2004; Scherer & Gummer, 2004; Spicer & Schulte, 1994; Zetes et al., 2012; He & Dallos, 1999; Ashmore, 2008). Many cochlear models rely on a hypothetical active process (the so-called "cochlear amplifier" (Davis, 1983; Kim, 1986)) to mimic contemporary physiological data, but evidence of cycle-by-cycle power amplification in real cochleae is sparse and indirect (De Boer & Nuttall, 2000; Lukashkin et al., 2007; Ren et al., 2011a; Dong & Olson, 2013), and the underlying assumptions made in many studies are not universally accepted (Allen & Fahey, 1992; Chen & Nuttall, 2009; van der Heijden & Versteegh, 2015a). A more complete understanding is currently limited by the difficulty of measuring the sound-evoked vibrations of key structures in intact cochleae. These structures are microscopic in scale and poorly accessible in vivo, and their vibrations are both small ($\sim$0.1–100 nm) and physiologically vulnerable (Robles & Ruggero, 2001).

Recent innovations in optical recording techniques, in particular high-speed optical coherence tomography (OCT), have begun to yield important new insights into the cochlea's micromechanics. One of the most significant recent findings is that the largest intra-cochlear vibrations do not occur on the basilar membrane (BM; Fig. 2.1), the structural element of the hearing organ that has been the focus of important experimental and theoretical work for over 50 years (Robles & Ruggero, 2001). Tissues located closer to the sensory inner and outer hair cells (IHC, OHC) of the organ of Corti, including the reticular lamina (RL) and tectorial membrane, have recently been shown to vibrate with much larger amplitudes, different phases (Chen et al., 2011; Ramamoorthy et al., 2014; Gao et al., 2014; Lee et al., 2015, 2016; Ren et al., 2016a,b;

Ren & He, 2018), and sharper tuning (Lee et al., 2015, 2016) than the BM.

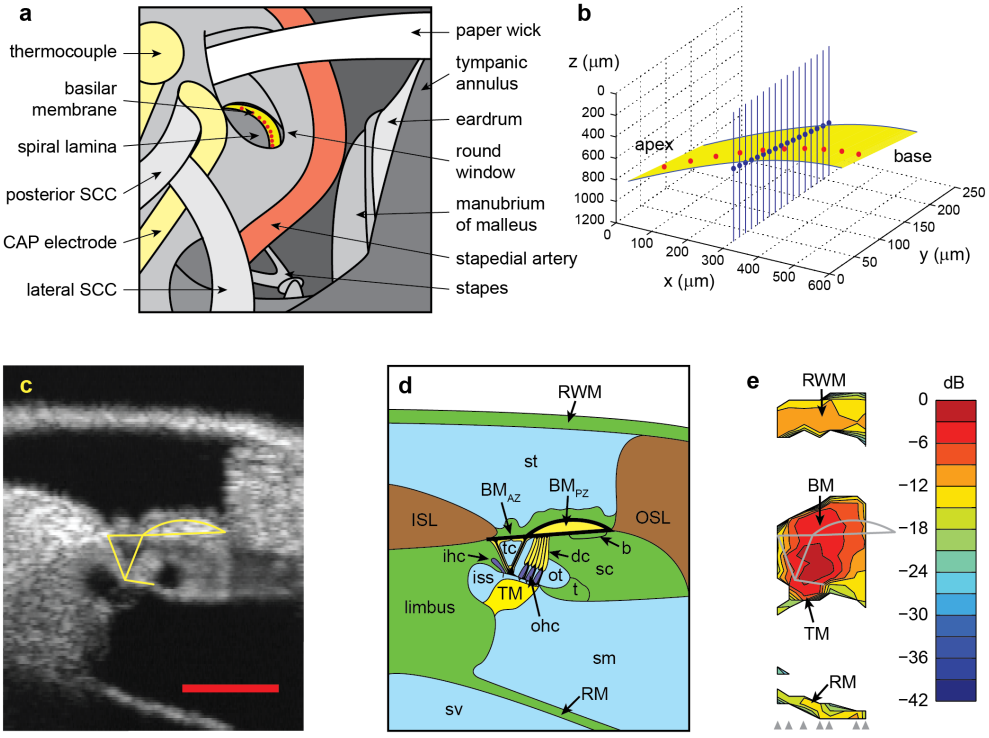

Figure 2.1: In vivo imaging and anatomy of the gerbil cochlear partition. (**a**) Experimental approach to the middle-ear, basilar membrane, and underlying structures of the cochlear partition in the round window region of the gerbil cochlea. (**b**) Vibration measurements are made by aligning the OCT beam with discrete points spanning the length (red dots) and width (blue dots) of the twisting, tilting, and spiraling cochlear partition (yellow). The measurement technique is sensitive only to vibration components that align with the near-vertical optical axis of each OCT beam. (**c**) OCT reflectance image (grayscale), with structural framework of Corti's organ (yellow) superimposed for reference (cf. **d**,**e**). Scale bar (red), 0.1 mm. (**d**) Underlying anatomical structures. The hearing organ's sensory cells are shown in dark blue, with key mechanical support cells and accessory structures in yellow. Thick black lines replicate elements of the main structural framework from **c**: the framework includes the collagen-rich arcuate and pectinate zones of the BM, the tubulin-rich inner and outer pillar cells that form the main (inner, triangular) tunnel of Corti, and the actin-rich reticular lamina (including the cuticular plates of the sensory inner and outer hair cells). (**e**) Map of vibration magnitudes evoked by a multi-tone stimulus at 70 dB SPL.

Magnitudes are expressed on a logarithmic color scale, in decibels (dB) relative to the maximum root-mean-square magnitude of 10 nm. Measurement beam ordinates are indicated at the base of the map using gray arrowheads. b Boettcher's cells, $BM_{AZ/PZ}$ basilar membrane arcuate and pectinate zones, CAP compound action potential, dc Deiters' cells, ISL inner (primary, osseus) spiral lamina, ihc inner hair cell, iss inner spiral sulcus, ohc outer hair cells, OSL outer (secondary) spiral lamina and ligament, ot outer tunnel of Corti, RM Reissner's membrane, RWM round window membrane, sc support cells, SCC semicircular canal, sm scala media, st scala tympani, sv scala vestibuli, t tectal cells, tc tunnel of Corti (inner). Preparation RG16760, CF 40 kHz.

In the current study, we apply OCT techniques to the basal turn of the gerbil cochlea. Unlike other OCT studies that image the intra-cochlear structures through the cochlea's bony wall, our recordings are made through the transparent round window membrane. The superior spatial resolution permitted by this approach allows us to construct detailed spatial maps of the intracochlear vibrations. These maps are inconsistent with the fundamental predictions made by many active models of cochlear mechanics. They reveal a sharply delineated vibration hotspot in the vicinity of the OHC and Deiters' cell bodies that stands out from the surrounding structures in several respects: it has much larger vibration amplitudes, broader frequency tuning, and a hyper-compressive dependence on sound intensity. Abstracts of this work have been presented at recent scientific meetings (Cooper & van der Heijden, 2018; van der Heijden & Cooper, 2018)

Methods

Animal preparation. Experiments were performed in accordance with the guidelines of the Animal Care and Use Committee at Erasmus MC, who approved all protocols. Sound-evoked vibrations were recorded from the cochlear partition and ossicles of healthy young female gerbils (n= 51, aged 44–188 days, weight range 54–82 g; the main reason for only studying females is that they are more sociable than males, and therefore more convenient to accommodate within Erasmus MC).

Animals were anesthetized using intraperitoneal injections of ketamine (80 mg/kg) and xylazine (12 mg/kg), with no recovery allowed at the end of the experiments. Maintenance (1/4) doses of the anesthetic were given at intervals of between 10 and 60 min, as required to abolish pedal withdrawal reflexes. Animals were tracheotomized, but self-ventilating. Core temperatures were maintained at 38 °C using a thermostatically controlled heating pad. The pinna and external meatus of the left ear was retracted

and a $4 \times 6\text{mm}^2$ wide opening was made into the postero-lateral bulla to expose the basal aspects of the cochlea, including the round window and the middle-ear ossicles (Fig. 2.1a). Additional heating of the environment around the animals head was provided using a thermostatically controlled infrared lamp, such that the temperature at the edge of the open bulla was maintained at 34–35 °C. A paper wick was used to prevent any buildup of exudate in the round window recess; the wick was positioned so as not to impede movements of the round window membrane itself (see Fig. 2.1a).

All experiments were performed in a sound-proof chamber, with the animals supported in a goniometric cradle mounted on a vibration isolated table. Imaging and vibration measurements were made in the first turn and hook region of the cochlea, as viewed through the intact round window membrane, and from the footplate and/or posterior crux of the stapes in the middle ear. All measurements were made under open-bulla conditions, but the cochlea itself was intact. The physiological condition of the cochlea was assayed using compound action potential measurements from a silver wire electrode placed on the wall of the basal turn of the cochlea (Johnstone et al., 1979).

OCT imaging and vibrometry. A spectral domain OCT system (Thorlabs Telesto TEL320C1, operating with a central wavelength of 1300 nm) was used for interferometric imaging and vibration measurements. The system provided cross-sectional (B-scan) and axial images (A-scans and M-scans) that were triggered externally using TTL pulses phase-locked to an acoustic stimulation system (Tucker Davies Technologies system III). The sampling rate of both the sound generation and OCT-recording system was 111.6 kHz. The M-scans consist of time-stamped optical spectra whose Fourier transforms provide depth-resolved images (i.e., maps of scattering intensity versus axial depth) and vibration information (i.e., maps of scatterer-displacement versus axial depth). Each optical spectrum (A-scan) had 2048 samples covering the $\sim$210 nm bandwidth of the interferometer's light source; each instantaneous axial image and vibration map correspondingly had 1024 spatial "pixels" covering the instrument's $\sim$3.5 mm depth-of-field (i.e., z-range). The optical recording system had an axial point spread function with a FWHM of $\sim$6 μm, a lateral resolution (in the xy plane) of 13 μm, and a linear operating range of > 500 μm (all assessed in air, with a refractive index of 1). For comparison with other studies, e.g., refs. (Chen et al., 2011; Ramamoorthy et al., 2014; Lee et al., 2015, 2016; Ren et al., 2016a,b), the theoretical axial resolution of our OCT system was $\sim$2.9 μm in perilymph (with

an assumed refractive index of 1.3); the numerical aperture of the imaging lens was 0.055, and the amount of light incident on the cochlea was ∼3.7 mW. The sensitivity of the A-scan's phase-spectra to vibration permitted measurement noise-floors that ranged from ∼ 30 pm/√Hz in the cochlea down to ∼ 3 pm/√Hz in the middle ear.

Intra-cochlear images (B-scans) were formed by scanning the OCT across a series of parallel, quasi-radial (but typically far from transverse) planes that sectioned the cochlear partition at different longitudinal positions (cf. Fig. 2.1b; in this example, quasi-radial B-scans were made at each of the positions indicated by the red dots). The spacing between the initial measurement planes was ∼50–100 μm. Readily identifiable loci within each of the resultant images (e.g., the characteristic junction between the arcuate and pectinate zones of the BM; cf. Fig. 2.1c, d) were then used to define the true longitudinal, radial and transverse axes of the partition post-hoc. Images were subsequently compensated for the oblique angles of incidence of the recording beam, and for the refractive index of the intracochlear fluids, which was assumed to be 1.3.

Vibration measurements (M-scans) were made by aiming the OCT at one particular x,y locus and recording a contiguous series of ∼1.5 million A-scans, before moving on to repeat the same procedure at subsequent sites if and when required (cf. Fig. 2.1b). For radial mapping purposes (cf. Figs. 2.1e, 2.2–2.4, and Supplementary Figs. 2.10, 2.11), measurement positions were typically spaced at intervals of between 6 and 12 μm in the xy plane (e.g., see blue dots in Fig. 2.1b).

It is important to note that the alignment of the measurement beams in most of our OCT recordings was far from perpendicular to any of the cochlea's principal anatomical axes (cf. Figs. 2.1b, 2.8): the measurements that we made from each angle should therefore be sensitive to structural movements in all three cochlear dimensions (radial, transverse, and longitudinal). Some fundamental consequences of this three-dimensional sensitivity are explored further in the Supplementary Note 4 (cf. Supplementary Fig. 2.12).

Post-hoc skew correction. Vibration measurements were corrected for the refractive index of the fluid, but not (directly) for the angle of incidence. Post-hoc corrections were made for the longitudinal skew of the measurement sites with sectioning depth (i.e., z in Fig. 2.1b): both the amplitude and the phase of the recorded vibrations were adjusted according to preparation-specific tonotopic maps derived by interpolation from the previous (longitudinal) series of measurements at well identified anatomical loci (see above, and red dots in Fig. 2.1b). The skew corrections result in maps of

vibration that correspond to planes that are perpendicular to the longitudinal axis of the organ of Corti, even though the measurement beam was not perpendicular to this axis. Without this correction, the slanted orientation of the cross sections would introduce a parallax, i.e., a confounding between transverse and longitudinal dimensions. The deeper structures in most of our cross-section are located further in the apical direction (Fig. 2.1b), resulting in larger phase lags and lower CFs than the more superficial structures. This parallax is undone by the correction.

Acoustic stimulation. To optimize the amount of useful information that could be collected in each experiment, multi-tone "zwuis" complexes (Versteegh & van der Heijden, 2012) were used as acoustic stimuli. Each complex had between 30 and 50 spectral components spanning most of the animal's hearing range (typically 0.2 to ∼30 or ∼50 kHz). All components had approximately equal amplitudes, but phases that were randomized across frequency. Each stimulus was presented for 12 s, and inter-stimulus intervals were ∼1 min. The stimuli were coupled into the exposed ear-canal using a pre-calibrated, closed field sound-system. Sound pressure levels are expressed in decibels re: 20 μPa (i.e., dB SPL) per spectral component.

Response analysis. Responses were analyzed by Fourier transformation of the vibration waveforms derived from contiguous groups of 3 pixels in each M-scan, where each pixel covers a depth of ∼2.7 μm in the fluid-filled spaces of the cochlea, and ∼3.5 μm in the air-filled spaces of the middle-ear. Responses from intracochlear locations were corrected for path-length differences originating in the movements of the overlying round window membrane (i.e., the air–fluid interface in our preparations; cf. ref. Cooper & Rhode (1992)). The statistical significance of each response component was assessed using Rayleigh tests of the component's phase stability across time (Versteegh & van der Heijden, 2012). Two-dimensional interpolation was used for spatial mapping purposes (see Supplementary Fig. 2.9).

Data availability. The data presented in Figs. 2.1-2.8 of this study can be found at `https://doi.org/10.6084/m9.figshare.c.4147139`.

Results

Imaging structure and function through the round window. Optical measurements of the cochlear partition's structure and mechanical function were made in

the basal turns of living gerbil cochleae (Fig. 2.1; see Methods). The views obtained through the transparent round window membrane yield anatomical and physiological measurements with high spatial resolution: the fluid-filled scalae, sulci, and tunnels are readily differentiated from the cellular and extracellular structures that make up the organ of Corti, and key cellular components can be identified from their positions within the organ (Fig. 2.1c,d). Observing this level of anatomical detail in intact,

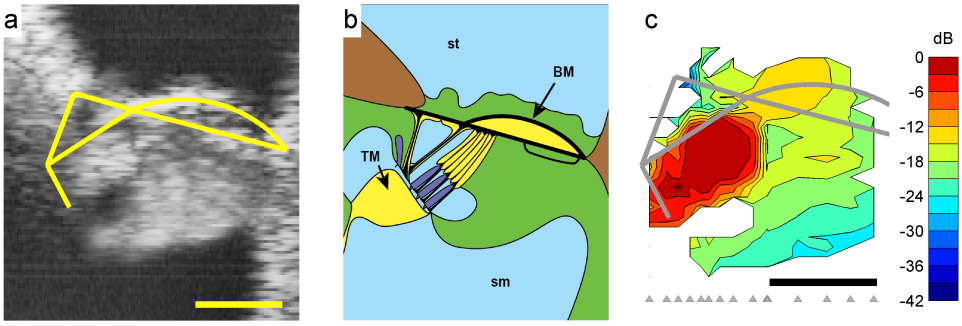

Figure 2.2: A vibration hotspot at low sound levels in the organ of Corti. (**a**) OCT reflectance image (grayscale), with structural framework of Corti's organ (yellow) superimposed for reference. Scale bar (bottom), 0.05 mm. (**b**) Underlying anatomical structures, labeled as in Fig. 2.1c. (**c**) Map of vibration magnitudes evoked by the 22.6 kHz component of a multi-tone stimulus at 40 dB SPL. Magnitudes are expressed in decibels relative to the 3-nm maximum observed at the location marked with an asterisk. Measurement beam ordinates are indicated at the base of the map using gray arrowheads, and the axial (vertical, z) resolution is $\sim$8 μm. Vibrations clearly focus on a hotspot that encompasses the OHC and Deiters' cell bodies, and sits well within the boundaries of the organ of Corti's structure (gray framework). Scale bar, 0.05 mm. Preparation RG16725, CF 23 kHz.

living cochleae is unprecedented: even the two layers of collagen fibers that make up the pectinate zone of the BM can be distinguished quite clearly in most images, the highly oriented fibers acting as strong scatterers of the infrared light. The intersection between the arcuate and pectinate zones of the BM is almost always clearly visible, and facilitates the precise registration of a virtual structural framework (Fig. 2.1c, yellow) that we will use to facilitate interpretation of our results in subsequent figures. This framework delineates the arcuate and pectinate zones of the BM, the tubulin-rich inner and outer pillar cells, and the actin-rich RL that reaches out laterally to the

tectal (support) cell region (Fig. 2.1d; see Slepecky (1996) for review). The anatomical structures and dimensions that we observe in vivo are consistent with anatomical studies on fresh postmortem preparations, but differ considerably from those observed in fixed tissue (Edge et al., 1998). The physiological measurements of Fig. 2.1e illustrate that sound-evoked structural motion is focused near the center of the organ of Corti, with distal structures, including the round window membrane, Reissner's membrane, and the limbal zone of the tectorial membrane, vibrating around 3–5× (i.e., 9–15 dB) less than those near the center of the organ. This focusing of the sound-evoked vibration is frequency-dependent, and becomes even more pronounced at lower sound pressure levels, as described below.

Vibration hotspots. Figure 2.2 compares an OCT image of the 23-kHz region of the cochlea with a map of the vibration amplitudes evoked by the characteristic frequency (CF) component of a 40-dB-SPL multi-tone stimulus. The vibration map (Fig. 2.2c; see Supplementary Note 1 for raw data) shows that the largest vibrations occur in a highly restricted and well-delineated area well within the main body of the organ of Corti. This vibration hotspot centers near the bases of the OHCs and the apices of the adjoining Deiters' cells. It extends depth-wise from the RL to within ∼20 μm of the BM, and width-wise from the outer pillar cells to the outer tunnel of Corti (i.e., the interface between the OHC/Deiters' cells and the Hensen's/tectal cell area). We refer to this region as the OHC/Deiters' cell vibration hotspot, and focus the current paper on characterizing its acousto-mechanical properties.

We estimate the dimensions of the OHC/Deiters' cell hotspot to be ∼50 μm × ∼30 μm at its 10-dB-down points. The hotspot has a sharp boundary, and the vibration amplitudes change only gradually either inside or outside this boundary. Away from the hotspot, vibration amplitudes decrease progressively across the radial extent (i.e., the width) of the cochlear partition, including the BM and supporting cells of the organ of Corti.

We observed sharply focused vibration hotspots in the OHC/ Deiters' cell region of all healthy cochleae ($n = 31$) tested, over wide ranges of sound frequency (Supplementary Note 2, Supplementary Figs. 2.10-2.11) and intensity (Fig. 2.3). Hotspots in the OHC/Deiters' cell region were reduced and/or absent at high sound levels (cf. Figs. 2.1e, 2.3c), and occasionally even inverted (i.e., turned into equally-distinct coldspots) for high-frequency and high-intensity stimuli. OHC/Deiters' cell hotspots were also reduced in physiologically compromised cochleae, and disappeared from healthy cochleae

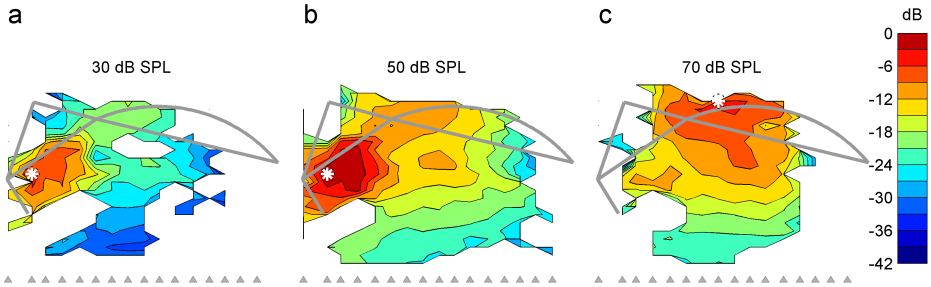

Figure 2.3: Level-dependent modes of vibration near CF. Maps of vibration magnitudes evoked by the 22.6 kHz component of a multi-tone stimulus at three sound pressure levels: (**a**) 30, (**b**) 50, and (**c**) 70 dB SPL. Magnitudes are expressed in decibels relative to the 4.1-nm maximum observed at the location marked with the white asterisk in **b** (asterisks in **a** and **c** mark the sites of peak amplitudes at 30 and 70 dB SPL = 2.6 and 2.1 nm, respectively). Measurement beam ordinates are indicated at the base of each map using gray arrowheads. The structural framework of the organ of Corti is shown for reference in gray (cf. Figs. 2.1, 2.2). Data were obtained from the same preparation as in Fig. 2.2, CF 23 kHz.

soon after death (Fig. 2.4). Whenever the OHC/Deiters' cell hotspot was reduced, inverted or absent, the organ of Corti's peak vibration amplitudes switched to one of two other locations in a frequency-dependent way: low-frequency ($<\sim$5–10 kHz) responses became dominated by vibrations in the lateral (Hensen's) support cell region $\sim$50–100 μm away from the OHC/Deiters' cell area, while high-frequency responses became dominated by BM vibrations (Fig. 2.3c).

Broader frequency tuning of the hotspot. Mechanical tuning of BM vibrations is remarkably similar (although not entirely identical) to electrophysiological tuning in IHCs, OHCs, and the auditory nerve (Sellick et al., 1982; Robles & Ruggero, 2001; Patuzzi & Robertson, 1988; Kössl & Russell, 1992; Narayan et al., 1998). As the OHC/Deiters' cell vibration hotspot is sandwiched between the BM and the site of stimulus transduction by the IHCs and OHCs, one might expect the frequency selectivity in the hotspot to approximate IHC, OHC, and neural tuning at least as well as the BM does. To test this hypothesis, we compared the tuning properties of three key locations in and around a vibration hotspot (Fig. 2.5). While all three

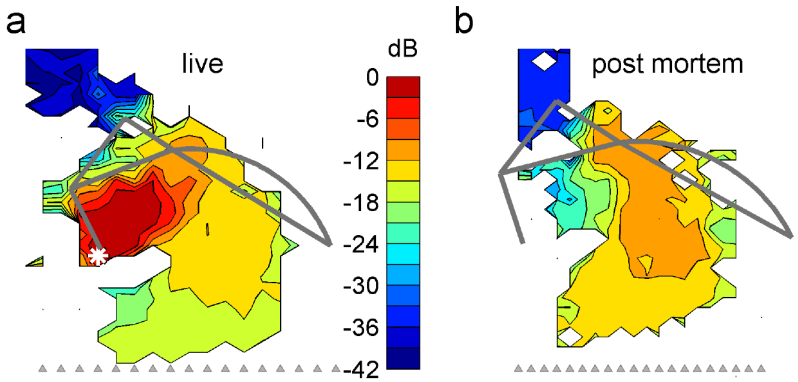

Figure 2.4: Post-mortem disappearance of a vibration hotspot. (**a**) In vivo vibration map for the 11.2 kHz component of a 65-dB-SPL multi-tone stimulus, showing a clear hotspot in the OHC/Deiters' cell region. (**b**) Post-mortem vibration map at the same frequency, and evoked by the same stimulus in the same cochlea, within 30 min after death. Vibration magnitudes in both panels are expressed in decibels relative to the 2.6-nm maximum observed in vivo at the location marked with the white asterisk in **a**. The hotspot vibrations reduce at least 10-fold (i.e., 20 dB) post-mortem, while vibrations elsewhere in the body of the organ of Corti increase and BM vibrations remain essentially unchanged. Preparation RG17793, CF 20 kHz.

of these locations are tuned to similar frequencies (∼23 kHz, Fig. 2.5a) and have similar overall phase characteristics (Fig. 2.5b), there are major differences between the overall shapes and/or depths of their tuning curves. The BM is the most sharply tuned of the three sites in terms of its tip-to-tail ratio (showing a 45-dB difference in gain from ∼0.4 to 23 kHz), followed by the heads of the Deiters' cells in the hotspot itself (tip–tail ratio ∼31 dB) and the tectal/Hensen's (supporting) cell region ∼50 μm lateral to the hotspot (tip–tail ratio ∼20 dB). Although a direct comparison with auditory nerve data from this region of the gerbil cochlea is difficult, the BM's tuning is the closest to matching typical high-frequency neural tuning curves, whose tip–tail ratios exceed 40 dB (Patuzzi & Robertson, 1988; Ohlemiller & Echteler, 1990).

Other differences between the tuning curves in Fig. 2.5 are also noteworthy. The heads of the Deiters' cells vibrate ∼3× more than the BM around CF, and >10× more than the BM at low frequencies. Hensen's and tectal cells vibrate ∼2–3× less than the BM near CF, but 3–10× more than the BM below 5 kHz. Deiters' cell vibrations phase-lead BM vibrations by ∼0.1 cycles around CF and up to 0.4 cycles at low

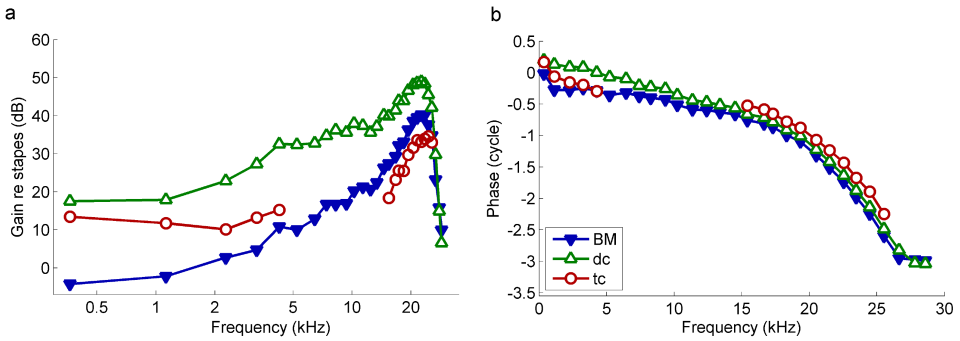

Figure 2.5: Tuning characteristics of the vibration hotspot and adjacent structures. (**a**) Amplitude- and (**b**) phase-transfer functions evaluated at three locations in the living organ of Corti: filled triangles, near the junction between the arcuate and pectinate zones of the BM; open triangles, in the Deiters' cell (dc) bodies near the center of the vibration hotspot, ∼40 μm away from the BM; and circles, in the Hensen's/tectal cell (tc) region ∼50 μm lateral to the Deiters' cells. Gain and phase are referenced to the stapes vibrations evoked by identical multi-tone stimuli. Preparation RG17805, CF 25 kHz (see Fig. 2.6). Stimulus level 50 dB SPL.

frequencies, while Hensen's/tectal cell vibrations phase-lead BM vibrations by ∼0.1 and 0.3 cycles at low and high frequencies, respectively (Fig. 2.5b). These systematic differences in tuning between different sites within the organ of Corti demonstrate that the organ's main vibration modes are frequency-dependent (further illustrated in Figs. 2.6, 2.7, and Supplementary Figs. 2.10, 2.11). As shown explicitly in Fig. 2.3 and implied in Fig. 2.6, some of these vibration modes are intensity dependent, too.

Hyper-compression in the hotspot. BM vibrations grow less than proportionally with sound pressure near CF (Rhode, 1971; Sellick et al., 1982; Robles & Ruggero, 2001; Cooper, 2004). The functional correlate of this nonlinear behavior is a compression of the huge dynamic range of everyday sounds to fit the much smaller dynamic range of the IHC transduction channels. As the OHC/ Deiters' cell hotspot is sandwiched between the BM and the IHC and OHC transduction sites (and contains the very OHCs that are thought to mediate compression), motion in the hotspot region is expected to show compressive behavior too.

To compare the nonlinear compression between BM and hotspot we constructed tuning curves, normalized to middle ear motion, for a wide range of sound intensities (Fig. 2.6a, b). At low frequencies (<0.7× CF) the normalized BM curves coincide

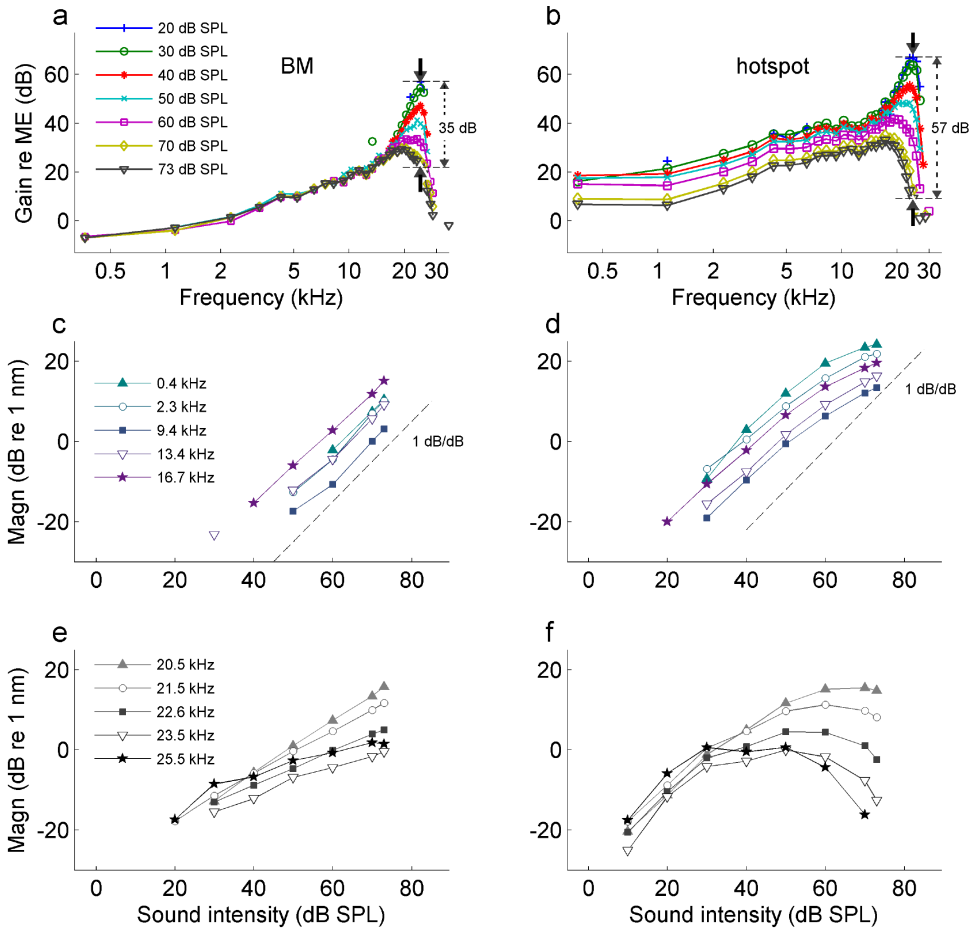

Figure 2.6: Compression on the BM (left) versus hyper-compression in the hotspot region (right). (**a**,**b**) Vibration magnitude as a function of frequency, normalized to stapes motion. Sound intensity is indicated in the key, with arrows indicating amounts of compression observed at CF (25 kHz) between 20 and 73 dB SPL. (**c**,**d**) Below-CF input–output functions for different frequencies, based on the tuning curves of panels **a**,**b**. Dashed lines illustrate linear growth for reference. (**e**,**f**) Near-CF input–output functions. Data were obtained from a single preparation (the same one as in Fig. 2.5, CF 25 kHz), and acquisition from the two locations was interleaved.

(Fig. 2.6a), indicating linear growth of BM vibration with sound pressure. Only near CF do the BM responses show compressive nonlinearity, visible in Fig. 2.6a as a gain reduction with increasing intensity. This spectrally selective form of compression agrees with a large body of historical BM data (Rhode, 1971; Sellick et al., 1982; Robles & Ruggero, 2001). The hotspot vibrations (Fig. 2.6b) also show compressive nonlinearity, but this differs from the BM in two major respects: the frequency range and the strength of the compression. Hotspot motion is compressive over the entire frequency range, down to the lowest frequencies tested (6 octaves below CF). Near CF, where both BM and hotspot are nonlinear, the compression is stronger in the hotspot than on the BM: between 20 and 73 dB SPL, the sensitivity at CF drops by 57 dB in the hotspot versus 35 dB on the BM (Fig. 2.6a, b).

The stark contrast in nonlinear behavior between BM and hotspot is further illustrated by input/output (I/O) functions (Fig. 2.6c–f). Well below CF, the BM exhibits linear (1-dB/dB) growth (Fig. 2.6c), whereas all of the low-frequency I/O functions for the hotspot (Fig. 2.6d) are compressive (<1 dB/dB). The hotspot tuning functions (Fig. 2.6b) in this frequency range run parallel, indicating that the hotspot nonlinearity behaves identically for all frequencies up to ∼17 kHz, i.e., 1/2 octave below CF. When increasing the frequency toward CF (25 kHz) and beyond, even stronger differences between BM and hotspot are revealed. The BM I/O functions become increasingly shallow at higher frequencies (Fig. 2.6e), but their growth rates remain positive. In contrast, the near-CF hotspot I/O functions exhibit systematic hyper-compression: following their initial growth at low intensities, the hotspot responses start to decrease beyond a certain stimulus intensity (Fig. 2.6f). The reversal point shifts to lower intensities for the higher frequencies.

Spatial dissection of hotspot motion. To analyze the spatial profile of the organ of Corti's vibrations and to further assess its frequency dependence, we defined a quasi-transverse pathway through the cochlear partition (Fig. 2.7a, red arrow). This path starts at the BM, follows a straight line that runs close to the main axes of the Deiters' cells and OHCs, and ends at the RL. Using the BM as reference for the motion across this pathway, we obtained spatial profiles (one per frequency) of the vibrations within the organ of Corti. These profiles show rapid, frequency-dependent spatial gradients of vibration amplitude (Fig. 2.7b) and phase (Fig. 2.7c) over extremely short distances—particularly at low frequencies. In this example, the steepest transitions occur within a 10-μm stretch starting ∼10 μm beneath the level of the BM, where

vibration levels increase by 15–20 dB (i.e., 5–10×) and phase-leads of over 0.25 cycles accumulate at low frequencies (a 0.25-cycle phase-lead means that hotspot velocity synchronizes with BM displacement).

Beyond the ∼10-μm-thick transition layer which forms one edge of the hotspot, vibration amplitude grows more gently and tends to plateau, typically peaking slightly around the middle of the OHC region. Beyond these peaks, the amplitudes fall by 2–3 dB (i.e., to 0.7–0.8×) towards the RL and tectorial membrane (at the OHCs' apices). Response phases (Fig. 2.7c) remain stable across most of the Deiters' and OHC region, particularly at low frequencies. Thus, most of the hotspot moves together, as a single unit (with a deformable framework, e.g., as illustrated in Fig. 2.7e, f). From a mechanical perspective (see Discussion), it is important that the amplitude and phase variations (from outside to inside the hotspot) are graded with frequency: the largest spatial gradients occur at low frequencies, and the smallest ones around CF (Figs. 2.5, 2.7, 2.8).

The relative motion of any pair of points on a pathway is readily determined by computing the vector difference of their vibrations. In the 50-dB-SPL data of Fig. 2.7, the differential motion between the two ends of the Deiters' cells soma is 2.0 ± 0.8 nm (mean ± standard deviation, $n = 26$ frequencies), while for OHCs the end-to-end motion is −0.9 ± 0.5 nm. Assuming that both the pathway illustrated in Fig. 2.7 and the cellular vibrations that we measure are closely aligned with the principal axis or axes of the OHCs and Deiters' cells, the ratio of these two differential motions should indicate the relative length changes of the two cell types. Under these one-dimensional assumptions, the data of Fig. 2.7 indicate that Deiters' cells change length (cyclically) during sound stimulation by ∼2× as much as OHCs do.

The suggestion that Deiters' cells undergo cycle-by-cycle length changes that are greater than the compliment of the OHCs' length changes is difficult to reconcile with prevailing ideas in cochlear mechanics (see Discussion), and there are many reasons to doubt that sound-evoked motion in the cochlea should be limited to the transverse and/or radial dimensions, as assumed in the one-dimensional analysis above. A more plausible alternative interpretation may be that motion in all three dimensions is involved, and that the longitudinal component of this motion becomes particularly significant, especially at low frequencies, in the hotspot region (see Supplementary Notes 3, 4 for the rationale behind this suggestion). It is this longitudinally directed form of motion that is illustrated in Fig. 2.7d–f and Supplementary Movie 1, and that is tested for experimentally below.

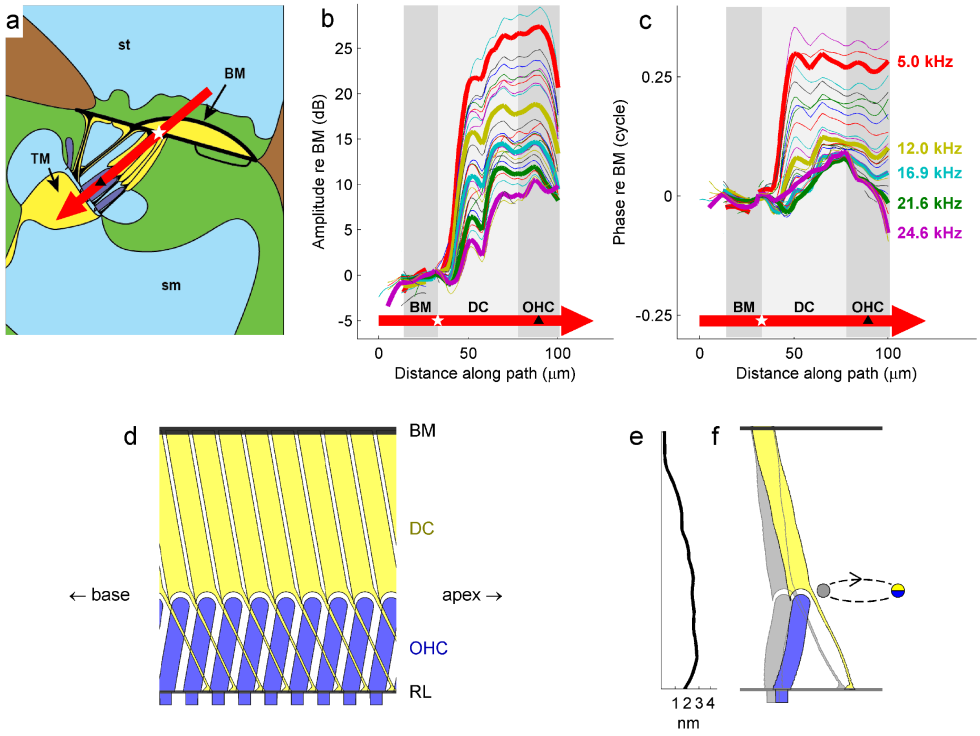

Figure 2.7: Frequency-dependent spatial profiles of a vibration hotspot. (**a**) Transverse anatomical schematic for the 23 kHz region of the gerbil cochlea (cf. Fig. 2.2a), illustrating the spatial pathway (red arrow) across which vibration amplitude (**b**) and phase (**c**) were analyzed. The white star marks the reference point on the BM; the black triangle the middle of the outer hair cell region. (**b**,**c**) Spatial profiles of vibration amplitude and phase for 21 different frequency components (color-coded) in a multi-tone stimulus. The curves for five frequencies (indicated in **c**) are highlighted by increased line width. Amplitudes and phases are expressed relative to those observed on the BM (cf. white star in **a**). Gray patches indicate the different regions traversed by the red arrow, including the BM, Deiters' cells (DC), and OHCs. (**d**) Schematized anatomical relationship between Deiters' cells (yellow) and OHCs (blue) along the longitudinal axis of the cochlea, perpendicular to the section shown in **a**. The cells are shown suspended between BM and RL, with the OHC stereocilia protruding downwards (beneath the level of the RL). The apical-ward projection of the Deiters' cells soma and phalangeal processes contrasts with the basal-ward projection of the OHC (Brownell et al., 1985; Soons et al., 2015). (**e**) Measured vibration profile for the 5-kHz data of **b**, recast onto linear coordinates, for comparison with the cartoon in **f**. (**f**) A hypothetical interpretation of the profile from **e**, based on the idea that motion in the OHC/Deiters' cell hotspot is primarily oriented in the longitudinal direction

(see text). Two snapshots of a single OHC/Deiters' cell "unit" are shown, one in gray and the other in colors (blue, OHC; yellow, DC). The snapshots depict the unit at the two extremes of an elliptical vibration cycle. The illustrated movement is highly exaggerated: the measured 2.8-nm maximum displacement is scaled up 1000-fold, relative to the scale of the cellular anatomy, to make it visible in the illustration. Data were obtained from the same preparation as in Figs. 2.2, 2.3, CF 23 kHz. Stimulus level 50 dB SPL.

Testing for longitudinal motion in the hotspot. To test for the existence of longitudinal motion in our recordings, we studied the effects of changing the angle of incidence of our measurement beam (Fig. 2.8). Knowing that the underlying BM's motion is almost entirely transverse in nature (Fig. 2.8a; see refs. von Békésy (1960); Lighthill (1978, 1981)), the simple geometrical considerations of Fig. 2.8b predict that any longitudinal motion in the nearby fluid or structures should be sensed with opposite polarities from the two sides of the cochlea's transverse plane (Fig. 2.8b,c; see Supplementary Note 4 for details).

In most of our experiments, the longitudinal viewing angle of our measurements was such that the incident light-beam pointed towards the apex of the cochlea (cf. α_1 in Fig. 2.8b). In all of these experiments, motion recorded from the hotspot region phase-led the BM in a frequency-dependent manner (cf. Figs. 2.5, 2.7, Supplementary Fig. 2.11). In two particularly revealing experiments, however, we managed to realize a viewing angle that was flipped longitudinally (cf. α_2 in Fig. 2.8b). In these two experiments, the hotspot region was found to phase-lag the BM in a frequency dependent manner, with the largest phase-differences and amplitude-gains observed at low frequencies (Fig. 2.8e,f).

This effect of viewing angle on the polarity (lead versus lag) of the relative hotspot/BM phase confirms two of six predicted measurable effects of longitudinal motion derived in Supplementary Note 4. The other four predicted effects were also observed without exception: both phase- and amplitude differences between hotspot and BM motion were larger at lower frequencies; low-frequency hotspot-to-BM phase-differences often exceeded 0.25 cycles, and occasionally approached 0.5 cycles; and significant hotspot-to-BM phase-differences were still observed from viewing angles that were almost perpendicular to the BM. These observations provide strong support for the idea that vibrations in the OHC/Deiters' cell hotspot involve longitudinal (in addition to transverse, and probably radial) motion, as schematized in Supplementary Movie 1.

Discussion

The high-resolution vibration maps presented here reveal a well delineated vibration hotspot whose epicenter lies partway between the RL and the BM. This hotspot extends as far as the RL, but it also contains both the basal poles of the OHCs and the heads of the adjoining Deiters' cells. This is a significant new finding, building on numerous studies which have already demonstrated that different structures within the cochlear partition move to differing degrees, in different directions, with different phases and different frequency-dependencies (von Békésy, 1960; Chen et al., 2011; Ramamoorthy et al., 2014; Gao et al., 2014; Lee et al., 2015, 2016; Ren et al., 2016a,b; Ren & He, 2018). These findings shed new light on the internal workings of the hearing organ, and are likely to pre-sage significant improvements in the understanding of a very complex system.

The sound-evoked vibration characteristics that we observe in the OHC/Deiters' cell hotspot are strikingly similar to those reported recently at the RL level by Ren et al. (Ren et al., 2016b; Ren & He, 2018) and by Oghalai's group (Gao et al., 2014; Lee et al., 2016). Ren et al. made sequential measurements from individual loci on the RL and BM, as viewed through the transparent round window membrane in the basal turn of the cochlea, whereas Oghalai's group made more panoramic, simultaneous measurements by applying the OCT technique through components of RL motion that are more broadly tuned, more extensively nonlinear, and up to 10× larger than BM motion. Additionally, Ren et al. (Ren et al., 2016b; Ren & He, 2018) report physiologically vulnerable low-frequency phase leads approaching 0.5 cycles between RL and BM, while Oghalai's group emphasize a much less-vulnerable 0.5-cycle phase difference between the BM and the lateral compartment of the organ of Corti at high frequencies (Gao et al., 2014). All of these findings are consistent with observations made in the present report, which combine the panoramic OCT technique with the improved optical access afforded by the round-window approach. The new information added by our study is that: (i) the entire OHC/Deiters' cell hotspot region shares many of the characteristics previously attributed to the RL; (ii) hotspot vibrations exhibit hyper-compression near their CF; and (iii) hotspot vibrations appear to involve longitudinal motion.

Sound-induced vibrations within the hotspot contrast sharply with those of nearby

structures like the BM, tectal, and Hensen's cells. The steep amplitude and phase gradients observed only 10–20 μm away from the BM (Figs. 2.2, 2.7) underscore the importance of good spatial resolution. Without this, BM, hotspot and other vibrations cannot be isolated with confidence (Cooper & van der Heijden, 2018). It is reassuring that our BM data are consistent with the extensively documented BM measurements obtained with traditional techniques (Robles & Ruggero, 2001), expressing large tip-to-tail ratios, linearity up to 1/2 octave below CF, and shallow but positive growth near CF. The hotspot region behaves very differently from the BM, however, and the challenge now is to identify its underlying mechanism from both physical and functional perspectives.

From a physical perspective, it is highly unlikely that the hotspot's spatial profile (as illustrated in Figs. 2.2–2.4, 2.7, 2.8) can be underpinned by purely transverse motion within the organ of Corti. This would involve enormous squeezing of the thin fluid-filled layers that make up the transition regions near the feet of the Deiters' cells (at one edge of the hotspot), and would not explain why phase differences of over 0.25 cycles occur between nearby layers at low frequencies. These characteristics are much easier to understand when assuming that the differences in measured magnitude and phase coincide with differences in the direction of motion across nearby layers, i.e., if the layers would be sliding with respect to each other in the radial and/or longitudinal direction. Such motion, with both radially and longitudinally directed components, has been observed directly in at least two previous studies: one using high sound levels in passive cochleae (von Békésy, 1960), and one using electrical stimulation in isolated turns of excised cochleae (Karavitaki & Mountain, 2007). The results of our study (Figs. 2.7, 2.8) provide strong evidence that longitudinal motion is also evoked by low-level sounds in vivo-i.e., in active, functioning cochleae.

Longitudinal motion (which is not to be confused with longitudinal coupling of transverse motion) has rarely been invoked in the analysis of traditional cochlear-mechanical (BM) data. This is partly because the BM is known not to undergo significant longitudinal motion (von Békésy, 1960). The ribbon-like BM is firmly clamped at both edges and contains dense layers of stiff, strongly interconnected fibers (von Békésy, 1960; Slepecky, 1996). It is also sandwiched between two fluid-filled ducts which act anti-symmetrically on its two faces (von Békésy, 1960; Lighthill, 1978), providing little net drag in the longitudinal direction. The situation is very different inside the OHC/Deiters' cell hotspot, where motion is likely to be subject to constraints intermediate to those on the BM and in the surrounding fluid (see

Supplementary Notes 3, 4). Deiters' cells and OHCs are suspended (or sandwiched) quite freely between the BM and RL (von Békésy, 1960; Slepecky, 1996; Karavitaki & Mountain, 2007; ter Kuile, 1900), and various observations suggest that the RL is much less stiff and less securely tethered than the BM (von Békésy, 1960; Scherer & Gummer, 2004; ter Kuile, 1900; Mammano & Ashmore, 1993). Deiters' cells, OHCs, and even the RL may therefore offer little opposition to movement in either longitudinal or radial directions (von Békésy, 1960; ter Kuile, 1900; Brownell et al., 1985; Lim, 1980).

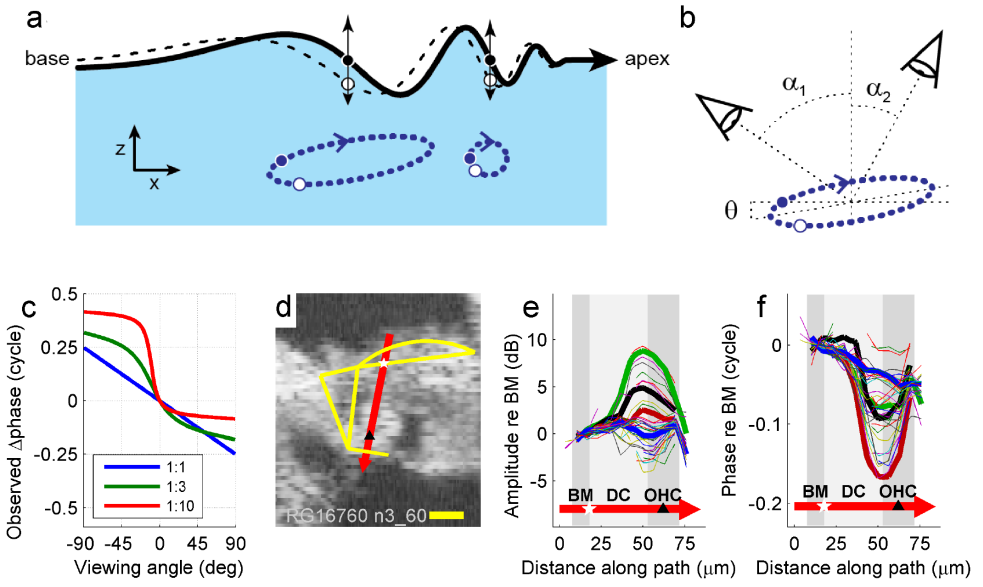

Figure 2.8:Viewing-angle dependent 'relative-phase inversion' of hotspot motion. (**a**) Contrast between the purely transverse motion of the BM (vertical arrows) and the elliptical trajectories predicted for fluid (and potentially structural) particles underlying a surface wave in the cochlea (von Békésy, 1960; Lighthill, 1978, 1981; Marquardt, 2018). The wave's surface (the BM, black line) is pictured at two instants in time, separated by 1/8 cycle, with neighboring fluid particle trajectories shown (using dashed blue lines) at two longitudinal positions. Coordinates: x = longitudinal; z = transverse. Longer wavelengths correspond to more elongated ellipses. The illustrated tilt of the ellipse (θ in **b**) may result from dissipation in either the fluids (Lighthill, 1981; Marquardt, 2018) or structures within the organ of Corti (see Supplementary Note 3). (**b**,**c**) Predicted effects of viewing angle on measured motion. In **b**, a "negative" angle α_1 views the wave traveling away from the measurement beam, with the measured (projected) motion of the ellipse phase-leading the transverse motion of the BM. By

contrast, a "positive" viewing angle α_2 observes the same wave as traveling towards the beam, such that the measured motion of the ellipse phase-lags the transverse BM motion. (**c**) Exemplar relationships between viewing angle and the relative phase of the projected motion for ellipses with 10-degrees of baseline tilt (θ, see **b**) and longitudinal/transverse elongation factors of 1, 3, and 10 (see key). Computations, see Supplementary Note 4. (**d**) OCT image from one of two preparations where vibration measurements were made from positive angles of incidence (α_2 in **b**). Scale bar, 0.025 mm. (**e**) Profiles of vibration amplitude across the path shown by the red arrow in **d**. Each curve represents one frequency component in the multi-tone stimulus. Four specific frequencies are identified by increased line width: 5.7 kHz (green), 10.6 kHz (black), 17.2 kHz (red), and 37.2 kHz (blue). (**f**) Corresponding phase data. All profiles are referenced to the vibrations observed at the BM location indicated with a white star in **d**. Gray patches indicate the different regions traversed by the red arrow, including the BM, Deiters' cells (DC) and OHCs (marked by the black triangle). Preparation RG16760, CF 40 kHz. Stimulus level 60 dB SPL.

From a functional perspective, it may be tempting to assign the much larger vibrations seen in the hotspot region a greater relevance to hearing than the smaller and seemingly more peripheral vibrations of the BM. Anatomically, the hotspot is clearly closer than the BM is to the transduction sites of the IHC and OHC stereocilia. However, the hotspot's poorer frequency selectivity and non-monotonic I/O functions (Figs. 2.5, 2.6) contradict a closer (than the BM) functional relationship: auditory nerve tuning is at least as sharp as BM tuning (Patuzzi & Robertson, 1988; Narayan et al., 1998), and strongly nonmonotonic I/O functions of the type illustrated in Fig. 2.6 are rarely seen in IHC, OHC, or neural recordings (Sachs & Abbas, 1974; Dallos, 1985). (The few nonmonotonic features that are observed in recordings from the auditory nerve (Liberman & Klang, 1984; Ruggero & Rich, 1983) and OHCs (Kössl & Russell, 1992) are not restricted to CF, and are rarely as strong as the mechanical nonmonotonicities of Fig. 2.6.) The mere location of the hotspot does not define its function, however, and it is entirely feasible that the BM is closer to the IHCs from a functional perspective than the hotspot region is. It has been known for over 100 years (ter Kuile, 1900) that the triangle of Corti can act as rotating wedge (Richter & Dallos, 2003) to couple transverse BM vibrations to radial motions in the sub-tectorial space.

The proposed longitudinal nature of the hotspot vibrations may explain why the hotspot's response characteristics are not passed on to the IHCs and auditory nerve. IHC stereocilia are arranged in rows which run almost parallel to the cochlea's spiraling longitudinal axis (Slepecky, 1996; Lim, 1980). This makes them highly sensitive to

radial deflections, however these might arise (ter Kuile, 1900; Guinan, 2012), but insensitive to longitudinal shear. In stark contrast, OHCs have characteristically V- or W-shaped stereociliary bundles (Lim, 1980; Soons et al., 2015) which may well be excited by longitudinal motion. Each wing of the OHC's bundle is oriented at a considerable angle to the cochlear spiral, and may therefore act independently to sense and rectify a longitudinally-directed stimulus (e.g., as illustrated in Fig. 1c of Beurg et al. (2016)). OHC electromotility (Ashmore, 2008; Brownell et al., 1985) may also induce longitudinal motion in the cochlea, both at the level of the RL (e.g., as illustrated in Fig. 1c of Brownell et al. (1985)) and near the OHCs' junctions with the Deiters' cells (Karavitaki & Mountain, 2007).

The very existence of a frequency-, intensity-, and physiologically-dependent vibration hotspot within the organ of Corti suggests that the classical way of modeling cochlear mechanics, with the BM as the dominant elastic structure and the surrounding fluid as amorphous mass load (Lighthill, 1981; Zwislocki, 1946) is incomplete. The anatomical structures within the organ of Corti clearly impose stringent constraints on the motion. These constraints require physiological integrity (the hotspot rapidly disappears post-mortem), suggesting a connection with physiologically active processes such as OHC motility (Brownell et al., 1985). However, the hotspot pattern is not restricted to the narrow frequency band around CF that is generally associated with active feedback or "cochlear amplification" (Ashmore, 2008; Davis, 1983; De Boer & Nuttall, 2000); hotspots are observed over the entire frequency range, down to at least 6 octaves below CF (Figs. 2.5, 2.6; Supplementary Fig. 2.10). Both the wideband character of the hotspot's motion and its wideband nonlinearity contrast with the fundamental feature of active models that "the region of activity is spatially limited" (De Boer & Nuttall, 2000).

A common idea about OHC length changes is that they serve to "enhance the peak BM response" (Ashmore & Kolston, 1994). This is difficult to reconcile with the observation that BM motion is actually smaller than hotspot motion, and the large (>0.25-cycle) phase-differences between hotspot and BM motion at low frequencies are inconsistent with the high speed of OHC length changes (Ashmore, 2008; Ashmore & Kolston, 1994). Active micromechanical models typically describe Deiters' cells as rigid rods that transfer OHC length changes to drive BM motion directly (e.g., Ramamoorthy et al. (2007)), thus predicting zero differential motion between the two ends of the Deiters' cell soma. Our measurements show that the end-to-end motion of Deiters' cells is in fact very large, exceeding the OHCs end-to-end motion

at least twofold across a wide range of frequencies (Fig. 2.7). Our measurements also fail to reveal the anti-phasic motion (or half-cycle phase shifts) between the top and bottom surfaces of the OHCs commonly predicted by active micromechanical cochlear models (e.g., refs. Ashmore & Kolston (1994); Ramamoorthy et al. (2007); Geisler & Sang (1995)). We see two potential explanations for this: either anti-phasic motion is not excited in healthy, acoustically stimulated cochleae (perhaps owing to the hearing organ's visco-elastic properties, cf. refs. Scherer & Gummer (2004); Nobili & Mammano (1996)), or it is so small that it becomes swamped by other forms of motion. Presently, we are unable to discriminate between these possibilities.

In the face of the above problems and inconsistencies, we propose an alternative hypothesis, namely that the hotspot motion results from structural constraints that require physiological integrity, and that OHCs act (on a slower timescale) as mechanical regulators (van der Heijden & Versteegh, 2015a; Allen, 1990), rather than as rapid, direct sources of BM vibrations. Supporting evidence for such parametric control comes from temporal sluggishness in cochlear compression (Cooper & van der Heijden, 2016). As shown below, a regulatory role of OHCs also helps explaining the peculiar nonlinear behavior of the hotspot (Fig. 2.6).

We propose that hotspot motion plays an important functional role in enhancing cochlear frequency selectivity. Deiters' cells and OHCs provide an internal scaffolding of the organ of Corti that strongly constrains its possible mechanical deformations under the influence of acoustic stimulation. In a healthy cochlea, this scaffolding funnels the longitudinal motion associated with the BM's traveling wave, causing it to become more tightly focused within the cross-section of the organ of Corti than it would be otherwise be (e.g., in the dead organ, cf. Fig. 2.4b). When the wave approaches its CF region, its wavelength decreases rapidly, and a second vibration mode emerges that involves larger transverse motion, and hence more BM displacement. Such a rapid change of vibration mode occurs in graded fluid waveguides with strong internal stiffness, and can enhance frequency selectivity without the need for cycle-by-cycle amplification (van der Heijden, 2014). In this scenario, the post-mortem decline in the integrity of the internal scaffolding explains the simultaneous loss of frequency selectivity and the hotspot pattern.

The nonlinearity of the hotspot motion differs from the well-known BM nonlinearity (Rhode, 1971; Sellick et al., 1982; Robles & Ruggero, 2001) in both its bandwidth and its strength (Fig. 2.6). Wideband mechanical compression similar to that seen in the hotspot has been observed previously near the apex of the cochlea in chinchillas,

guinea-pigs, and mice, using traditional as well as OCT techniques (Lee et al., 2016; Rhode & Cooper, 1996; Recio-Spinoso & Oghalai, 2017). These findings have been interpreted to expose qualitative differences between low-frequency hearing (at the apex) and high-frequency hearing (at the base) (Robles & Ruggero, 2001; Rhode & Cooper, 1996; Recio-Spinoso & Oghalai, 2017). However, basal turn data in the present study and elsewhere (Ren et al., 2016b; Ren & He, 2018) show that wideband compression is not unique to the apex. The actual dichotomy may therefore be that between the BM and the organ of Corti.

The wideband character of nonlinearity within the organ of Corti may also have a major impact on the interpretation of otoacoustic emissions (sounds of intra-cochlear origin recorded in the ear canal). Decades of BM data have shaped the widely accepted view that cochlear nonlinearities are confined to a narrow spatial region near CF, and this assumption forms the backbone of nearly all models of distortion product generation. However, there is considerable indirect evidence that some emissions originate more remotely from the CF region, at more basal cochlear sites (Martin et al., 1999). The wideband nonlinearity of the hotspot provides further evidence that nonlinear responses to tones are not restricted to the CF site at all, and actually occur over an extended cochlear region spanning multiple octaves. For decades, this phenomenon has been hiding just 20 μm beyond the BM. Its discovery may help to resolve the apparent contradiction between the otoacoustic (Martin et al., 1999) and BM data (Robles & Ruggero, 2001), and could call for a major revision of models of distortion products in the cochlea.

The wideband compression observed in the hotspot is puzzling from a functional point of view. At the 25-kHz place, frequencies as low as 400 Hz show compressive growth in the OHC/Deiters' cell hotspot (Fig. 2.6b). Attempts to interpret such compression in terms of amplification (e.g., Ren et al. (2016b)) are problematic. Low-frequency hearing sensitivity depends only on physiological integrity in apical cochlear structures and is unaffected by the basal OHCs involved in the wideband compression in Fig. 2.6. Even stranger is the fact that the same 400-Hz component that grows compressively in the hotspot at the 25-kHz place, becomes perfectly linear when observed on the BM at more apical locations. Regardless of whether compression originates from saturating amplification (Zwicker, 1979b) or controlled friction (van der Heijden & Versteegh, 2015a), it should cause the entire wave to accumulate nonlinearity during its travel, excluding such a return to linearity.

We therefore postulate that the linear BM motion represents the true carrier of

the low-frequency wave, and the hotspot motion merely feeds off this low-frequency, linear BM wave without affecting it in return. The compressive growth evoked by low-frequency sounds in the hotspot (Fig. 2.6d) then informs us that the hotspot's coupling to the BM is not constant, but becomes weaker with growing intensity. This variable coupling is consistent with the proposed regulatory role of OHCs. Specifically, we propose that the parametric impedance control is performed by the OHCs, which are known to change their axial stiffness tonically when excited (He & Dallos, 1999). Such a proposal is by no means new (see refs. He & Dallos (1999); Allen (1990)), but has been overshadowed for many years by the competing hypothesis that a "cochlear amplifier" injects extrinsic energy into the BM's traveling wave on a cycle-by-cycle basis. The functional role of a parametric impedance regulation is to compress the inputs to local IHCs, rather than to amplify the BM's motion, and the functional part of this compression is restricted to a narrow frequency band around CF (as reflected by the BM's nonlinearity). But even if the impedance regulation serves to compress only the near-CF input to nearby IHCs, it may still affect other responses to non-CF components-especially the vibrations of the very structures involved in the impedance control (OHCs and Deiters' cells). When the intensity increases, the ensuing impedance regulation will reduce the BM-to-hotspot pickup at any frequency: not only for near-CF tones that excite local IHCs and OHCs well, but also for off-CF tones that don't. The low-frequency compression is thus demoted to a side effect that nevertheless exposes an underlying compressive mechanism.

In a similar vein, parametric impedance adjustment may account for the other peculiarity of the hotspot's nonlinearity, its non-monotonic I/O functions for near-CF components (Fig. 2.6f). Traveling waves at and beyond CF have already been subject to compression by the OHCs at more basal locations. The local OHCs serve to compress the slightly lower-frequency waves that are on their way to stimulate IHCs at a slightly more apical place. But the mechanism by which the local OHCs exert this control— the parametric impedance adjustment—cannot help also shaping their response to the already compressed CF waves, namely, by adding even more compression. This naturally leads to the hyper-compression observed in the hotspot (but not on the BM). Again, the hotspot motion itself may bear little resemblance to local IHC input, but exposes the mechanism of dynamic range compression in the cochlea, which is one of its two major functions.

Cochlear frequency selectivity and dynamic range compression are two of the cornerstones of auditory processing, and our current understanding of these processes

is limited. New measurements, including those presented here, offer a fascinating glimpse of the actual structures performing these tasks, and we are confident that their systematic study will soon lead to a sound understanding of cochlear function.

Acknowledgments

We thank Drs. Gerard Borst, Mary Palmer, and Natalie Cappaert. This work was supported by the Netherlands Organization for Scientific Research, ALW 823.02.018, and an EU Horizon 2020 Marie Sklodowska-Curie Action Innovative Training network, H2020- MSCA-ITN-2016 [LISTEN - 722098].

Supplementary information

Supplementary Note 1: Interpolation method for the vibration maps

Supplementary Fig. 2.9 illustrates the effects of two-dimensional interpolation in the derivation of a spatial vibration map. The measurement technique provides vibration estimates at all depths along each measurement pathway (Supplementary Fig. 2.9a). Only those estimates that exceed a statistically defined noise-floor are used for subsequent analysis (see Methods). The results of interpolating these data and fitting contours at 3 dB intervals (as used throughout the current paper) are shown in Supplementary Fig. 2.9b. Note that the construction of contour maps from the pixelated data involves no form of smoothing or averaging

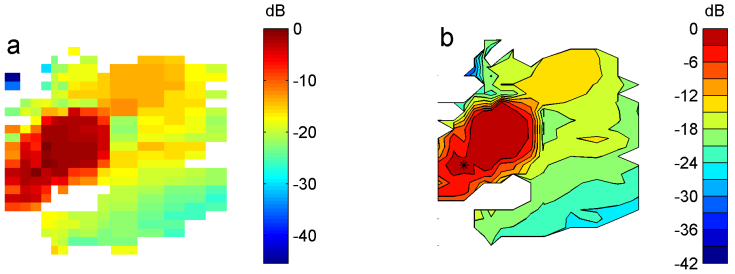

Figure 2.9: Vibration mapping technique. (**a**) Vibration magnitudes plotted as color-coded "pixels" form a two-dimensional spatial map across the width and depth of the cochlear partition. This particular map is based on measurements made at 476 loci, obtained by combining data from 17 positions of the OCT beam, each with a 'vertical' resolution of ∼8 μm. Loci providing non-significant vibration estimates are shown as white spaces in the figures. (**b**) Two-dimensional interpolation permits the derivation of iso-amplitude contours within the field of measurement. No smoothing of these contours is performed. Color codes indicate vibration magnitudes (mapped on a logarithmic scale) relative to the maximum observed vibration (in this case 3 nm). The location of the maximum is marked by the asterisk in **b**. Preparation RG16725, CF 22.6 kHz (see Fig. 2.2 of main text).

Supplementary Note 2: Frequency dependence of vibration hotspots

Supplementary Figs. 2.10 and 2.11 illustrate the frequency dependence of the vibration hotspots that form the main focus of this work. The hotspot becomes more prominent (i.e. more tightly focused, with steeper edges) as frequency increases towards the preparation's CF (e.g. compare the amplitude patterns at 1.4 and 20 kHz in Supplementary Fig. 2.10). At and above CF, the hotspot becomes less prominent, and gives an impression that its vibration is "leaking out" progressively onto the BM (e.g. from 23.5 to 25.5 kHz). Phase differences of up to 0.5 cycles are observed between the hotspot and surrounding regions (e.g. the tectal and Hensen cell area $\sim$50 μm lateral to the hotspot) at both low and high frequencies (e.g. 1.4 kHz and >22 kHz; Supplementary Fig. 2.11).

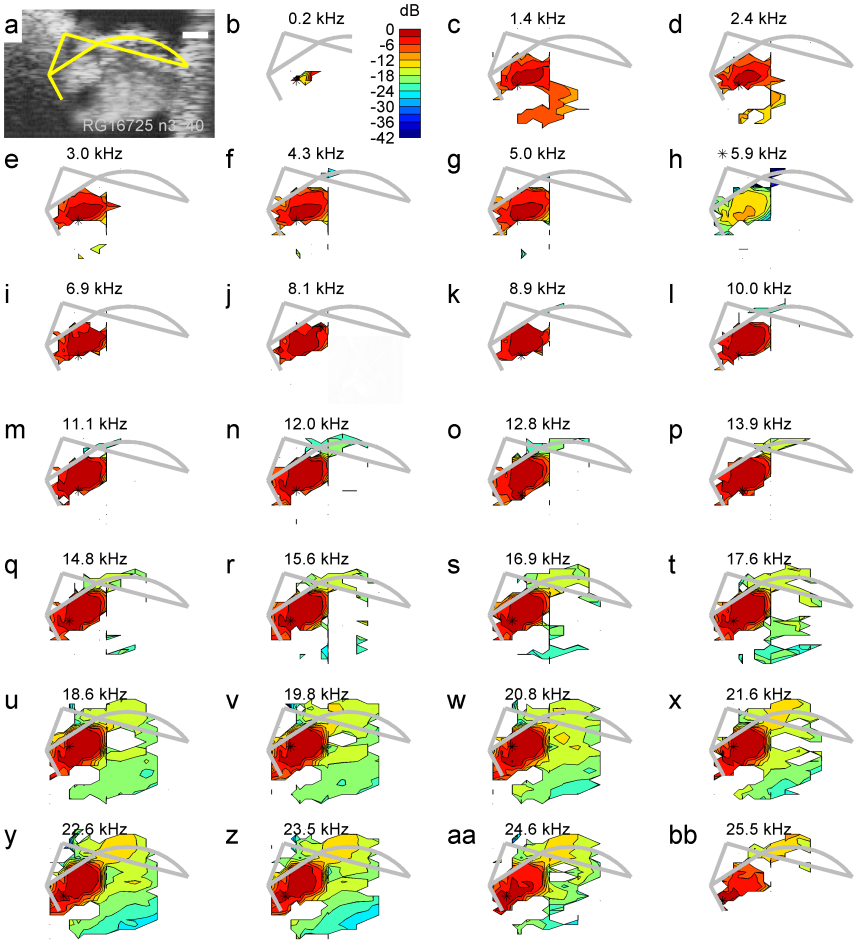

Figure 2.10: Maps of vibration magnitude for acoustic frequencies spanning 0.2- 25.5 kHz (panels **a**-**bb**) in the same preparation illustrated in Figs. 2.2 and 2.3. All stimulus components were presented simultaneously at 40 dB SPL, and their responses were isolated by Fourier analysis. Scale bar in panel **a**, 25 μm. Color code (legend in panel **b**) indicates vibration magnitude normalized to the peak magnitude for each frequency. The location of the peak is marked by an asterisk. CF was 22.6 kHz (see Fig. 2.2 of main text).

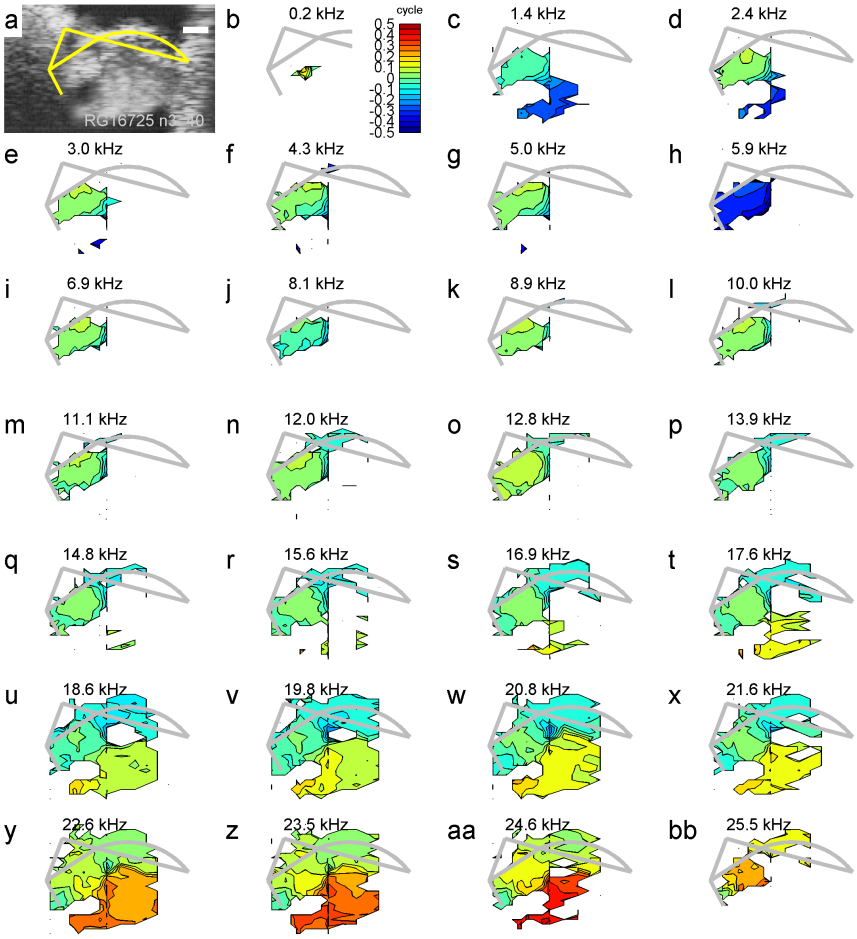

Figure 2.11: Maps of vibration phase for acoustic frequencies spanning 0.2-25.5 kHz (panels **a**-**bb**) in the same preparation shown in Figs. 2.2 and Supplementary Fig. 2.10. Scale bar in panel **a**, 25 μm. Color code (legend in panel **b**) indicates vibration phase normalized to the phase observed at the position of the magnitude peak (locations marked by asterisks in Supplementary Fig. 2.10). CF was 22.6 kHz, sound level 40 dB (see Fig. 2.2 of main text)

Supplementary Note 3: Physics of longitudinal motion in surface waves

This note discusses the occurrence of longitudinal motion in surface waves in general and cochlear traveling waves in particular.

Cochlear traveling waves are surface waves, i.e., they propagate on the interface between layers having different material properties. Familiar examples of surface waves are waves on the sea and Rayleigh (seismic) waves. Such waves are never purely transverse or purely longitudinal; they always involve a mix of these two displacement directions (Lighthill, 1978; Graff, 1991). This mixed character is particularly inevitable in surface waves on incompressible fluids, because volume conservation prohibits fluid moving in columns in the presence of rigid boundaries.

Importantly, longitudinal and transverse displacements are not in phase, resulting in elliptical orbits of the wave medium. In the absence of friction, one of the axes of the ellipse is aligned with the direction of propagation (Lighthill, 1978; Graff, 1991), so the longitudinal and transverse components are "in quadrature" (i.e., they have a 0.25-cycle phase difference). Friction typically causes the ellipses to tilt with respect to the propagation axes (Lighthill, 1992; Marquardt, 2018), even in isotropic media. Structural anisotropy (which is abundant in the organ of Corti) is another potential source of tilt. Ellipse tilting further complicates the phase relationship between longitudinal and transverse vibration components; it is no longer a simple 0.25-cycle difference. Tilted ellipses are illustrated in Fig. 2.8a,b of the main text and in more detail in Supplementary Fig. 2.12a. The exact aspect ratio of the ellipse (ratio of axis lengths) and its tilt depend on wavelength and on details of the propagating medium that are unknown in the case of the cochlea (e.g. anisotropy of both elastic and frictional properties). The incompressibility of the cochlear fluid and the nearby presence of rigid boundaries, however, impose a number of characteristics that may be experimentally tested. These characteristics are derived in Supplementary note 4.

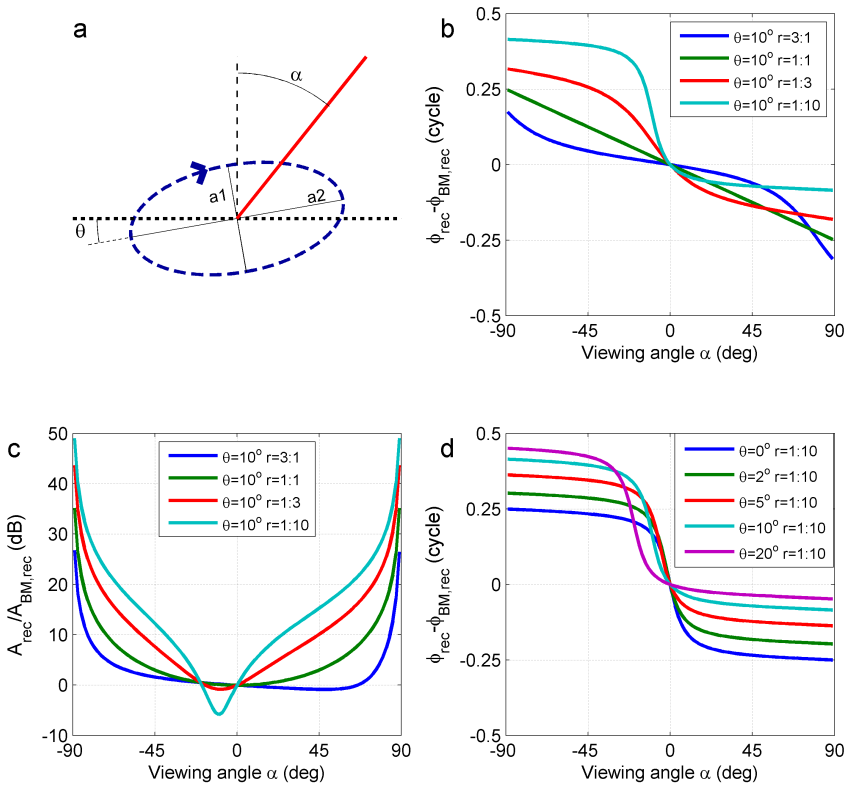

Figure 2.12: Measurable effects of longitudinal wave motion. (**a**) Diagram of the clockwise elliptical motion (see text), with ellipse axes a1, a2, tilt angle θ and viewing angle α as indicated. The *dotted horizontal line* represents the longitudinal direction as defined by the BM, which is also the direction of wave propagation (from left to right). The *vertical dashed line* is the normal to the BM, which defines the transverse direction. The *red line* represents the measurement beam. (**b,c**) Dependence of measured phase difference $\Delta\phi$ and amplitude ratio R_{A} (see text) on viewing angle α for various values of aspect ratio a1:a2 indicated in the key. Ellipse tilt θ fixed at 10 degrees. (**d**) Dependence of measured phase difference $\Delta\phi$ on viewing angle α for various values of ellipse tilt θ. Aspect ratio of the ellipse fixed at 1:10.

Supplementary Note 4: Testing for longitudinal motion in OCT data

This Supplementary Note analyzes the consequences of longitudinal motion for vibration measurements. The analysis leads to the identification of six experimentally testable characteristics of longitudinal wave motion.

From the experimenter's viewpoint elliptic motion causes methodological complications not previously addressed in cochlear mechanics. Elliptic vibration lacks a unique amplitude and phase because the two vibration components along the ellipse axes are in quadrature and generally have unequal amplitudes. The vibration recorded by the interferometer is the projection of the elliptical motion onto the measurement beam. The recorded amplitude A_{rec} and phase ϕ_{rec} thus depend on the viewing angle α with respect to the transverse direction and on the tilting angle θ of the ellipse (Supplementary Fig. 2.12). In formulas:

$$\begin{aligned} A_{\mathrm{rec}} &= A\sqrt{\cos^2(\theta+\alpha) + r^2\sin^2(\theta+\alpha)} \\ \tan\phi_{\mathrm{rec}} &= -r\tan(\theta+\alpha)), \end{aligned} \tag{2.1}$$

where A is the amplitude of the vibration component along axis α_1 of the ellipse (Supplementary Fig. 2.12a); r is the aspect ratio of the ellipse (so rA is the amplitude along α_2, the other ellipse axis); θ is the ellipse tilt and α is the viewing angle as indicated in Fig. 2.8b and Supplementary Fig. 2.12a.

Assuming that BM motion is transverse (see Discussion) and matches the transverse component of the nearby elliptical trajectories (Lighthill, 1992; Marquardt, 2018), its motion is a projection onto the transverse axis:

$$\begin{aligned} A_{\mathrm{BM}} &= A\sqrt{\cos^2(\theta) + r^2\sin^2(\theta)} \\ \tan\phi_{\mathrm{BM}} &= -r\tan(\theta)). \end{aligned} \tag{2.2}$$

Because BM motion is one-dimensional, its subsequent projection onto the measurement beam leaves its phase unaffected and reduces its amplitude by a factor $\cos\alpha$. This yields:

$$\begin{aligned} A_{\mathrm{BM,rec}} &= \cos\alpha A\sqrt{\cos^2(\theta) + r^2\sin^2(\theta)} \\ \tan\phi_{\mathrm{BM,rec}} &= -r\tan(\theta). \end{aligned} \tag{2.3}$$

for the observed BM motion. We used Supplementary Equations 2.1 and 2.3 to compute the predicted dependence on viewing angle α of the amplitude ratio $R_{\mathrm{A}} = A_{\mathrm{rec}}/A_{\mathrm{BM,rec}}$ and phase difference $\Delta\phi = \phi_{\mathrm{rec}} - \phi_{\mathrm{BM,rec}}$ (Supplementary Fig. 2.12b,c). Their dependence on the ellipse tilt is illustrated in Supplementary Fig. 2.12d. This analysis reveals that the observed phase difference between the hotspot and the BM can exceed 0.25 cycle and approach 0.5 cycle. This means that during a substantial fraction of the stimulus cycle, hotspot and BM move in opposite directions when viewed from an oblique angle.

At first sight this phase opposition seems to contradict the basic assumption, expressed by Supplementary Equation 2.2, that the BM moves in sync with the transverse component of the hotspot motion. The paradox is resolved by realizing that the observed BM motion involves a double projection: first onto the transverse axis, then onto the measurement beam. The situation is analogous to a sailboat's ability to sail partially against the wind. The wind force is first projected onto the normal of the sail and then onto the longitudinal axis (the keel) of the boat.

As a final step toward an inventory of experimentally testable consequences of longitudinal motion we note that (i) lower frequencies correspond to larger wavelengths; (ii) larger wavelengths produce an increasing dominance of longitudinal motion, causing an increasing longitudinal stretching of the ellipses (Lighthill, 1978). Combining this with Supplementary Equations 2.1-2.3 and Supplementary Fig. 2.12b-d, we arrive at the following list of characteristics:

1. Larger phase differences $\Delta\phi$ occur at lower frequencies;
2. Larger amplitude ratios occur at lower frequencies;
3. Low-frequency $\Delta\phi$ values may exceed 0.25 cycle and approach 0.5 cycle;
4. When watching the wave "run away" ($\alpha < 0$), the hotspot leads BM ($\Delta\phi > 0$)
5. When watching the wave approach ($\alpha > 0$), the hotspot lags BM ($\Delta\phi < 0$)
6. Almost-perpendicular beams (small $|\alpha|$) can still cause $\Delta\phi$ values that differ substantially from zero.

In the last paragraph of subsection of Results, *Testing for longitudinal motion in the hotspot*, we evaluate whether the data presented in this work comply with these predicted characteristics.

Supplementary Movie 1

Link: https://www.nature.com/articles/s41467-018-05483-z

Chapter 3

Tuned vibration modes in a miniature hearing organ - insights from the bushcricket [1]

Bushcrickets (katydids) rely on only 20 to120 sensory units located in their forelegs to sense sound. Situated in tiny hearing organs less than 1 mm long (40x shorter than the human cochlea), they cover a wide frequency range from 1 kHz up to ultrasounds, in tonotopic order. The underlying mechanisms of this miniaturized frequency-place map are unknown. Sensory dendrites in the hearing organ (crista acustica, CA) are hypothesized to stretch, thereby driving mechanostransduction and frequency tuning. However, this has not been experimentally confirmed. Using optical coherence tomography (OCT) vibrometry, we measured for the first time the relative motion of structures within and adjacent to the CA of the bushcricket *Mecopoda elongata*. We found different modes of nano-vibration in the CA that have not been previously described. The two tympana and the adjacent septum of the foreleg that enclose the CA were recorded simultaneously, revealing an antiphasic lever motion strikingly reminiscent of vertebrate middle ears. Over the entire length of the CA we were able to separate and compare vibrations of the top (cap cells) and base (dorsal wall) of the sensory tissue. The tuning of these two structures, only 15-60 μm apart, differed systematically in sharpness and best frequency, revealing a tuned periodic deformation of the CA. The relative motion of the two structures, a potential drive of transduction, demonstrated sharper tuning than either of them. The micromechanical complexity indicates that the bushcricket ear invokes multiple degrees of freedom to achieve frequency separation with a limited number of sensory cells.

[1] Vavakou, A., Scherberich, J., Nowotny, M., & van der Heijden, M. (2021). Tuned vibration modes in a miniature hearing organ: Insights from the bushcricket. *Proceedings of the National Academy of Sciences, 118*(39).
https://doi.org/10.1073/pnas.2105234118

Introduction

A hearing organ converts sound-induced mechanical vibrations to receptor potentials that are further processed along the auditory pathway. Bushcrickets (katydids) *Mecopoda elongata* (Insecta, Orthoptera, Tettigoniidae) have a miniature hearing organ, the crista acustica (CA), that is located in their front tibia, and can sense frequencies up to 70 kHz (Hummel et al., 2014). To achieve that, they rely on less than 50 sensory units (Strauß et al., 2012; Hummel et al., 2017), each consisting of a sensory cell, a cap cell (CC) and a scolopale cell (Fig. 3.1D; see 3.3B). The total length of the CA is ∼0.9-mm, which is ∼40 times shorter than the uncoiled cochlea in humans. Still, the CA with its limited cellular machinery is able to mechanically separate a wide range of frequencies, but the underlying mechanisms are not well understood.

In bushcrickets, the sound-induced nano-vibrations reach the sensory tissue through two routes. The main source of airborne sound is the spiracle (Lewis, 1974), a horn shaped opening in the thorax that delivers and enhances the sound input to the CA via an acoustic trachea (Hoffmann & Jatho, 1995; Michelsen et al., 1994; Veitch et al., 2021). Secondly, the two tympana on the anterior and posterior side of the front legs are also reported to deliver sound to the sensory tissue (Heinrich et al., 1993; Hummel et al., 2011). The sensory units of the CA are surrounded by haemolymph fluid and are protruding from the dorsal side of the dorsal wall (DW) of the acoustic trachea. Each ciliated tip of a sensory dendrite is embedded in the cap of a CC (Figs. 3.1D,3.3B). These CCs are part of a continuous tectorial membrane that connects the sensory units (Schumacher, 1975). Transduction takes place as the mechanosensitive channels on the sensory dendrite open due to displacement of the cap cell (Yack, 2004; Hummel et al., 2016). The CA in bushcricket ears is tonotopically organized along the proximal-distal axis (Oldfield, 1982; Hummel et al., 2016; Montealegre-Z & Robert, 2015) following an anatomical gradient, with increasing height and width of the sensory units (Lin et al., 1993; Hummel et al., 2017) towards the proximal end. Mechanical measurements of sound-induced responses revealed that high frequencies induce greater motion magnitude in the distal part of the CA (Palghat Udayashankar et al., 2012; Montealegre-Z et al., 2012). Spatial phase gradients in tone-evoked vibrations indicate the existence of waves traveling from the distal, high-frequency end to the proximal end of the CA (Palghat Udayashankar et al., 2012). Whereas traveling waves in the mammalian cochlea accumulate several cycles of phase delay (Robles & Ruggero,

2001), the total phase accumulation in the bushcricket CA is only 0.5-1 cycle (Olson & Nowotny, 2019). The exact mechanisms that drive transduction and tonotopy in the CA are undefined yet.

Recently, it was reported that the mechanical responses of the CA show different frequency tuning than the neural response at the same location (Hummel et al., 2016). The CCs are located dorsally to the DW and the dendrite of the sensory neuron is approximately perpendicular to the DW. The relative motion between the two structures may drive the opening of the transduction channels, and could explain discrepancies between mechanical and neural tuning. However, it has not been possible to probe such relative motion experimentally, due to technical limitations of the technique used in laser Doppler vibrometry (LDV), which has been extensively used to measure vibrations in insect hearing organs (Palghat Udayashankar et al., 2012).

LDV measurements do not provide inherent depth resolution, and the optical inhomogeneities of biological tissues cause diffraction, scattering and lensing effects that adversely affect optical focus. Therefore, most LDV measurements in the insect hearing organs were done on the most accessible and reflective structures, like the tympana (Michelsen & Larsen, 1978), antenna (Gopfert et al., 1999), and cuticle as an indirect measurement of organ motion (Montealegre-Z et al., 2012). Measurements of hearing organ motion were also obtained through a transparent cuticle (Sarria-S et al., 2017) or after the surgical removal of the cuticle (Palghat Udayashankar et al., 2012). Optical coherences tomography (OCT) provides opportunities to reliably attribute vibrations to anatomical structures, as it resolves depth and allows for fast nano-vibrometry measurements (Gao et al., 2013). OCT has yielded vibration maps of cross sections of the mammalian organ of Corti (Gao et al., 2014) and the description of different vibration modes of the cochlear partition (Cooper et al., 2018). The new OCT results revealed structural interconnections in the micromechanics that stirred up the understanding of cochlear function (Olson & Strimbu, 2020), but has not yet been used to shed light on the operation of insect hearing organs.

In the current study, we used OCT-vibrometry to perform non-invasive measurements of nano-vibrations in the bushcricket hearing organ for the first time. First, we used this technique to describe the relative motion of the two tympana and the septum of the trachea (Fig. 3.2) in response to broadband, multi-tone sound stimuli. Next, we approached the CA from the dorsal side (Fig. 3.1B) to perform simultaneous vibration measurements of the CC and the DW, and this allowed us to determine the relative motion between these closely neighboring structures. We observed systematic

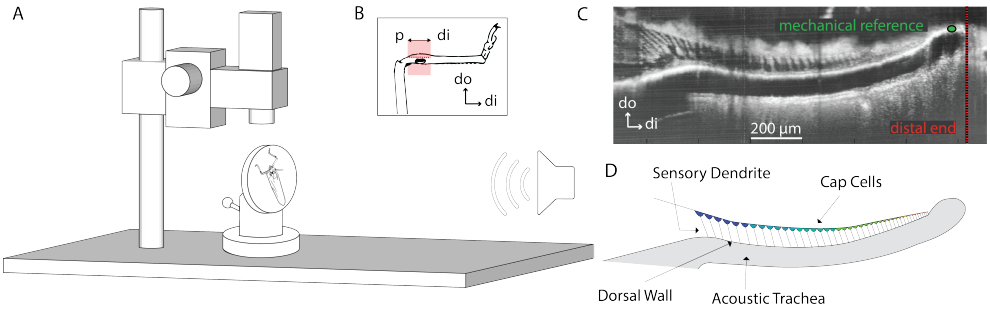

Figure 3.1: OCT-imaging (**A**) Illustration of the experimental setup. The fixed animal was placed under the OCT-vibrometer and sound was delivered using an open field stimulation paradigm. (**B**) Schematic drawing of the foreleg that holds the hearing organ, crista acustica (CA), including a proximal-distal/dorsal-ventral section of the CA. (**C**) A cross-section OCT image ("B-scan") obtained from the top view of the hearing organ, following an image section plane as shown in panel B, across the proximal-distal axis. (**D**) Sketch relating the B-scan to the anatomy, across the proximal-distal axis. The dorsal wall (DW) and the cap cells (CC) can be identified. The CA position at the distal end indicated with the green circle is the reference position used in this study to normalize sound-induced vibrations. By convention, all the distances are expressed relative to the red line that illustrates the very distal part of the CA. di = distal, do = dorsal, p = proximal.

differences in the frequency-place map and sharpness between CC and DW. The relative motion between CC and DW was found to be more sharply tuned than either of the individual structures.

Materials and Methods

Animal Preparation

In total, 19 bushcrickets of the species *Mecopoda elongata* were used for in-vivo sound-induced vibration measurements on the CA and the tympana. CA recordings were made on 11 individual tibial hearing organs belonging to 9 animals. The animals were anesthetized by lowering their body temperature after placing them in a container filled with ice. When they were not responsive (usually after approx. 10 min) and their mandibles were loose, their middle and rear legs were removed. The animal was placed with its thorax on the animal holder and it was stabilized using melted medical wax. The front legs were stabilized in a position where the CA were accessible to the

OCT beam. In 2 particular experiments (BC0007, BC00013) it was possible to record through the intact cuticle. The individual measurements that are shown in the current report come from experiment BC0007. For other animals the dorsal cuticle obscured the view of the CA. For that reason, it was removed surgically and replaced by a glass cover slip. After the cuticle removal, the CA were inspected using OCT imaging, to ensure they were not harmed by the preparation. Viewing through the glass cover slip allowed us to identify the underlying structures and perform mechanical measurements and it is a common method in mammal hearing research (Cooper & Rhode, 1995). As was the case in previous bushcricket studies (Olson & Nowotny, 2019), there are no signs that removing the cuticle adversely affected auditory sensitivity. The population data in Fig. 3.4H-J are combined from animals with an intact cuticle and animals with the cuticle removed. Tympanum measurements were obtained by placing the anterior tympanum perpendicular to the OCT beam. All measurements were acquired in-vivo. In total, tympanum measurements were acquired from 11 legs belonging to different animals. At the end of the experiment, the animal was anesthetized and subsequently euthanized by decapitation.

Acoustic Stimulation

Broad-band multi-tone "zwuis" complexes (van der Heijden & Joris, 2003) were used, following an open field stimulation paradigm, using a ScanSpeaker R2904/700005 loudspeaker placed 35 cm from the animal, inside a sound proof booth. The ipsilateral acoustic trachea opening on the thorax was facing the loudspeaker. Calibration of the sound pressure was done by temporarily replacing the animal holder by a microphone. The surfaces of the OCT probe, animal holder, etc., were covered with cotton wool in order to minimize acoustic reflections. The most commonly used broadband stimulus consisted of 51 spectral components, spanning from 0.4 kHz to 50 kHz (average frequency spacing: 990 Hz), presented at 75 dB, 79 dB or 85 dB per component. The components all had equal amplitudes, with levels expressed in dB re 20-μPa (i.e., dB SPL), but stimulus phase was randomized across frequency. Each stimulus was presented for 12 s, and inter-stimulus intervals lasted for approximately 60 s.

OCT imaging and vibrometry

Vibration measurements were obtained using Optical Coherence Tomography (OCT). For more details on the experimental setup see Cooper et al. (2018). OCT is an imaging

technique, based on low-coherence interferometry. An SD-OCT system (Thorlabs Telesto TEL320C1) was used for interferometric imaging and vibration measurements. Its field of view is 10 mm x 10 mm; its depth range is 3.5 mm. The working distance of the objective was 24 mm. Cross-sectional (B-scan) and axial images (A-scans and M-scans) were triggered externally using TTL pulses phase-locked to the acoustic stimulation system (Tucker Davies Technologies system III) at a sampling rate of 111.6 kHz. The optics of our recording system (Mitotoyu IR imaging lens with an NA of 0.055) introduced an axial point spread function of 6-μm FWHM and a lateral resolution (in the xy plane) of 13-μm (all assessed in air, with a refractive index of 1). For our dorsal view measurements, the OCT measurement beam was manually aligned with the dorsal-ventral anatomical axis of the CA. The vibration measurements that we made should therefore be favouring measuring vibrations along this axis.

The refractive index n of the various anatomical structures affects the recorded vibration magnitude. Phase data are not affected by n, whereas magnitude is shifted upward by $20 \log n \approx 3$ dB for most fluids. The effect of correcting the data for n is illustrated in Supplementary Fig. 3.10, including the case where DW and CC have different n, motivated by the suggestion that fluid composition between the CC and DW may differ from that of the haemolymph canal around the CA (Montealegre-Z et al., 2012; Montealegre-Z & Robert, 2015). Since the corrections are small and uniform, and the proper n values are unknown, we did not apply such corrections to the main figures.

The anatomy of the distal end of the CA is quite distinct and it is possible to define the same anatomical structure across experiments. In order to compare recorded positions across animals, we therefore used the distal end of the hearing organ as an anchor point. The recorded structures were labeled by the horizontal distance between the measuring beam and the vertical line that intersects the distal end of the CA (red line in Fig. 3.1C). The depth resolution of the OCT allowed us to record the DW and the CC simultaneously, along one recording beam, at different positions of the CA. That way, a DW and a CC measurement obtained from the same beam shared the same distance from the distal end of the CA.

Response analysis

Mechanical vibrations were obtained from i) the Dorsal Wall and the Cap Cells and ii) both tympana and septum. Responses were analyzed by Fourier transformation of the vibration waveforms derived from contiguous groups of 3 pixels in each M-scan, where

each pixel covers a depth of 3 μm, depending on the exact value of the refractive index of the structures. Each frequency component in a vibration measurement was assessed using the Rayleigh test ($p = 0.001$) for significance of phase locking (Versteegh & van der Heijden, 2012). Upon repeated recordings, vibration magnitude and phase are typically reproduced to within 0.5 dB and 0.02 cycle, respectively. The mechanical measurements from the CA were normalized to vibrations recorded on the distal end of the organ (green marker in Fig. 3.1C) analogous to normalization using the middle ear ossicles commonly used in the field of cochlear mechanics (Rhode, 1971). This accounted for imperfection in the calibration of the acoustics. We made sure that the reference vibration measurement and the CA recordings were performed while using the exact same configuration, in particular the same height of the adjustable optical probe. The use of a mechanical reference rather than a microphone makes the data less suited for the estimation of acoustic transfer functions, but is adequate for the aims of the present study, namely, the direct comparison of vibrations across different location in a single hearing organ. The absence of ripples in normalized magnitude-frequency data (e.g. Fig. 3.3D-F) indicates that any acoustic reflections had little impact on our recordings.

Different recorded positions are identified by their distance from the most distal part of the CA, as shown with a red vertical line in Fig. 3.1C. Data were analysed using custom software developed in MatLab (MathWorks, USA) environment. The spatial and spectral peak was detected by using a polynomial fit on a 15-dB range around the peak of the normalized magnitude data. The order of the polynomial varied from 2nd to 4th, according to the number of fitting points that fulfilled the 15-dB range criterion. In a minority of cases, manual exclusion of the fitting points was applied if the automated peak detection algorithm failed. Phase averaging (indicated as white stripes in the legend of Fig. 3.2B) was obtained as follows. The phases ϕ_k of individual pixels in each subdomain (anterior and posterior tympanum) were determined by taking the angle of $\sum_\mathrm{k} \exp(i\phi_\mathrm{k})$, where i is the square root of -1.

Group delay was estimated from the data in Fig. 3.3M-O by fitting straight lines to the portions of the phase-frequency curves that correspond to the magnitude peaks (highest 10 dB) in 3.3J-L. The reported group delays estimates are the negative slopes of these fit lines. Wavelengths and phase velocity were derived from the data in Fig. 3.3G-I by fitting straight lines to the portions of the phase-position curves that correspond to the magnitude peaks (highest 10 dB) in 3.3D-F. Wavenumber estimates (k in cycle/μm) are the negative slopes of these fit lines. Wavelength λ and phase

velocity c were derived from k by $\lambda = 1/k$ and $c = f/k$, respectively, with f the stimulus frequency.

Data Availability

Vibration measurement data have been deposited in Figshare (`https://figshare.com/authors/MarcelvanderHeijden/5457377`).
Data for the figures have been deposited in Figshare (`https://figshare.com/articles/dataset/VavakouScherberichNowotnyvanderHeijden2021/15292230`).
All other study data are included in the article and/or Supplementary Information

Results

The relative motion of the two tympana

The two tympana are easily accessible for imaging in a non-invasive manner, so they were the first structures we aimed to study. For this purpose, the OCT recording beam was aimed perpendicular to the anterior tympanum. When imaging through the anterior tympanum, the recording beam traverses through the tracheal septum before it reaches the posterior tympanum. Light intensity can be a limiting factor when imaging with the OCT as highly reflective surfaces tend to obscure deeper structures. Our results demonstrate that with our setup it is possible to image both tympana and identify them with certainty (Fig. 3.2A,D), which afforded a means to record sound induced vibrations on the two tympana (Fig. 3.2B,C) simultaneously. By doing so, we exclude any effects that rotating the preparation has on the acoustic delivery of the stimulus.

The colormap in Fig. 3.2B illustrates how the phase of the vibrations is distributed along the B-scan (details: see methods / Response analysis) for a 14.3-kHz stimulus at 79 dB SPL. The motion of each tympanum had a constant phase profile along the recorded width, from the dorsal end until halfway to the ventral end. The two tympana moved with an approximately 0.5-cycle (=180°) phase difference, and this phase opposition was consistent across the whole recorded width of the tympana. Across different frequencies (0.4-38 kHz), the two tympana shared similar vibration magnitudes (Fig. 3.2F) and showed a ∼0.5-cycle phase difference (Fig. 3.2B,E), confirming previous findings (Bangert et al., 1998). For both tympana, the magnitude followed a dorsal-ventral displacement gradient, with the higher values towards the

ventral side (Fig. 3.2C). Both tympana describe a hinged motion anchored at their dorsal ends (Fig. 3.2G). These observations were systematic across all our tympanum measurements (n=11 bushcricket legs, Supplementary Fig. 3.7).

In addition to the two tympana, we were also able to observe the phase of the vibrations on the anterior part of the DW and the tracheal septum, a structure splitting the acoustic trachea in two compartments, for which no vibration data have been reported before (Fig. 3.2B). In Fig. 3.2B, the anterior end of the CA is seen to move in phase with the anterior tympanum (deepest cyan squares) while the septum moves in phase with the posterior tympanum (dark orange squares halfway between the two tympana). These structures are very close to the sensory unit and their antiphasic motion could be of functional significance if it resulted in a mechanical stress on the CA that could be felt by the sensory dendrites. We did, however, not further pursue this analysis here because the anterior-posterior viewing angle is sub-optimal for studying relative motions within the sensory unit; the DW in particular is hardly visible. Instead, we studied the DW motion along the dorsal-ventral axis, where it is clearly visible.

Micromechanics: dissecting the motion within the crista acustica

Aiming to explore further motions within the sensory units, we imaged the CA through a dorsal view as illustrated in Figs. 3.1 and 3.3. That way, our recording beam travels through the CA aligned with the dorsal-ventral anatomical axis, allowing us to distinguish these structures in our B-scans. As a consequence, motion of the CC and the DW can be disentangled. The mechanical measurements were normalized to vibrations recorded in the distal end of the CA. The results presented in detail below come from a preparation where vibrations on the CA were measured through the intact dorsal cuticle (BC0007; details in Methods)

Using OCT-vibrometry we can expand the datasets in the existing literature. Previous studies have reported a tonotopic response of the CA with high and low frequencies exciting the distal and proximal parts of the organ, respectively (Oldfield, 1982; Palghat Udayashankar et al., 2012; Montealegre-Z et al., 2012). The tonotopic gradient coincides with a gradient in the size of the anatomical structures (Hummel et al., 2017). In Fig. 3.3 the recordings of the DW (black curves) are shown alongside those of the CC (blue curves). Spatial and spectral patterns of the sound-induced CA motion demonstrate the tonotopy in two complementary ways. Panels D-F of Fig. 3.3 show the CA vibration magnitude evoked by three different frequency components

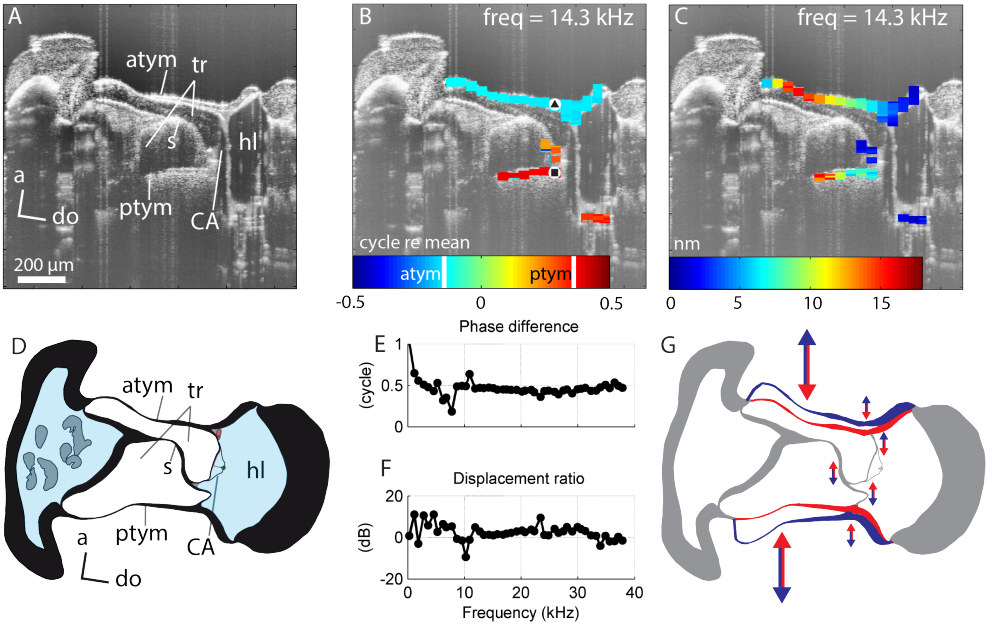

Figure 3.2: Mechanical responses of the anterior and posterior tympana to sound stimulation. (**A**) OCT B-scan of a front leg, viewed through the anterior tympanum. *atym: anterior tympanum, ptym: posterior tympanum, tr: trachea, s: septum, CA: crista acustica, hl: haemolymph* (**B**) The same B-scan overlaid with colour-coded phase information for a stimulus frequency of 14.3 kHz presented at 79 dB SPL. Notice that a phase difference of 0.5 cycle is 180° (an out-of-phase motion) The haemolymph fluid behind the anterior tympanum caused the position of the dorsal part of the posterior tympanum to shift to a more posterior position. This optical distortion does not affect the vibration data. The white stripes in the color map mark the average phases of the two tympana. (**C**) The same B-scan overlaid with the companion color-coded vibration magnitude information. (**D**) Anatomical sketch of a cross-section of the bushcricket front leg. (Adapted from ref. (Hummel et al., 2017)). (**E**) The displacement phase difference between posterior and anterior tympana across different stimulus frequencies. The mechanical measurements were obtained at the positions indicated by the markers in panel **B**. (**F**) Displacement magnitude difference between posterior and anterior tympanum across different stimulus frequencies at the marked positions in panel **B**. (**G**) Two extreme configurations of the tympana within one cycle of stimulus frequency are illustrated with red and blue. Displacement amplitude is enlarged 5000x for illustration purposes. The two tympana bulge in (red) and out (blue) synchronously. The septum follows the posterior tympanum motion direction. The arrows illustrate the magnitude of vibrations, which increases towards the ventral side of the tympanum. The ventral part of the tympanum moves ∼3.6 times more than close to the CA at the stimulus frequency. The tympana motion resembles a hinge, anchored at the dorsal end. More data in Supplementary Fig. 3.7.

(6.3, 12.5 and 23.4 kHz) as a function of longitudinal position, as measured on the DW and the CC. Each of these excitation patterns is peaked; with decreasing frequency the peak location shifts towards the proximal end. The corresponding phase data (Fig. 3.3G-I) display an accumulation of ∼0.5-1-cycle of phase from the distal end to the peak region. These phase data yielded estimates of wavelength and phase velocity in the peak region as detailed in the legend of Fig. 3.3. Wavelength ranged from 345-599 μm (DW) and 222-370 μm (CC); phase velocity ranged from 3.7-8.1 m/s (DW) and 2.4-5.2 m/s (CC). These values are consistent with previous reports in *M. elongata* (Palghat Udayashankar et al., 2012; Olson & Nowotny, 2019).

The spectral representation of tuning is illustrated in the lower half of Fig. 3.3 by plotting magnitude (Fig. 3.3J-L) and phase (Fig. 3.3M-O) as a function of frequency recorded at three positions along the tonotopic axis. The tonotopy and phase patterns in Fig. 3.3 are consistent with previous reports of CA vibrations (Hummel et al., 2016; Olson & Nowotny, 2019). The overall tuning and tonotopy of the DW is similar to that of the CC, but we also found systematic differences between the tuning of the two structures in the 5-25-kHz frequency range. The differences in tuning between DW and CC will be detailed below.

Distinct modes of vibration within the CA

When comparing the tonotopic response to three distinct stimulus frequencies, the DW has a wider peak than the CC, and this widening is unilateral. Specifically, it is the proximal flank that is different between DW and CC (Fig. 3.3D-F). The phase data (Fig. 3.3G-I) reveal that the DW accumulates less phase between the distal end and the peak region. The frequency tuning of three different positions along the CA length (Fig. 3.3J-L) shows that the DW is less sharply tuned. When recorded at the same distance from the distal end, the DW is tuned to higher frequencies than the CC. Finally, the DW phase curves are shallower than their CC counterparts, implying that DW vibrations have a shorter group delay than CC vibrations. These systematic differences between CC and DW vibration were observed in all animals tested (Supplementary Fig. 3.8). In the curves of Fig. 3.3M-O group delay for the CC exceeded that for the DW by 110, 284, and 248 μs, respectively. Since group delay is a metric of the latency with which the vibration energy arrives at the recording site (van der Heijden & Versteegh, 2015a), this suggests that the acoustic energy reaches the DW prior to reaching the CC.

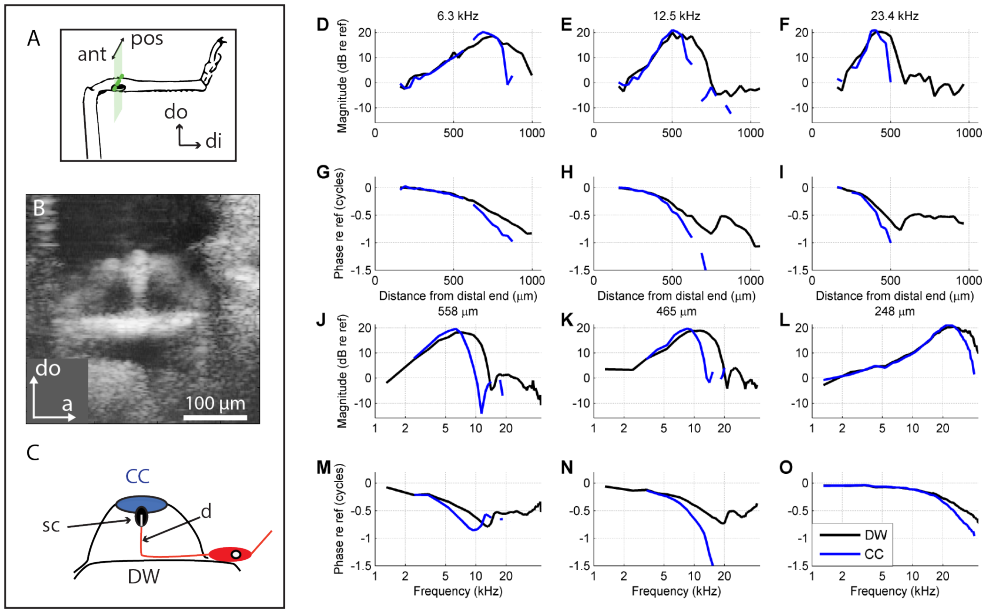

Figure 3.3: Differences in the tonotopic response and frequency tuning of the Dorsal Wall and the Cap Cells. (**A**) An anterior-posterior cross section of the front leg (**B**) OCT B-scan obtained from the top view of the CA, following an image section plane as shown in panel **A**, across the anterior-posterior axis. (**C**) Sketch relating the B-scan to the anatomy, across the anterior-posterior axis. *sc: scolopale cell, CC: cap cell, DW: dorsal wall, d: sensory dendrite.* The height of the CA is in the range of 15-60-μm, following the tonotopic axis from distal to proximal (Hummel et al., 2017). (**D,E,F**)Normalized magnitude of the dorsal wall (black line) and the cap cells (blue line) tonotopic response for different frequencies along the CA. Since a single reference was used for both structures (see Methods), the graph conveys their relative vibration magnitude. (**G,H,I**) Normalized phase of the dorsal wall and the cap cells tonotopic response for different frequencies at the same stimulus frequencies as in **D,E,F**. DW wavelength estimates: 590, 455, 346 μm, respectively. CC wavelength estimates: 370, 256, 222 μm, respectively. This corresponds to phase velocities of 3.7, 5.7, 8.1 m/s (DW) and 2.4, 3.2, 5.2 m/s (CC). (**J,K,L**) Mechanical tuning of the normalized magnitude of the dorsal wall and the cap cells at different positions that are marked by their distance to the distal end of the CA. (**M,N,O**) Normalized phase of the dorsal wall and the cap cells frequency tuning at the same positions as shown in J,K,L. DW group delay estimates: 344, 294 and 330 μs respectively. CC group delay estimates: 454, 578 and 578 μs respectively. (Data from experiment BC0007, recorded through the intact cuticle. Stimulus level 75 dB SPL. For population data, see Supplementary Fig. 3.8.)

Two parallel but shifted place-frequency maps for the DW and the CC

Are the tuning differences between the two structures apparent on the whole length of the sensory tissue? To test for that, we measured vibrations on the DW and the CC along 800-μm of the CA using 33-μm steps, while presenting stimulus frequencies from 0.4-50 kHz in ∼950-Hz steps. The spatial and frequency sampling of our measurements allowed us to construct heat maps of the tuning of the two structures (Fig. 3.4A-D). This way of presenting magnitude (Fig. 3.4A,B) and phase data (Fig. 3.4C,D) combines the spatial and spectral tuning shown separately in Fig. 3.3D-I and 3.3J-O. We were able to determine the location of the spatial peak and the spatial 5-dB-down points for each stimulus frequency, as indicated in the graphs. Consistent with the individual spectral and spatial tuning data in Fig. 3.3, the DW had a wider peak width than the CC over the entire frequency range, and the DW peaked more proximal than the CC peak. The phase responses confirm the greater accumulation of phase in the CC compared to the DW.

A detailed quantitative analysis of the tuning differences between CC and DW reveals that the tuning of the DW is shifted proximally compared to the CC (Fig. 3.4E,F). The tuning of the DW is wider than that of the CC (Fig. 3.4G). The systematic differences between the tuning of the CC and the DW span the entire length of the hearing organ, as well as the entire spectral range tested (2.4-50 kHz). When averaged over this range, the tuning difference amounts to 0.19 octave in spectral terms (Fig. 3.4E) and 31 μm in spatial terms (Fig. 3.4F).

The current dataset allows for population metrics of the tuning of the two structures. The place-frequency maps of the DW and the CC of 10 hearing organs are shown in Fig. 3.4H and I respectively. Place-frequency maps of the DW and CC motion from ten different CAs show overlapping results, which imply that the used method of anchoring the different measurement positions to the distal end of the CA is robust. The DW and the CC share a similar slope on their place frequency maps. Each octave of "best frequency" occupies 170-μm along the CA for both the DW and the CC (Fig. 3.4J), a stretch containing 9 sensory cells. The systematic differences in tuning between DW and CC were observed in all 10 animals tested, both in terms of peak location (Fig. 3.4K) and peak width (Fig. 3.4L).

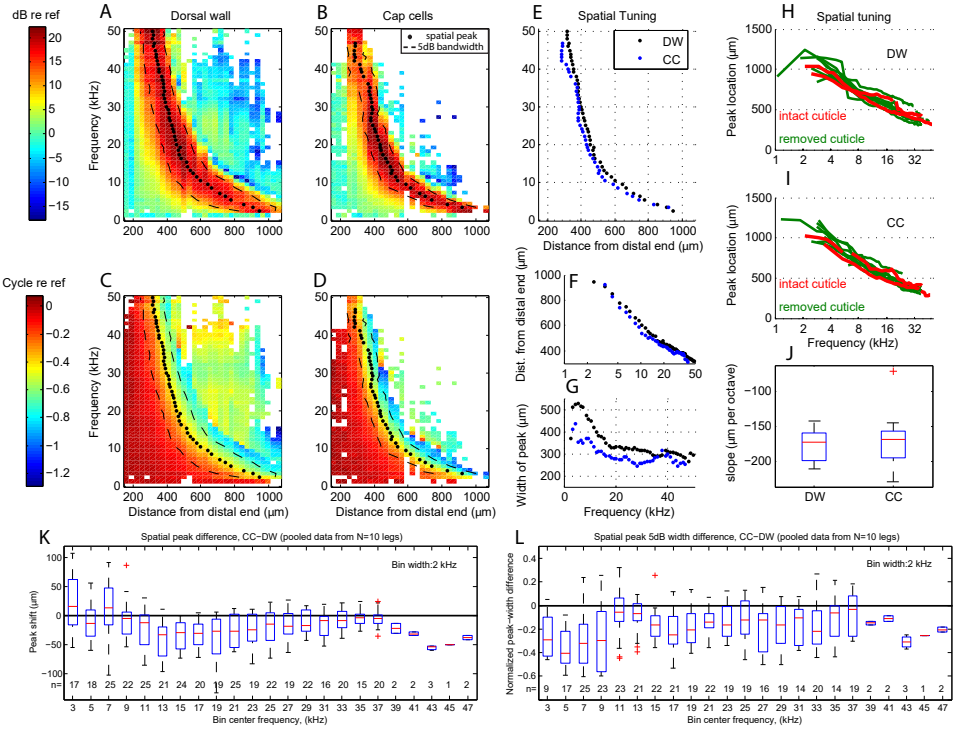

Figure 3.4: Longitudinal vibration maps reveal tuning differences between the DW and the CC. (**A,B**) Normalized magnitude responses of the DW (**A**) and CC (**B**), across different frequencies and recorded positions along the CA. The spatial peak for each frequency (black dot) and the associated 5-dB bandwidth (black lines) are overlaid. (**C,D**) Normalized phase responses of the DW (**C**) and CC (**D**), across different frequencies and recorded positions along the CA. The spatial peak for each frequency (black dot) and the associated 5dB bandwidth (black lines) are overlaid. (**E**) The frequency-dependent spatial peak per stimulus frequency for the DW and the CC. (**F**) The frequency-dependent spatial peak per stimulus frequency for the DW and the CC. In log-lin axis, both tonotopic maps are approximately straight, parallel but shifted relative to one another. (**G**) Minus-5-dB peak width versus stimulus frequency for the DW and the CC. (Data in **A-G** come from experiment BC0007. Stimulus level 75 dB SPL. More data in Supplementary Fig. 3.9.) (**H**) The place-frequency map of the DW across $n = 10$ hearing organs. (**I**) The place-frequency map of the CC across $n = 10$ hearing organs. (**J**) Median slopes of the 10 place-frequency maps are not significantly different. Data are extracted from panels **H,I**. (**K**) Population data of the relative peak position of CC versus DW, $N = 10$ legs. Spatial peak locations were pairwise subtracted between DW and CC for each frequency. The difference was statistically evaluated using 2-kHz-wide bins. The boxes have lines at the lower

quartile, median, and upper quartile values. Whisker pairs at each box show the extent of the rest of the data, with outliers marked by red plus signs. Individual bin sizes n are indicated. Over most of the frequency range, spatial peaks in the CC were shifted distally compared to the DW. (L) Corresponding comparison of the spatial peak width between DW and CC; same $N = 10$ hearing organs as in panel K. Denoting the 5-dB-down peak widths of the DW and CC by W_{DW} and W_{CC}, their normalized difference is $\Delta = (W_{\mathrm{CC}} - W_{\mathrm{DW}})/W_{\mathrm{DW}}$. Statistical analysis and layout as in panel K. The spatial peaks in the CC were systematically narrower than the peaks in the DW.

Internal motion within the crista acustica

The relative motion of the DW and the CC is a candidate for the "drive" of transduction, as the two structures coincide with the two ends of the sensory dendrite, which is oriented perpendicular to the DW (Fig. 3.3C, Supplementary Fig. 3.11). The motion here is measured along the dorsal-ventral axis, that is approximately parallel to that of the dendrite tip. The CC/DW magnitude ratio (Fig. 3.5A) shows that the two structures share similar magnitude of vibrations in positions distal to the spatial peak for each frequency. Proximal to the spatial peak, the DW magnitude dominates, resulting in negative dB values for the ratio. This analysis further characterizes how the CC magnitude decreases more distally than the DW magnitude (compare Fig. 3.4).

The direct comparison of the phase between CC and DW (Fig. 3.5B) reveals that the two structures move in phase at positions distal to the spatial peak. Consistent with the examples in Fig. 3.3, the phase difference increases drastically at locations proximal to the spatial peak of each frequency. For most frequencies, the DW accumulates a phase lead over the CC of ∼0.25-cycle over a distance of just 30-70-μm proximal to the spatial peak, but for some frequencies, the difference is larger (up to ∼0.5-cycle). The location where the phase difference occurs coincides with the divergence of the amplitudes, again consistent with the three frequency examples shown in Fig. 3.3D-I.

We further assessed the relative motion of CC and DW by computing the vector difference of their mechanical motions, i.e., taking into account both their relative amplitude and phase (Fig. 3.5C). The spatial tuning of the vector difference was somewhat sharper than that of either structure (e.g., the 5-dB-down peak width in Fig. 3.5D was 286, 202 and 187 μm for the DW, CC and vector differences, respectively). Toward the distal end, its magnitude was smaller than either individual motion. This is further illustrated in Fig. 3.5D-F, which shows the tonotopic response of the DW, the CC and their relative motion at three different stimulus frequencies, 9.4, 18.4

and 30 kHz. The differences are asymmetric: it is primarily the distal flank of the tonotopic response that is steeper for the vector difference data than it is for the DW and the CC.

The spectral data (magnitude versus frequency) reveal a consistent asymmetric sharpening of the tuning of the vector difference data compared to the DW and CC. It is primarily the steeper low-frequency flank that distinguishes the vector-difference data from the data of DW and CC alone. The spectral tuning of the vector difference is shown for a total of nine experiments in Supplementary Fig. 3.8; a further example is shown in Fig. 3.6E.

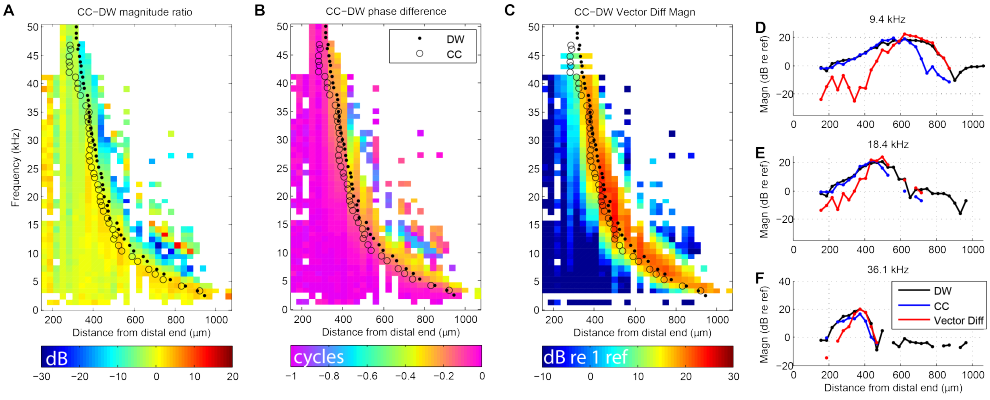

Figure 3.5: Relative motion of cap cells (CC) and dorsal wall (DW). (**A**) Colour-coded magnitude difference (in dB) between the CC and the DW mechanical response. Markers (point = DW, circle = CC) illustrate the spatial peak for each stimulus frequency, as in Fig. 3.4E. (**B**) Phase difference between the CC and the DW mechanical response of the same data as shown in **A**. (**C**) Magnitude of the vector difference between the DW and the CC mechanical response for the same data as displayed in **A,B**. (**D,E,F**) The tonotopic response of the DW, the CC and their vector difference shown for three stimulus frequencies as indicated. (Data in **A-F** come from experiment BC0007. Stimulus level 75 dB SPL. More data in Supplementary Fig. 3.8. re ref, relative to the reference)

Discussion

In summary, we recorded sound-induced vibrations in the bushcricket hearing organ using OCT vibrometry. The depth resolution of this technique yielded an unprecedented set of measurements. First, we measured the sound-induced motion of the

anterior and the posterior tympanum at the same time. Our measurements confirmed that the two tympana bulged in and out simultaneously (Bangert et al., 1998; Jonsson et al., 2016) (Fig. 3.2E). Second, the septum between them followed the motion of the posterior tympanum (Fig. 3.2B). Third, we made a detailed and quantitative comparison between the sound-induced vibrations of DW and the CC. The responses of both structures were tuned (Fig. 3.3) and there exist systematic differences between them in their tuning across the whole length of the sensory organ (Fig. 3.4). The differential motion of these structures was more sharply tuned than the absolute motion of either of them (Fig. 3.5, Supplementary Fig. 3.8).

The tympana of the bushcricket hearing organ have been studied extensively, but their contribution to the hearing function is not entirely clear. Previous studies (Bangert et al., 1998; Montealegre-Z et al., 2012) reported that the anterior and posterior tympana in different Tettigoniidae species moved inward and outward synchronously in response to sound. With LDV, one cannot measure the tympana simultaneously, and rearranging the preparation across recordings may have affected the microacoustic environment in these studies. Our simultaneous recordings provide a direct test of the relative motion of the tympani. Our data confirm and extend findings of previous studies (Bangert et al., 1998; Montealegre-Z et al., 2012). Not only the two tympana, but also the adjacent septum bulges in and out simultaneously. This antiphasic motion may periodically stretch and squeeze the DW and the dorsally placed sensory epithelium. The dorsal part of the tympanum sits on top of incompressible haemolymph, so acoustic stimulation may cause a translocation of the CA. Such a coupling somewhat resembles the scheme proposed by Montealegre-Z et al. (2012) in which the dorsal part of the tympana compresses the heamolymph overlying the CC, but the latter scheme depends on a tympanal plate mechanism in Montealegre-Z et al. (2012) that we did not find in *M. elongata*. The resemblance of the two schemes is that CA motion is not directly driven by the air pressure in the trachea but indirectly, either by the anterior tympanum and the septum through its connection to the posterior tympanum (Fig. 3.2) or via the tympanal plate and the haemolymph (Montealegre-Z et al., 2012). The antiphasic motion of the tympana is likely to cause (or reflect) air pressure variations in the trachea which will push and pull the adjacent DW, but the air-haemolymph interface may render this direct route inefficient. Intriguingly, the double hinged motion (Fig. 3.2) shows a striking resemblance with the coupling of sound into vertebrate inner ears, where a lever system (middle ear ossicles) converts the larger motion of a larger surface (eardrum) to smaller motions of a smaller area

(stapes). In vertebrate ears this configuration provides an impedance match between airborne sound and the vibrations in the fluid-filled inner ear. The hinged motion of the bushcricket tympana and adjacent septum may well serve the same purpose.

Bangert et al. (1998) reported that blocking the trachea spiracle with Vaseline decoupled the two tympana. Repeating these experiments while using OCT will allow the simultaneous measurement of the two tympana, the tracheal septum, and the CA. This may help to further disentangle the contribution of different acoustics paths to the bushcricket hearing organ. Phase differences along the ventral-dorsal axis of the tympanum, as shown in other bushcricket species (Montealegre-Z et al., 2012), were not present in *M. elongata*.

The mechano-transduction channels in the CA sensory neurons are probably located at the tips of their cilia (Hummel et al., 2016; Yack, 2004) and they are commonly assumed to open and close upon longitudinal stretching of the sensory dendrite's cilium (French, 1988). Hummel et al. (2016) observed additional microtubules at the level of the scolopidial cap. They surrounded the ciliary tip and could therefore anchor filaments relevant to gating (Liang et al., 2013). In that case, transduction is likely to be driven by any relative motion between the DW and the CC, since this would stretch and shorten the dendrite. Figure 3.6 illustrates several potential realizations of this relative motion. A relative motion between the two structures along the dorsal-ventral axis would elongate and shorten the dendrite (Fig. 3.6B). An anterior-posterior motion of the CC could also drive transduction, by pivoting of the sensory dendrite (Fig. 3.6C). Finally, a more complex elliptical motion of the two structures is possible, which could result in a frequency dependent stretching and pivoting of the sensory dendrite (Fig. 3.6D). As will be discussed further in following paragraphs, more measurement angles are needed to disentangle the different components of motion and thus find the correct interpretation of the internal motion.

Our simultaneous recordings of the DW and the CC are a first step toward answering these questions. The systematic differences in tuning between the DW and CC (Figs. 3.3,3.5, Supplementary Fig. 3.8) indeed reveal a nontrivial relative motion between different structures within the CA. Stated differently, acoustic stimuli evoke a periodic deformation of the CA. Importantly, this micromechanical motion is sharply tuned. If transduction is indeed driven by such micromechanical motion, our data may explain discrepancies in best frequency and tuning sharpness between mechanical and neural tuning in the bushcricket CA (Hummel et al., 2016). In particular, it would explain the sharper tuning of the neural response compared to the mechanics. A promising

way to address such questions in future studies is to combine OCT vibrometry with neural recordings in the same hearing organ.

Our observations have implications for the understanding of the physical principles shaping the CA vibrations. Despite their close vicinity (15-60 μm apart, depending on longitudinal position), the DW and CC differ in response phase, best frequency and bandwidth. This calls for an explanation in terms of vibration mechanics. It is possible that the longitudinal stiffness and size gradients of the DW provide a preliminary stage of frequency selectivity which is then further sharpened by local resonances of the individual scolopedia. The larger group delay of the CC compared to the DW (Fig. 3.3) is consistent with such a two-stage filtering. The hypothetical scheme is also reminiscent of the mammalian cochlea, where a physiologically robust, weakly tuned, response is complemented by a physiologically vulnerable, sharply tuned response (Robles & Ruggero, 2001). Further exploration of such hypotheses will require a more detailed characterization of the micromechanical motion of the CA using OCT, combined with mathematical or numerical modelling.

The mapping of a wide audio range onto a short (<1-mm) sensory organ necessarily leads to a very dense representation of frequencies. The slope of the frequency-place map amounted to ∼170-μm/octave and was nearly identical in DW and CC (Fig. 3.4J). In comparison, the length of the unrolled cochlea is 35 mm in humans and 11 mm in gerbil, and the tonotopic slope in these species is 5000-μm/octave (von Békésy, 1960) and 1500-μm/octave (Müller, 1996), respectively. Despite these large quantitative differences, it is remarkable that the tonotopic map is well represented by a straight line on a log-frequency scale in both the bushcricket (Fig. 3.4H,I) and most mammals (with deviations occurring only at very low frequencies <500 Hz (Greenwood, 1996), and in some echolocating species having an acoustic fovea (Kössl & Vater, 1995)). This striking similarity suggests that, despite vast anatomical differences (e.g. the basilar membrane is an interface between two fluids, whereas the DW is an interface between air and fluid (Supplementary Fig. 3.11)), common mechanisms may underlie frequency selectivity in the hearing organs of insects and mammals. Since these mechanisms are equally poorly understood in mammals and insects, any progress in the field of insect hearing may advance our understanding of mammalian hearing and vice versa. Species with well accessible hearing organs like the bushcricket are highly suited for such comparative studies.

In mammals, the tonotopic map directly determines the density of neural representation of frequency bands, because the spacing of sensory cells is uniform over the

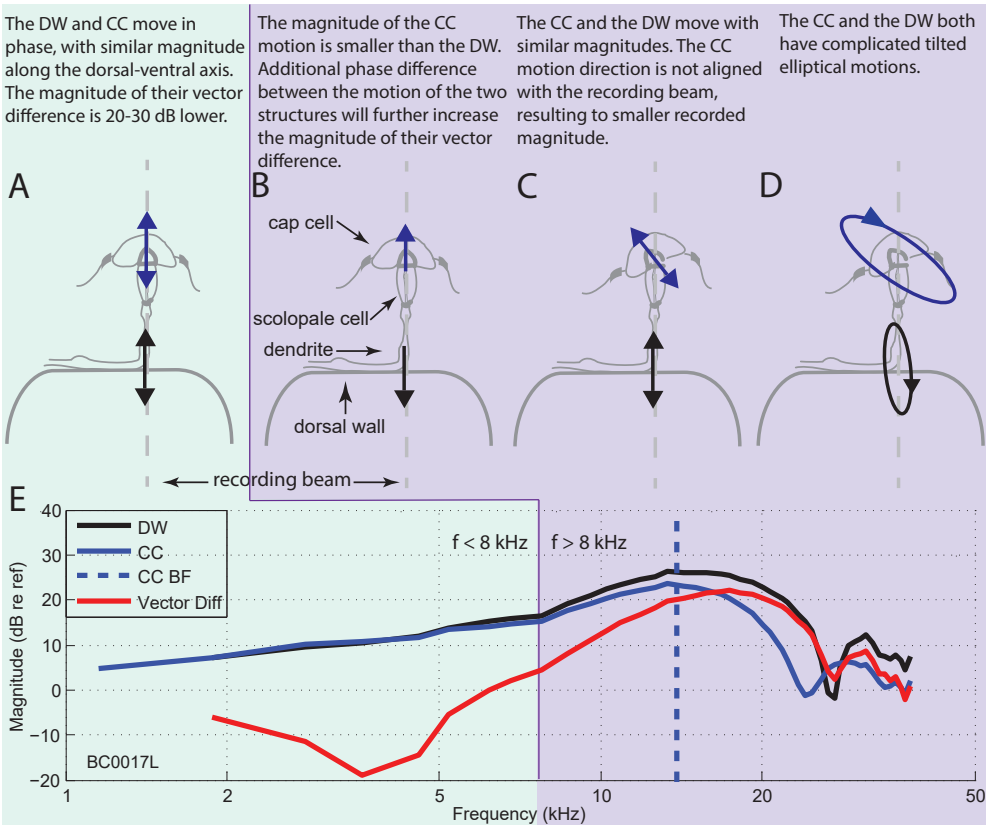

Figure 3.6: Different geometric interpretations of the relative motion between DW and CC observed in this study. (**A**) In the absence of relative motion (here, <8 kHz, light green background), the DW and the CC move in phase and with similar magnitude along the dorsal-ventral axis (aligned with our recording beam). (**B-D**) Potential internal motion patterns that may underlie the observed differences in magnitude and phase (here, >8 kHz, light purple background). (**E**) Tuning curves of DW, CC and their vector difference recorded at the medial part of the CA. (Experiment BC0017L, 79 dB SPL) Population data, see Supplementary Fig. 3.8.

cochlear length. Thus a typical (non-foveal) mammalian map reveals an equal number of neural frequency channels per octave over most of the range, with a somewhat poorer representation towards the very lowest frequencies. In *M. elongata* the lower frequencies are also less densely represented, but this time because of the wider spacing of proximal sensory units (Hummel et al., 2017). It is unclear whether this similarity is rooted in a common functional requirement.

In the context of comparative hearing science, it is also noteworthy that the spatial phase patterns in bushcrickets (e.g. Fig. 3.3) have their main features in common with those in the mammalian cochlea: an initial flat portion ending in a sharp downward kink, followed by a steep downward slope ending in a plateau (van der Heijden & Cooper, 2018). Phase accumulation has been interpreted in terms of traveling waves in both mammals (von Békésy, 1960) and bushcrickets (Olson & Nowotny, 2019). The amount of phase lag accumulated at the peak location is larger in mammals (∼1.5-cycle (Robles & Ruggero, 2001) than in the bushcricket (∼0.5-cycle), and this may reflect sharper tuning in the mammals (Joris et al., 2011). With all the similarities, one marked difference between the bushcricket and mammalian cochlea is the effect of sound intensity. Cochlear responses are very nonlinear: they show strongly compressive growth over a large dynamic range (68 dB of compression over a 96-dB range, (Robles & Ruggero, 2001)). Changes in sound intensity strongly and systematically affect sharpness of cochlear tuning, peak location of the wave (Robles & Ruggero, 2001) as well as its wavelength, phase velocity and group velocity (van der Heijden & Versteegh, 2015a; van der Heijden & Cooper, 2018). In comparison, the bushcricket CA is much more linear, only showing a slight compression (7 dB of compression over an 80-dB range, mostly concentrated at intensities >100 dB SPL), and there is no apparent effect of intensity on sharpness of tuning or wave propagation (Palghat Udayashankar et al., 2012).

Although OCT vibrometry is a powerful technique for the study of hearing organs, it is important to briefly consider some limitations and potential ways to overcome them. Recorded vibrations are projections of the actual motion onto the recording beam. The more aligned the two are, the closer the measured magnitude resembles the actual magnitude. For our DW and CC recordings we aligned the recording beam with the dorsal/ventral axis, which is perpendicular to the anterior/posterior alignment used for our tympanum recordings. A direct comparison between tympanum and CA motion magnitude is thus of limited scope. Our alignment choices optimize consistency with existing literature, but it is well possible that there exist other, functionally relevant, directions of motion between the DW and the CC that we failed to measure (Fig. 3.6). For a discussion of the spatial and directional interpretation of OCT vibrometry we refer to Cooper et al. (2018).

These geometric unknowns caution against oversimplification. It may appear attractive to interpret the different spatial phase profiles in CC and DW in terms of two "parallel waves" traveling at different speeds, but they may as well reflect a

gradual change in vibration mode of a single wave (van der Heijden, 2014). A more comprehensive exploration of the micromechanics of the bushcricket CA will require measuring the same structures from different angles, so that different directions of motion can be disentangled. In the current study, we did image the CA from both an anterior-posterior view and a dorsal-ventral view. At this stage, however, we cannot determine the direction of motion with certainty. This would require a reliable method of registration: ensuring that the exact same location is targeted across viewing angles. In the literature, the lateralization of the CC responses towards the anterior side of the CA has been described (Palghat Udayashankar et al., 2014). With a validated registration method, one could record the CC from the two angles mentioned above, test whether the CC indeed pivots around the scolopale cell, and assess the relevance of this motion for tuning.

Other complications may arise from uncertainties in interpreting OCT images in heterogeneous tissues. Our study demonstrates that OCT produces anatomically faithful images of the bushcricket hearing organ (Figs. 3.1B-D 3.2A-C, 3.3B). The same technique has been used to study the morphogenesis of insects in a non-invasive manner (Nioi et al., 2019) and insect heart pulsations (Choma et al., 2006). OCT imaging is based on the delay times of back-scattered light from different depths of the sample, which not only depend on the pathlength, but also on the speed of light of the medium as quantified by its refractive index n. For a homogeneous medium the delay times are easily corrected for the refractive index. The insect leg, however, is heterogeneous: it is partly filled with fluid (haemolymph, $n \approx 1.5$) and partly with air ($n \approx 1$). Figure 3.2 illustrates this: the dorsal, haemolymph filled part of the leg is distorted compared to the ventral, air-filled part. Detailed knowledge of the refractive index of the imaged structures would enable one to correct for such imaging artifacts, but the optical characterization of the bushcricket hearing organ exceeded the purposes of the current study.

This study has employed the opportunities for studying nonvertebrate hearing organs offered by OCT vibrometry. It revealed complexities in the micromechanics of the bushcricket CA that had not been found with previous methods. On the one hand, these findings bring new challenges in understanding insect hearing. On the other, they offer new views and suggest new solutions to known fundamental problems, including the delivery path of acoustic energy to the sensory tissue, the biophysics of auditory frequency selectivity and the exact mechanisms that drive transduction. From a wider perspective, current technology facilitates the comparative study of hearing

organs in general and the similarities and differences between hearing in insects and mammals in particular. For all these scientific problems, we now have the technical means to explore them. This opens up a wide range of theoretical and experimental exploration of hearing in miniaturized systems, with numerous technical and scientific applications.

Acknowledgments

We thank Ana-Maria Marchidan for her help with the illustrations. This work was supported by Deutsche Forschungsgemeinschaft Grant 841/8-1.

Supplementary Information

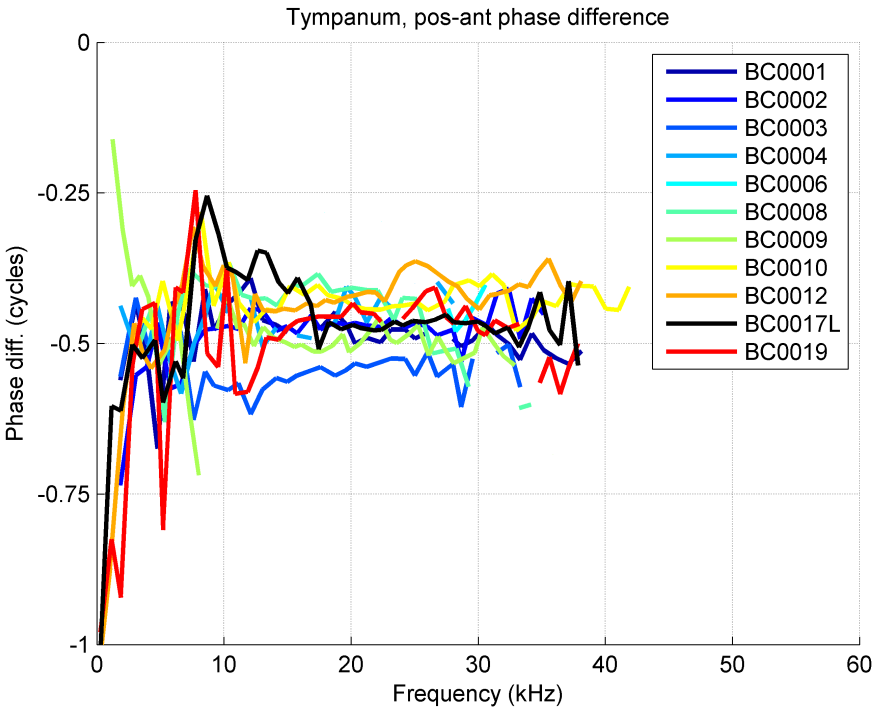

Figure 3.7: Phase difference between the two tympana across n = 11 different legs. Data from BC0017L (black line) were obtained from a preparation where the dorsal cuticle was removed and replaced by a glass cover slip. Stimulus level: 75, 79 or 85 dB SPL

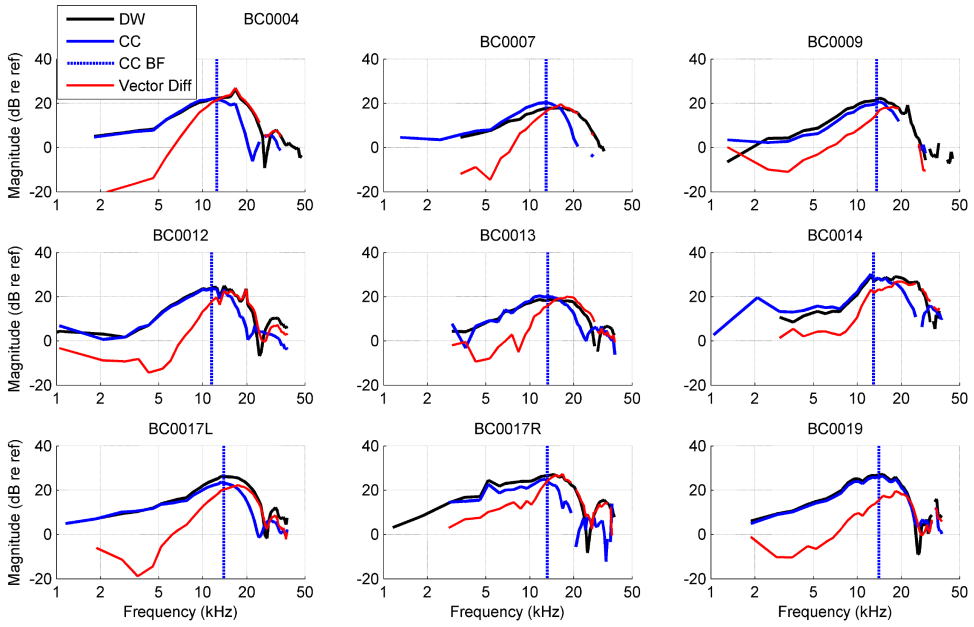

Figure 3.8: Vibration magnitudes of the CC, the DW and their vector difference recorded at positions with similar tuning (∼13.3-kHz), across $n = 9$ different legs. The DW and the CC were recorded using the same recording beam. The dashed line illustrates the best frequency

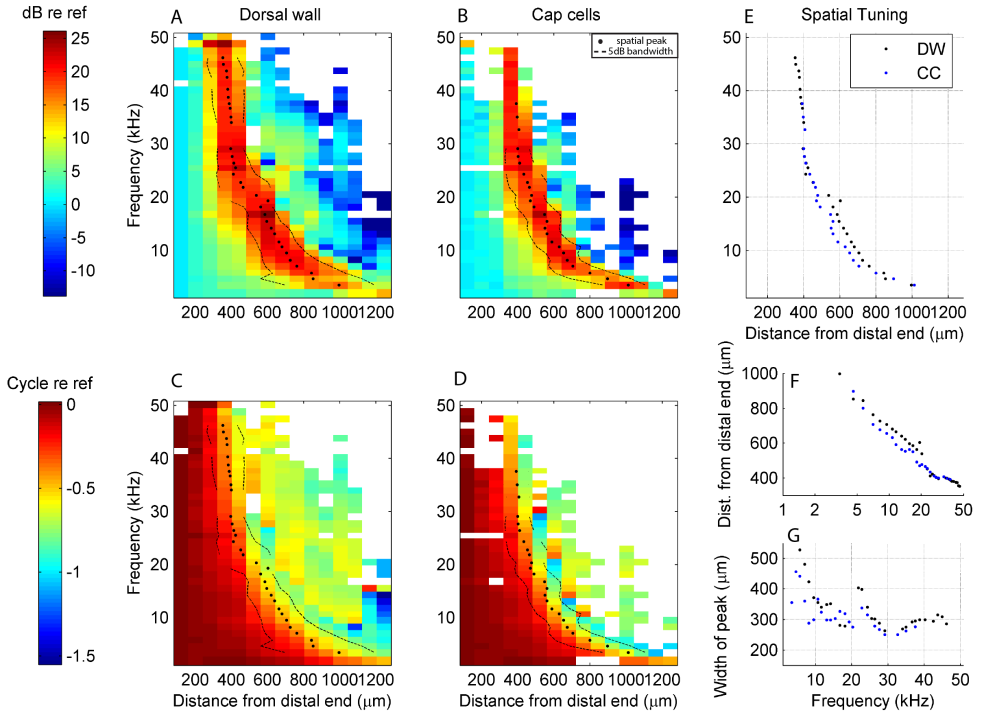

Figure 3.9: Longitudinal vibration maps reveal tuning differences between the DW and the CC. Data in **A-B** come from experiment BC0004, a preparation where the dorsal cuticle was removed and replaced by a glass cover slip. (**A**,**B**) Normalized magnitude responses of the DW (**A**) and CC (**B**), across different frequencies and recorded positions along the CA. The spatial peak for each frequency (black dot) and the associated 5-dB bandwidth (black lines) are overlaid. (**C**,**D**) Normalized phase responses of the DW (**C**) and CC (**D**), across different frequencies and recorded positions along the CA. The spatial peak for each frequency (black dot) and the associated 5-dB bandwidth (black lines) are overlaid. (**E**) The frequency-dependent spatial peak per stimulus frequency for the DW and the CC. (**F**) The frequency-dependent width of the peak (5-dB) per stimulus frequency for the DW and the CC. (**G**) Minus-5-dB peak width versus stimulus frequency for the DW and the CC. Stimulus level 85 dB SPL.

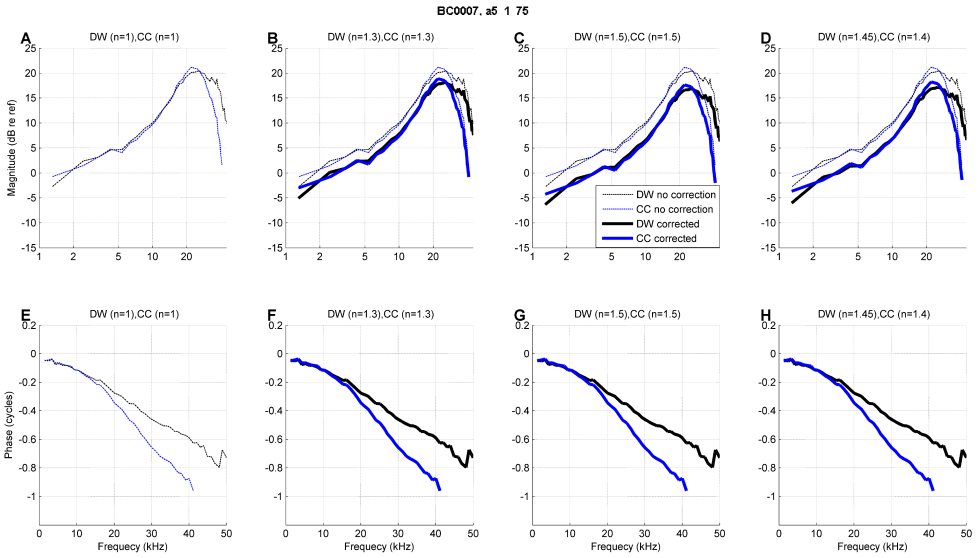

Figure 3.10: The effect of the refractive index on the recorded vibration magnitude and phase. The recorded structures are likely to have a refractive index higher than 1, which results to an overestimation of the vibration magnitude. We can correct for the refractive index as long as the optical properties of the surrounding fluids and structures are known, following the frequency formula: $\Delta_{\text{Magn}} = -20log_{10}(n)$. For biological fluids, the refractive index is not expected to exceed $n = 1.5$, which would amount for a - 3.52-dB correction. (**A**) Vibration magnitude with no correction applied. (**B**) Vibration magnitude corrected for the refractive index of water. (**C**) Vibration magnitude corrected for the refractive index of dense lipids. (**D**) Vibration magnitude corrected differently for the two structures. (**E-H**) The measured phase is not dependent on the refractive index.

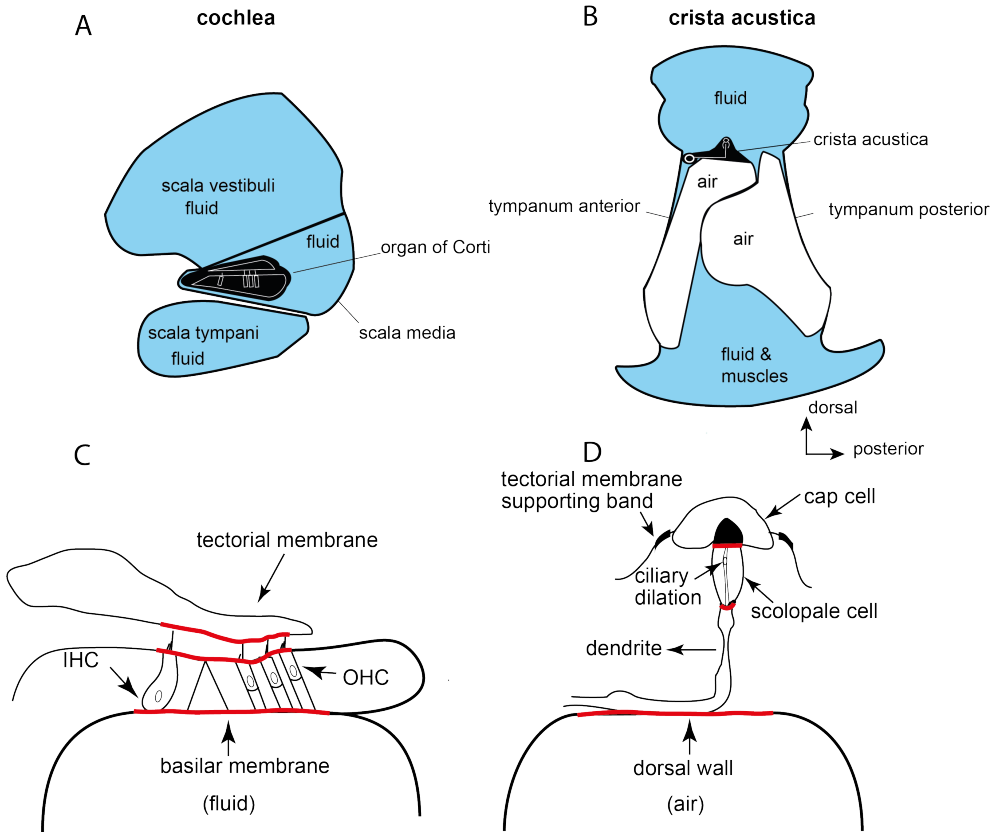

Figure 3.11: Comparison of the mammalian cochlea and insect crista acustica. (**A**) Schematic of the mammalian cochlea. (**B**) Schematic of the bushcricket crista acustica. The upper graphics shows the position of the hearing organs and how they are surrounded (fluid/air). (**C**) A close up of the organ of Corti. The anatomical structures that that surround the transduction side (hair bundle) are marked in red. (**D**) A close up of the crista acustica. The anatomical structures that that surround the transduction side (ciliated tip of the dendrite) are marked in red.

Chapter 4

Elliptical sound-induced motion in the bushcricket hearing organ [1]

The bushcricket Mecopoda elongata can hear a wide range of frequencies, utilizing less than 50 sensory units. It is known that transduction takes place in the sensory dendrite but the underlying mechanisms are still unexplained. In a recent study we used optical coherence tomography (OCT) to characterize the relative motion in the dorsal-ventral direction between anatomical structures near the transduction site. In the current study, we combined OCT vibrometry with the use of a mirror to measure vibrations of the same structures from two different angles. By developing a method to identify measurement locations across the two viewing angles, we were able to decompose the motion into a anterior-posterior and a dorsal-ventral component. In the structures surrounding the transduction site we observed elliptical sound-induced motion that varied systematically with frequency. The motion in the cap cells (CC) was more tilted towards the anterior-posterior axis than that of the dorsal wall (DW). Finally, the two-dimensional relative motion between the DW and the CC, a candidate for the drive of transduction, was sharply tuned, and for ultrasound it was similar to the neural tuning described in the literature for this species.

[1] Vavakou, A., Scherberich, J., Nowotny, M., & van der Heijden, M. (2022). Elliptical sound-induced motion in the bushcricket hearing organ. Submitted in the *Proceedings of the Mechanics of Hearing 2022.*

Introduction

Acoustically communicating insects have minuscule hearing organs, smaller than 1 mm, in their front tibia, the crista acoustica (CA). These organs allow them to hear a wide range of frequencies, from few hundreds of Hertz up to ultrasounds (Hummel et al., 2014). This is achieved by few sensory units (less than 50 (Strauß et al., 2012; Hummel et al., 2017)) that are tonotopically organized along the proximal-distal axis (Palghat Udayashankar et al., 2012; Oldfield, 1982). The sound input reaches the CA through the acoustic trachea and the two tympana that surround the sensory tissue (Lewis, 1974; Hoffmann & Jatho, 1995; Michelsen et al., 1994; Heinrich et al., 1993; Hummel et al., 2011). Each sensory unit consists of a sensory dendrite, that is located dorsally to the dorsal wall (DW) and a cap cell (CC) that is found on the dorsal tip of the sensory dendrite (Fig. 4.1 C,D). The sensory dendrite is surrounded by a scolopale cell.

The frequency-selective transduction of mechanical energy to electrical responses is thought to take place through stretching of the sensory dendrite (Yack, 2004; Hummel et al., 2016). The neural tuning of the sensors is sharper and shifted towards lower frequencies compared to the mechanical tuning (Hummel et al., 2016). The actual mechanism of sensory transduction remains unknown. A step towards unraveling the mechanism was taken by Vavakou et al. (2021), who used OCT-vibrometry to measure sound-induced vibrations of both the DW and the CC. A crucial aspect of that study was the use, for the first time in insect hearing, of OCT vibrometry, a technique that allows for depth resolution of the recorded tissue. They reported that the CC and the DW mechanical responses to sound stimuli differ in response phase, best frequency, and bandwidth. Further micromechanical exploration of the recorded structures revealed that the relative motion among the DW and the CC is tuned more sharply and to higher frequencies than the individual structures (Vavakou et al., 2021).

However, with the customary vibrometry approach, it is only possible to measure the projection of the overall motion of the recorded structure on the recording beam (Lee et al., 2016; Cooper et al., 2018). Vavakou et al. (2021) aligned their measurement beam with the dorsal ventral axis of the recorded structures. As a result, any other possible directions of motion are underrepresented in their measurements. As discussed by the authors, transduction could be driven by more complex, two-dimensional motion of the CC relative to the DW, and they concluded that an accurate description of the overall motion requires the measurement of the same structure from different

recording angles (Vavakou et al., 2021). Facing a similar challenge, Lee et al. (2016) disentangled two motion directions in structures within the mouse cochlea, by rotating the preparation relative to the recording beam.

In the current report, we measured sound-induced vibrations of the CA from two different angles, using a mirror (Fig. 4.1 A). The direct view (DV) was aligned with the dorsal-ventral axis, and the CA was imaged through the dorsal cuticle. Using the mirror, the CA were imaged through the anterior tympanum (Fig. 4.1 B-D). An important and nontrivial step in the processing of the data is an accurate method of "registration", i.e., finding the corresponding recorded positions across the viewing angles by embedding them in a three-dimensional coordinate system (see section **"Three-dimensional (3D) registration"**). Using geometrical calculations, the same target structures were detected in both views. We applied this registration method to characterize the sound-induced vibrations of both the DW and the CC (Fig. 4.1 E,F). This allowed us to decompose the recorded motion to the dorsal-ventral and anterior posterior components. We report that elliptical motion is prevalent in both the DW and the CC. We further quantify the elliptical character of the recorded motion using geometrical metrics.

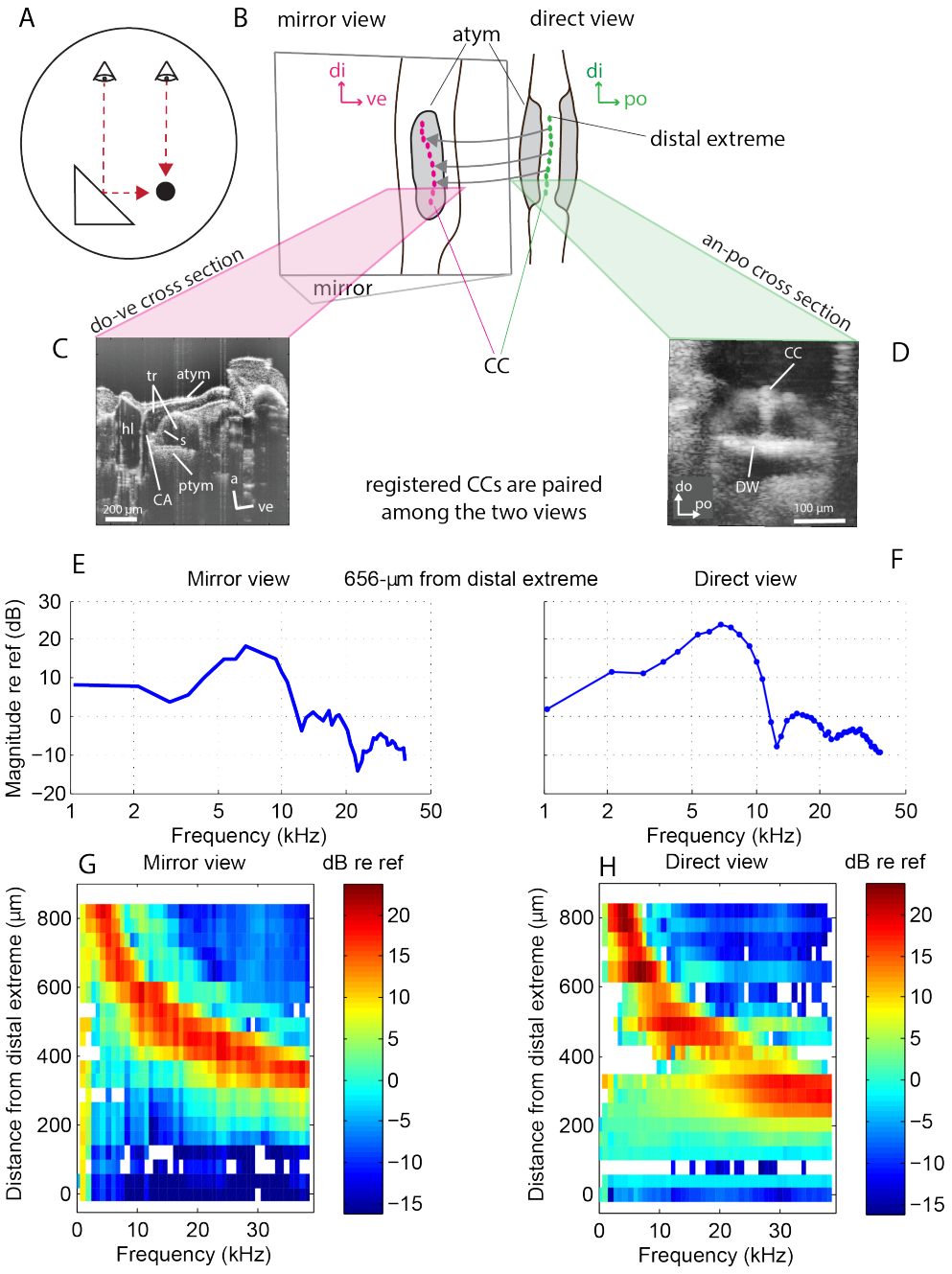
A
B
mirror view
direct view
atym
di
ve
di
po
distal extreme
do-ve cross section
an-po cross section
mirror
C
CC
D
tr
atym
hl
s
ptym
CA
a
ve
200 µm
CC
DW
do
po
100 µm
registered CCs are paired
among the two views
E
Mirror view
656-µm from distal extreme
F
Direct view
Magnitude re ref (dB)
Frequency (kHz)
G
Mirror view
dB re ref
H
Direct view
dB re ref
Distance from distal extreme (µm)
Frequency (kHz)

Figure 4.1: Measuring the CA from two different angles. (**A**) Combining the depth resolution of OCT vibrometry with the use of a mirror allowed us to measure vibrations on the same structures from two distinct viewing angles. (**B**) Illustration of the measured sample. The hearing organ was recorded from two different views, the probe facing the dorsal cuticle directly (DV, direct view), and it facing the anterior tympanum indirectly via a mirror (MV, mirror view)(di: distal, ve: ventral, po: posterior, atym: anterior tympanum.) The coordinates of the measured CC and DW positions (magenta and green markers respectively) were registered in 3D space. Corresponding measured positions were paired among the two views. (**C**) Cross-section OCT image ("B-scan") obtained with the mirror view, with the measurement beam (vertical direction in B-scan) directed along the anterior-posterior axis of the hearing organ, and the scanning direction (horizontal direction of B-scan) along the dorsal-ventral direction as shown in panel B. This view favors the measurement of vibrations in the anterior-posterior direction. (do: dorsal, atym: anterior tympanum, ptym: posterior tympanum, tr: trachea, s: septum, CA: crista acustica, hl: haemolymph) (**D**) B-scan obtained with the direct view, with the beam along dorsal-ventral axis and the scanning direction along the anterior-posterior image section plane as shown in panel B. This view favors vibrations in the anterior-posterior direction. (CC: cap cell, DW: dorsal wall). (**E,F**) Tuning of the normalized vibration magnitude of the cap cells located 656 μm from the distal extreme of the CA as imaged mirror view (E) and direct view (F). (**G,H**) Longitudinal vibration maps of paired recorded CC positions between the mirror and the direct views. (**G**) Normalized magnitude responses of the CC across different frequencies and recorded positions along the CA, as recorded from the mirror view. (**H**) Normalized magnitude responses of the CC across different frequencies and recorded positions along the CA, as recorded from the direct view. (Data from experiment BC0013)

Materials and Methods

Animal preparation

In total, 8 bushcrickets of the species *Mecopoda elongata* were used for in vivo sound-induced vibration measurements on the CA. The animals were anesthetized by lowering the body temperature using ice. The wings, the middle and the rear legs were removed. The thorax of the animal was mounted on the animal holder using medical wax. The front legs were stabilized in a position where the CA were accessible to the OCT through the dorsal cuticle, again using medical wax. The cuticle was usually surgically removed and replaced by a glass cover slip, to improve the optics and ensure the CA were visible in the OCT image. For more details, look into Vavakou et al. (2021). In experiment BC0013 the CA were recorded through an intact cuticle. The position of the tibia was optimized so that the dorsal-ventral axis of the CA was aligned with the

recording beam. The CA were also measured through the anterior tympanum, using a mirror that was placed close to the anterior tympanum. For that purpose, a 3-mm Protected Gold Coated, N-BK7 Right Angle Mirror 65-844 by Edmund Optics (EO) was used. The mirror was attached to a rigid cable, allowing for finer control during the placement. The rigid cable attached to the mirror was stabilized using plasticine, at the position where the CA image quality through the anterior tympanum was optimal. At the end of the experiment, the animal was anesthetized, and subsequently euthanized by decapitation. In the current report, data from experiments BC0013, BC0014 and BC0017L are presented in detail.

Acoustic stimulation

Broadband multi-tone "zwuis" complexes were used, following an open field stimulation paradigm (van der Heijden & Joris, 2003). We used a ScanSpeaker R2904/700005 loudspeaker, placed 35 cm away from the animal, inside a sound-proof booth. The ipsilateral acoustic trachea opening on the thorax was facing the loudspeaker. The surfaces of the OCT probe, animal holder, etc., were covered with cotton wool in order to minimize acoustic reflections. The most commonly used broadband stimulus consisted of 47 spectral components, spanning 0.3 kHz to 38 kHz (average frequency spacing: 817 Hz), presented at 79 dB SPL per component. The components all had equal amplitudes, with levels expressed in dB re 20-μPa (i.e., dB SPL), but stimulus phase was randomized across frequency. Each stimulus was presented for 12 s, and inter-stimulus intervals lasted for approximately 60 s.

OCT imaging and vibrometry

Vibration measurements were obtained using OCT. More details on the experimental setup are in ref. (Cooper et al., 2018; Vavakou et al., 2021). OCT is an imaging technique based on low-coherence interferometry. A spectral domain - optical coherence tomography system (Thorlabs Telesto TEL320C1) was used for interferometric imaging and vibration measurements. Its field of view was 10 $\times$ 10 mm; its depth range, 3.5 mm. The working distance of the objective was 24 mm. Cross-sectional (B-scan) and axial images (A- and M-scans) were triggered externally using monophasic rectangular pulses phase-locked to the acoustic stimulation system (Tucker Davies Technologies System III) at a sampling rate of 111.6 kHz. The optics of our recording system (Mitotoyu IR imaging lens with a numerical aperture of 0.055) introduced an axial

point spread function of 6-µm full width half maximum and a lateral resolution (in the XY plane) of 13 µm (all assessed in air, with a refractive index of one).

For our dorsal view measurements, the CA was imaged directly, without using a mirror. The OCT measurement beam was manually aligned with the dorsal–ventral anatomical axis of the CA. Therefore, these vibration measurements favor the vibrations along this axis. The depth resolution of the OCT allowed us to record the DW and the CC simultaneously, along one recording beam, at different positions of the CA. Therefore, the DW and CC measurements obtained with a single optical beam share the same distance from the distal end of the CA.

Additionally, the CA was imaged through the anterior tympanum, using a mirror (Fig. 4.1 A,B). Viewed through the anterior tympanum, the DW and the CC can not be obtained from the same recording beam. For that reason, vibration measurements on these structures were obtained separately (see Fig. 4.2 C).

The sample was not moved when recorded through the mirror and directly. Still, the OCT probe had to be adjusted vertically to ensure that the recorded structure was in the focal plane.

Response analysis

Mechanical measurements were obtained from (1) the DW imaged along the dorsal-ventral axis, (2) the CC measured along the dorsal-ventral axis, (3) the DW measured along the anterior-posterior axis, (4) the CC measured along the anterior-posterior axis. Responses were analyzed by Fourier transformation of the vibration waveforms derived from contiguous groups of three pixels in each M-scan, each pixel covering a depth of 3 μm. For more details, consult Vavakou et al. (2021).

The mechanical measurements from the CA were normalized to vibrations recorded on the distal end of the organ obtained from the dorsal-ventral view (as in Vavakou et al. (2021)). All the measured structures shared the same mechanical reference. This use of a common reference is analogous to normalization to the vibrations of middle ear ossicles commonly used in the field of cochlear mechanics (Rhode, 1971). It corrects imperfections in the calibration of the acoustics. In some cases (3 experiments), the readjustment of the probe height among the two views altered the microacoustical environment, and the measurement had to be discarded. Usually, this effect could be avoided by using sound absorbing material.

Three-dimensional (3D) registration

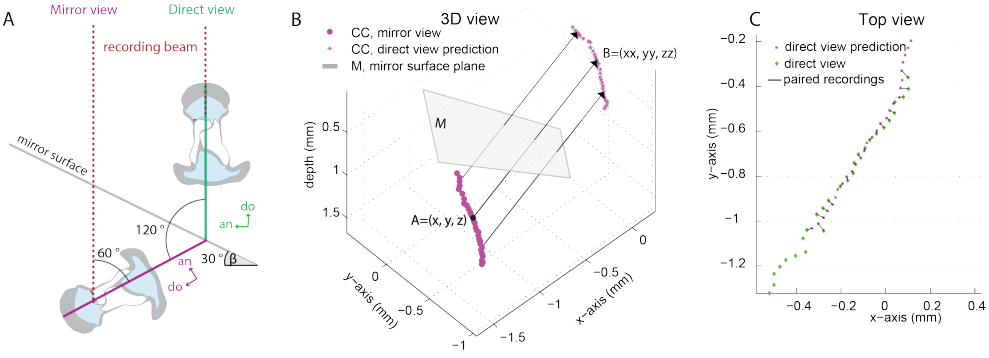

Figure 4.2: Registration of measured points in 3D space. (**A**) Geometric reconstruction of a CA cross-section viewed directly and through the mirror. In the direct view, the recording beam is aligned with the dorsal-ventral anatomical axis. In the mirror view, the dorsal-ventral axis is tilted relative to the recording beam. (**B**) Geometric prediction of the direct view coordinates ($\vec{B}$ = (xx, yy, zz)) derived from the mirror image coordinates ($\vec{A}$ = (x, y, z)) and the mirror surface plane (M) for all the recorded positions. (**C**) Top view of the original (DV) and the predicted direct view (pDV). Each DV recording (green) is paired with a pDV recording (magenta), following minimum Euclidean distance criteria in the XY plane. (Data in B and C are from experiment BC0013)

An essential methodological aspect of this study is to ensure a proper match ("registration") of measurement points between the direct and the mirror views. That was achieved post-hoc, by first measuring vibrations in a dense array of locations along the length of the CA, using both views, and then registering all the measurement points and the mirror surface plane in a global 3D coordinate system. By convention, the measurement beam in the direct view is aligned with the dorsal-ventral anatomical axis of the CA. The mirror surface is visible in the B-scans captured from the mirror view (MV), allowing for manual registration of points that belong to the mirror surface plane in a global 3D coordinate system. For each experiment, the 3D coordinates of 13-57 points belonging to the mirror surface were registered manually. Using these points $\vec{p}$, the mirror surface (M) with a normal $\vec{\nu}$ was found by fitting these data to the geometric equation of the plane:

$$M = \{\vec{p} \in \mathbb{R}^3 : \vec{p} \cdot \vec{\nu} = 1\} \tag{4.1}$$

by the method of least squares. The angle β between the mirror surface and the horizontal (XY) plane is then given by

$$\cos\beta = \hat{\nu} \cdot \hat{z}, \tag{4.2}$$

with $\hat{z}$ the unit vector in the Z direction, and $\hat{\nu} = \vec{\nu}/\|\vec{\nu}\|$ the unit vector along $\vec{\nu}$. Expressed in 3D video coordinates, each CA point shows up at two locations: at $\vec{A} = (x, y, z)$ through the mirror, and at $\vec{B} = (xx, yy, zz)$ observed directly, as illustrated in Fig. 4.2B. Knowing $\vec{A}$ and the mirror plane vector $\vec{\nu}$ (eq. 4.1) is sufficient to predict the coordinates of $\vec{B}$:

$$\vec{B}_{\text{pred}} = \vec{A} + \frac{2\vec{\nu}}{\|\nu\|^2}(1 - \vec{A} \cdot \vec{\nu}) \tag{4.3}$$

This reduces the registration problem to matching the observed DV points $\vec{B}$ to the predicted DV (pDV) points $\vec{B}_{\text{pred}}$. A full 3D match, however, was not possible, because during the experiment the probe position was adjusted vertically between DV and the MV imaging to ensure that the recorded structures were in the focal plane of the OCT. The exact vertical displacements of the probe were not logged for these experiments. As a result, the z coordinate of the measured CA (the distance of the CA from the probe), could not be expressed in the global coordinate system shared by the DV and the MV. Still, the pDV and the DV should coincide in the XY plane (top view), and this is sufficient for a unique registration between the arrays of CA points imaged in DV and MV (Fig. 4.2C). The z-coordinates of points $\vec{A}$ were not included in the registration procedure, and the overlap between the pDV and the DV was maximized in the XY plane (Fig. 4.2C). Each DV measurement position was paired with a pDV measurement, following a minimum Euclidean distance criterion in the XY plane. For consistency, the two views were paired using the CC registration results for both the CC and the DW.

2D motion decomposition

Successful registration ensured that the same structure was measured from two different angles, obtained from the DV and the MV. For each position on the CA, vibration measurements were performed on both the CC and the DW (Fig. 4.3A-D). The DV is

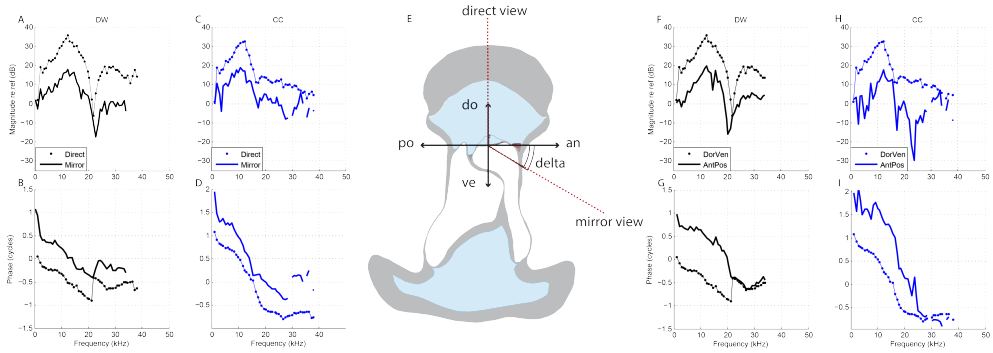

Figure 4.3: Measured motion is decomposed into the dorsal-ventral and anterior-posterior components. (**A-D**) Normalised displacement magnitude and phase as measured through the mirror and the direct view, for the DW and the CCs. (**E**) The mirror view and the direct view are related with a known angle delta, that is derived from the OCT images. The direct view is aligned with the dorsal-ventral axis by convention. The dorsal-ventral motion component is identical to the direct view measurement. The anterior-posterior motion component is derived by the obtained measurements through the mirror and the direct view. (**F-I**) Normalized displacement magnitude and phase of the measured structure along the dorsal-ventral and posterior-anterior axis, for the DW and the CCs. (Data from experiment BC0014. CC and DW were recorded 703 μm away from the distal extreme of the direct view.)

aligned with the do-ve anatomical axis by convention. The B-scans in MV are tilted relative to the an-po axis by an angle δ (Fig. 4.3E) that is related to the angle β of eq. 4.1 as follows (see Fig. 4.2A:

$$\delta = 90^\circ - 2\beta \tag{4.4}$$

The overall motion measured through the MV contains contributions of motion components along the do-ve and the an-po directions, as it coincides with neither of these axes. The measured motion can be decomposed into the do-ve and an-po components as follows. Denoting by r and m the complex 2D vectors, in the plane of the B-scans, of the recorded and the decomposed motion, respectively, their components are related by

$$\begin{bmatrix} r_{\mathrm{MV}} \\ r_{\mathrm{DV}} \end{bmatrix} = \begin{bmatrix} \cos\delta & -\sin\delta \\ 0 & 1 \end{bmatrix} \begin{bmatrix} m_{\text{an-po}} \\ m_{\text{do-ve}} \end{bmatrix}. \tag{4.5}$$

The decomposition, i.e., finding m from r, is realized by inverting this matrix equation.

Quantitative description of the elliptical motion

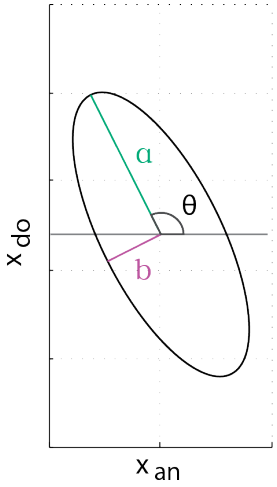

Figure 4.4: Quantitative description of the elliptical motion. a and b represent half the length of the major and minor axis of the ellipse, respectively. By convention, the tilt θ of the ellipse is the angle between the dorsal major axis and the anterior-posterior axis x_{an}.

A superposition of two harmonic oscillations at the same frequency but along different directions results in elliptic trajectories. The shape and orientation of the ellipse depends on the relative amplitude and phase of the two oscillations. An ellipse is described mathematically by the major axis ($2a$) and the minor axis ($2b$), as shown in Fig. 4.4. Momentarily abbreviating the components of the complex motion vector as m_{d} (along the do-ve axis) and m_{a} (along the an-po axis), a and b can be expressed as

$$a = \sqrt{\frac{|m_{\mathrm{a}}|^2 + |m_{\mathrm{d}}|^2 + |m_{\mathrm{a}}^2 + m_{\mathrm{d}}^2|}{2}} \tag{4.6}$$

and

$$b = \sqrt{\frac{|m_{\mathrm{a}}|^2 + |m_{\mathrm{d}}|^2 - |m_{\mathrm{a}}^2 + m_{\mathrm{d}}^2|}{2}}. \tag{4.7}$$

Given a and b, the eccentricity e of the ellipse is

$$e = \sqrt{1 - \frac{b^2}{a^2}}, \tag{4.8}$$

where the lowest and highest possible values $e = 0$ and $e = 1$ correspond to circular and linear motion, respectively. Finally, the tilt θ of the ellipse, defined as the angle between its major axis and the anatomical an-po axis (Fig. 4.4) is calculated from

$$\tan\theta = \frac{\Re(m_{\mathrm{d}}\, e^{-i*\chi/2})}{\Re(m_{\mathrm{a}}\, e^{-i*\chi/2})}, \tag{4.9}$$

where $\Re$ denotes the real part, and

$$\tan\chi = \frac{\Im(m_{\mathrm{a}}^2 + m_{\mathrm{d}}^2)}{\Re(m_{\mathrm{a}}^2 + m_{\mathrm{d}}^2)}, \tag{4.10}$$

where $\Im$ denotes the imaginary part.

Results

CA motion disentangled along the two anatomical axes

In previous measurements along the do-ve axis, Vavakou et al. (2021) reported that the spectral tuning of the DW is shifted at higher frequencies than the CC when recorded at the same longitudinal position. The reported difference in tuning cannot be generalized for the overall motion of the recorded structures, as one recording angle is not sufficient to describe 3D motion. Stated differently, it is possible that the motion direction changes with frequency.

With the use of a mirror, we were able to measure sound-induced motion on the CA from two different angles. That way, we disentangled motion along the do-ve and the an-po axis for both the DW and the CC.

We measured sound-induced vibrations on the CA, covering at least 800 μm of the sensory tissue CA with a spatial resolution of 30-40 μm, while presenting multi-tone broad band stimuli ranging from 0.3-38 kHz, in $\approx$ 817-Hz steps. These measurements allowed us to construct heat maps of the CA vibration magnitude along the do-ve and an-po axis. The longitudinal profile of CC vibration magnitude along the do-ve axis is shown for three experiments (Fig. 4.5A,D,G). A manual estimate of the spectral tuning of the CC along the do-ve axis is illustrated with a black line for reference. To facilitate magnitude comparison among the two studied directions of motion for the CCs, we plot their magnitude ratio (Fig. 4.5B,E and H). When the do-ve component is dominant, the magnitude ratio is positive. Likewise, negative values indicate that the magnitude along the an-po axis is greater. The magnitude of the an-po component increased relative to the magnitude of the do-ve component at frequencies slightly higher ($\approx$0.6 octaves) than the CCs do-ve tuning. The magnitude ratio ranged from $\sim$10 dB to negative values. Especially in experiment BC0013 the an-po motion component took over (Fig. 4.5B). In contrast, the DW motion is characterized by a do-ve dominant component. For the same frequencies, the ratio among the two motion components was exclusively positive (Fig. 4.5C,F and I). In summary, the motion direction in the CC varies in a frequency dependent manner, whereas the DW motion was exclusively dominated by a do-ve component. Note that the high frequency plateau we observed (blue "valley" at frequencies $\approx$0.6 octaves higher than the CC do-ve tuning), is likely a interference effect (Palghat Udayashankar et al., 2012) and not relevant for hearing.

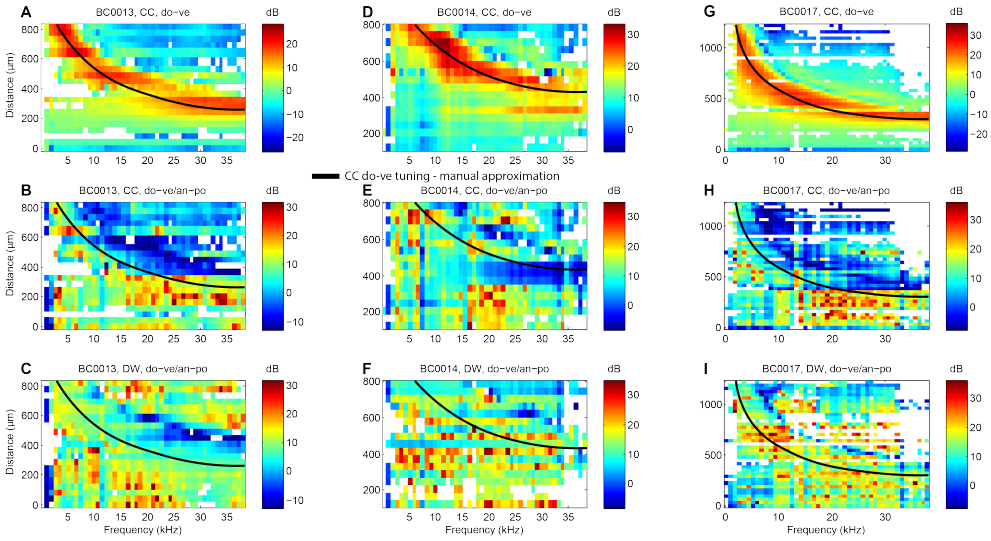

Figure 4.5: DW and CC sound-induced motion along two anatomical axis. (**A,D,G**) Normalised displacement magnitude for the CC, as measured along the do-ve axis, for 3 experiments. The black line is a manual annotation of the CC spectral tuning along the do-ve axis. (**B,E,H**) The CC displacement ratio among the two disentangled axis of motion. The black lines are shared with panels A, D and G respectively. (**C,F,I**) The DW displacement ratio among the two disentangled axis of motion. The black lines are shared with panels A, D and G respectively.

Elliptical motion in the CA

The CC magnitude and phase at a single location was measured from two different angles, and motion components along the an-po and the do-ve axis were disentangled (Fig. 4.6A-B) as described in Methods. From these data the cyclic trajectories of motion with respect to the two anatomical axes were reconstructed for each of the frequency components of the stimulus (Fig. 4.6C).

The 2D motion increased in relative amplitude for frequencies near the best frequency of this recorded position, 11.5 kHz. The elliptical character of the motion was most pronounced near the best frequency. The an-po component took over at frequencies above 13 kHz, where the ellipse flattened. Finally, the 2D motion decreased in amplitude and became more tilted for frequencies higher than 20 kHz.

The normalized magnitude and phase along the an-po and the do-ve axis were also measured for the DW (Fig. 4.6E-F). Compared to the CC, the elliptical motion in the DW was consistently more uniform and elongated across frequencies (Fig. 4.6D). For

higher frequencies, the direction of the 2D motion along the an-po axis reversed. The direction change occurred at the frequency region where the high frequency plateau has been reported in previous studies (Palghat Udayashankar et al., 2012). Overall, a frequency-dependent elliptical motion in the do-ve/an-po plane was observed for both the DW and the CC.

Quantitative description of elliptical motion

The elliptical motion per recorded position and stimulus frequency was quantified using four different metrics, namely, the major axis a, the minor axis b, the eccentricity e, and the tilt θ of the elliptical motion. For one recorded position, the major axis a was sharply tuned for both the CC and the DW, with the DW showing greater amplitude for the specific position (Fig. 4.7A). The frequency tuning of the minor axis b was less sharp for the DW, and the CC b amplitude dominated over the DW. The elliptical character of the motion is best described by the eccentricity of the ellipse (Fig. 4.7B). Eccentricity values range from 0, for a circular motion, to 1, for a motion along a line. The CC, with frequency-dependent e values that approached 0.5, showed more elliptical motion than the DW (Fig. 4.7C). The DW motion was tilted at 75 degrees for a wide range of frequencies, including those near the best frequency of the recorded position. Compared to the DW, the CC motion was tilted 25 degrees for frequencies near the best frequency of the recorded position (Fig. 4.7D). The ellipse tilt approached 0 degrees at frequencies above the CC do-ve best frequency, where the elliptical motion was dominated by the an-po component.

Overall, our vibration measurements covered 800-1200-μm of the CA. The ellipse major axis was calculated for all the recorded positions and stimulus frequencies in 3 different CA for both the DW (Fig. 4.8A,D,G) and the CC (Fig. 4.8B,E,H). A qualitative assessment of the data indicates that the CC a amplitude was more sharply tuned than the DW. That is further illustrated when calculating the amplitude ratio of the CC relative to the DW (Fig. 4.8C,F,I). The DW and the CC shared similar amplitudes for frequencies lower than the CC best frequency along the do-ve axis (manually annotated, indicated with a black line). The ratio of the two amplitudes drops below 1 for frequencies slightly above the best frequency of the CC a. In other words, the DW a was tuned more broadly, and to higher frequencies than the CC. The ratio of the two amplitudes again approached 1 as the frequency increased, approaching the high-frequency plateau.

The ellipse minor axis was calculated for all the recorded positions and stimulus

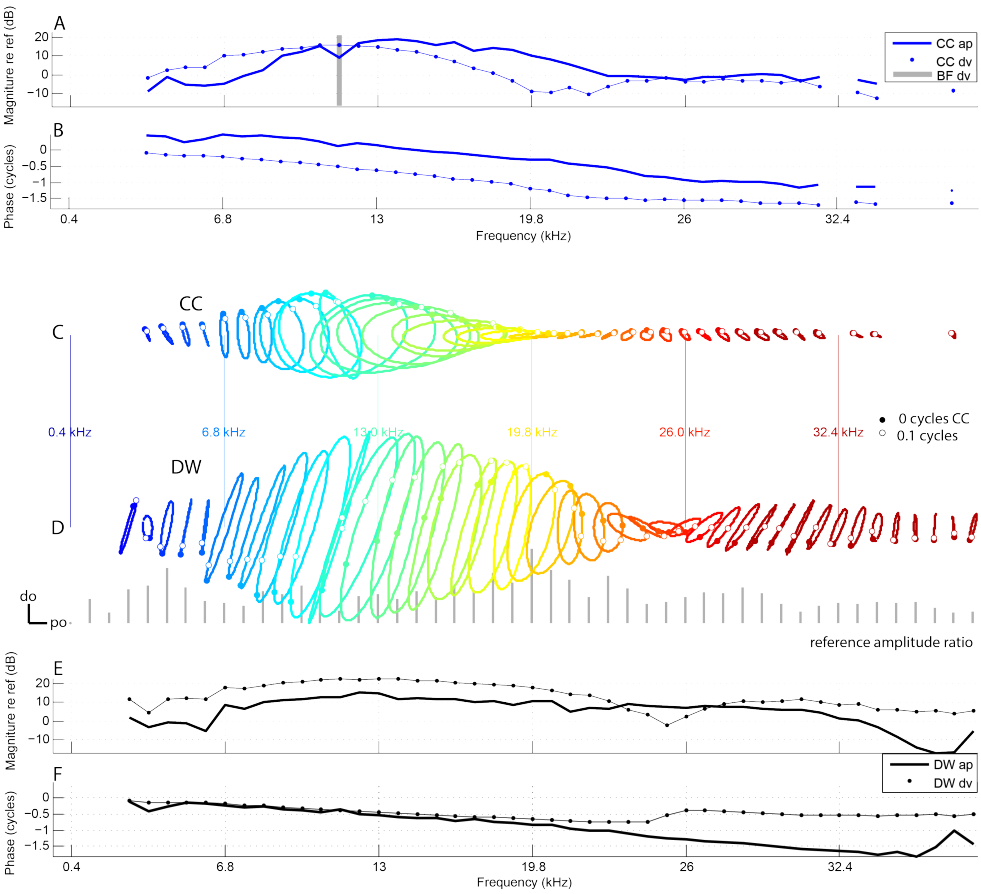

Figure 4.6: Elliptical motion in the CA.(**A,B,E,F**) Normalised displacement magnitude and phase as measured through the mirror and the direct view, for the DW and the CCs. The mirror view and the direct view are related with a known angle delta, that is derived from the OCT images. The direct view is aligned with the dorsal-ventral axis by convention. The dorsal-ventral motion component is identical to the direct view measurement. The anterior-posterior motion component is derived by the obtained measurements through the mirror and the direct view. (**C,D**) Reconstructed elliptical motion for one stimulus frequency cycle. (Data from experiment BC0013. CC and DW were recorded 533 μm away from the distal extreme of the direct view. Best frequency for do-ve CC: 11.5-kHz)

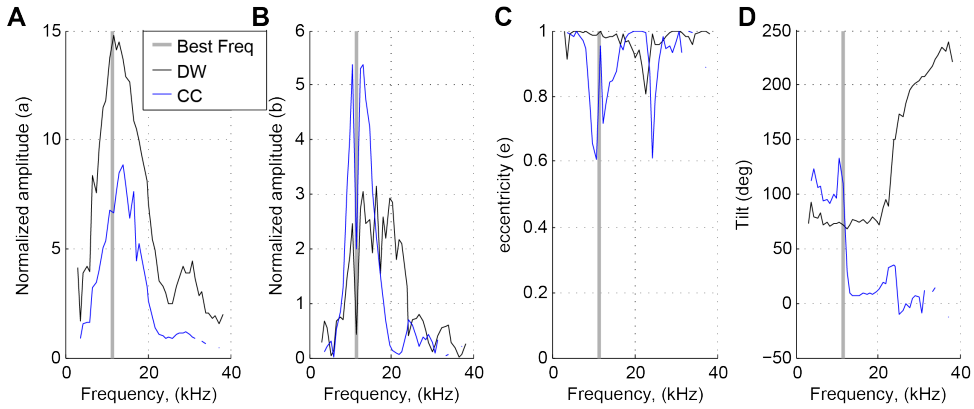

Figure 4.7: Metrics of the elliptical motion. (**A**) The normalized amplitude of a per stimulus frequency. Data shown for the DW and the CC. (**B**) The normalized amplitude of b per stimulus frequency. Data shown for the DW and the CC. (**C**) The eccentricity, e, of the ellipse per stimulus frequency. Data shown for the DW and the CC. (**D**) The tilt of the ellipse in degrees. Data shown for the DW and the CC. (Data from experiment BC0013, same as in Fig. 4.6.) Best frequency is 11.5-kHz, as measured on the CC along the do-ve axis

frequencies in 3 different CA for both the DW (Fig. 4.9A,D,G) and the CC (Fig. 4.9B,E,H). The amplitude of b was more broadly tuned than that of a. Additionally, the amplitude of b was 3-10 times lower than that of a. The ratio of the CC amplitude relative to that of the DW did not reveal a clear pattern, in contrast to that of a (Fig. 4.9C,F,I).

The eccentricity quantifies the elongation of the ellipse, with values ranging from 0 (circular motion) to 1 (linear motion). Overall, the DW (Fig. 4.10A,D,G) moved more linearly than the CC (Fig. 4.10B,E,H). Across experiments there was quite some variability. In experiment BC0013, the motion was more circular, following the tuning of a and b. Additionally, in this experiment, the CC moved in a more circular manner than the DW in a frequency-dependent way (Fig. 4.10C). In experiments BC0014 and BC0017, the motion became less linear as the frequency approaches the plateau, that is most probably not relevant for hearing (Fig. 4.10F,I).

The DW and the CC both moved along the do-ve axis (tilt $\simeq 90°$) at frequencies that are relevant for hearing for each position, i.e., near its best frequency. The CC was consistently more tilted than the DW by about 10-20 degrees at the frequencies that are relevant for hearing (near the black line) (Fig. 4.11C,F,I).

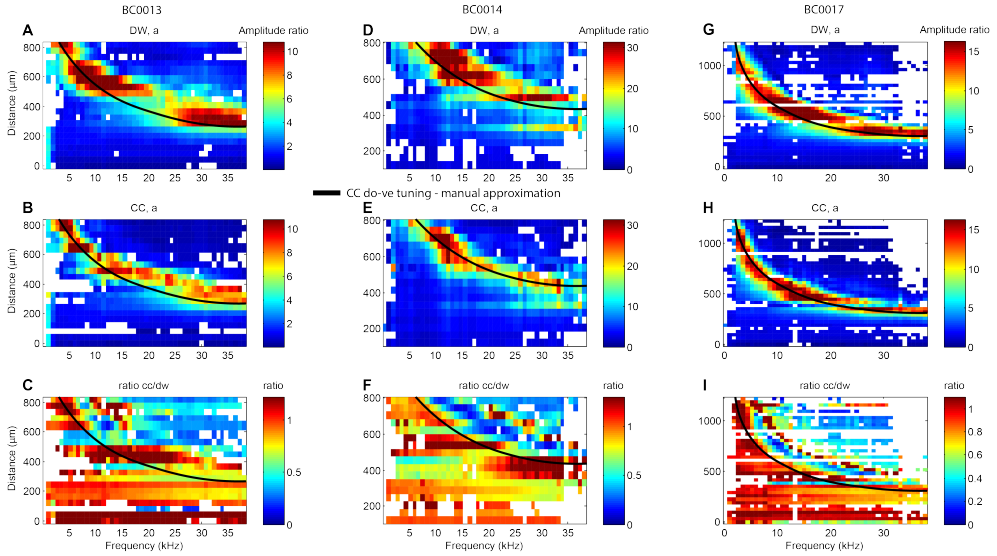

Figure 4.8: The ellipse major axis half length along the CA. (**A,D,G**) The DW a per frequency for different experiments. (**B,E,H**) The CC a per frequency for different experiments. (**C,F,I**) The CC/DW a ratio per frequency for different experiments. (Data from experiments BC0013, BC0014 and BC0017). A manual interpretation of the CC spectral tuning along the do-ve axis is replicated among all the plots per experiment for comparison.

Relative motion

We further assessed the relative motion of CC and DW along the do-ve (Fig. 4.12 A,B,C) and the an-po axis (Fig. 4.12 B,E,H), by computing the vector difference of their mechanical motions (i.e., taking into account both their relative amplitude and phase). In all cases, we found that the relative motion was shifted towards higher frequencies than the do-ve spectral tuning of the CC. For the do-ve axis this was expected from the measurements of Vavakou et al. (2021). For motion along the an-po axis, this is reported for the first time.

The relative motion of two elliptical motions in the same plane is also an elliptical motion. For that reason, it is possible to calculate the major axis a of the ellipse for vector difference, and to use it as a metric for the amplitude of the overall relative motion (Fig. 4.12 C,F,I). For all the reported experiments, the a of the relative elliptical motion was sharply tuned.

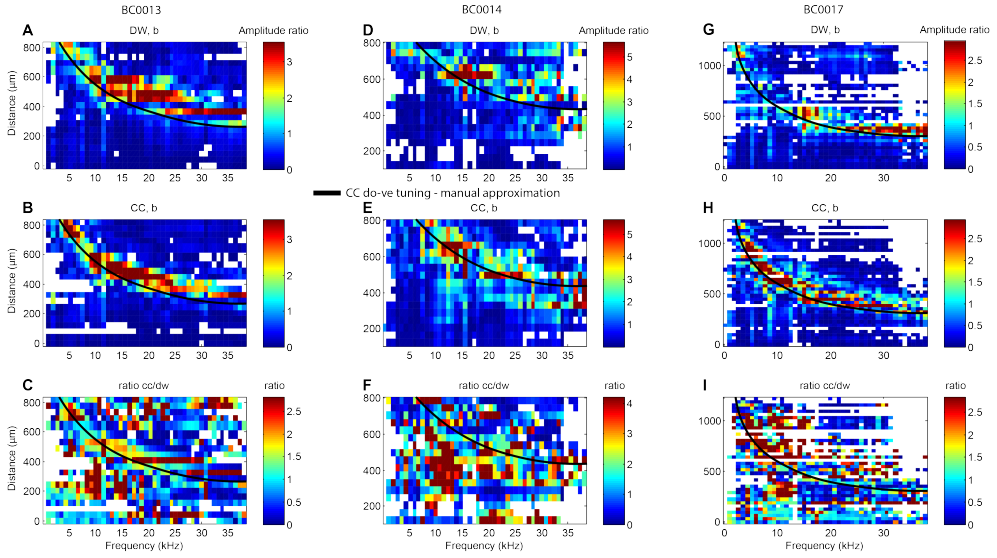

Figure 4.9: The ellipse minor axis half length along the CA. (**A,D,G**) The DW b per frequency for different experiments. (**B,E,H**) The CC b per frequency for different experiments. (**C,F,I**) The CC/DW b ratio per frequency for different experiments. (Data from experiments BC0013, BC0014 and BC0017). A manual interpretation of the CC spectral tuning along the do-ve axis is replicated among all the plots per experiment for comparison.

Discussion

In summary, we recorded sound-induced vibrations in the bushcricket hearing organ from two different angles, using a mirror. First, the recorded structures were registered geometrically, ensuring that the same points were measured from both views (Fig. 4.1, 4.2). Secondly, the overall measured motion was decomposed in two vertical components, aligned with the do-ve and the an-po anatomical axis respectively (Fig. 4.3). Thirdly, we compared quantitatively the DW and the CC vibration magnitude along the two anatomical axes (Fig. 4.5). Next, we reconstructed the 2D motion of the DW and the CC for a given position (Fig. 4.6), along the do-ve and the an-po axis. Both structures demonstrated elliptical motion. We then quantified the elliptical character of the motion along the whole length of the sensory organ (Fig. 4.8,4.9,4.10,4.11), and found that the elliptical motion of the CC was tilted relative to DW motion for frequencies relevant for hearing in the recording position. Finally, the elliptical relative motion among the DW and the CC was calculated (Fig. 4.12), and

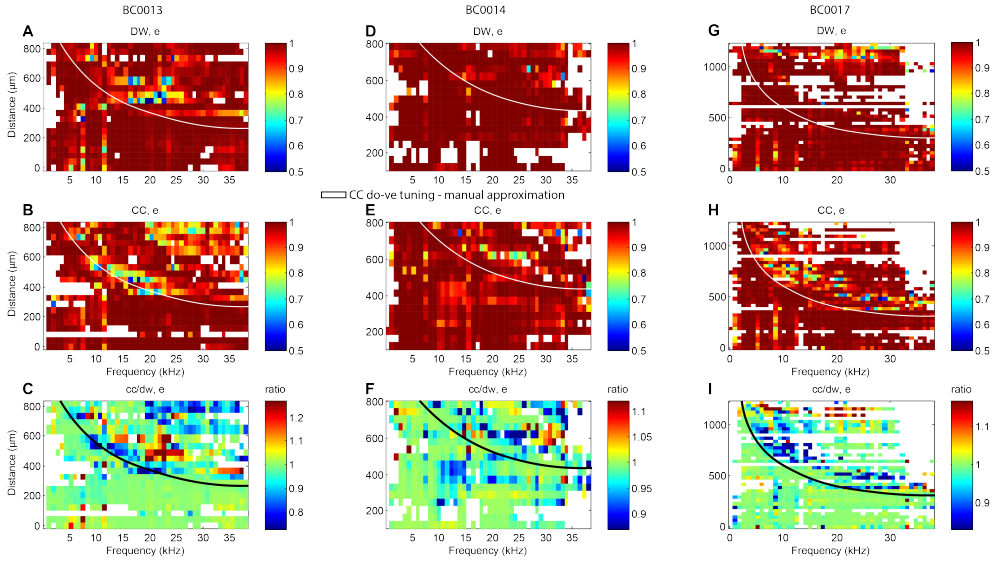

Figure 4.10: The ellipse eccentricity along the CA. (**A,D,G**) The DW e per frequency for different experiments. (**B,E,H**) The CC e per frequency for different experiments. (**C,F,I**) The CC/DW e ratio per frequency for different experiments. (Data from experiments BC0013, BC0014 and BC0017). A manual interpretation of the CC spectral tuning along the do-ve axis is replicated among all the plots per experiment for comparison.

was found to be sharply tuned.

Micromechanical motion along the transduction axis

Recent vibration measurements of the DW and the CC along the do-ve axis reveal that the the CC tuning is sharper and shifted towards higher frequencies than the DW (Vavakou et al., 2021). Vavakou et al. discuss in detail whether this difference in tuning among the two structures is specific for the do-ve view, or it is consistent with the overall motion of the two structures (Fig. 6 in Vavakou et al. (2021)). Specifically, they considered the following question: is it possible that the DW motion is dominated by the do-ve component across different frequencies, whereas the direction of CC motion changes in a frequency dependent manner?

In our current measurements we were able to disentangle motion components along the do-ve and the an-po axes. A comparison of the vibration magnitude among the two views for both structures revealed that the DW motion was dominated by the

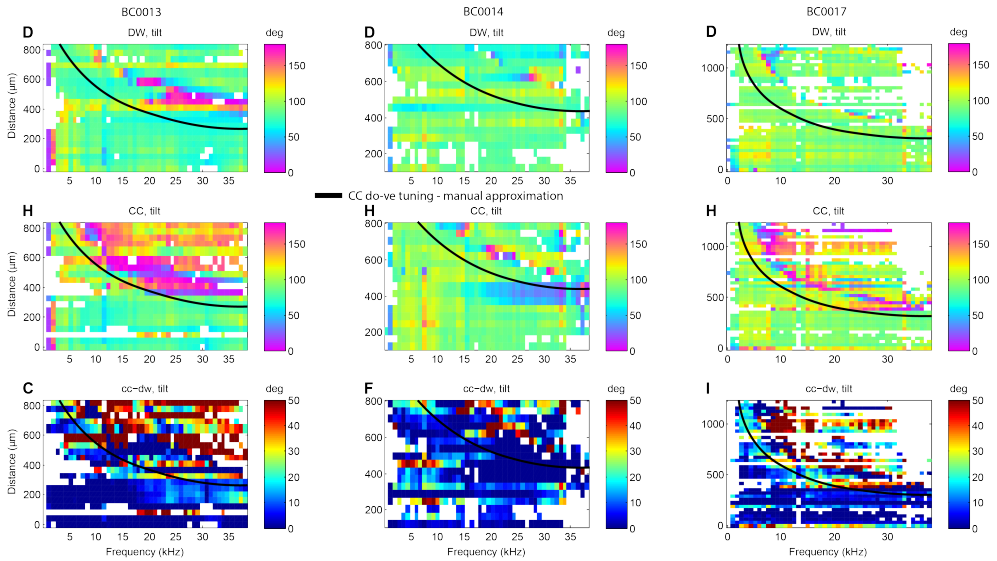

Figure 4.11: The ellipse tilt along the CA. (**A,D,G**) The DW tilt per frequency for different experiments. (**B,E,H**) The CC tilt per frequency for different experiments. (**C,F,I**) The CC/DW tilt difference per frequency for different experiments. (Data from experiments BC0013, BC0014 and BC0017). A manual interpretation of the CC spectral tuning along the do-ve axis is replicated among all the plots per experiment for comparison.

do-ve component (Fig. 4.5 B,E,H). For the CC, the an-po component seemed to take over at higher frequencies (Fig. 4.5 C,F,I). As a result, the mechanical tuning of the CC overall motion will be shifted to higher frequencies. It should be noted that the overall motion may also contain a proximal-distal component that can not been disentangled with the current methodology.

Mechanical and neural data

Hummel et al., in 2016, performed simultaneous neural and mechanical measurements of the bushcricket hearing organ (Hummel et al., 2016). Their mechanical measurements were performed on the CC along the do-ve direction. Their results indicate that the neural characteristic and best frequency is shifted towards higher frequencies compared to the mechanical tuning, especially for frequencies above 20 kHz (Hummel et al. (2016), Fig. 1E,F). This discrepancy between neural and mechanical tuning could possibly be explained by considering the mechanical coupling that underlies

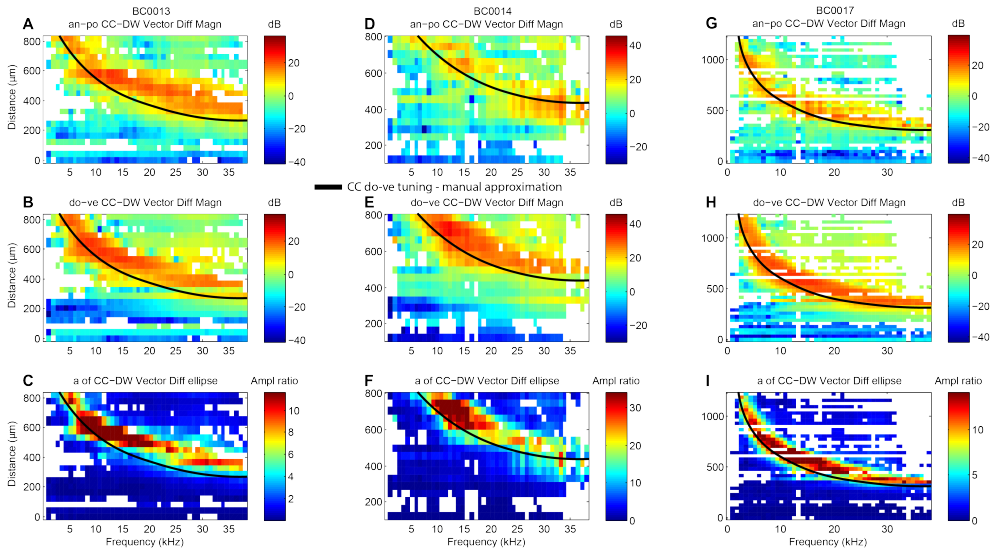

Figure 4.12: The relative motion of structures within the CA. (**A,D,G**) The relative motion of the DW and the CC along the do-ve axis for different experiments. (**B,E,H**) The relative motion of the DW and the CC along the an-po axis. (**C,F,I**) The a of the elliptical relative motion of among the DW and the CC along two dimensions. (Data from experiments BC0013, BC0014 and BC0017). A manual interpretation of the CC spectral tuning along the do-ve axis is replicated among all the plots per experiment for comparison.

transduction.

Our measurements of the CA along two anatomical axes show that the relative motion of the DW and the CC is elliptical and sharply tuned at frequencies higher than that of the individual structures. It is likely that the relative motion of the DW and the CC is driving transduction, by stretching of the sensory dendrite, especially for ultrasounds.

Technical considerations

This study sets the methodological basis for disentangling different directions of sound-induced motion in a hearing organ by using a mirror. Although this is a powerful tool to unravel the geometry of sound-induced motion and its contribution to transduction, it is important to consider some of the limitations of this approach.

First, the mirror allows us to perform these measurements without rotating the

animals among measurements. That is critical for open-field stimulation paradigms, as it avoids changes in the microacoustical environment surrounding the sensory organ between measurements. (Note that, when studying the bushcricket, it is not advisable to use a closed stimulation paradigm, as the sound reaches the CA through both the spiracle and the tympanum (Lewis, 1974; Hoffmann & Jatho, 1995; Michelsen et al., 1994).) Still, the probe height needs to be adjusted for around 300 μm among measurements, to ensure that the recorded side is within the focal plane of the OCT. This can have an effect on the microacoustical environment. Especially if the animal holder position is placed vertical to the probe, there can be pronounced reverberations. The experimenter needs to make sure that the position of the animal holder does not facilitate reverberations, and that sufficient sound-insulating material is used to minimize acoustic reflections. The need for adjusting the probe height could be eliminated by using additional mirrors to equalize the optical path lengths corresponding to the two viewing angles.

Alternatively, an improvement could be achieved by an accurate control and registration of the vertical readjustment of the probe position. That way, the recorded structures from the two views can be matched following criteria that minimize the euclidean distance among the predicted and the measured direct using all three spatial coordinates, instead of having to exclude the z coordinate as in the present study. Using the full 3D information is likely to make the registration of the recorded structures among the to views more robust and accurate. Finally, it would be worth examining which choice of anatomical structure for the registration procedure yields the most reliable and reproducible results. In this report, we used the CC registered position to align both the DW and the CC per recorded CA position. That choice was made considering that the CC is below fluid in both recording views and that way the refractive index difference would be less dramatic among the two views.

Finally, motion along the pr-di axis is not disentangled following the current methodology. Still, it is quite likely that it has contributed to our measurements. The way to minimize this contribution is to ensure that the measurement beam is perpendicular to the pr-di axis of the CA.

Disentangling the longitudinal motion

Hummel et al. (2016) report phase delays in the mechanical response of the organ that coincided with the sensory cell responses. They hypothesize that there might be a tilt of the CC along the longitudinal direction that drives transduction.

To achieve motion decomposition along 3 anatomical axes, one needs to place an additional mirror (or a prism) above the leg. This opens the way to systematically quantify any longitudinal components of motion. One methodological complication in this configuration is that the measured positions might fall outside the focal plane of the OCT, because the pathlength of the recording beam increases as the angle between the measuring beam and the pr-di axis decreases.

Future directions

This study has shown that it is possible to disentangle two directions of motion using a mirror and also that there is elliptical motion in the bushcricket hearing organ. The sample size of this study is quite small, and to put our findings on a firmer footing, there need to be more measurements that reproduce the current findings in a reliable manner. For that purpose, for future experiments we recommend to perform spatially dense measurements (30 B-scans in 10-μm steps), thus making sure that the same structure is measured from two different angles. If possible, these blocks of measurements should be repeated across different locations on the CA along the pr-di axis. With this method one can test if the discrepancy between neural and mechanical data along the pr-di axis that Hummel et al. report (Hummel et al. (2016), Fig. 2C,D) can be explained by different directions of motion of the CC.

For the current dataset, the recording beam was aimed at the middle of the CA along the an-po axis. That is not an ideal measurement point to disentangle the an-po motion if the CC pivots around that point. In future measurements, one should perform additional measurements of the CC and the DW towards the anterior and posterior extremes of the CA. The contribution of an-po motion to the recorded motion will thus more pronounced, whereas the overall results should be consistent with our current findings.

Further applications

Our findings underscore that it is crucial to consider the overall motion when reporting the mechanical tuning of measured structures, including its spatial direction. That is a general consideration when studying the mechanics of hearing organs. In the mammalian cochlea there already are indications (Cooper et al., 2018) and measurements (Lee et al., 2016) of longitudinal and radial motion, respectively. Given the elaborate anatomy of the mammalian cochlea, it is expected that there exist complex patterns of

motion along multiple anatomical axes of the sensory organ, and that these patterns change in nontrivial ways when varying the frequency and intensity of the stimulus. It is crucial to describe in detail the micromechanical motion of hearing organs in order to generate realistic models that are consistent with mechanical data.

Chapter 5

The frequency limit of outer hair cell motility measured in vivo[1]

Outer hair cells (OHCs) in the mammalian ear exhibit electromotility, electrically driven somatic length changes that are thought to mechanically amplify sound-evoked vibrations. For this amplification to work, OHCs must respond to sounds on a cycle-by-cycle basis even at frequencies that exceed the low-pass corner frequency of their cell membranes. Using in vivo optical vibrometry we tested this theory by measuring sound-evoked motility in the 13–25 kHz region of the gerbil cochlea. OHC vibrations were strongly rectified, and motility exhibited first-order low-pass characteristics with corner frequencies around 3 kHz– more than 2.5 octaves below the frequencies the OHCs are expected to amplify. These observations lead us to suggest that the OHCs operate more like the envelope detectors in a classical gain-control scheme than like high-frequency sound amplifiers. These findings call for a fundamental reconsideration of the role of the OHCs in cochlear function and the causes of cochlear hearing loss.

[1]Vavakou, A., Cooper, N. P., & van der Heijden, M. (2019). The frequency limit of outer hair cell motility measured in vivo. *Elife, 8*, e47667.
https://doi.org/10.7554/eLife.47667.001

Introduction

The hair bundles of auditory sensory cells are deflected by sound-driven vibrations, causing mechano-electric transduction channels to open and close. The resulting receptor current modulates the cell's membrane potential. The mammalian cochlea contains two distinct types of hair cells. The vast majority of nerve fibers that carry the acoustic information to the brain innervate the inner hair cells (IHC). Up to a few kilohertz, IHC synapses can 'phase-lock,' that is, code the individual cycles of tones. At higher frequencies (>3 kHz), phase-locking rapidly declines and neural coding relies on the DC component of the IHC receptor potential generated by the asymmetric, or rectifying, nature of the IHC receptor current (Russell & Sellick, 1978).

Outer hair cells (OHC) modify the mechanical vibrations inside the organ of Corti (OoC), enabling frequency tuning and dynamic range compression. Dysfunctional and missing OHCs strongly reduce sensitivity, and this is a major cause of sensorineural hearing loss (Ryan & Dallos, 1975). The discovery of electromotility, length changes of isolated OHCs (Brownell et al., 1985) driven by variations in the membrane potential (Santos-Sacchi & Dilger, 1988), has intensified the study of OHCs and their functional significance. The membrane protein responsible for electromotility has been identified (Zheng et al., 2000), and prestin knockout mice have profound hearing loss (Liberman et al., 2002). The dominant view is that OHC electromotility drives vibrations within the OoC in a cycle-by-cycle manner (Ashmore, 2011) over the entire audible range, which extends up to 150 kHz in some species (Vater & Kössl, 2011). If this view is correct, the AC receptor potentials of OHCs must be large enough to be effective up to high frequencies, even though the membrane capacitance is expected to reduce the AC receptor potentials (and hence the OHCs' motility) at a rate of 6 dB per octave (Dallos, 1984). The functional implication of this electrical low-pass filtering is a limitation in the OHC's ability to provide cycle-by-cycle mechanical feedback, known as the RC problem (Ashmore, 2011; Housley & Ashmore, 1992). The electrical corner frequency of OHCs has been measured electrophysiologically in vitro, with highest values ranging from 480 Hz (Mammano & Ashmore, 1996) to 1250 Hz (Johnson et al., 2011), but no systematic in vivo data exist due to technical limitations and the cochlea's extreme vulnerability. In addition to the electrical filtering, the motile process itself may also be too slow to provide high-frequency mechanical feedback. An early in vitro report claiming a bandwidth for electromotility of at least 79 kHz (Frank et al., 1999) was recently challenged (Santos-Sacchi & Tan, 2018). Again, in

vivo estimates of the corner frequency of motility are missing. Here we use optical vibrometry to measure non-linear components of the OHCs' motile response and determine the corner frequency of OHCs in the high-frequency region of the intact gerbil cochlea.

Methods

The materials and methods employed in this study are summarized below. More extensive details are provided elsewhere (Cooper et al., 2018).
Sound evoked vibrations were recorded from the ossicles and cochlear partitions of deeply anesthetized female gerbils (n = 27, weight = 53–75 g). Spectral-domain optical coherence tomography (SD-OCT) measurements were made from the first turn of the intact cochlea, under open-bulla conditions – optical access to the partition being provided through the transparent round window membrane. The hearing thresholds of the animals were assayed using tone-evoked compound action potential (CAP) measurements from a silver electrode placed on the wall of the basal turn of the cochlea.

Animal Preparation Animals were anesthetized using intraperitoneally injected mixtures of ketamine (80 mg/kg) and xylazine (12 mg/kg). Supplementary (1/4) doses of the same mixture were administered at intervals of 10–60 min to maintain the anesthesia at surgical levels throughout subsequent procedures. All experiments were performed in accordance with the guidelines of the Animal Care and Use Committee at Erasmus MC (protocol AVD101002015304).

OCT vibrometry An SD-OCT system (Thorlabs Telesto TEL320C1) was used for interferometric imaging and vibration measurements. Cross-sectional (B-scan) and axial images (A-scans and M-scans) were triggered externally using TTL pulses phase-locked to the acoustic stimulation system (Tucker Davies Technologies system III) at a sampling rate 111.6 kHz. The theoretical resolution of the OCT system was $\sim$3.5 μm across a 3.5 mm depth-of-field (i.e., z-range), but the optics of our recording system (a Mitotoyu IR imaging lens with an NA of 0.055) introduced an axial point spread function of $\sim$6 μm FWHM and a lateral resolution (in the xy plane) of 13 μm (all assessed in air, with a refractive index of 1; corresponding intracochlear measurements should scale inversely with the refractive index of perilymph, which we

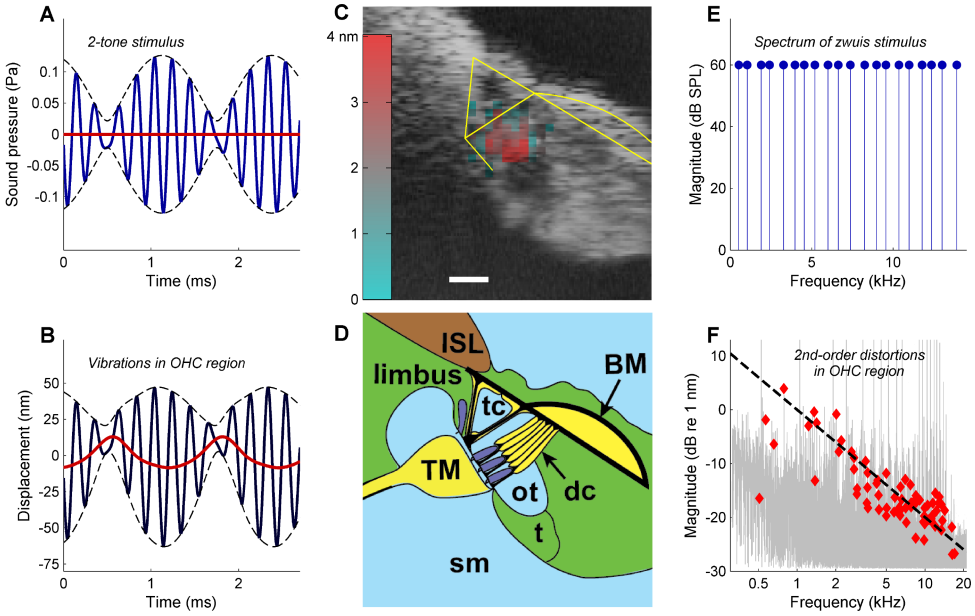

Figure 5.1: Rectification in the mechanical response of OHCs. (**A**) Two-tone stimulus with primary frequencies 4600, 5400 Hz; 70 dB SPL. *Blue line*, waveform; *dashed black lines*, envelope; *red line*, lowpass-filtered waveform (2000-Hz cut-off). (**B**) Mechanical displacement evoked by the two-tone stimulus, recorded in the gerbil OHC/Deiters' cell region (13 kHz CF). *Black line*, displacement waveform; *dashed black lines*, envelope. Rectification is illustrated by the *red line* obtained by low-pass filtering (2000-Hz cut-off). Positive polarity indicates displacement away from the measurement probe, that is vertically downwards in (C) and (D). (**C**) OCT reflectance image (*grayscale*), with structural framework of Corti's organ (*yellow*) superimposed for reference. Color-coded overlay: total RMS value of 2^{nd}-order distortion products (DP2s) evoked by a 12-tone complex, 2–12 kHz; 60 dB SPL. DP2s dominate in the OHC region. Scale bar, 0.025 mm. (**D**) Underlying anatomical structures. BM = basilar membrane; ISL = inner spiral lamina; sm = scala media; dc = Deiters' cells; t = tectal cells; TM = tectorial membrane; tc = tunnel of Corti; ot = outer tunnel. Hair cells, *dark blue*. (**E**) Zwuis stimulus (see text). (**F**) Vibration spectrum recorded in OHC region in response to the zwuis stimulus. *Red diamonds*, Rayleigh-significant DP2s. Dashed line, 6-dB/octave roll-off.

assumed to be 1.3). The linear operating range of the OCT system was >500 μm. The amount of light incident on the cochlea was ∼3.7 mW. The sensitivity of the A-scan's phase-spectra to vibration permitted measurement noise-floors that ranged from ∼30 pm/√Hz in the cochlea down to ∼3 pm/√Hz in the middle ear.

The OCT's measurement beam was not aligned with any of the cochlea's principal anatomical axes. The vibration measurements that we made should therefore be sensitive to structural movements in all three of the cochlea's principal dimensions (radial, transverse, and longitudinal). Specifically, in all recordings used for this study, the measurement beam pointed toward scala vestibuli, toward the apex of the cochlea, and away from the modiolus.

When mapping vibrations across the width of the cochlea partition (cf. Figure 5.1C, Supplementary Figure 5.9), measurements were spaced at intervals of between 6 and 12 μm in the xy-plane

Basic response analysis Responses were analyzed by Fourier transformation of the vibration waveforms derived from contiguous groups of 3 pixels in each M-scan, where each pixel covers a depth of ∼2.7 μm in the fluid-filled spaces of the cochlea, and ∼3.5 μm in the air-filled spaces of the middle-ear. The statistical significance of each response component was assessed using Rayleigh tests of the component's phase stability across time (Cooper et al., 2018). In Fig 5.1B, the data are comb-filtered to isolate the stimulus-evoked components. The candidate components extracted from the response spectrum are the primaries f1 and f2, the even order DPs (n(f2-f1) with n=1,2,...) and the odd order DPs (f1 + k(f2-f1) with k = -...-2,-1,0,1,2...). Only the candidate components that passed the Rayleigh test (p=0.001) were included.

Acoustic stimulation Acoustic stimuli were tailored to fit the nature of each experiment, as described below. Each stimulus was coupled into the exposed ear-canal using a pre-calibrated, closed field sound-system. Stimuli were generally presented for 12 s, with inter-stimulus intervals ∼1 min.

Broad-band multi-tone 'zwuis' complexes (van der Heijden & Joris, 2003) were used to determine the characteristic frequency and sensitivity functions of each recording site (e.g. see Supplementary Figure 5.12). Each broad-band stimulus had 43 spectral components, spanning from 0.4 to 30 kHz with an average spacing of 705 Hz. The components all had equal amplitudes, with levels expressed in decibels *re*: 20 μPa (i.e., dB SPL), but stimulus phase was randomized across frequency.

The unique property of a zwuis stimulus is that the frequencies of all of its primary components, and all of its potential inter-modulation distortion products up to the third order, are unambiguous. This means that all of the second-order distortion products (i.e. DP2s) studied in this paper can readily be attributed to a unique pair of spectral 'parents' (see Appendix 1).

Narrow-band zwuis stimuli were used to simplify the analysis and interpretation of DP2 spectra. They consisted from 10 to 15 components, ranging from few hundred hertz to at least one octave below the characteristic frequency of the recording side. The first presentation of each narrow-band stimulus had equal primary amplitudes, but their relative amplitudes were adjusted during subsequent presentations (fixing the average magnitude in dB SPL) in order to equalize the input to the OHCs. This procedure is described in the Appendix 1.

Results

In response to a tone pair (Figure 5.1A), vibrations in the OHC/Deiters' cell region showed a strong envelope-following component (Figure 5.1B). This reveals a significant degree of rectification in OHC motion, producing 2nd-order distortions (DP2s) such as the "quadratic difference tone" at f2-f1. Using multitone stimuli, we mapped the spatial profile of the DP2s inside the OoC by cross-section measurements. DP2s were concentrated in the OHC/Deiters' cell 'hotspot area' (Cooper et al., 2018) (Figure 5.1C and D). They were observed at stimulus levels as low as 25 dB SPL (Supplementary Figure 5.8), and disappeared post mortem (Supplementary Figure 5.9). These observations confirm that OHCs are the source of the DP2s long known to exist from psychophysical (Zwicker, 1979a), electrophysiological (Kim et al., 1980; Nuttall & Dolan, 1993) and cochlear-mechanical (Cooper & Rhode, 1997) studies. The OHC origin of DP2s is consistent with the significant rectified ("DC") component and 2nd harmonics observed in in vivo recordings of OHC receptor potentials (Dallos, 1986; Cody & Russell, 1987) and cochlear microphonics (Gibian & Kim, 1982).

Because rectification by OHC bundles produces DP2s in the receptor current, DP2s are an inevitable part of the electromotile response. More importantly, this part can be isolated through spectral analysis from recorded cochlear vibrations. This makes the DP2 spectrum ideally suited to studying the RC problem. To assess spectral trends, we employed a zwuis tone complex (Figure 5.1E), a stimulus designed to produce a rich DP2 spectrum upon rectification (van der Heijden & Joris, 2003; Victor, 1979).

Rectifying an N-component zwuis stimulus generates N^2 distinct DP2 components at frequencies $f_k \pm f_m$, each of which can be traced back to a pair of interacting primary frequencies (f_k, f_m). The vibration spectrum obtained in the OHC region (Figure 5.1F) evoked by this stimulus reveals a rich family of DP2s having a systematic 6-dB/octave roll-off. This roll-off confirms the action of a low-pass filter between the hair bundle's rectification and the motile response. Accurate estimation of the corner frequency, however, is hampered by the ∼10-dB scatter of DP2 magnitudes within each frequency band. We identified three causes of this scatter (Figure 5.2). Their elimination reduces the scatter substantially, paving the way to accurate estimates of OHC corner frequencies.

The first cause of scatter is combinatorial: when supplying an equal-amplitude input to a rectifier, the resulting second harmonics $2f_k$ are 6 dB below the remaining DP2s ($f_k \pm f_m, k > m$) (Figure 5.2A). This reflects the binomial coefficients occurring in the second-order terms of the power series describing the nonlinearity (Meenderink & van der Heijden, 2010). Since each DP2 component can be uniquely traced back to its "parent primaries", this is readily corrected. The second cause of scatter is the spatially distributed nature of DP2 generation. The primaries and DP2s propagate as traveling waves (Kim et al., 1980; Gibian & Kim, 1982), (Supplementary Figure 5.10), so the recorded DP2s are a vector sum of contributions along the path from stapes to recording place (Schroeder, 1969). The magnitude of slowly propagating components is affected by interference across generation loci (Figure 5.2B), and the growth and subsequent decay of components entering their peak region further obfuscates their original magnitude. These confounding effects of propagation are eliminated by setting an upper frequency limit to the primaries and DP2s used for stimulation, analysis and iterated adjustment of the stimulus as described below. For this frequency limit we choose half the characteristic frequency (CF/2). Wave propagation below CF/2 is too fast to cause interference and magnitudes change little during fast propagation (Ren et al., 2011b) (Supplementary Figure 5.10).

The third cause of scatter in the DP2 spectrum is the unequal amplitude of the primary components entering the rectifier, that is, the effective input that deflects the OHC bundles. Possible causes of unequal amplitudes at the OHC input include imperfections in the sound calibration as well as non-flatness of middle-ear transfer and intracochlear propagation. Even a perfectly regular trend in the input spectrum such as a roll-off creates a scattered effect in the DP2 spectrum (see Appendix 1). The amplitude of a DP2 component is proportional to the product of its parents' amplitudes

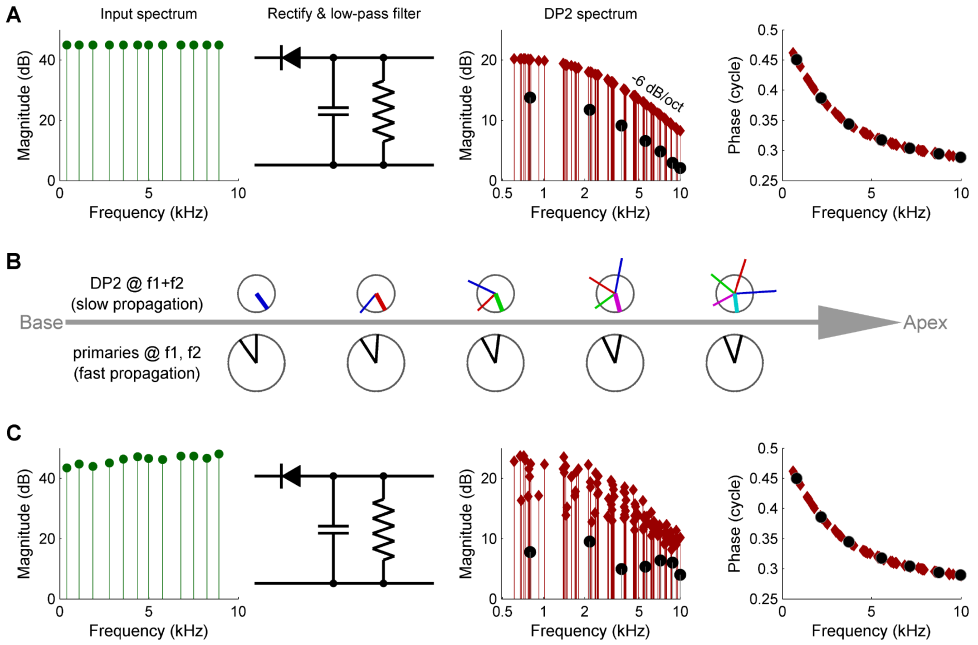

Figure 5.2: Three causes of magnitude scatter in DP2 spectra. (**A**) Combinatorial effect illustrated by feeding an equal-amplitude zwuis tone complex to a nonlinear circuit comprising a rectifier and low-pass filter (corner frequency 2.5 kHz). The 2nd harmonics (*solid circles*) are 6 dB weaker than the remaining DP2s (*red diamonds*). (**B**) Vector addition of DP contributions along the traveling wave (left to right). Lower row of "clocks" depict amplitude and phase of the primaries $f_1, f_2 \ll$ CF. They accumulate little phase and their amplitude hardly grows upon traveling. Upper clocks depict a near-CF DP2 at $f_1 + f_2$. Colors indicate the origin of each local contribution. Near-CF DP2 components suffer considerable phase accumulation and amplitude variation while traveling. The eventual amplitude (rightmost location) is the vector sum of multiple contributions widely differing in phase and amplitude. This interference obfuscates the spectral properties of DP2 generation investigated here. (**C**) Unequal primary amplitudes entering the nonlinear circuit generate a predictable scatter in DP2 magnitudes (see text). Companion phases are not affected by lack of equalization of the input. The 0.5-cycle low-frequency limit of the phase reflects the "negative polarity" of the rectification.

(van der Heijden & Joris, 2003). This bilinearity causes a scatter in DP2 magnitude (expressed in decibels) equal to twice the range of the primary input magnitudes (Figure 5.2C and Appendix 1—Figure 5.5). If the OHC input were known, it would take a simple adjustment of the stimulus spectrum to equalize the primary amplitudes

at the OHC input, and thereby regularize the DP2 spectrum as in Figure 5.2A. Current in vivo measurement techniques lack the spatial resolution to determine OHC bundle deflection, but the effective OHC input can be retrieved from the rich DP2 spectrum by exploiting the bilinear relationship between primary and DP2 amplitudes. This computational method was previously used to retrieve the effective IHC input from auditory-nerve responses (van der Heijden & Joris, 2003). Here we use it to compute the effective OHC input (see Appendix 1) and to adjust the stimulus accordingly. The OHC input thus obtained differs from the linear component of OHC motion, and in fact resembles basilar membrane motion more closely (Supplementary Figure 5.11). This means that motion recorded in the OHC region may not be used as a proxy for OHC input. The resemblance between basilar membrane motion and computed OHC input may shed light on the mechanisms underlying the deflection of OHC hair bundles. Within the current study, however, the OHC input is primarily of methodological interest.

Experimental equalization of the effective OHC input and compensation for the combinatorial effect had the predicted effect of markedly reducing the scatter in the DP2 spectrum (Figure 5.3). After equalization, the DP2 spectrum recorded from the OHCs closely resembles that of the simple nonlinear circuit of Figure 5.2A with its first-order low-pass characteristics. This holds for both the magnitude and the phase, having a minus 6-dB/octave high-frequency slope and a 0.25-cycle high-frequency asymptote (Figure 5.4C) respectively. The corner frequency was 2.5 kHz, 2.7 octaves below the 16-kHz CF.

We obtained data from different cochlear regions in different animals, with CFs ranging from 13 to 25 kHz. The adjustment of the relative stimulus amplitudes always reduced the scatter of the DP2 magnitudes. First-order low-pass characteristics were consistently found across CFs (Figure 5.4). The corner frequencies obtained ranged from 2.1 to 3.3 kHz, showing a weak trend of increasing with CF (Figure 5.4D).

In summary, the rectification displayed in vivo by OHC motility provides a unique opportunity to directly measure OHC corner frequencies without opening the cochlea. When equalizing the primary amplitudes at the OHC input, the DP2 spectra reveal an unmistakable first-order low-pass character, both in terms of magnitude and phase. In the frequency range probed here (below CF/2) stiffness dominates OoC impedance rendering displacement proportional to force (Dong & Olson, 2009). Thus within the framework of models in which OHCs directly push the basilar membrane (e.g., Ramamoorthy et al. (2007)), electromotile force itself suffers from the 6-dB/octave

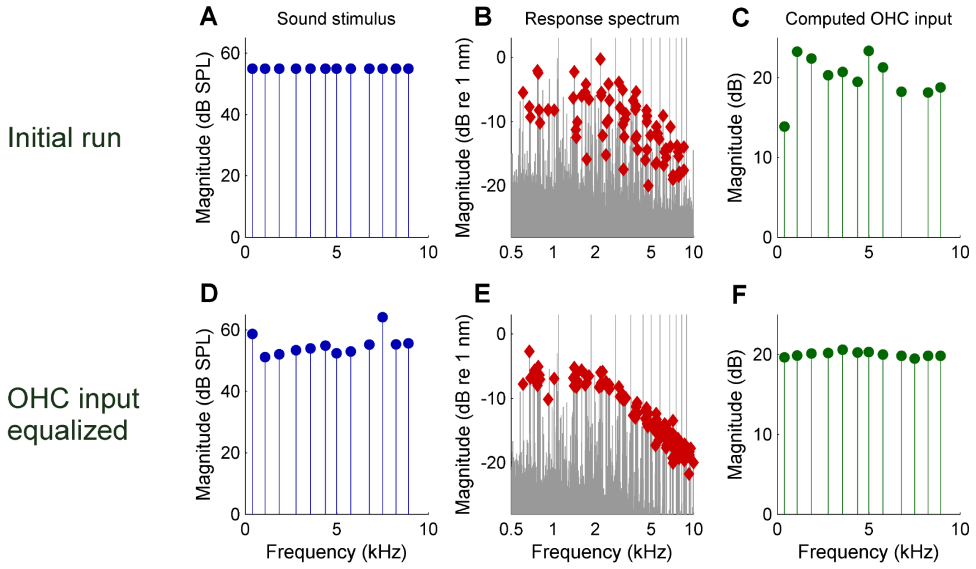

Figure 5.3: Reducing the scatter of DP2 magnitudes by equalizing the effective OHC input during an experiment. (**A**) Spectrum of the initial zwuis acoustic stimulus. (**B**) Spectrum of the vibrations recorded in the OHC region; CF = 16 kHz. Rayleigh-significant DP2s marked as *red diamonds*; 2nd harmonics corrected for the 6-dB combinatorial effect. (**C**) Effective OHC input computed from the DP2 magnitudes. (**D**) Spectrum of the adapted stimulus (4^{th} iteration) aimed at equalizing the effective OHC input. (**E**) Resulting DP2 spectrum. (**F**) Effective OHC input. Note that the equalized input spectrum in F (compared to C) reduces the DP2 scatter in E (compared to B).

roll-off.

The corner frequencies of 2.1–3.3 kHz that we measured in vivo were 2.8 ± 0.2 octaves below the CFs of our recording locations. These corner frequencies are higher than values of membrane corner frequency from in vitro studies at lower CF: 480 Hz (guinea pig, CF ∼7 kHz) (Mammano & Ashmore, 1996); 300–1250 Hz (gerbil, CF,∼350–2500 Hz) (Johnson et al., 2011). The in vivo data fall considerably short of the extrapolations to higher CFs made in the in vitro gerbil study (Johnson et al., 2011) (which predict electrical corner frequencies of 6.5–11 kHz for the CFs tested here). Our observation of a simple 6-dB/octave roll-off and minus 0.25-cycle phase asymptote indicates the dominance of a single low-pass mechanism in the entire frequency range tested. Comparison with the in vitro data suggests that this dominant factor is the

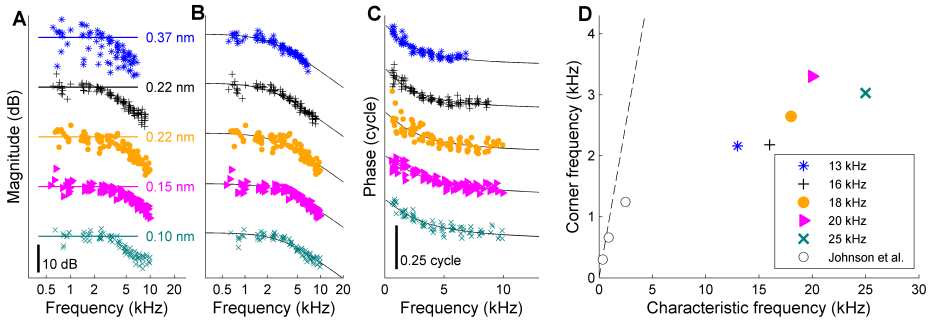

Figure 5.4: Low-pass filtering and corner frequencies of OHCs. (**A**) DP2 magnitude versus frequency measured across different cochleas at different CFs. Stimuli, 10–12 component zwuis not exceeding CF/2; component intensities 55–65 dB SPL, optimized to equalize OHC input. Individual curves are offset to avoid overlap; labeled straight lines indicate absolute displacement. CFs, see legend of panel D. Second harmonics were corrected for the 6-dB combinatorial deficiency. (**B**) The same magnitudes corrected post-hoc for the effects of residual magnitude inequality in the effective input (see Appendix 1— Figure 5.7). Black lines, first-order low-pass filters fitted jointly to the magnitude and phase data of each recording. (**C**) Companion phase data: the difference between the recorded DP2 phases and the predictions obtained by adding or subtracting the primary phases of the OHC input (Appendix 1, Equation 5.3). *Black lines*, phase curves of the fitted low-pass filters. (**D**) Corner frequencies from the fits versus CF. Symbols as in panels A-C. Open circles reproduce in vitro data from Johnson et al. (2011). Dashed line, unity line (corner frequency = CF). Explained variance of the fits (in order of increasing CF): 90%, 91%, 80%, 85%, 87%. When omitting the correction for residual scatter, and instead using the raw magnitudes from panel A, the estimates of the corner frequencies were lower by 1% to 10% (mean, 7%) compared to the estimates based on the corrected magnitudes.

RC time of the cell membrane, which is fundamental to the operation of all biological cells. The somewhat higher corner frequencies of the present study (compared to the in vitro data) may be attributed the more basal location of the OHCs of the present study.

A corner frequency at 2.8 octaves below CF implies a 17-dB attenuation of the CF component. The shallow increase of OHC corner frequency with increasing CF suggests an even stronger attenuation at higher CFs than studied here. When driven by a sufficiently large electrical input, OHC motility can generate vibrations up to very high frequencies, both in vitro (Frank et al., 1999) and in vivo (Ren et al., 2016a), but for acoustic stimulation the low-pass filtering of the receptor potential will limit

the frequency range. Various schemes (reviewed in Johnson et al. (2011)) have been proposed to push the frequency limit of electromotility beyond the corner frequency of the OHC cell membrane into the CF range. Our findings do not support such schemes, as the ∼2.5-kHz corner frequency is evident in the motile response itself.

We assessed the quantitative effect of low-pass filtering by the OHCs (Appendix 2). A 16-kHz tone at the behavioral threshold of the gerbil is estimated to evoke an AC component of the OHC receptor potential of 5.7 μV at the peak of traveling wave. At the slightly more basal location where cycle-by-cycle amplification is assumed to start, it is ∼1 μV. Inspection of the in vivo OHC recordings in guinea pig of Cody and Russell (1987) yield an 3.6-μV AC component at CF for a 17-kHz tone near the behavioral threshold, corresponding to ∼0.6 μV at the spatial onset of the putative amplification. Even if these minute variations in the membrane potential could evoke a significant electromotile response, such a motile feedback is unlikely to improve sensitivity because of its expected poor signal-to-noise ratio (van der Heijden & Versteegh, 2015b).

Overall our data suggest that OHCs and IHCs have similar properties, namely, considerable rectification (Pappa et al., 2019) and a corner frequency not exceeding a few kilohertz. Thus, just like in high-frequency IHCs, the receptor potential of high-frequency OHCs is expected to mainly follow the envelope of the waveform that stimulates their hair bundles. In this sense both IHC and OHCs operate as envelope detectors. We therefore propose that OHC motility does not provide cycle-by-cycle feedback, but rather modulates sound-evoked vibrations (Cooper et al., 2018; van der Heijden & Versteegh, 2015a). In this scenario the dynamic range compression in the cochlea is based on an automatic gain control system (van der Heijden, 2005) in which the degree of OHC depolarization determines the gain. The spatial confinement of the motile response to the OHC/Deiters' cell region presents another challenge to the prevailing theory that OHCs drive basilar membrane motion directly. It rather suggests that electromotility controls the local coupling between OHCs and Deiters' cells in a parametric fashion, perhaps dynamically adjusting the amount of dissipation in the Deiters' cell layer. This fundamentally different view of the function of OHCs has great consequences for the experimental study of their role in hearing loss and the origins of the vulnerability of cochlear sensitivity. As to theoretical work, it is important that models of cochlear function, whether invoking cycle-by-cycle feedback or not, incorporate the findings of the present study.

Appendix 1

Reduction of DP2 scatter by equalizing the effective OHC input Here we describe the computational procedure leading to the reduction of magnitude scatter in the DP2 spectra (Figures 5.3 and 5.4). The computations are illustrated using the example primary spectrum of Figure 5.2C with its unequal primary magnitudes.

In a zwuis tone complex the primary frequencies $\mathrm{f}_1 \ldots \mathrm{f}_N$ are chosen such that all possible combinations $f^+_{km} = f_k + f_m (k \geq m)$ and $f^-_{km} = f_k - f_m (k > m)$ are distinct and never coincide with any primaries. This means that all the N^2 second-order distortion products (DP2s) generated by rectifying the stimulus are different, and can be uniquely traced back to their "parent" primaries. Figure 5.2C of the main text shows the DP2 spectrum obtained by half-wave rectification of a 12-tone zwuis stimulus with unequal linear amplitudes $A_1 \ldots A_{12}$. To good approximation, and up to a common scale factor, the amplitude of a DP2 component at frequency $f_k \pm f_m (k > m)$ is equal to the product $A_k A_m$ of the parent amplitude (van der Heijden & Joris, 2003) whereas the amplitude of second harmonics at $2f_k$ equals $\frac{1}{2}A_k^2$ (Meenderink & van der Heijden, 2010).

Appendix Figure 5.5A shows a numerical test of the amplitude approximation. The unequal-amplitude stimulus shown in Figure 5.2C of the main text, was rectified (but not low-pass filtered) and the DP2 spectrum was extracted, corrected for the 6-dB combinatorial effect, and compared against the bilinear prediction. The predictions are accurate with a fraction of a dB except for the very weakest DP2s, which are up to 1.2 dB lower than predicted. (This deviation stems from the imperfect approximation of half-wave rectification in terms of a second-order distortion.) The prediction for the phase of a DP2 at $f_k \pm f_m$ is $\phi_k \pm \phi_m$, where $\phi_1 ... \phi_N$ are the primary phases (Meenderink & van der Heijden, 2010). Appendix Figure 5.5B shows the test of the prediction of DP2 phases from the primary phases using the same stimulus as in Appendix Figure 5.5A. The phase predictions are accurate to within 0.0025 cycle.

The "forward prediction" (DP2s from primaries) illustrated in Appendix Figures 5.5A,B is of less importance; it is the reverse procedure that is used to reconstruct from the measured DP2 data the underlying primary amplitudes and phases. Specifically, denoting the primary magnitudes by $M_k = 20 log A_k$, and denoting DP2 magnitudes of sum tones at $f^+_{km} = f_k + f_m$ and difference tones at $f^-_{km} = f_k - f_m$ by M^+_{km} and

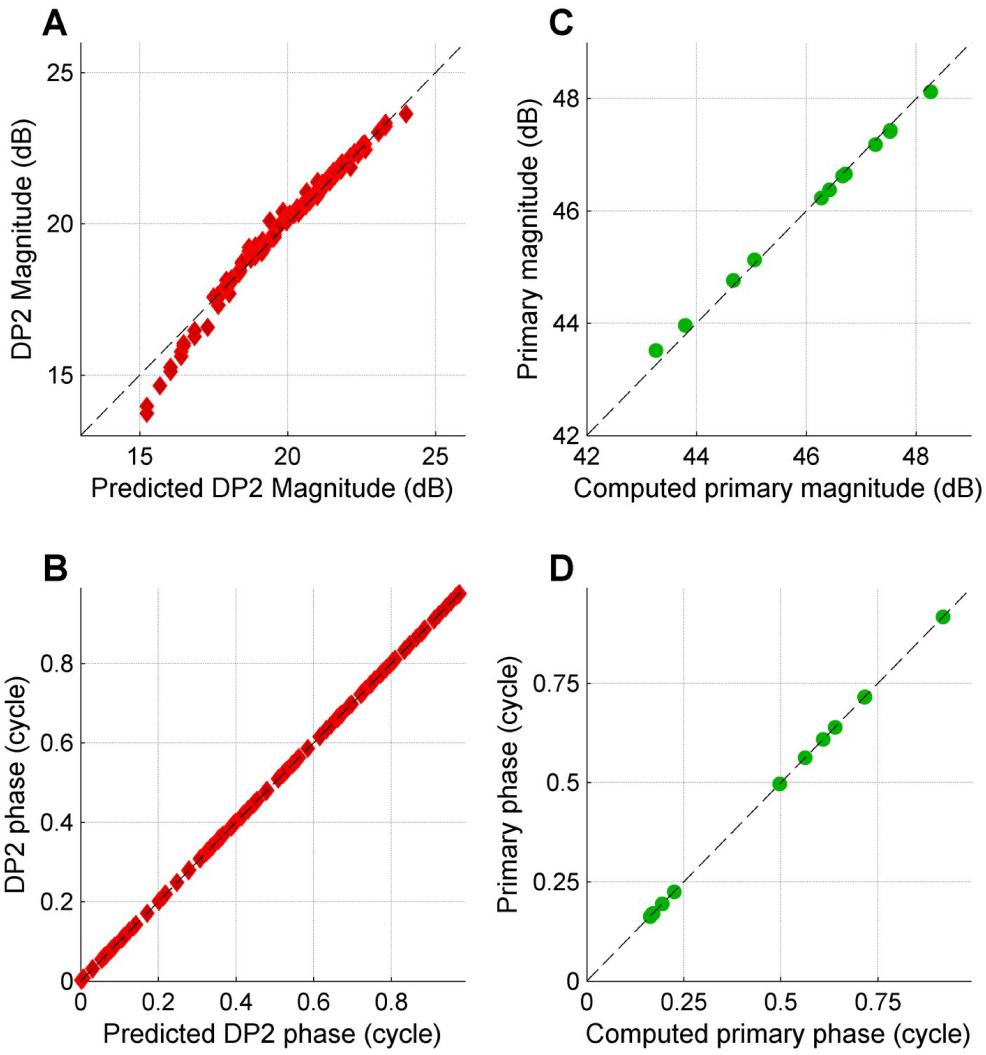

Figure 5.5: Predicting the DP2 spectrum from a primary spectrum and *vice versa*; no low-pass filtering. (**A**) Actual DP2 magnitudes obtained by rectifying (not followed by filtering) the tone complex with unequal primary magnitudes shown in Figure 5.2C, left panel, plotted against the approximation of Equation 5.1. (**B**) As in (A), but now for the phase. (**C**) Retrieving the primary magnitudes from the DP2 spectrum by inverting (fitting) Equation 5.1. Actual primary magnitudes are plotted versus computed magnitude. (**D**) As in (C), but now for the phase.

M_{km}^{-}, respectively, and analogously for the phase, we obtain:

$$\begin{aligned} M_{km}^{\pm} &= M_k + M_m \\ \phi_{km}^{\pm} &= \phi_k + \phi_m \end{aligned} \tag{5.1}$$

Note that scatter in the DP2 magnitudes results from any variation of primary magnitudes results.This includes regular trends in the primary magnitudes such as the deviation of a single primary component (e.g. due to a dip in the middle-ear transfer) or a systematic roll-off. Such regular trends in the input give scatter throughout the DP2 spectrum because each primary component affects DP2 components at multiple frequencies.

Retrieving the N primary magnitudes and phases (up to overall offsets) from the N^2 DP2 magnitudes and phases amounts to solving the overdetermined set of Equation 5.1 in a least squares sense. Because Equation 5.1 is linear this leads to a unique and stable solution, and the numerical implementation is straightforward and efficient (e.g. MATLAB left matrix division). For $N = 12$ (as in Appendix Figure 5.5), 2×11 unknowns are retrieved from 2×144 knowns. The overdetermined character makes the procedure accurate and robust. A test of the retrieval of the relative primary magnitudes and phases from the DP2 spectrum is shown in Appendix Figures 5.5. The deviations in the retrieved magnitude are systematic but small ($\leq$0.25 dB); the phase is retrieved to within 0.00025 cycle.

When the rectifier is followed by a filter (whether low-pass or not) having complex transfer function $H_\alpha(f)$, where α stands for a set of parameters that characterize the filter, Equation 5.1 is extended to:

$$\begin{aligned} M_{km}^{\pm} &= M_k + M_m + 20log|H_\alpha(f_{km}^{\pm})| \\ \phi_{km}^{\pm} &= \phi_k + \phi_m + arg(H_\alpha(f_{km}^{\pm})) \end{aligned} \tag{5.2}$$

In principle, Equation 5.2 can be used to fit the DP2 data in a least-squares sense as before, now also incorporating the new parameters α to the fit (in addition to the primary magnitudes and phases). When fitting experimental data, however, it is unclear a priori what type of filter to anticipate. To accommodate a variety of possible filter shapes, we extended Equation 5.1 by adding 7^{th}-order polynomials (increasing the order did not change the results):

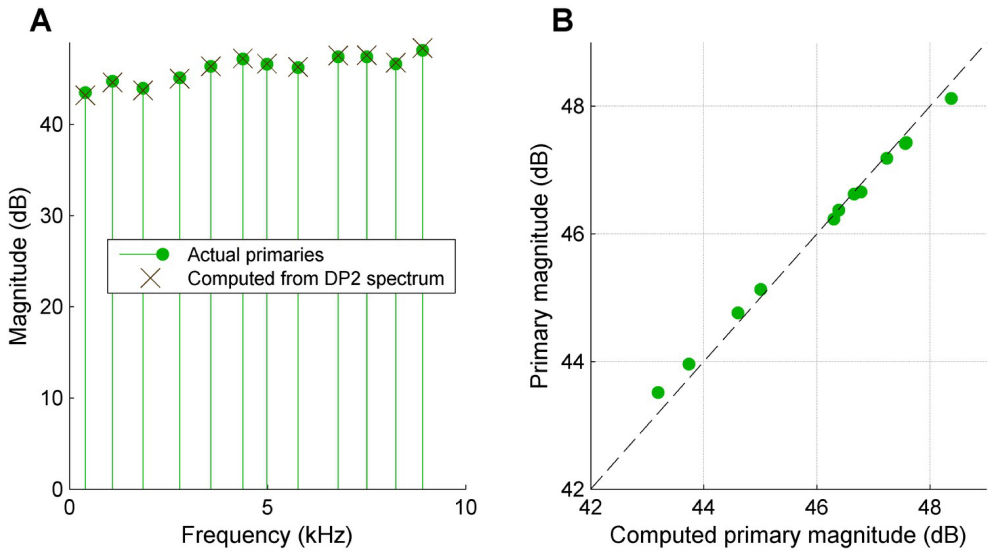

Figure 5.6: Retrieving the primary spectrum from the low-pass filtered DP2 spectrum. (A) A tone complex with non-equalized primary spectrum (*green circles*) was rectified and low-pass filtered at 2.5 kHz. From the resulting DP2 spectrum, the primary spectrum was reconstructed (*black Xs*). (B) Scatter plot comparing the actual primary spectrum entering the rectifier + low-pass filter scheme to the primary spectrum reconstructed from the DP2 spectrum at the output of the low-pass filter.

$$
\begin{aligned}
M_{km}^{\pm} &= M_k + M_m + \sum_{n=1}^{7} \beta_n (f_{km}^{\pm})^n \\
\phi_{km}^{\pm} &= \phi_k + \phi_m + \sum_{n=1}^{7} \gamma_n (f_{km}^{\pm})^n
\end{aligned}
\tag{5.3}
$$

Like Equation 5.1, this model is linear in its fit parameters, so it leads to a unique solution (in a least squares sense). In Equation 5.3 the primary magnitudes M_k and M_m describe the 'within-band' scatter of DP2 magnitudes, and the polynomial describes the post-rectifier filter. Fitting Equation 5.3 to the DP2 spectrum of Figure 5.2C (which includes the low-pass filtering) reproduces the primary spectrum accurately (Appendix Figure 5.2). The largest deviations are 0.3 dB and 0.07 cycle.

Having retrieved the primary spectrum (whose lack of flatness causes the scatter of DP2s), we can assess the post-rectifier filter. This is illustrated in Appendix Figure

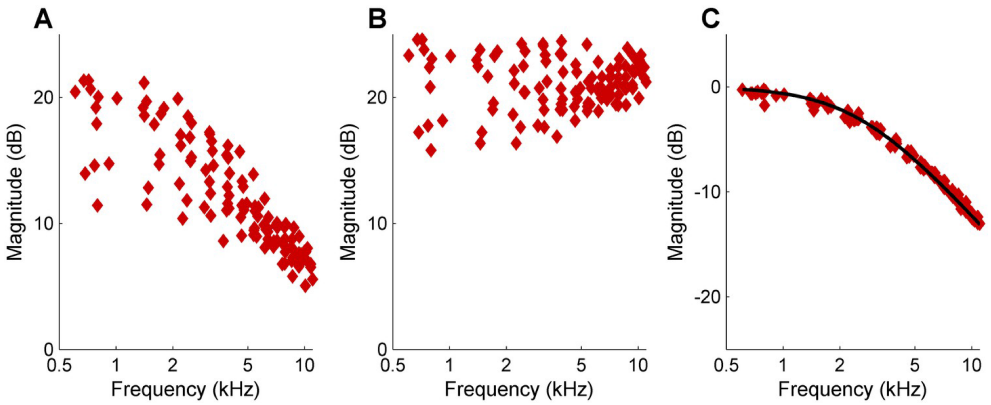

Figure 5.7: Computational separation of DP2 scatter and filter effect. (A) DP2 spectrum obtained by rectifying and low-pass filtering a zwuis multitone waveform having unequal primary amplitudes. (B) Magnitude scatter in the DP2 spectrum of panel (A), computed by inserting the retrieved primary magnitudes into Equation 5.1. (C) The effect of the low-pass filter isolated by subtracting the scatter contribution of panel (B) from the DP2 spectrum in (A). For reference, the gain curve of actual filter that was used to generate the DP2 spectrum (first-order low-pass; corner frequency 2.5 kHz) is also shown (*black line*).

5.7 for the magnitudes; the phase analysis is analogous. The actual DP2 spectrum of the rectified + low-pass filtered waveform is shown in Appendix Figure 5.7A. Inserting the retrieved primary magnitudes (shown in Appendix Figure 5.6A) into Equation 5.1 yields the predicted unfiltered DP2 spectrum (Appendix Figure 5.7B). This isolates the scatter. Subtracting the scatter from the actual DP2 spectrum retrieves the effect of the filter (Appendix Figure 5.7C). This is the DP2 spectrum "corrected for scatter" (for the experimental data this scatter-corrected version of the magnitudes is shown in Figure 4B of the main text). It clearly reproduces the first-order low-pass filter used to generate the DP2 spectrum, which is shown in Appendix Figure 5.7C for reference. Note that up to this point nothing in the fitting procedure has presumed a low-pass filter; the polynomial terms of Equation 5.3 are agnostic in this respect.

Theoretically, the above computational procedure is all that is needed to isolate and estimate the filter contribution to the DP2 spectrum (Appendix Figure 5.7C). In the experiments, we went further and used the retrieved OHC input to adapt the acoustic stimulus aimed at equalizing the OHC input and reducing the DP2 scatter (this step was iterated if necessary). We had two reasons for doing so. (1) Equalized OHC input spectra yield higher numbers of Rayleigh-significant DP2 components,

thus richer datasets. This can be understood from the limited dynamic range of the measurements: if the DP2 magnitude scatter is too large, the weaker DP2s will drop below the noise floor. (2) Scatter reduction by adapting the stimulus is a powerful way of interrogating the system. The simple rectifier + filter scheme predicts that an adjustment of the relative SPLs of N primaries (i.e. using N-1 degrees of freedom) reduces the scatter in as many as N^2 distortion components in the raw data. This is a strong prediction (recall that $N \geq 10$ in our recordings), and to see it happening in the real data (Figures 5.3 and 5.4) confirms that the simple scheme is an adequate description of the DP2 spectra generated by the OHCs.

Fitting a first-order low-pass filter to the scatter-corrected DP2 spectrum (the last analysis step) was done jointly to the magnitude (Figure 4B) and phase data (Figure 5.4C). Consider a DP2 having a magnitude of M dB and a phase of ϕ cycles. In the complex spectrum of the response it is represented by a component $Z = 10^{M/20} e^{2\pi i\phi} = e^{(ln10/20)M + 2\pi i\phi}$, or

$$lnZ = (ln10/20)M + 2\pi i\phi \tag{5.4}$$

an expression that exposes the common logarithmic nature of M and ϕ, and provides the natural conversion factor between the two in the form of the ratio $\Theta = 2\pi/(ln10/20) \simeq 54.6$ dB/cycle (this conversion factor would be unity if magnitude and phase were expressed in nepers and radians, respectively). The joint fit of magnitude data M (in dB) and phase data ϕ (in cycles) then amounts to minimizing the sum of squares:

$$x^2 = \sum (M_{\text{data}} - M_{\text{model}})^2 + \Theta^2 \sum (\phi_{\text{data}} - \phi_{\text{model}})^2 \tag{5.5}$$

This expression was minimized to produce the fits shown as black lines in Figure 5.4B and C.

Appendix 2

Estimate of the AC receptor potential of OHCs near threshold

In this Appendix estimates are made of the AC receptor potential in OHCs in response to high-frequency tones near behavior threshold. Specifically, the AC receptor potential evoked by a 17-kHz tone at 5 dB SPL in guinea pig are derived from the in vivo OHC recordings of Cody & Russell (1987), and the AC receptor potential evoked by a 16-kHz, 5-dB-SPL tone in gerbil is estimated by combining recordings of basilar-membrane vibrations with electrophysiological data.

Figure 6B of Cody & Russell (1987) shows a 160-μV AC receptor potential for a 17-kHz tone at 15 dB SPL. These data were corrected for the membrane time constant, for which the authors used 6 dB per octave above 1200 Hz. Thus the raw AC component $V_{\rm AC}$, corrected for equipment filtering but not for the membrane time constant, was $160 \times 1200/17000 = 11.3$ μV. In this low-SPL regime the growth is linear, leading to an estimate of $V_{\rm AC} = 3.6$ μV for a 5-dB-SPL tone. These recordings originate from the 17-kHz location, where the wave is assumed to have been amplified. At the spatial onset of the putative amplification, basal to the best 17-kHz location, the excitation is smaller by $\sim$15 dB (see below), leading to $V_{\rm AC} = 0.6$ μV at the spatial onset of compressive growth.

The AC receptor potential of OHCs measured in vivo saturates with low-frequency (200 Hz) stimulation at $\sim$95 dB SPL (Fig. 11 of Dallos (1986) and this matches the saturation of the cochlear microphonic potential at the round window, which is dominated by basal OHCs (Dallos & Cheatham, 1976), observed with 95-dB-SPL tones at 200 Hz (Fig. 4 of Patuzzi et al. (1989)). In gerbil, a 95-dB-SPL tone at 200 Hz evokes a basilar membrane displacement of $\sim$300 nm. Combining these two findings, the Boltzmann function relating BM displacement $d_{\rm BM}$ to the mechanotransducer channel conductivity $G_{\rm MT}$,

$$G_{\rm MT}(d_{\rm BM}) = G_{\rm max}/(1 + e^{-\beta d_{\rm BM}}) \tag{5.6}$$

has $\beta \approx 0.01$ nm^{-1}. ($G_{\rm max}$ is the maximum value with all transducer channels open.) Assuming that the resting value $G_{\rm MT,0}$ of the MT conductivity equals $G_{\rm max}/2$ (this is where the Boltzmann function is steepest, maximizing the AC component of the receptor current), the fractional conductivity variation (modulation m) for small BM

displacements equals

$$m = \Delta G_{\mathrm{MT}}/G_{\mathrm{MT,0}} = \frac{\beta}{2} d_{\mathrm{BM}} \tag{5.7}$$

The behavior threshold for 16-kHz tones in gerbil is 5 dB SPL (Ryan, 1976), and at the 16-kHz location of the sensitive gerbil cochlea, this evokes a BM displacement of d_{BM} ≈0.1 nm, corresponding to $m \approx 5 \times 10^{-4}$. This is the value at the peak excitation following the putative amplification. The actual SPL-dependent (physiologically vulnerable) amplitude growth occurs basal to the peak. In the 16-kHz region the amplitude growth amounts to ∼15 dB at the lowest SPLs (Fig. 3A of Ren, 2002). Thus at the spatial onset of the putative amplification of the near-threshold 16-kHz tone, $d_{\mathrm{BM}} \approx 0.018$ nm, corresponding to $m \approx 9 \times 10^{-5}$.

The AC receptor potential follows from a straightforward linearization of the equivalent OHC circuit (e.g., Fig. 6B of Johnson et al. (2011),

$$V_{\mathrm{AC}} = \frac{m(E_{\mathrm{K}} + E_{\mathrm{EP}})}{(\frac{1}{G_{\mathrm{K}}} + \frac{1}{G_{\mathrm{MT,0}}})(G_{\mathrm{K}} + G_{\mathrm{MT,0}} + i\omega C)} \tag{5.8}$$

using a total basolateral membrane capacitance C = 5 pF (neglecting the apical membrane capacitance); deriving the basolateral membrane resting conductance $G_{\mathrm{K,0}}$ from our corner frequency: $G_{\mathrm{K,0}} = C\omega_0 = 2\pi C f_{\mathrm{corner}}$ with $f_{\mathrm{corner}} = 2200$ Hz (our Figure 5.4); the K^+ reversal potential of $\mathrm{E_K}$ = -75 mV; the resting value of MT conductivity $G_{\mathrm{MT,0}}$ = 75 nS (Fig S1 of Johnson et al. (2011); an endocochlear potential $\mathrm{E_{EP}}$ = 90 mV; and the angular stimulus frequency $\omega = 2\pi f$. Applying Equation 5.8 to the values of fractional MT conductivity m, we obtain $V_{\mathrm{AC}} \approx 5.7$ μV at the peak of the wave and $V_{\mathrm{AC}} \approx 1.0$ μV at the spatial onset of its nonlinear growth.

Supplementary Information

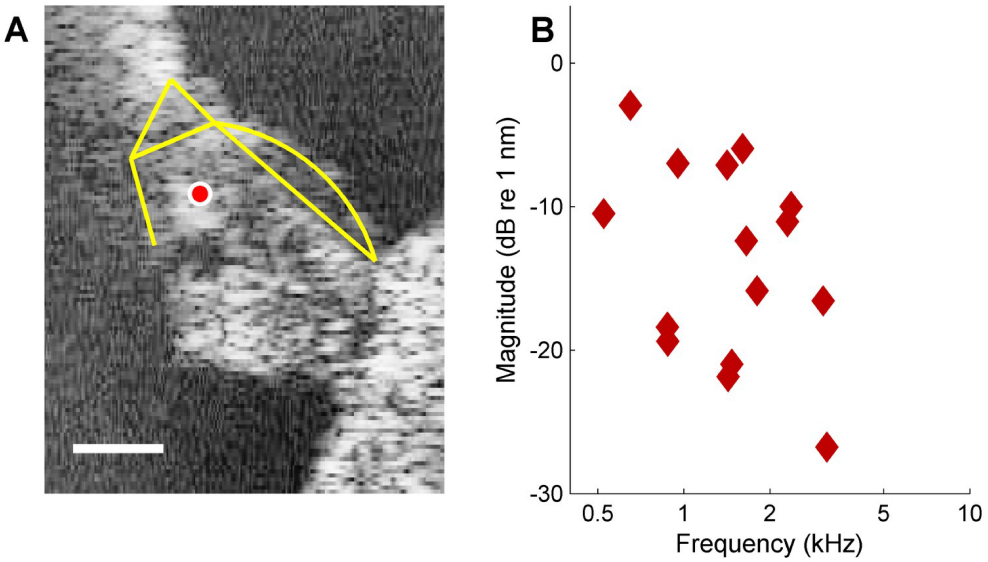

Figure 5.8: DP2s at low sound intensities. (**A**) OCT reflectance image (*grayscale*), with structural framework of Corti's organ (*yellow*) superimposed for reference. CF = 14 kHz. The red circle in the OHC/Deiters' cell region marks the recording position. Scale bar, 0.05 mm. (**B**) Magnitude spectrum of Rayleigh-significant (p=0.001) DP2s evoked by a 43-component zwuis stimulus presented at 25 dB SPL per component, recorded at the position marked in panel (A).

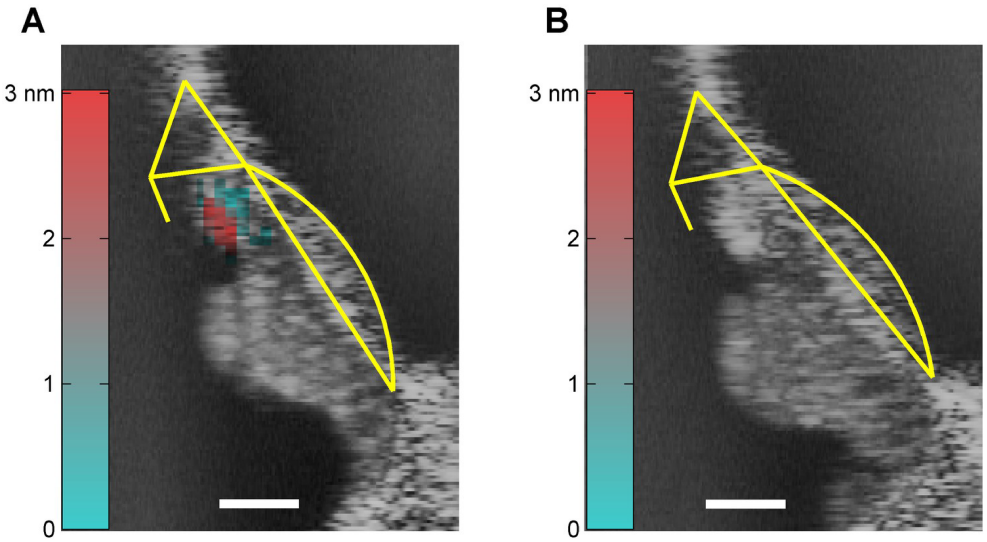

Figure 5.9: Post mortem disappearance of DP2s. (**A**) In vivo OCT reflectance map (*grayscale*) of the organ of Corti (CF = 22 kHz) with structural framework of Corti's organ (*yellow*) superimposed for reference. Color-coded overlay: total RMS value of 2^{nd}-order distortion products (DP2s) evoked by a 16-tone complex, 2-15 kHz; 65 dB SPL. DP2s dominate in the OHC region. Scale bar, 0.05 mm. (**B**) Same as (A) (identical stimulus, same ear), but recorded within 20 minutes post mortem. The DP2s have disappeared

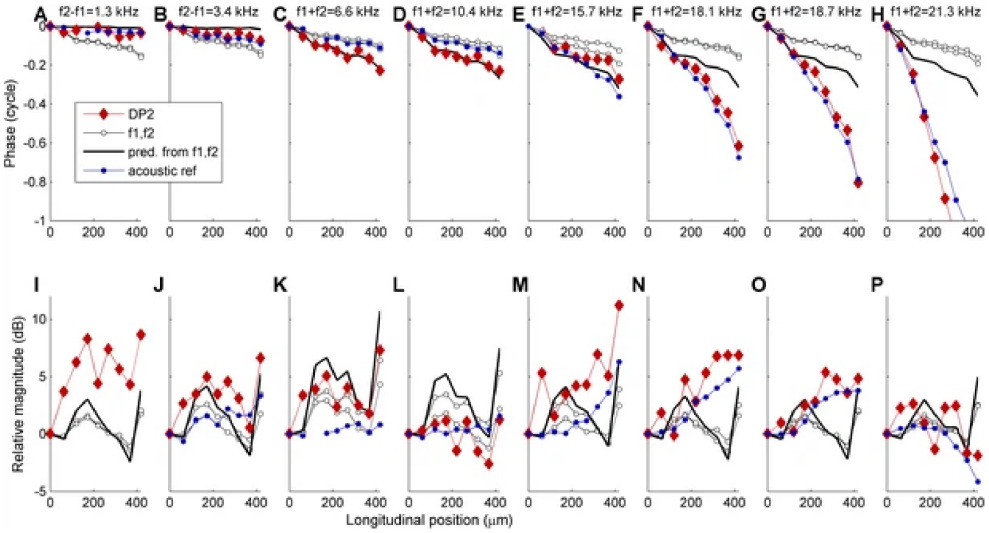

Figure 5.10: Propagation of DP2s in the 18-25-kHz region. Recordings were made at 9 adjacent longitudinal locations spanning ∼400 μm. Phase (upper row) and magnitude (lower row) are shown of: 6 example DP2 components (*red diamonds*); its two parent primaries f_1 and f_2 (*open black circles*); phase and amplitude predicted by Equation 1, that is assuming local generation (*black line*); a reference acoustically presented component of approximately the same frequency (*blue circles*). DP frequency is indicated above each phase graph. For the lowest DP2 frequencies (1.3-10.4 kHz) the actual DP2 phase matches the prediction within ∼0.05 cycle. For the higher DP2 frequencies systematic deviations occur. The phase accumulation of the high-frequency DP2s matches the phase of the acoustic reference much better than the prediction based on local generation. Thus these high-frequency DP2 components are dominated by their own propagation rather than local contributions from the primaries as in Equation 1. The increasing dominance of propagation with increasing DP2 frequency was observed for all DP2s.

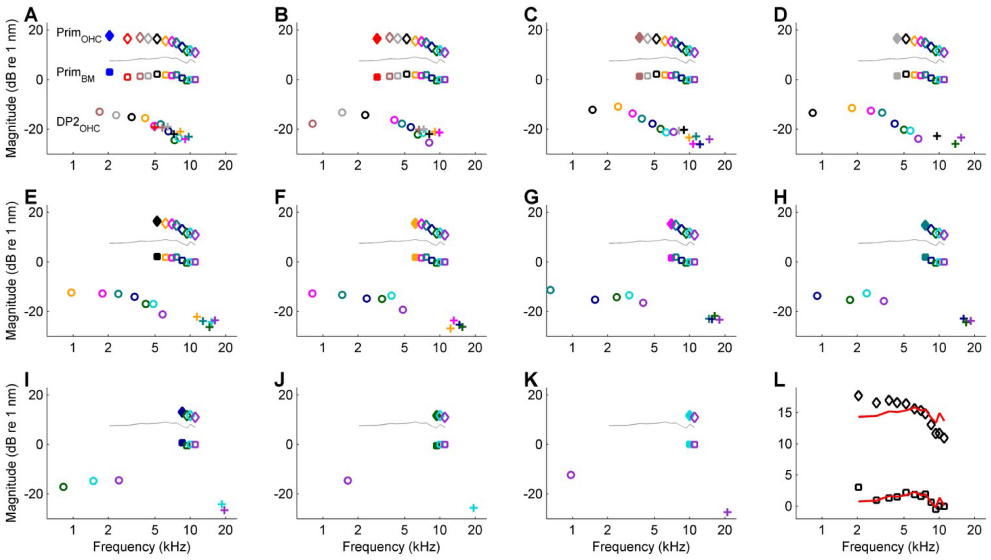

Figure 5.11: Comparison of linear response components and second-order distortion products (DP2s). Data from recording shown in the lowest curves in Figure 5.4A–C (CF = 25 kHz; estimated cutoff frequency, 3006 Hz). (**A**–**K**) The DP2s are split according to their "heritage" and the linear response components ("parents") are also shown. In A all the DP components relating to the lowest primary are shown. In B, that lowest primary is excluded and all the DP components relating to the new lowest primary are shown, and so on through panel K. *Diamonds*, linear response component (primary response) measured in the hotspot (OHC/Deiters' region). *Squares*, primary response measured on the basilar membrane (BM). *Circles*, difference tones at $f_2 - f_1$ measured in the hotspot. *Plus signs*, sum tones at $f_1 + f_2$ measured in the hotspot. The *solid lines* in all panels are identical; they show the effective OHC input determined from the DP2 spectrum. Their overall magnitude is unknown; the vertical position of the curves is chosen halfway the linear responses of BM and hotspot to facilitate comparison. The DP2s are split according to the lower primary f_1. The filled symbol in each panel marks the f_1 of all the DP2 components in that panel. The colors of the DP2s at $f_1 + f_2$ (plus signs) and $f_2 - f_1$ (circles) match the colors of the linear responses at f_2 in the same panel. (L) Detailed comparison between effective OHC input and primary responses. The effective OHC input (*red lines*) is shown at two different vertical positions: shifted for maximum overlap with primary responses at the hotspot (*diamonds*) and the BM (*squares*). The overlap is better for the BM data (RMS deviation, 0.9 dB) than for the hotspot data (RMS deviation, 1.9 dB).

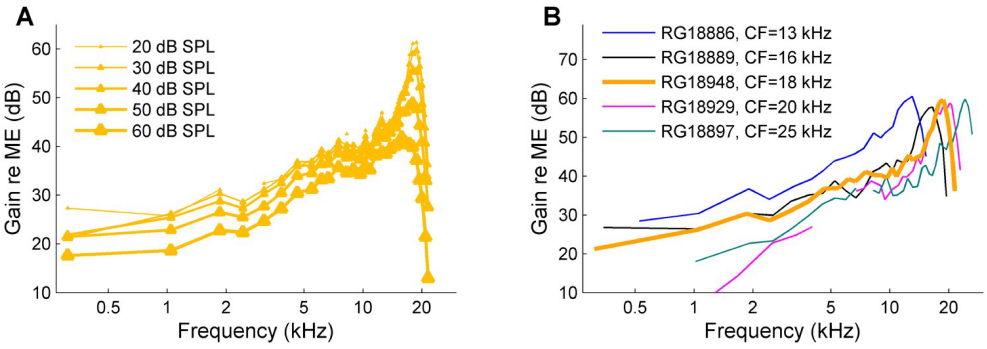

Figure 5.12: (**A**) A set of responses to a wideband zwuis stimuli at multiple SPLs as indicated in the graph, recorded from the CF = 18 kHz cochlea of Figure 5.4. The curves display the familiar compressive behavior of sensitive cochleae. (**B**) 30-dB-SPL recordings obtained from all five cochleae displayed in Figure 5.4, using the same colors as in that figure

Chapter 6

Rectifying and sluggish: Outer hair cells as regulators rather than amplifiers[1]

In the cochlea, mechano-electrical transduction is preceded by dynamic range compression. Outer hair cells (OHCs) and their voltage dependent length changes, known as electromotility, play a central role in this compression process, but the exact mechanisms are poorly understood. Here we review old and new experimental findings and show that (1) just audible high-frequency tones evoke an ∼1-microvolt AC receptor potential in basal OHCs; (2) any mechanical amplification of soft high-frequency tones by OHC motility would have an adverse effect on their audibility; (3) having a higher basolateral K+ conductance, while increasing the OHC corner frequency, does not boost the magnitude of the high-frequency AC receptor potential; (4) OHC receptor currents display a substantial rectified (DC) component; (5) mechanical DC responses (baseline shifts) to acoustic stimuli, while insignificant on the basilar membrane, can be comparable in magnitude to AC responses when recorded in the organ of Corti, both in the apex and the base. In the basal turn, the DC component may even exceed the AC component, lending support to Dallos' suggestion that both apical and basal OHCs display a significant degree of rectification. We further show that (6) low-intensity cochlear traveling waves, by virtue of their abrupt transition from fast to slow propagation, are well suited to transport high-frequency energy with minimal losses (∼2-dB loss for 16-kHz tones in the gerbil); (7) a 90-dB, 16-kHz tone, if transmitted without loss to its tonotopic place, would evoke a destructive displacement amplitude of 564 nm. We interpret these findings in a framework in which local dissipation is regulated by OHC motility.

[1]van der Heijden, M., & Vavakou, A. (2021). Rectifying and sluggish: Outer hair cells as regulators rather than amplifiers. *Hearing research*, 108367.
https://doi.org/10.1016/j.heares.2021.108367

Introduction

The anatomical differentiation between inner and outer hair cells (IHC, OHC) in the mammalian cochlea has been known since the work of Retzius in the early 1880s (Grant, 1999), but the functional correlate of this dichotomy remained obscure for almost a century. Because OHCs outnumber IHCs more than threefold, it came as a surprise when Spoendlin (Spoendlin, 1969, 1972) reported that 95% of the afferent auditory nerve fibers innervate IHCs. This strongly suggested that auditory information processing is primarily carried by the IHCs. What, then, is the function of OHCs? An important step was the discovery that kanamycin-induced OHC destruction caused a ∼40-dB elevation of behavioral threshold exactly in the frequency region where OHC were absent (Ryan & Dallos, 1975). The authors concluded that "OHCs are specialized to perform a facilitatory function on the IHCs." The mechanisms of this facilitation, however, were unclear.

Around the same time other studies, not directly related to OHCs, provided accumulating evidence that the classic view of the cochlea as a passive, linear mechanical device needed revision. Rhode (Rhode, 1971, 1978) found that basilar membrane (BM) vibrations measured in vivo show a compressive growth with sound pressure. Indirect evidence of the strongly nonlinear character of inner-ear vibrations was obtained from auditory nerve (AN) recordings by Goblick Jr & Pfeiffer (1969) and Rose et al. (1971). In their analyses, both papers explore the possibility of a cochlear gain control mechanism. Rose et al. (1971) wrote "[our findings] suggest the existence of a cochlear sensitivity control mechanism which may, but perhaps need not be, mechanical in nature. Such a mechanism could be a major source of the demonstrable nonlinearity of the system [...]." They went on to discuss the potential role of DC response components in the operation of the sensitivity control.

The discovery of prolonged otoacoustic emissions in the ear canal following transient acoustic stimulation (Kemp, 1978) quickly led to speculations about some form of wave amplification at low intensities (Kemp, 1979; Zwicker, 1979b). OHCs were the obvious candidate for providing such "active" feedback. Davis (1983) proposed a "motor function for OHC" and speculated that "a piezoelectric effect may be involved in the putative transduction of electrical energy [...] to mechanical vibration in the BM." Note that the scenario proposed by these authors, in which active feedback actually *drives* the motion, is a specific realization of the "facilitatory function" posited by Ryan and Dallos, but by no means the only possible realization. To illustrate,

releasing the handbrake of a car parked on a slope facilitates the ensuing motion, but does not drive it – gravity does.

At this point it is important to clearly distinguish two possible ways in which OHCs may provide cochlear feedback. (1) They may control the mechanical properties of the partition, e.g. modify the stiffness or resistance on a time scale of one or several cycles; (2) alternatively, they may act as direct sources of vibrational energy. We refer to these roles as regulatory and cycle-by-cycle , respectively (see Cooper et al. (2018)). The two roles are not mutually exclusive, and other roles may exist, too.

The possibility of cycle-by-cycle feedback was quickly embraced by modelers, who sought to explain the apparent discrepancy between the sharply tuned AN responses and the poor frequency selectivity of basilar membrane (BM) vibrations in cadaver cochleas (von Békésy, 1960). The first one to incorporate active feedback into a cochlear model was Zwicker (1979b), who presented "a preliminary model assuming that the outer hair cells act as an amplifier which contains saturation (corresponding to 40 dB) and feed back to sensitize the inner hair cells." One of his motives to consider this type of model was his thorough knowledge of distortion products, audible nonlinear distortions generated in the cochlea that he had studied in psychoacoustic tests (Zwicker, 1955). At the time, in vivo data on tuning sharpness of the BM were inconclusive, and Zwicker assumed that it was as poor as it is post mortem. In that sense, he was modeling a "second filter" in terms of an active process.

Unlike Zwicker, Kim (1980) and Neely & Kim (1983) build their active models on the assumption that the sharp tuning in the AN has mechanical origins – even though the evidence was controversial at the time. Whereas Kemp (1979) had stated that, to preserve stability, "net damping must never become negative," Neely and Kim went further and used a "BM damping function that is negative in a small region basal to the [peak]" (Neely, 1981). In this scenario, the vibrations in the peak region are truly driven by an internal energy source, and the energy flux at the peak exceeds the flux at more basal locations. The active model of Neely & Kim (1983) produced results that matched quite well the sharp tuning known from AN data and from sensitive BM measurements at the time (Sellick et al., 1982). Neely and Kim conclude their paper with the suggestion that "the negative damping components in the model may represent some physical action of the outer hair cells, functioning in the electromechanical environment of the normal cochlea and serving to boost the sensitivity of the cochlea at low levels of excitation."

It is against this background that Brownell et al. (1985) reported that isolated

OHCs reversibly change their length upon current injection. In their introduction the authors mention the circumstantial evidence for energy injection from the work of Kemp (1978) and Neely & Kim (1983), but for methodological reasons their own pioneering study was restricted to DC mechanical responses (to both DC and AC current injection). Consequently, the discussion of their results hardly touches upon cycle-by-cycle feedback, and instead focuses on the regulatory effects that OHC length changes may induce in the mechanical properties of the cochlear partition. Referring to the triangle formed by one OHC, the phalangeal process of the Deiters' cell underneath it and the stretch of reticular lamina spanned by them (their fig. 1C) as a "mechanical unit", Brownell et al. remark that "increases in OHC length would make this unit more rigid whereas decreases would make it more compliant."

Although they do not state it explicitly, their description of a regulatory action of OHCs fits well in the sensitivity control schemes considered by Goblick Jr & Pfeiffer (1969) and Rose et al. (1971) and in particular the DC effects discussed in the latter study.

The perspective rapidly changed in the years to follow. On the experimental side, advances in measurement techniques, reviewed in Ashmore (2008), allowed the recording of AC motile responses at increasingly higher frequencies. Frank et al. (1999) reported a frequency limit (3-dB down point) of OHC electromotility of 79 kHz. While this may seem to support the physiological feasibility of cycle-by-cycle feedback in the spirit of (Kemp, 1979; Zwicker, 1979b) and Kim (1980), other studies seemed to spell trouble for this hypothesis, notably the finding that electromotility is driven by the OHC membrane potential rather than by transmembrane currents (Santos-Sacchi & Dilger, 1988). Especially at very high frequencies, the AC receptor potential is strongly attenuated as it is shunted by the membrane capacitance. This is commonly referred to as the "RC problem" (Santos-Sacchi, 1989), although it may be argued that this name is misleading (see Section "Temporal and spectral effects of rectification"). Corner frequencies for the OHC membrane, measured in vitro, range between 480 Hz to 1250 Hz (Mammano & Ashmore, 1996; Johnson et al., 2011) and this contrasts with their purported role as high-frequency amplifiers up to 150 kHz in some species (Vater & Kössl, 2011).

On the theoretical side, the vast majority of cochlear models published since the mid-1980s incorporate cycle-by-cycle feedback by OHCs. Refinement of "negative resistance models" improved the match with the sharply tuned BM responses of sensitive ears (Neely & Kim, 1986) and reproduced their nonlinear compressive behavior, too (e.g.,

De Boer & Nuttall (2000). Based on a mathematical analysis of AN data, it was claimed by De Boer (1983) that it was impossible to explain the frequency selectivity of the cochlea unless "the resistance component of the BM impedance is negative over a part of the length of the cochlea." Similar analyses applied to BM data have aimed at proving that power injection cannot be dispensed with (Brass & Kemp, 1993; Shera, 2007). However, such mathematical analyses are based on (often implicit) premises that may turn out to be wrong, and one is reminded of John Bell's aphorism that "what is proved by impossibility proofs is lack of imagination" (Bell, 2004). In that context it is worth pointing out that the same cochlear models that successfully reproduced existing BM data, failed to anticipate the complex vibration patterns and wideband nonlinearities within the organ of Corti that were revealed by recent advances in measurement techniques (Lee et al., 2015; Ren et al., 2016b; Cooper et al., 2018). At the moment it is fair to say that in the field of cochlear mechanics, experiment is ahead of theory.

Over the last two decades, the hypothesis of cycle-by-cycle feedback has gained terrain, and only a limited number of studies was published that explicitly question it (Allen & Fahey, 1992; van der Heijden, 2014; van der Heijden & Versteegh, 2015a; Cooper et al., 2018; Vavakou et al., 2019; Santos-Sacchi & Tan, 2018). Cycle-by-cycle amplification is often presented in textbooks as an accomplished fact, even though direct evidence is absent and the micromechanical operation of the cochlea is still poorly understood. The purpose of this article is to review a number of facts, findings and insights, both old and new, that suggest that an unconditional acceptance of the cycle-by-cycle character of OHC function is not justified, and that there are good reasons to consider potential regulatory aspects of OHC function. In our opinion it is important to keep an open mind toward such alternative explanations as long as we cannot claim that we understand how the cochlea works.

High-frequency motility and its limitations

Some mammals hear up to 150 kHz (Vater & Kössl, 2011). The cycle of a 150-kHz tone is 6.7 μs. If hearing at such frequencies is indeed aided by cycle-by cycle feedback from OHCs, electromotility must be extremely fast and accurately timed. Recent work by Santos-Sacchi's group indicates that the motility process itself (mediated by conformational changes of prestin) may be much slower than previously believed (Santos-Sacchi & Tan, 2018). They report inherent motility corner frequencies of $\sim$5

kHz, in marked contrast with the 79 kHz of Frank et al. (1999). This sluggishness is hard to reconcile with the hypothesis of cycle-by-cycle amplification at high frequencies. But even if the motile process itself would be extremely fast, it would still need a sufficiently large AC receptor potential to provide amplification because it is voltage driven.

Magnitude of the AC receptor potential in OHC

Cody & Russell (1987) reported in vivo recordings of the receptor potential of hair cells in the basal turn of the guinea pig cochlea. Their fig. 6B shows the AC component of the receptor potential in an OHC in the 17-kHz region. They corrected their raw data for two effects: (1) the low-pass characteristics of their equipment; (2) the low-pass filtering by the cell membrane, which they estimated from the 1200-Hz corner frequency of the cell. Fig. 6.1 reproduces the 17-kHz curve after undoing the second correction. This restores the AC receptor potential seen by the cell, which cannot ignore its own membrane filtering.

In the low-SPL range, the AC receptor potential varies linearly with sound pressure (dashed lines in Fig. 6.1). The behavioral threshold for guinea pigs is ∼0 dB SPL near 16 kHz (Prosen et al., 1978). Extrapolating Cody and Russell's data, the AC receptor potential evoked by a just audible 17-kHz tone amounts to 2.0 μV. Note that this is at the tone's best place, already after the putative amplification. The 17-kHz recording site is where waves of lower frequencies acquire their "amplitude boost" on their way to peaking at a more apical location. The lowest frequency subject to this boost is half an octave below the characteristic frequency (CF) (Robles & Ruggero, 2001), here 12 kHz. Thus, 15 kHz, for which Cody and Russell present data, falls well into the range of frequencies eligible to receive local cycle-by-cycle feedback from this OHC. Extrapolating the 15-kHz curve to the 0-dB-SPL hearing threshold (Fig. 6.1) yields an estimated 0.6-μV AC receptor potential.

The foregoing estimates of the receptor potential are based on a straightforward extrapolation of Cody and Russell's in vivo data. They do not depend on any assumptions regarding corner frequencies or other parameters. It is unfortunate that Cody and Russell did not report 12-kHz data, as this would have enabled an even more critical test. A 12-kHz wave is one that just enters its "active region" when arriving at the 17-kHz place. A plausible estimate can still be derived. Knowing that low-SPL waves in the base receive a total amplitude gain of ∼15 dB when traveling from the spatial onset of their active region to their peak (fig. 3A of Ren (2002)), this

estimate amounts to 15 dB below the 17-kHz receptor potential, yielding 0.36 μV.

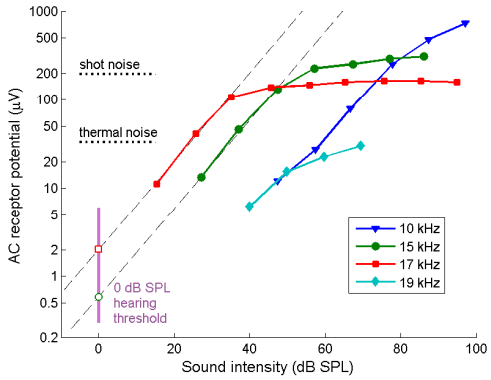

Figure 6.1: Extrapolating OHC recordings of Cody & Russell (1987) to a just audible level. Data (closed symbols) extracted from fig. 6B of Cody and Russell (see text) show the AC component of the OHC receptor potential in response to tones at different intensities and frequencies. Dashed lines capture the linear growth observed at the lower intensities and serve to extrapolate the receptor potential to the just-audible intensity (open symbols) for guinea pigs, ~0 dB SPL (vertical line). Horizontal dotted lines indicate estimated noise floors (see text).

These estimates of receptor potential of just audible tones, directly derived from Cody and Russel's data, are consistent with independent estimates based on the equivalent electrical circuit of OHCs (Appendix 2 of Vavakou et al. (2019)), which also yield values in the order of 1 μV.

To put these estimates in context, we note that in isolated OHC, a 1-μV variation in membrane potential evokes a fractional length change of 3×10^{-7} , or 1 part in 3.3 million (Ashmore, 2008). For the ~25-μm tall OHC from the 17-kHz region (Dannhof et al., 1991), this is a length change $\Delta L = 0.0075$ nm, or 7.5% of the diameter of a hydrogen atom. It is difficult to assess the resultant motion in the in vivo situation. One may argue that the in vivo displacement is even smaller, because OHCs are firmly constrained by the structural embedding in the organ of Corti. Alternatively, one may argue that resonances within the organ could boost the motion of structures coupled to the OHC. A more insightful way to assess the magnitude of the receptor potential of soft sounds is by relating it to the expected noise floor, since this is what limits audibility (De Vries, 1948; Allen, 1997).

Amplifying internal noise

The ~1-μV amplitude of the AC receptor potential evoked by just audible tones is very small, not only when compared to the >200-mV range of membrane potentials that evoke OHC length changes (Ashmore, 2008), but in particular when compared to the expected electrical noise, i.e., statistical fluctuations in the absence of stimulation. We briefly consider thermal (Johnson) noise and shot (quantization) noise. For an insightful discussion of thermal noise in hair cells and its fundamental impact on their

dynamic range, see Allen (1997). The variance of Johnson noise is $\sigma^2 = kT/C$, where k is Boltzmann's constant, T the absolute temperature and C the cell membrane capacitance (Allen, 1997). With $C = 4$ pF in the 17-kHz region (Johnson et al., 2011), the RMS value of the thermal noise is 33 μV.

Shot noise arises from the bimodal character of the mechanotransducer (MT) channels which, in the absence of stimulation, spontaneously clatter between their open and closed states. It is a form of quantization noise: the fewer MT channels ("bits") a cell has, the poorer its S/N ratio is. With 60 MT channels (Beurg et al., 2006) the RMS of the shot noise amounts to 13% of the peak-to-peak range $V_{\rm pp}$ of the receptor potential at maximum stimulation, i.e., all channels closed versus all channels open (van der Heijden & Versteegh, 2015a). From the maximum value of the 10-kHz curve (Fig. 1) of Cody and Russell's recording, $V_{\rm pp}$ is at least 1.5 mV for this OHC, yielding a lower boundary for the shot-noise floor of 195 μV.

Even if a 1-μV AC receptor potential could somehow produce significant electromotile feedback, this would not serve its purported goal, namely to enhance auditory sensitivity. It would achieve the very opposite. For a tone evoking a 1-μV receptor potential, the S/N ratio of the OHC feedback is -30 dB and -46 dB for thermal and shot noise, respectively. Any motile response would then be completely hijacked by stochastic fluctuations, drowning the soft tone in amplified noise. It would take the parallel, synchronized, operation of 1000 OHCs to just overcome the thermal noise and improve the S/N ratio to a meager 0 dB. It would take 40000 synchronized OHC to just overcome the shot noise. The "active region" that determines the sensitivity to single tones, spans $\sim$0.5 mm and contains $\sim$150 OHCs. And even these $\sim$150 OHC cannot work in synchrony: wave propagation is slow in the active region, creating sizeable phase differences within that region ($>$ 1 cycle total, Ren (2002)). This means that OHCs must work in series rather than in parallel. If they really were amplifiers, they would be cascaded – exactly as in the wave amplifier envisioned by Kemp (1979). Indeed, cochlear compression exhibits a spatial build-up that reflects a cascaded OHC action (Versteegh & van der Heijden, 2013). But if the nature of that action is amplification, the cascaded configuration only exacerbates the problem, because the S/N ratio further degrades at every link of the chain. The noise will grow exponentially.

Finally, it is worth noting that even a hypothetical high-fidelity mechanical amplifier would not improve detection of soft tones. Detection of faint signals is limited by noise and in the best case the S/N is preserved by the amplifier, which means that

detectability is spared, not improved. Put differently, by postulating a mechanical amplifier the detection problem is pushed from the input of transduction (IHCs) to the input of the amplifier (OHCs). To quote Ray Meddis, "The idea that the system is detecting a signal in order to amplify it in order to detect it has always seemed odd."

The (R)C problem

In vitro measurements of OHC corner frequency f_c or, equivalently, the RC time constant $\tau_{RC} = \frac{1}{2\pi f_c}$ have yielded values of 480 Hz (7-kHz region of the guinea pig; Mammano & Ashmore (1996)) and 300–1250 Hz (300-2500-Hz regions of the gerbil; Johnson et al. (2011)). In addition, Cody & Russell (1987) used current pulses to measure f_c in vivo for a 17-kHz OHC, yielding a 1200-Hz value.

Such f_c values seem hard to reconcile with the putative role of OHCs as high-frequency amplifiers. Reconciliation has been sought along two different lines: (1) the motile process somehow "circumvents" the lowpass character of the receptor potential; (2) RC times of OHCs in more basal regions are much smaller than in the apical and middle turns.

The first class of proposals accepts the low-pass character of the receptor potentials, but introduces hypothetical schemes that somehow overcome or compensate it in an attempt to make the electromotile output less band-limited than its electrical drive. Examples of such "circumvention schemes" include: gating by extracellular potential (Dallos & Evans, 1995); chloride influx by stretch activation of the lateral membrane (Rybalchenko & Santos-Sacchi, 2003); current flow in a 3D model of the organ of Corti (Mistrík et al., 2009); the purported wideband character of the imaginary component of piezoelectrics postulated to drive electromotility (Rabbitt, 2020). For more details on such schemes, see Ashmore (2008). The circumvention schemes often invoke hypothetical processes that are difficult to test directly by experiment. The proposal of Rabbitt (2020) was experimentally tested by Santos-Sacchi et al. (2021), who found that the effect of the imaginary component was too small to alleviate the lowpass character of electromotility.

A generic experimental approach to addressing circumvention schemes was taken in Vavakou et al. (2019). They measured sound-evoked vibration in the basal turn of the gerbil cochlea (CF, 13–25 kHz) and determined the spectral characteristics of OHC motility in vivo by an analysis of the vibrations in the OHC area. They found a clearcut first-order low-pass characteristic (6-dB/octave roll-off; 0.25-cycle phase

accumulation) with corner frequencies ranging from 2 to 3.1 kHz, i.e. three octaves below CF.

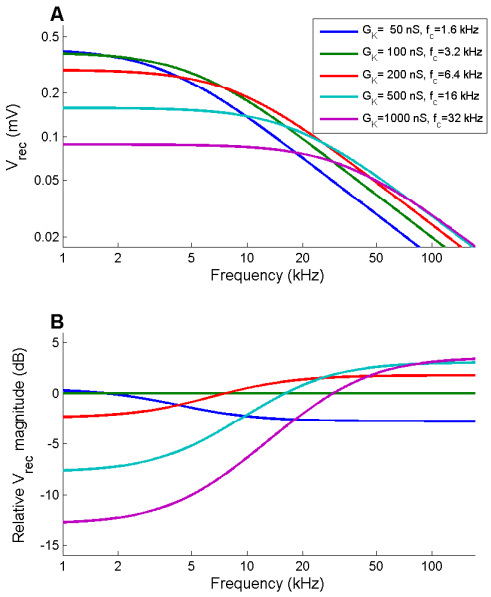

Figure 6.2: The effect of K^+ conductance on the AC receptor potential of OHC. Model calculations based on the OHC equivalent electrical circuit in fig. 6B of Johnson et al. (2011). (**A**) Amplitude of the AC component of the receptor potential across frequency, evoked by a constant 1% modulation depth of MT conductance. Different curves illustrate the effect of lowering the K^+ conductance G_K as indicated in the graph. When G_K is increased beyond 100 nS, the corner frequency f_c increases proportionally, but the effect on the receptor potential above 10 kHz is marginal. (**B**) Data of panel A normalized to the G_K = 100 nS curve. The gain resulting from increasing G_K never exceeds 3.5 dB, and for it to exceed 2 dB, a value of $G_K > 200$ nS is required. (Model parameters: resting value of MT conductance, 60 nS; total membrane capacitance, 5 pF; endocochlear potential, 90 mV; reversal potential of K^+ channels, -75 mV).

Importantly, these corner frequencies were extracted from the mechanical responses of the intact cochlea, so they directly reflect the low-pass character of electromotility itself rather than the electrical properties of OHCs that the circumvention schemes sought to outsmart. With respect to circumvention schemes Vavakou et al. therefore remarked "Our findings do not support such schemes, as the ∼2.5-kHz corner frequency is evident in the motile response itself."

We now turn to the proposal that the RC times at higher CFs are smaller in the base, which allegedly makes them fast enough to provide cycle-by-cycle feedback at CF Johnson et al. (2011). There is experimental evidence against that proposal: Cody and Russell's f_c = 1200 Hz in the 17-kHz OHC, and the data of Vavakou et al. (2019), who measured the corner frequency of motility in the basal turn (CF, 13–25 kHz) and found it to be much lower than the values proposed by Johnson et al. (2011). There is, however, a more fundamental issue at stake here, namely the implicit assumption that a higher corner frequency implies a larger high-frequency drive to electromotility.

Basal OHCs are smaller than apical OHCs, but R and C scale in opposite ways with membrane surface, so size per se does not affect RC times. Capacitance

of bilipid cell membranes is quite universally given by $\sim$1 μF/cm^2 , and OHCs are no exception (Huang & Santos-Sacchi, 1993). This leaves the option of having increasingly leaky OHC toward the base (smaller R , hence smaller RC and larger f_c), as indeed argued by Johnson et al. (2011), based on the observation that the K^+ conductance of OHC increases from apex to base.

Apart from the experimental underpinning, the question is: would this help high-frequency motility? Lowering R makes f_c larger, but does it also boost the amplitude of the receptor potential? After all, time constants and corner frequencies only inform us about the relative amplitudes of low- and high-frequency components.

Fig. 6.2 answers this question. Using the equivalent electrical circuit of the OHC from fig. 6 of Johnson et al. (2011), the AC component of the receptor potential is shown as a function of frequency for a constant stimulation level of the hair bundle (1% modulation of the MT conductivity, well within the linear range of the model). The different curves illustrate the effect of varying K^+ conductance from 50 nS to 1000 nS. The corner frequency increases proportionally, from 1.6 kHz to 32 kHz, but this primarily reflects a loss in low-frequency sensitivity, as illustrated in Fig. 6.2B. The gain at high frequencies is marginal once G_K exceeds 100 nS. It never exceeds 3.5 dB, and for it to exceed 2 dB, a value of $G_K > 200$ nS is required, whereas the highest experimental value in fig. 6 of Johnson et al. is 155 nS. In summary, pushing the corner frequency beyond 3 kHz has little effect on the high-frequency receptor potential. We conclude that corner frequencies and RC times *per se* are not the key to high-frequency motility. It is the membrane capacitance that shunts the high-frequency receptor potential, so perhaps the "RC- problem" should rather be called the "C-problem."

Rectification by OHCs

IHC receptor currents are strongly rectified. This yields a DC component in the receptor potential that follows the envelope of the acoustic stimulus (Russell & Sellick, 1978). The ability to hear frequencies above a few kHz (the phase locking limit of the AN) entirely depends on this rectification. If cochlear compression is based on a regulatory action by OHCs, their receptor current would also need to be rectified in order to produce a "control signal" that regulates the gain. Rectification in OHCs should then occur over the range of sound intensities that evoke compressive growth of the vibrations, i.e., starting below 30 dB SPL and extending to at least 100 dB SPL

in many cases (Robles & Ruggero, 2001). In this section we review the experimental evidence for rectification by OHC.

Electrophysiological data

In the intact cochlea, the resting position of OHC hair bundles is determined by their embedding in the tectorial membrane, so in vitro hair bundle stimulation of isolated OHCs provides little information concerning the extent of rectification. In vivo recordings of OHCs in the basal turn (Cody & Russell, 1985) only showed DC responses to CF tones at high (> 90 dB SPL) sound levels. In contrast, OHC recordings by Dallos and colleagues in the apical and middle turns (reviewed in Dallos (1986) showed a significant DC component at intensities as low as 30 dB SPL. Dallos (1986) discusses potential explanations for the apparent discrepancy with the basal-turn data of Russell and colleagues, including the possibility of abnormal polarization of the OHC in the latter data set.

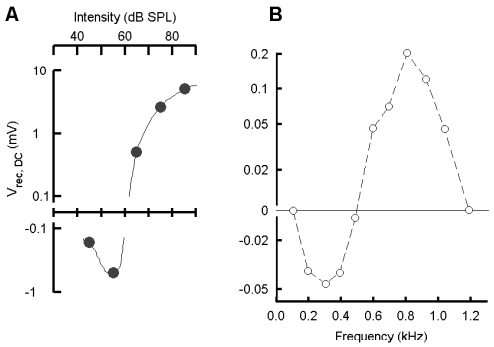

Figure 6.3: DC component of the OHC receptor potential from Dallos' in vivo recordings. (**A**) Data from fig. 9 of Dallos (1985), third turn of the guinea pig cochlea. Stimulus frequency 150 Hz. The polarity of the DC component reversed (from hyperpolarized to depolarized) when sound intensity was increased beyond 60 dB SPL. (**B**) Data from fig. 5 of Dallos (1986), third turn of the guinea pig cochlea. Stimulus intensity, 30 dB. The polarity of the DC component reversed when the stimulus frequency was increased beyond 500 Hz.

An intriguing aspect of Dallos' (Dallos, 1985, 1986) data is the polarity reversal of the DC response, both as a function of stimulus level for a fixed frequency and vice versa. Fig. 6.3 reproduces some of Dallos' observations.

Similar level- and frequency dependent polarity reversals had been observed in the summating potential (SP), the extracellular cochlear response generally attributed to collective OHC receptor currents (Dallos & Cheatham, 1976; Pappa et al., 2019). The in vivo intracellular recordings of Dallos and colleagues suggest that the polarity reversals in the SP are not the result of interference between different groups of OHCs (or between OHCs and IHCs), but that they reflect properties of the DC receptor current of individual OHCs.

Temporal and spectral effects of rectification

Fig. 6.4 illustrates the effect of rectification on waveforms and their spectra.

Rectification of single tones creates a DC component and even harmonics, predominantly the second harmonic (Fig. 6.4B,C). For complex stimuli such as tone pairs ("beats"), rectification also produces an envelope-following difference tone ($f_2 - f_1$) and a sum tone ($f_1 + f_2$), as shown in Fig. 6.4D,E. These 2nd-order distortion products (DP2s) are the generalizations of the DC response and the second harmonic, respectively. The main message of Fig. 6.4 is that DC responses, envelope-following components and difference tones are inseparable aspects of one and the same rectification process.

Also illustrated in Fig. 6.4 is the fact that immediately after the rectifying process (prior to any subsequent filtering) difference tones ($f_2 - f_1$) and sum tones ($f_1 + f_2$) have equal magnitude. This also applies to the single-tone case where the DC component ($f - f$) and the 2nd harmonic ($f + f$) have the same magnitude. These amplitude equalities between DPs having identical "parent primaries" are explained in Meenderink & van der Heijden (2011). Thus, if the magnitudes of such DP2 pairs are unequal in actual recordings, this reveals the operation of a frequency selective process ("filter") subsequent to the rectifying process. For the familiar case of a low-pass filter, this is illustrated in Fig. 6.4C,E.

Rectification in cochlear-mechanics

Evidence for the presence of rectification products in cochlear vibration predates the discovery of OHC motility. Difference tones f2-f1 had been studied in psychoacoustics (Zwicker, 1955, 1979b), and the fact that they can be canceled by acoustic tones at ($f_2 - f_1$) shows that there exist cochlear-mechanical correlates of rectification. Responses to tone pairs recorded from the AN (Kim et al., 1980) and cochlear microphonics (Gibian & Kim, 1982) showed that DP2s propagate from the best place of the primaries to their own best place.

Until recently, most cochlear mechanical studies reported BM vibrations in the base of the cochlea (Robles & Ruggero, 2001). Despite initial claims of tone-evoked DC shifts of the BM (LePage, 1987), DC shifts of the BM were shown to be insignificant, except at very high ($>$ 90 dB SPL) stimulus levels (Cooper & Rhode, 1992). However, large DC shifts were later found in the apical turn of the guinea pig and chinchilla (Rhode & Cooper, 1996; Cooper & Dong, 2003). These data differed in two methodological aspects from the majority of cochlear mechanics data

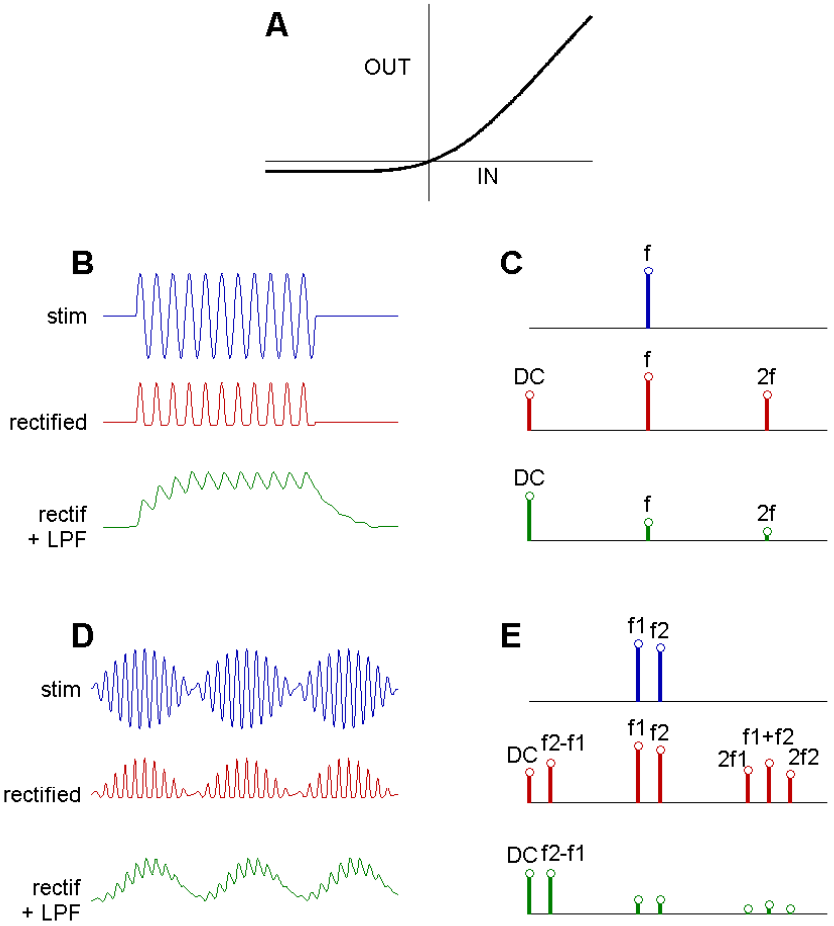

Figure 6.4: Effects of rectification on waveforms and spectra. (**A**) I/O function featuring rectification, i.e., having unequal gains for negative and positive excursions of the input. (**B**) Effect of rectification on a single-tone input. The three rows show the stimulus waveform (blue), waveform after rectification (red) and low-pass filtered (1st-order, $\tau = 2$ tone cycles) version of the rectified waveform (green), which is dominated by the envelope of the tone, with its fine structure reduced to a superimposed ripple. (**C**) Schematic power spectrum of the three waveforms shown in B. Only the dominant spectral components are shown: the stimulus component and the 2nd-order distortion products (DP2s) as indicated. This includes the DC component, which is a DP2 at frequency $f - f = 0$ Hz. (**D**) Waveforms as in B, but now for a "beating" tone pair . The low-pass filtered (1st-order, $\tau = 1.5$ tone cycle) version of the rectified waveform (green) is dominated by the envelope of the original waveform (blue), while its fine structure is reduced to a mere ripple. (**E**) Schematic power spectrum of the waveforms in C. The envelope-following waveform in D is spectrally represented by the combination of DC and the difference tone ($f_2 - f_1$).

known at the time: (1) they were recorded in the apex of the cochlea; (2) the recordings were not obtained from the BM, but from structures inside the organ of Corti.

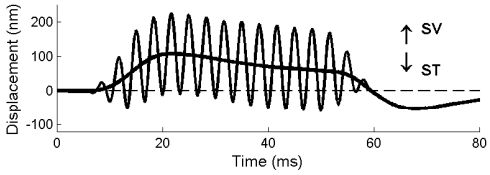

Figure 6.5: Hensen's cell vibrations recorded in the apex of the guinea pig, data from Fig. 1 of Cooper & Dong (2003). The stimulus consisted of 50-ms long 300-Hz tones presented at 70 dB SPL. The waveform is the response averaged over 32 repetitions. Baseline position shifts (bold line) are revealed by low-pass filtering of the waveform. SV = scala vestibuli; ST = scala tympani.

As an example of these apical data, the stimulus-evoked Hensen's cell displacement from fig. 1 of Cooper & Dong (2003) is reproduced in Fig. 6.5. The 300-Hz tone evoked a substantial DC shift towards scala vestibuli that was comparable to the amplitude of the AC response. Figure 9B of Rhode & Cooper (1996) shows DC shifts in the tectorial membrane (CF, 600 Hz). Over a wide range of frequencies (200–1000 Hz), 50 dB-SPL tones evoked DC shifts of ∼2 nm, while 60 dB SPL tones evoked ∼10-nm DC shifts. The DC shifts were typically smaller than the AC displacements and were physiologically vulnerable. The DC shifts reported by Rhode & Cooper (1996) were directed towards scala vestibuli, except for low-intensity tones about an octave below CF, which evoked small displacements toward scala tympani. As noted by the authors, this polarity reversal strikingly resembles Dallos' intracellular OHC recordings in the apex (reproduced in our Fig. 6.3).

The mechanical DC shifts that Rhode & Cooper (1996) and Cooper & Dong (2003) found in the apex were not the only observation that made their data very different from the more familiar basal BM recordings. Another peculiarity of the apical data was the very wide frequency range (spanning several octaves) over which the responses were compressive, compared to the narrow (∼1/2 octave) compressive range consistently found in basal BM recordings. The authors primarily discussed these contrasting behaviors in terms of base-versus-apex differences, and so did later commentators (Robles & Ruggero, 2001). However, recent studies of vibration inside the organ of Corti show that Rhode & Cooper (1996) findings in fact foreshadowed very similar observations in the base of the cochlea: wideband compression (Ren et al., 2016b; Cooper et al., 2018) as well as strong rectification (Vavakou et al., 2019; He & Ren, 2021). As discussed by Cooper et al. (2018) and by Vavakou et al. (2019), the actual dichotomy is not base versus apex, as had previously been assumed, but

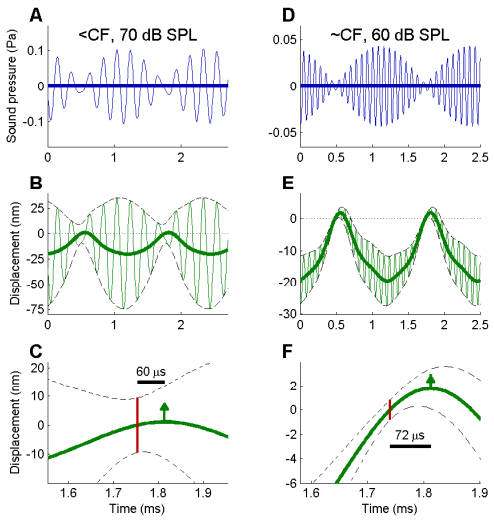

Figure 6.6: Two-tone responses recorded in the OHC area of the basal turn of the gerbil (CF, 13 kHz). (**A**) Stimulus waveform of a tone pair (800-Hz beat rate) centered at 5 kHz. (**B**) Waveform of the mechanical response in the OHC/Deiters' cell area (thin green line), lower and upper envelope (dashed black lines), and rectified ("DC") component obtained by low-pass filtering (2000-Hz cut-off). (**C**) Zoom-in of the response, highlighting the relative timing between the minimum of the peak-to-peak amplitude (red line connecting the envelopes) and the reversal of the rectified component (green arrow). The black scale bar indicates the lag between these two. (**D-F**) Same as A-C, but now for a tone pair centered at CF (13 kHz). Positive displacements in panels B,C,E,F are away from the measurement beam, with approximately equal components along the 3 anatomical axes, being directed toward the apex, modiolus and scala vestibuli. Panels A-C show data from Vavakou et al. (2019). Data in panels D-F are from the same recording location in the same cochlea.

rather BM versus organ of Corti. Thus, there is less reason than existed formerly to postulate essential differences between apical and basal cochlear mechanics, and this is reassuring in view of the basic anatomical homogeneity of the cochlear partition along its length.

The rectified response to two-tone stimuli of fig. 1 of Vavakou et al. (2019), recorded in the OHC area of the gerbil basal turn (13-kHz location), is reproduced in Fig. 6.6A-C, together with another two-tone response from the same cochlea (Fig. 6.6D-F). In both cases, the distance between the tones (the beat rate) was 800 Hz, but the tones were centered at 5 kHz and 13 kHz, respectively. The extent of rectification, as manifested by the relative contributions of the envelope-following and fine-structure response components, is much larger in the 13-kHz case; its envelope-following component (Fig. 6.6E, thick line; 21 nm peak-to-peak) exceeds the fine structure (Fig. 6.6E, thin line; max 16 nm peak-to-peak). As illustrated in Fig. 6.4D, this dominance of the envelope-following component is expected from the low-pass filtering of the rectified waveform reported by Vavakou et al. (2019)(corner frequency for this location: 2.1 kHz). As illustrated in Fig. 6.4B, single CF-tones in the base should then evoke baseline shifts that exceed the AC component, as indeed observed in fig. 1E of He & Ren (2021).

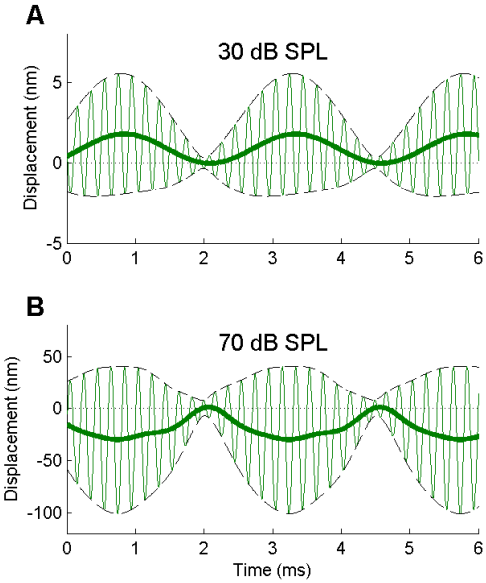

Figure 6.7: Polarity reversal of the rectified displacement component in the OHC area. Same cochlea and recording location (CF, 13-kHz) as in Fig. 6.6. Format as in Fig. 6.6 B. (**A**) Response to a tone pair centered at 5 kHz, beat rate 400-Hz, presented at 30 dB SPL. (**B**) Response to the same stimulus waveform presented at 70 dB SPL.

The lower panels of Fig. 6.6 zoom in on the relative timing of the envelope-following component (solid lines in Fig. 6.6C,F) and the peak-to-peak amplitude of the fine structure, which is the distance between the lower and upper envelopes (dashed lines in Fig. 6.6C,F). The reversal of the envelope-following component (green arrow in Fig. 6.6C,F) is seen to lag the minimum of the peak-to-peak amplitude (vertical red line in Fig. 6.6C,F) by 60 μs and 72 μs, respectively, which is close to one CF cycle. Close inspection of Fig. 6.4D shows that this lag stems from the low-pass filtering of the rectified waveform.

Intriguingly, these lags are comparable to the $\sim$50-μs "reaction time" of cochlear compression reported by Cooper & van der Heijden (2016). That study in the basal turn of the gerbil cochlea analyzed BM responses to fluctuating stimuli and found that cochlear compression was not instantaneous. For slowly varying magnitudes, the time-varying cochlear gain faithfully followed the stimulus envelope, but for more rapid ($>$ 200 Hz) fluctuations the gain started to fall behind the envelope and became smoothed and flattened. This caused an increasing amount of hysteresis in the dynamical input/out functions. The authors analyzed their results in terms of an automatic gain control scheme. The similar values of the delays observed in both studies suggest that the rectified (DC) component in the OHC area (Fig. 6.6) may actually reflect the regulatory input or "control signal" to the gain mechanism that affects BM vibration. Obviously, more experimental work is needed to explore the link between compression and rectification by OHCs.

In our recordings in the basal turn of the gerbil we also found polarity reversals of the rectified displacement component for frequencies well below CF (Fig. 6.7),

similar to the polarity reversals observed in Dallos (1985) intracellular OHC recordings (reproduced here in Fig. 6.3A) and in the cochlear mechanical recordings of the tectorial membrane in the apex by Rhode & Cooper (1996). Although the polarity reversals themselves are as difficult to interpret as they were in the 1980s and 1990s, they represent yet another agreement between apical and basal cochlear mechanics, and appear to confirm Dallos (1986) generalization to basal OHCs of his observations in the apex.

Discussion

We have reviewed old and new findings concerning

- the inherent sluggishness of electromotility
- the minute amplitude of high-frequency AC receptor potentials
- the inability of motility to improve high-frequency sensitivity
- significant rectification by apical and basal OHCs.

They call for the exploration of mechanisms of OHC function other than cycle-by-cycle feedback.

Given the crucial role of OHCs in cochlear compression, we begin by considering what it takes to deal with a large dynamic range. The low end of the large dynamic range of hearing requires a sensitive system, while the high end requires the ability of the same system to cope with high intensities without getting saturated or damaged. Of these two requirements, sensitivity has received most attention. The common view appears to be that sensitivity is something that needs explanation in terms of a "special feature" of the system. In comparison, the ability of the cochlea to operate at high (noise) levels without being deafened - temporarily or permanently - often appears to be taken for granted. It is important to test whether these presumptions are justified. The current level of knowledge of the cochlea allows a quantitative assessment of this question

Soft sounds and damping in the cochlea

Concerning sensitivity, it is often stated that the fluid in the cochlea is too viscous to mediate efficient high-frequency transport, thus necessitating power injection from

an internal source. A popular metaphor invoked to demonstrate the alleged need for power injection is a spring-mass system submerged in water; the viscous drag would damp its resonance. A more specific and quantitative analysis is needed here.

First of all, resistance by itself rarely defines the mechanical behavior of a system. When a pingpong ball and a tennis ball are thrown at the same speed, the tennis ball will travel farther even though it meets with more resistance due to its larger size. In this case the slowdown is determined by the ratio of resistance to mass. An example from electrical engineering illustrates an important general principle. Given a power plant that supplies a town over an electrical power line with a total resistance of 1 Ω, what is the maximum achievable transport efficiency? The answer is that there is no theoretical limit: transport losses can be made arbitrarily small by choosing increasingly higher voltages, thereby reducing the current and the resistive losses. This is why long-distance power lines are operated at very high (> 100 kV) voltages.

The mechanical equivalent of this strategy to achieve efficient transport in the face of friction, is the use of high pressure and small velocity, i.e., a stiff system. This appears to apply to the cochlear base where the BM is stiff and displacements are minute, resulting in BM velocities $\ll 1$ mm/s near hearing threshold (Robles & Ruggero, 2001).

The theoretical possibility to minimize dissipative losses, however, does not mean that the actual system can achieve low-loss performance. Any system has its design constraints. In the example of the electrical power line, safety requirements (e.g. arc flash hazard) limit the use of arbitrarily high voltages. Likewise we can expect there to be cochlear "design constraints" that prevent the use of extremely stiff structures for the processing of high frequencies. A plausible estimate, however, can be made of the minimum attainable frictional losses in the cochlea.

The transport of acoustic energy from stapes to IHC is provided by the traveling wave (Fig. 6.8). The local speed of the transport is the group velocity, which is not constant, but diminishes drastically between the stapes and the peak location (Fig. 6.8C). As illustrated in Fig. 6.8, the transition from the initial, fast part of the wave to the slower part is quite abrupt for soft tones. For low-intensity tones it involves a drop in group velocity by a factor 10 or more (van der Heijden & Versteegh, 2015a; Cooper et al., 2018).

In order to appreciate the functional implications of this abrupt deceleration, note that damping is a measure of energy loss per time unit. For a propagating wave this means that significant losses can occur only in regions where the wave spends enough

time, i.e., where propagation is slow (Lighthill, 1978). In cochlear waves this occurs only over a short (∼0.5-mm) stretch basal to their peak (Ren, 2002; van der Heijden & Cooper, 2018). Although this region (gray bands in Fig. 6.8) is only a small portion of the travel distance from stapes to the peak, it represents the vast majority of the travel *time*. Therefore, the analysis of dissipative losses can be restricted to this slow-wave stretch.

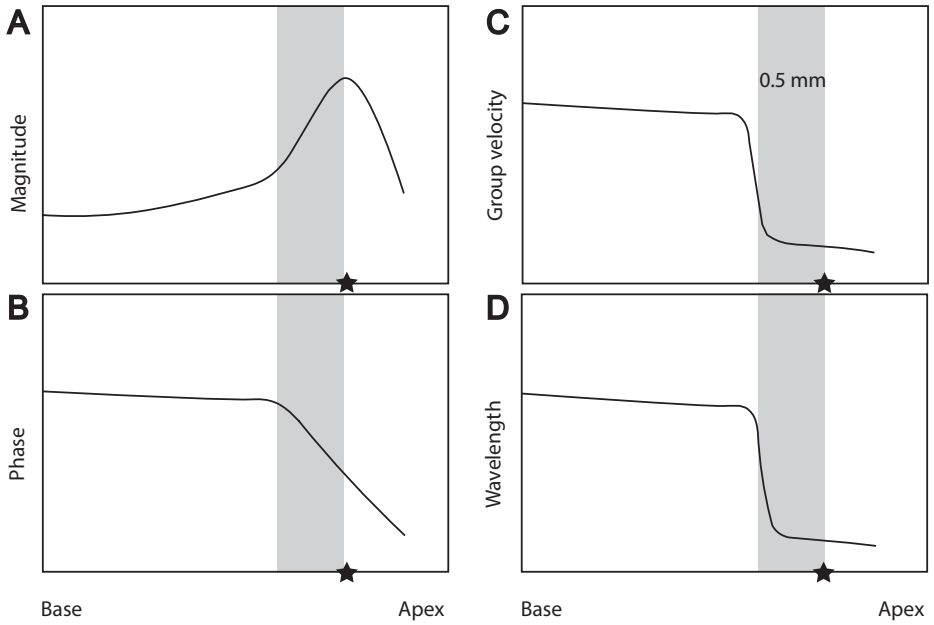

Figure 6.8: Schematic illustration of the characteristics of low-intensity traveling waves that determine their susceptibility to viscous damping (see text). (**A**) Spatial amplitude profile with the peak ("best place") marked by an asterisk. (**B**) Corresponding phase profile showing a sharp bend that signifies an abrupt reduction of the phase velocity at a location about 0.5 basal to the amplitude peak. (**C**) Corresponding diagram of the group velocity (speed of energy transport), which also drops sharply. The energy travels at a low speed over a ∼0.5 mm stretch (gray band in all panels) before reaching the best place. This slow-wave region is where the wave is susceptible to damping. (**D**) Corresponding diagram of the wavelength. The slow region coincides with the short-wave region, where dissipation is dominated by internal damping from fluid viscosity.

The slow-wave stretch coincides with the so-called short-wave portion (Fig. 6.8D) for which the wavelength is smaller than 2π times the diameter of the scalae (van der

Heijden & Versteegh, 2015a). The main characteristic of short waves (also referred to as "waves on deep water") is the negligible fluid motion near the rigid boundaries, leaving the internal friction in the fluid as the only source of attenuation. Damping of short waves on water was analyzed by Stokes in the 1840s, who found the proportional loss of wave energy per cycle to be:

$$L = \frac{16\pi^2\nu}{\lambda^2 f} \tag{6.1}$$

where ν is the dynamic fluid viscosity, λ the wavelength and f the frequency (Lighthill, 1978). Stokes' formula predicts that sea waves with $\lambda = 30$ m (which count as "short waves" whenthe water is deeper than $\lambda/2$ π= 4.8 m) can travel more than halfway around the globe before accumulating a threefold attenuation of their amplitude. The reason for the very low susceptibility to damping of short waves is the low degree of shearing in the fluid motion pattern they evoke.

In order to apply Stokes' formula for the internal friction of the fluid (eq. 6.1) to the energy transport by cochlear waves, we must follow the pace of the transport by counting the number of cycles that fit in the group delay from stapes to the BM location. For low-intensity tones in the base of the cochlea, this amounts to $\sim$7 cycles. In the 16-kHz region of the gerbil, we have $\lambda \cong 300$ μm for 16-kHz tones, and eq. 6.1 gives a proportional energy loss per cycle $L = 7.2\%$. The efficiency of the 7-cycle energy transport from stapes to best place is thus $(1 - 0.072)^7 = 0.6$, which amounts to an attenuation of 2.3 dB. We conclude that low-loss transport of high-frequency energy by traveling waves is well possible, as long as the slow portion of the wave is in the short-wave regime, i.e., as long as the vibrating structures are surrounded by a sufficiently large fluid chamber.

Boundary layers

In hydrodynamic models of the cochlea, damping is either introduced by a free parameter (e.g. Siebert (1974); Steele & Taber (1979a) or, as we did in the previous section, explicitly attributed to fluid viscosity (e.g., Steele & Taber (1979b); Wang et al. (2016). In the latter models, however, the main locus of viscous losses is not the internal friction of the fluid, but a Stokes boundary layer, a shearing motion pattern that arises when fluid moves periodically along a rigid surface with a no-slip condition (Fig. 6.9). Boundary layers have been proposed to occur near the BM (Steele & Taber, 1979b) and between the reticular lamina and the opposing surface

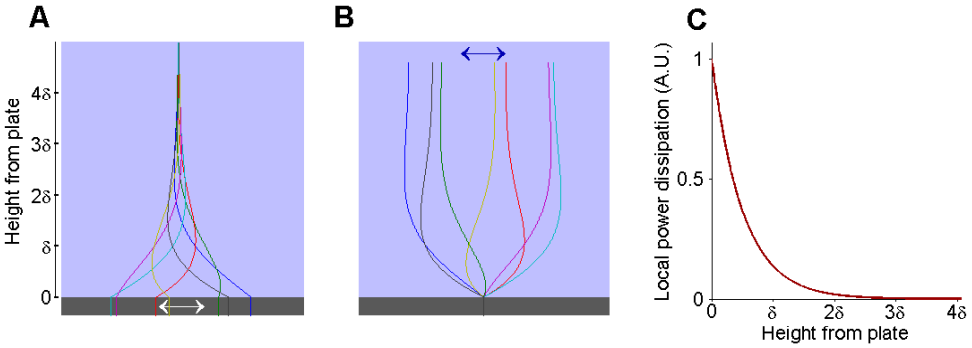

Figure 6.9: (**A**) Fluid (blue) dragged along by a rigid plate (dark gray bar) that oscillates along its surface (double headed arrow). A no-slip condition is assumed at the surface. The curves display the horizontal displacement of the fluid at subsequent instants of the vibration cycle. With increasing distance from the plate, displacement decays exponentially with characteristic depth $\delta = (2\nu/\omega)^{1/2}$, where ν is the kinematic viscosity of the fluid (6.5 ×10 -7 m^2/s for water at 37 °C) and ω the angular frequency. For 10 kHz, $\delta = 4.6$ μm; for 50 kHz, $\delta = 2.0$ μm. (**B**) Complementary situation in which the bulk of the fluid oscillates horizontally (double headed arrow) and the bottom plate is horizontally fixed. This pattern is considered in hydrodynamical models of the cochlea (see text). (**C**) Spatial profile of dissipation caused by the shearing of fluid layers in the boundary layer (equally applicable to the patterns in A and B). The loss falls off exponentially with characteristic depth $\delta/2$. Fluid layers of thickness δ, 2δ and 3δ (measured from the surface of the plate) contribute 86%, 98% and 99.8% of the total viscous loss, respectively.

of the tectorial membrane (Allen, 1990). It is assumed without justification that the material properties and motion of these structures are adequately modeled by the vibration of fluid-immersed, rigid objects along their surface, i.e., the conditions for creating a boundary layer. In a cochlear context, "rigid" means: unable to move by a few nanometers in the longitudinal direction. These are strong assumptions and they are not self-evident. Boundary layer losses can be reduced with simple means. Lubrication, a method abundantly used in biological systems, can minimize damping by simply replacing water by a less viscous substance in the thin (< 5 μm above 10 kHz) layer where shear motion occurs [2]. Furthermore, neither the BM nor the tectorial membrane are rigid structures like the beams featuring in theoretical

[2]Little is known about fluid composition in the subtectorial space and its viscosity, but the tectorial membrane has a glycocalyx layer (Takumida et al., 1988) similar to the mucus layer on fish scales that serves as a drag-reducing agent during swimming (Videler, 1993)

models. Their intricate composition with layers of oriented fibers permits elastic deformations that can soften the transition between their own motion and that of the adjacent fluid, thereby reducing the amount of shear and friction. In fact, the very function of the fiber networks may well be to minimize shear. Reduction of viscous drag is of major importance in industrial transport and processing of fluids, and the extensive engineering literature on this topic (e.g., Bushnell (1990)) describes many methods to reduce viscous drag, including lubrication, surfactants, microbubble injection, suspension of polymers and the use of compliant walls.

Very little is known about the (passive) viscoelastic properties of the intact organ of Corti on a nanometer scale. Modeling this delicate organ as a system of standard elastic plates and rigid rods immersed in water might provide a crude approximation of their potential behavior, but cannot be claimed to be physiologically realistic or accurate. These biological structures serve a highly specialized function and must be expected to have adapted to their task. If one nevertheless insists on modeling the BM as an elastic plate with a rigid surface, the proportional loss per cycle from the boundary layer is:

$$L_{\mathrm{BL}} = \frac{\pi^2 \delta}{\lambda} \tag{6.2}$$

where δ is the boundary layer thickness (see Appendix). For the 16-kHz wave considered in the previous section, δ= 3.6 μm, and this would give a 3.8-dB boundary loss on top of the 2.3 dB from internal friction, yielding a total loss of 6.1 dB. This is for two-dimensional (2D) waves; for 3D waves the boundary losses will be smaller because the area-to-volume ratio is smaller (i.e., less boundary area per fluid mass).

The second aspect in which our analysis of energy transport differs from most cochlear models is the abruptness of the transition between fast and slow propagation of low-intensity waves (Fig. 6.8). This abruptness, a key ingredient of our analysis, is an experimental fact (Kim et al., 1980; Ren et al., 2011b; van der Heijden & Versteegh, 2015a; van der Heijden & Cooper, 2018), but it is not reproduced by prevailing hydrodynamic models. Even in Steele & Taber (1979b) who analyzed strongly dispersive 3D waves, the transition is smooth and fails to reproduce the sharp kink observed in measured phase curves (e.g. fig. 3 of Kim et al. (1980)). In our opinion, this intriguing aspect of cochlear waves deserves more attention from experimenters as well as modelers. An elementary waveguide model (van der Heijden, 2014) offers a potential mechanism of the sharp deceleration, but its relevance to cochlear mechanics is presently unclear.

High intensities and the harnessing of damping

We now turn to the other end of the dynamic range: the processing of high-intensity sounds. For this task the cochlea urgently needs lots of damping. To demonstrate this, we evaluate what would happen if all the energy of a 90-dB-SPL tone would make it to its tonotopic place. This is a straightforward calculation based on data on BM stiffness and group velocity of the traveling wave (for details, see van der Heijden & Versteegh (2015a), where an independent computation based on fluid inertia is shown to match it to within 1.7 dB). Traveling waves satisfy a proportionality relation $A^2 = \gamma P$ between energy flux P and the square of the displacement amplitude A. The coefficient γ is a metric of the compliance. For the 16-kHz region of the gerbil cochlea $\gamma = 4.8 \times 10^{-5}$ m·s/N. A 90-dB-SPL tone at 16 kHz provides an acoustic power input into the gerbil cochlea of ∼6.7 μW. If all of this acoustic power would travel to the 16-kHz place, the wave amplitude would be 564 nm – an extremely destructive vibration amplitude in the basal turn. In reality the displacement is ∼11 nm (Ren et al., 2011a). Thus in the actual gerbil cochlea only $(11/564)^2$ or 0.04% of the acoustic power of the 90-dB-SPL tone reaches its transduction site. The remaining 99.96% of the acoustic energy entering the cochlea must be dissipated in the ∼0.5-mm region just basal to the 16-kHz place where propagation has slowed down. Such very high rates of dissipation suggest that the system is specifically equipped to absorb mechanical energy – when needed.

The 0.04% of the acoustic power that does reach the transduction site amounts to 2.5×10^{-9} W. This number is directly derived from experimental data of BM displacement, group velocity and BM stiffness, and does not depend on any theoretical assumptions other than wave propagation. It is important to realize that the cochlear response remains strongly compressive well beyond 90 dB SPL. In order to explain this high-SPL compression in terms of the customary "saturating amplifier" one would have to postulate that (1) most of the 2.5×10^{-9} W is generated by OHCs (otherwise the amplifier would already be exhausted); (2) prior to being amplified, even less than 0.04% of the acoustic power reaches the onset of amplification, that is, more than 99.96% is lost on the way. The first postulate is hard to reconcile with estimates of maximum power output of OHCs, which are in the order of 10^{-14} W (Wang et al., 2016), 4 to 5 orders of magnitude smaller than the experimentally determined power of the wave. The second postulate cannot be rejected on the basis of first principles, but we find it difficult to see the functional benefits of a scheme that first discards more than 99.96% of the acoustic power and then mechanically amplifies the tiny residual

in order to realize the desired magnitude. To paraphrase Ray Meddis, it seems odd that the system is amplifying the signal in order to attenuate it.

At lower intensities the net loss is less, and one is naturally led to consider a feedback scenario in which the amount of local damping is continually regulated to suit the intensity of the spectral components processed in the region in question. In engineering terms, this is a multi-band automatic gain control operating in the negative-gain range. OHCs are well equipped to play a central role in it. They sense the local excitation with their hair bundles. By rectifying and low-pass filtering their receptor currents they provide a temporally integrated metric of local excitation. By changing their length or stiffness accordingly, they can regulate the local impedance of the adjacent structures. In other words, OHCs have what it takes to cope with a large dynamic range. It is unlikely, however, that the OHCs themselves are the main absorbers, because when OHCs are damaged or absent, the affected portion of the cochlea is known to fall into the high-SPL, high-resistance state [3] (Ryan & Dallos, 1975). So it seems more likely that OHCs regulate the amount of dissipation of adjacent structures.

The earliest instance of a model based on regulated damping (Allen, 1980) predated the discovery of OHC motility and sought to explain nonlinear damping in terms of variable OHC bundle stiffness. The concept of nonlinear damping, however, is more fundamental than specific hypotheses concerning its anatomical correlate. Thus from a wider perspective, the proposal by van der Heijden & Versteegh (2015a) that OHC length changes regulate local damping, perhaps by changing the impedance of the Deiters' cell layer (Cooper et al., 2018), falls in the same category as Allen (1980) model.

An attractive feature of regulated-damping schemes, also discussed in Versteegh & van der Heijden (2013), is the clever use of slowly propagating waves to realize strong compression with minimal means: friction causes exponential decay, so a slight regulation of the damping coefficient (the exponent of the decay) suffices to accumulate a considerable loss over the region of slow propagation. Instead of counteracting friction, electromotility carefully regulates it. This interpretation puts both the traveling wave and its unusual dispersion properties into a clear functional framework.

[3] This is reminiscent of the dead man's brake in trains.

Appendix: viscous loss in the Stokes boundary layer of 2D waves

Here we derive the viscous damping of 2D short waves caused by a Stokes boundary layer at its surface, i.e., arising from a no-slip surface that is completely rigid in the longitudinal direction. This is a common assumption in cochlear models, even though there is no compelling reason to assume that it holds for the BM. Note that the ability of the BM to mediate waves does not depend on this assumption; the only necessary condition for wave propagation is elasticity in the transverse direction.

The boundary layer is assumed to occur at the side of the surface that faces the freely moving fluid, to be identified with the scala tympani side of the BM. The derivation is based on the analysis of fluid waves in chapters 2 and 3 of Lighthill (1978). Denoting the amplitude of the transversal velocity of the surface by U, the time-averaged kinetic energy T per unit area is

$$T = \frac{\rho\lambda U^2}{4\pi} \tag{6.3}$$

with ρ the specific mass of the fluid and λ the wavelength, and where it is taken into account that the mass of the wave is twice that of ordinary water waves, which have air on one side. The total (kinetic + potential) energy per unit area is $2T$. For short waves, the trajectory of the fluid particles is circular, so the amplitude of the longitudinal component of the fluid motion just outside the boundary layer (i.e., the sliding motion that evokes the boundary layer) is also U. The amplitude F of the force per unit surface area exerted by the fluid on the surface (and vice versa) is:

$$F = \rho U\sqrt{2\pi f\nu} \tag{6.4}$$

with f the frequency and ν the kinematic viscosity of the fluid. This force leads the fluid velocity by $\pi/4$ radians (equal inertial and resistive contributions). The amplitude F_{R} of the resistive component is therefore:

$$F_{\mathrm{R}} = F/\sqrt{2} = \rho U\sqrt{\pi f\nu} \tag{6.5}$$

The rate of loss R is the time-averaged product of resistive force F_{R} and velocity U:

$$R = \frac{1}{2}\rho U^2\sqrt{\pi f\nu} \tag{6.6}$$

The proportional loss per cycle, L , becomes:

$$L = \frac{R}{2Tf} = \frac{\pi^2}{\lambda}\sqrt{\frac{\nu}{\pi f}} = \frac{\pi^2 \delta}{\lambda} \tag{6.7}$$

with δ the thickness of the Stokes boundary layer.

Chapter 7

General Discussion

The experimental chapters of this thesis concern the micromechanical responses of hearing organs to sound. Using optical coherence tomography (OCT) vibrometry, we studied the micromechanical responses within the mammalian Organ of Corti (**Chapter 2**) and the insect crista acoustica (**Chapter 3**) and we report distinct vibration modes within the organs. By measuring vibrations from two different angles, we disentangled the elliptical motion within the crista acoustica (**Chapter 4**). Additionally, we measured the corner frequency of OHC motility in vivo at the base of the mammalian cochlea (**Chapter 5**). A combined study of measurements performed by us and other colleagues reveals that the OHCs act a regulators rather than amplifiers of the cochlea's mechanical responses (**Chapter 6**).

OCT vibrometry in the mechanics of hearing organs

The measurement of sound-induced vibrations in hearing organs in vivo is a challenging experimental procedure. The magnitude of the vibrations is quite low, in the range of nanometers, even picometers, while the audible frequencies range from few Hz up to hundreds of kHz. Additionally, hearing organs are often deep-seated, and invasive surgery is needed in order to expose them optically. A further challenge is to maintain the function and sensitivity of the hearing organ. The exposed mammalian cochlea is very susceptible to hearing loss induced by surgery related damage, anoxia and cooling.

Before the advancement of OCT, experimenters used LDV to measure sound-induced vibrations in hearing organs. LDV is a very sensitive vibration measurement technique that lacks depth resolution. As a consequence, the measured structure had to be superficial and directly accessible to the recording beam. LDV measurements were performed on the surface of a structure, if it was sufficiently reflective. In the cochlea studies, due to low reflectivity of the measured structures, vibrations were measured on reflective beads that landed on the structure of interest. For measurements in

the cochlear base (*round window approach*), these beads were introduced into scala tympani through a tear of the round window membrane. In that case, the reflective beads landed on the BM, restricting the measurement site there. In few experiments, measurements were performed on the apex of the cochlea. In that case, the bone was opened, reflective beads were introduced into scala vestibuli and the bone was resealed with a cover slip. In this arrangement, the reflective beads landed on Reissners' membrane or, after making a small tear in this membrane, on structure of the organ of Corti such as Hensen's cells and the tectorial membrane (Cooper & Rhode, 1995). The basal approach is less invasive, as it does not involve bone drilling, and it was preferred by most experimenters. Consequently, the cochlear vibrometry datasets were dominated by basal BM measurements (Robles & Ruggero, 2001). Insect hearing organs have also been studied using LDV techniques. Due to the lack of depth resolution, vibrations were measured primarily on the surface of the tympana of tibial hearing organs, on the CC of the CA after surgical removal of the dorsal cuticle, or on the antenna of antennal insect hearing organs.

OCT vibrometry allows for depth resolution, and for that reason, vibration measurements can be obtained from structures within hearing organs in a minimally invasive manner. It is now possible to obtain measurements of the OHC region in the base of the cochlea and of the BM in the apex of the cochlea, as the OoC can now be imaged through the bone of the cochlear capsule (for an overview of OCT measurements in the mammalian cochlea look into Olson & Strimbu (2020)). Another advantage is that the experimenter is no longer bounded to the use of reflective beads, and can choose more freely the measurement site. Utilizing this liberty, experimenters can construct vibration maps of cross sections of the organ of Corti, and also follow the propagation of the travelling wave longitudinally across the cochlea. That way the micromechanics of the hearing organ can be described in detail. More importantly, it is now possible to experimentally test the predictions of cochlear models concerning the mechanical responses of structures within the organ of Corti. In particular, the role of the OHCs in cochlear function is still unknown, and OCT vibrometry allows us to measure their mechanical responses in vivo. Finally, applying the same technique to the insect tibial hearing organs, we can measure simultaneously the tympana, the DW and the CC. It is now possible to test model predictions for insect hearing organs, and to begin answering long standing scientific questions, for instance, what drives transduction in the CA.

Vibration modes inside the Organ of Corti

In the last decade, several research groups have reported measurements of structures within the OoC. In the literature there are data reported for the Reticular Lamina (RL) from Ren's group (using scanning heterodyne low-coherence interferometry in gerbils and mice, (Ren et al., 2016b; He et al., 2018; Ren & He, 2020)), the OHCs and the RL from the Oghalai group (volume OCT vibrometry, or VOCTV, in mice: Lee et al. (2016); Dewey et al. (2019, 2021)), the so called hotspot region (OHC-DC region) from the Van der Heijden group (SD-OCT in gerbil, **Chapter 2**, Cooper et al. (2018),**Chapter 5**, Vavakou et al. (2019)) and Olson group (SD-OCT in gerbil, Fallah et al. (2019); Strimbu et al. (2020); Strimbu & Olson (2021)). All these measurements, irrespective of the claimed recorded site, share similar response characteristics that are quite distinct from the BM. Finally, the BM measurements acquired via SD-OCT, VOCTV and scanning heterodyne low-coherence interferometry are consistent with the bulk of LDV data that were acquired the previous decades.

The BM mechanical responses are sharply tuned and show compressive growth in a narrow frequency band ranging from 1/2 octave below the local characteristic frequency (CF) to the upper limit of excitation slightly above CF. In contrast, the mechanical responses from the OHC area are characterized by wider tuning (tail to peak magnitude difference), compressive responses at frequencies down to many octaves below the CF and hypercompression (nonmonotic growth) near and above the CF at high SPLs (**Chapter 2**). Additionally, the low-frequency tail of the HS responses can be subjected to suppression (Dewey et al., 2019), which is never observed on the BM. Finally, the mechanical responses of this region are found to be highly rectified even at low SPLs, which is not the case for the BM mechanical responses (**Chapter 5**, Vavakou et al. (2019); Ren & He (2020)). All these findings are consistent among different research groups, also when using different OCT vibrometry technical approaches.

A recurring discussion in the field of cochlear mechanics is whether the base and the apex of the organ have different mechanical responses, perhaps mediated by different mechanisms. Some have even expressed the question whether there are two components in the cochlea, one for low frequencies and one for high frequencies (Ashmore, 2020). Partially, this debate was fueled by the discrepancy between LDV data acquired from the base and the apex, respectively. It is important to note that in the era of LDV recordings, experimenters measured vibrations of the BM at the cochlear base

through the RW membrane, and, in a few cases of apical measurements, vibrations were recorded from the Hensen's cells and the tectorial membrane through an opening at the apex of the cochlea (Cooper & Rhode, 1995; Rhode & Cooper, 1996; Cooper & Dong, 2003). The latter study reported highly rectified mechanical responses, that showed broader tuning. With OCT, we can now have data from both the BM and the OHCs, covering both the base and the apex of the cochlea. Rectification, previously thought to be apex specific, has now been found to be rather OHC-region specific. It is now also possible to report gradients of BM and OHC mechanical responses along the longitudinal axis, and examine what is the micromechanical process that shapes the input to the IHCs.

Recordings of the AN reflect the input to the IHCs. For measurements at the base of the cochlea, the tuning of AN recordings closely resembles the BM. Recent OCT data from the apex of the cochlea report a low-pass filter mechanical behavior of the recorded site (Recio-Spinoso & Oghalai, 2018b,a; Dong et al., 2018), in contrast to the bandpass characteristics of AN fibers that innervate the apex. Interestingly, the selection of the location from which the recordings are further analyzed is commonly based on a criterion of maximum displacement, which often falls within OHC region. When asked in a conference, Recio-Spinoso & Oghalai (2018a) stated that the BM also shows low-pass characteristics. Still, systematic mechanical exploration of the BM in the apex of the mammalian cochlea in low-frequency hearing animals is missing in the literature. These data would be necessary in order to relate the broad tuning of the AN at low frequencies with the micromechanics of the organ of Corti, and further investigate the base versus apex discrepancies.

Existing models have mostly focused on explaining the BM data under the assumption that the OHCs push and pull the BM on a cycle-by-cycle basis (Ramamoorthy et al., 2007). The numerous discrepancies between OHC and BM vibrations revealed by OCT recordings were not anticipated by this line of modelling. (Namely, the asymetrically wider tuning, the low tail non-linearities, strong rectification and hyper-compression of the OHC mechanical responses). It is crucial to explore other lines of modelling than cycle-by-cycle amplification to explain the discrepancies between the BM and the OHCs. In other words, we now have the tools to generalize the base-vs-apex debate, or the BM-vs-OHC debate that stems from fragmented observations, and rethink our views of the function of the OHCs in the cochlea.

Micromechanical exploration of Hearing organs

The study of micromechanical motion of hearing organs in vivo has long been hampered by the restrictions of vibration measurements to the surface of the recorded structure. For that reason, until recently, it has not been possible to describe the exact mechanism that drives transduction within a hearing organ. The advancement of OCT allows to measure in-depth vibrations and describe the relative motion of recorded structures. The exploration of different directions of motion of the recorded structures remains challenging.

In **Chapter 2** we report vibration modes within the mammalian cochlea. Additionally, we measure the mammalian cochlea from two different viewing angles and we report strong suggestions of longitudinal motion. Similarly, in **Chapter 3** we report vibration modes within the insect crista acoustica, and in **Chapter 4** we utilize the anatomical properties of the insect leg to measure the same structures from two different angles using a mirror. Following this elaborate method, we manage to describe the sound induced elliptical motion within the insect crista acoustica in detail. The two hearing organs share similar properties (tonotopy, travelling wave) and comparative aspects of the above mentioned chapters facilitate progress in the understanding of hearing organs.

The Crista Acoustica

The hearing organ of the bushcricket *Mecopoda elongata* is an ideal system to study sound-induced micromechanical motion, as it is located superficially in the front tibia, and, thus, very accessible to imaging. In **Chapter 3**, we used OCT vibrometry to measure sound-induced vibrations on the tympana and within the crista acoustica. The bushcricket *Mecopoda elongata* relies on only 45 sensory units to hear a wide range of frequencies (2-80 kHz). Additionally, this hearing organ can support a travelling wave and is organized in a tonotopic manner.

Using OCT-vibrometry for the first time in insect hearing organs, we report that the two tympana move in an antiphasic manner. Our results corroborate previous findings by Bangert et al. (1998). We managed to measure the two tympana simultaneously, thus avoiding any effect that rotating the preparation can have on the microacoustical environment. More importantly, our results show that the septum within them moves in phase with the posterior tympanum. The two tympana act as a lever that squeezes in and out the sensory epithelium, in a frequency-dependent manner. As the CA are

located on the DW, towards the anterior tympanum, the above-mentioned motion is close to the transduction site. Transduction is reported to take place at the sensory dendrite, which is located between the DW and the CC (Yack, 2004). We were able to measure vibrations on the structures that surround the transduction site across the dorsal-ventral axis (the CC and the DW ventrally to it). The tuning of the two structures differed consistently across the whole length of the hearing organ. Interestingly, the vector difference of the motion of the two structures was more sharply tuned than the individual structures, resembling the individual sensory unit tuning in that respect.

The different tuning across the two structures can be a result of different 3D geometrical realizations of the overall motion that our measuring technique misrepresents because of the projection onto the measurement beam. To disentangle different directions of motion in the CA, we measured vibrations from two different directions, using a mirror (**Chapter 4**). It is possible to do that in the bushcricket, owing to the accessibility of their hearing organs. Indeed, we report that the recorded structures are moving in an elliptical manner, along the two directions of motion that we were able to disentangle. Finally, we report the relative motion of the two structures in 2D. Interestingly, this motion is more sharply tuned than other motions and is a candidate to drive transduction. Mhatre et al. (2021) also report elliptical motion of the DW of the western tree cricket. However, in their measurements, they rotated the preparation without registering their measurement site, so it is uncertain whether they measured the same structure after rotating the preparation. Given our observations in the bushcricket, it is well possible that elliptical motion also occurs in the hearing organ of the western tree cricket, but the above-mentioned results are not conclusive.

The use of OCT in the insect ear is very promising for revealing the mechanisms that underlie transduction in the insect hearing organ and for describing the different directions of motion that sound elicits in the hearing organ. In the current study, we did not explore how the elliptical character of motion changes with different sound intensities, and this should be studied in the future. Also, it is necessary to repeat paired neural and mechanical measurements, like the ones by Hummel et al. (2016). These authors report that the tuning of the sensory unit is narrower than the mechanical tuning. Additionally, they report that the relative frequency tuning of the mechanical and neural measurements changes in a frequency-dependent manner. In our measurements, the relative motion is tuned to higher frequencies than the CC mechanical measurements, and that is consistent with part of their data. It is possible

that the longitudinal direction of motion further shapes the mechanical tuning, but we were not able to disentangle it with the current technique. When relating neural data to mechanical data, one should aim at measuring the overall motion (magnitude and direction). If that is not technically possible, it is necessary to report the direction of motion of the recording beam in terms of the anatomical axes, and discuss the results accordingly.

Finally, the bushcricket hearing organ can be a model for the micromechanical exploration of other hearing organs. Already, the report of sharply tuned relative motion, and the disentanglement of motion along two anatomical axis is successful. These aspects of micromechanics have not been studied extensively in the mammalian cochlea. Additionally, they have not been implemented in models of hearing organs, and this is a challenge worth taking in the future.

Longitudinal motion in the mammalian cochlea

Our micromechanical measurements of the mammalian cochlea strongly suggest elliptical motion along the longitudinal direction of the organ, in the region of the OHCs. In **Chapter 2** it is pointed out that elliptical motion is expected to be frequency dependent, and that fluid dynamics predicts that the longitudinal component is more pronounced at low frequencies. The anatomy of the hotspot region (Edge et al., 1998) is well consistent with the notion that it supports a longitudinal component of motion. Combined with the radial motion described by Lee et al. (2016), it becomes apparent that there may exist complex elliptical motion inside the OoC. In contrast, the anatomy of the BM is highly suggestive of a dominant transverse component: the fibers in the BM are continuous and run along the radial direction, and the BM is restrained bilaterally (Slepecky, 1996).

In the literature, overall motion is commonly assumed to be transverse. That is in part because the BM measurements, on which the field has mostly focused, are most likely dominated by transverse motion. In a simplified view where the OHCs push and pull the BM, the transverse component of OHCs motion is relevant for shaping the BM responses, and indirectly, the input to the IHCs. However, with current measurement techniques motion is measured within the OoC, where the anatomy is more complex than the BM. It is crucial to carefully interpret measured motions as the projection of the overall motion onto the measuring beam. Intriguingly, the basal hotspot measurements are quite likely dominated by longitudinal motion at low frequencies (far below the CF of the location), as the measuring beam favors this

motion direction.

In the past, researchers have electrically stimulated the OoC in excised cochleas (Mammano & Ashmore, 1993; Karavitaki & Mountain, 2007), and no longitudinal motion was observed. However, in these measurements there was no travelling wave, as there was no mechanical stimulation. Recently, Jabeen et al. (2020) combined mechanical and electrical stimulation with OCT vibrometry in excised cochlea. Their measurement paradigm does not explore the presence of travelling waves, instead they focus on micromechanics in a cross section of the cochlear partition. Their measurement beam was favoring transverse motion, but their technical approach could be suited to examine micromechanical motions along different directions.

The sluggish OHC

The OHCs are commonly thought to amplify mechanical induced vibrations inside the OoC on a cycle-by-cycle basis. The proposed mechanism is that OHCs change their length following changes in the membrane voltage. These length changes are caused by transformational changes of the protein prestin that are voltage driven. Prestin is found in the basolateral membrane of the OHCs. Power is thought to be injected via OHC length changes that are in phase with the sound-induced mechanical vibrations. When considering the range of frequencies that the OHCs are expected to amplify, the obvious question is how fast can OHCs change their length. As prestin is voltage gated, it follows changes in the receptor potential, which in turn follows the receptor current. However, the receptor potential is shunted by the cell membrane, which has capacitive properties and is expected to act as a 1^{st}-order low-pass filter. In the field of cochlear mechanics, this is referred to as the *RC problem*.

In vitro measurements of OHC corner frequency obtained from isolated OHCs ranged from 480 Hz (Mammano & Ashmore, 1996) up to 1250 Hz (Johnson et al., 2011). One in vivo study (Cody & Russell, 1987) did measure the corner frequency of an OHC in the 17-kHz region of the base of the guinea pig cochlea, and found it to be 1200 Hz, which is 4 octaves below CF. In the absence of further in vivo measurements of the OHC corner frequency in the base of the mammalian cochlea, modelling studies have postulated very high corner frequencies for basal OHCs, up to tens of kilohertz (Johnson et al., 2011).

Using OCT vibrometry, we were able to measure the corner frequency of OHC motility in vivo at the base of the gerbil cochlea for the first time (**Chapter 5**). Our

measurements revealed that the corner frequency of the OHCs is 2.5-3 kHz, which is close to 3 octaves below the frequencies that these cells are expected to amplify (13-25-kHz in our report). Overall, the basal OHCs are quite leaky, but they still have a corner frequency that is in the range of few kHz, which is consistent with the well known electrical properties of their cell membrane.

Recently, Dewey et al. (2021) measured harmonic distortion evoked by single tones in the mouse cochlea. In contrast to our multitone measurements (**Chapter 5**), this method does not yield a definite value of the corner frequency of motility. Nevertheless, they observed a low-pass trend and estimated that the corner frequency of the mouse OHCs in vivo is lower than 4 kHz. They also reported gradual phase differences in the vibrations along the length of the OHCs, which they interpreted as length changes of the OHCs. However, length changes of the OHCs should elicit a 180 degree phase difference between the two ends of the OHCs, which is not the case. Elliptical motion is a more parsimonious explanation of such phase gradients. The overall elliptical motion within the radial and the longitudinal plane is expected to differ along the distance from the BM, one end of the cell being more constrained or hinged than the other, resembling the motion of an elliptical pendulum. Interestingly, Dewey et al. (2021) also reported OHC length changes with subnanometer magnitudes at high frequencies. Even if such length changes were driven by electromotility, it is questionable to which extent these small motility magnitudes can be the underlying cause for sharply tuned responses on the BM.

Apart from the OHC corner frequency, prestin kinetics were also recently shown to be limiting high-frequency OHC motility (Santos-Sacchi & Tan, 2018), which was previously thought to have a corner frequency of 79 kHz (Frank et al., 1999). Overall, the corner frequency of OHC motility is much lower than the frequencies that are sensed at the recording site.

This finding challenges the classical view of cycle-by-cycle amplification. What is then the function of the OHCs? Rectification followed by low-pass filtering, as reported in **Chapter 5** is a very effective way to extract the overall magnitude of the displacement envelope. That is indicative of an automatic gain control mechanism, in which the OHCs sense the overall displacement magnitude and act as regulators by adjusting the local micromechanics to achieve sensitivity control.

The input to the OHCs

When measuring mechanical responses of OHCs to sound stimulation, it is crucial to isolate the active motile response generated by the OHCs from the passive motion that is the result of the propagation of the mechanical energy that is provided by the stimulus. This is achieved in **Chapter 5**, as we are able to spectrally separate the two components of motion. The sound stimulus was carefully designed to maximize the distortions in the response, while minimizing their spectral overlap with the stimulus components. One step of the experimental protocol required the equalization of the relative amplitudes of the individual frequency components that stimulate the OHCs. This amounts to finding the "effective input" to the OHC bundles. In our effort to do so, it was revealed that the OHC input closely resembled the BM displacement. More specifically, the flatter slope of the low-frequency tail of OHC *motion* (when compared to BM tuning) was not seen in the tuning of the *input* to the OHC bundles.

The above mentioned methodology is a minimally invasive in-vivo way to explore the input to the OHCs. OHCs have characteristically V or W shaped stereociliary bundles, which are likely to be excited by longitudinal motion, in contrast to the IHCs. In **Chapter 2** we report strong indications of a longitudinal component in the OHC motion, that is expected to be pronounced towards lower frequencies. However, the BM motion that best resembles the OHC input is dominated by transverse motion. These two observations seemingly contradict each other and it is not easy to find a satisfying explanation. One consideration is that the active motile OHCs response might differ in direction from the passive motion. The former can be defined by the structural properties of the OoC, whereas the latter can be defined by motion of the surrounding fluid. It would be necessary to better describe these motions before further postulations.

Two distinct non-linearities in the OHCs response

The mechanical response of OHCs is characterized by (1) a wideband compressive nonlinearity that is absent on the BM, (compressive low tail), (2) a narrowband nonlinearity centered at the characteristic frequency, similar to the BM (BF peak) and (3) an elevated low frequency tail relative to the BM (elevated tail).

Recently, pharmacological applications of furosemide (Strimbu et al., 2020) and salicylate (Strimbu & Olson, 2021) were performed in vivo in the gerbil cochlea (IV

and RWM administration respectively), combined with OCT vibrometry. Furosemide is known to reduce the endocochlear potential (EP), and salicylate blocks OHC electromotility and reduces OHC stiffness and turgor pressure. In both cases, the BM responses became linear and weakly tuned, whereas the HS responses retained the compressive low tail, while also losing its sharp tuning. The compressive low tail remained after applying furosemide, and the BF peak recovered following the EP recovery. However, after salicylate application, the compressive low tail remained, but both wideband and the BF nonlinearities recovered further on a similar time scale.

These results indicate that there are two distinct non-linearities in the HS responses: a robust, wideband nonlinearity at moderate to high intensities and a vulnerable, narrowband nonlinearity that starts at lower intensities and is centered at the frequency sensed at the recorded region. The latter nonlinearity is familiar from classical BM data. In a sensitive cochlea, the HS combines the two types of nonlinearity.

Interestingly, the elevated low-frequency tail that is part of the OHCs response is resilient to furosemide and salicylate application. Furthermore, it is also reported in pressure measurements, with the pressure probe approaching the OoC from the Scala Media (Kale & Olson, 2015). According to the authors the stria vascularis is damaged and the EP is reduced. However, the elevated pressure at low frequencies in the SM persists, similarly to the results that Strimbu et al. (2020) and Strimbu & Olson (2021) report.

Bringing these observations together, it seems that the two distinct OHC nonlinearities are driven by different mechanisms. The BF peak follows changes in the EP, and it is manifested in a similar manner on the OHCs mechanical response, the BM mechanical response, DPOAEs and the LCM (local cochlear microphonics) (Wang et al., 2019). In contrast, the compressive low-frequency tail is more resilient, as it persists in the OHC mechanical responses and the LCM after the EP drops. The elevated low-frequency tail remains in the OHC response and presumably in the SM pressure after the EP drops, and only disappears post mortem. That indicates that the elevated tail is associated with basic anatomical structural properties of the OoC, irrespective of the EP. It can also be an indication of passive longitudinal motion driven by the fluid motion. Moreover, the joined recovery of low tail and BF peak nonlinearities following salicylate application indicates that the intact mechanical properties of the OoC are a prerequisite for sharp tuning. Finally, pharmacological applications of furosemide and salicylate can affect several aspects of the OoC and the stria vascularis and should not be over interpreted.

The function of OHCs inside the organ of Corti

The exact function and mode of operation of the OHCs inside the OoC is still unclear. After using OCT to measure OHCs in vivo, we now know that they are sluggish and rectified, and that they are characterized by longitudinal motion at low frequencies and demonstrate two different non-linear responses (the low tail compressive wide-band responses and the CF associated sharp tuning). It is challenging to find a theory that unifies all these observations and explains frequency separation and sharp tuning in the cochlear responses.

The OHCs could control IHC input via funneling motion towards the longitudinal or the transverse direction in a frequency-dependent manner. Longitudinal motion is unlikely to be sensed by IHCs, since their stereocilia are perpendicular to the radial axis of the cochlea. That way, low frequency travelling waves can pass from positions that are sensing high frequencies without being sensed by the IHCs. Similarly, near-CF frequencies can be directed towards transverse motion, favoring IHCs stereocilia stimulation. This could be a micro-mechanical process that takes place on top of the passive tuning of the cochlea, and that would still require a functional Organ of Corti.

Following that reasoning, the overall compliance of the cochlear partition to transverse motion may be controlled by an AGC mechanism. The overall gain is then adjusted by an AGC mechanism that senses the local overall magnitude through the rectified, envelope-following component. In that scheme, rectification is a functional necessity for proper cochlear function, and the speed of the suggested mechanism is within the slow time scales of biophysical systems. That could possibly be realized by controlling the rigidity and compliance of the OHCs and the Deiters' cells. If the degree of viscous damping by Deiters' cells depends on this controlled state of compliance, electromotility would function as a resistance regulator.

Considering that losses due to viscous damping are probably negligible at very low sound intensities, the main challenges for the cochlea are to selectively funnel and dissipate mechanical energy that is not supposed to be sensed at that location, and to protect the cochlea from local overstimulation and damaging vibration magnitudes (**Chapter 6**). The next experimental challenge for the mechanics of hearing organs is to perform volumetric 3D vibrometry measurements. By varying the recording angle, it should be possible to reconstruct the overall motion of the measured structures. Some straightforward approaches are rotating the preparation (Lee et al. (2016), preprint by Mhatre et al. (2021)), simultaneous recording using 3 OCT probes placed at different

angle (ongoing work by Brian Applegate and colleagues), or using mirrors (**Chapter 4**) to obtain vibrometry measurements from a varying recording angle. One of the main technical challenges is to register the measured points in space, and ensure that the very same position is captured from different angles. An additional complication is that the refractive index of structures across the varying recording beams may not be consistent. This will distort the image and possibly complicate the consistency of registration across different viewing angles. These measurements have to be performed on consecutive cross sections. The desired spatial resolution should be in the order of a few micrometers, close to the dimensions of the anatomical structures of interest. This requirement will increase the dataset size to a range of many Terabytes. As a consequence, the hardware and software should be optimized for fast data acquisition, processing and storage. Similar technical challenges have been faced by researchers using functional ultrasound to monitor brain activity in vivo. Transfer of technical expertise between the two disciplines could be potentially beneficial.

The above-mentioned volumetric 3D vibrometry measurements would allow us to produce a complete micromechanical description of the OoC vibration modes. Then it will be possible to study the relative motion of structures within the OoC, across different frequencies and sound intensities. If the spatial resolution is sufficient, the mechanical input to the hair cells of the OoC could be determined. It is possible that such measurements will reveal a sharply tuned mechanical response that closely resembles the auditory nerve responses. Using such high-resolution volumetric 3D vibrometry it should be possible to see if the direction of OHC motion differs in a frequency-dependent manner, and to disentangle passive mechanical responses and motile responses of the OHCs. This would be an insightful experimental accomplishment, that could reveal the function of the OHCs in vivo.

English Summary

Insect and mammalian hearing organs mechanically process the incoming auditory stimulus. As a result, incoming frequencies are separated mechanically and are sensed at different locations of the organ. In the mammalian cochlea, additionally, the amplitude of incoming sounds is compressed in order to fit the limited dynamic range of the sensory hair cells. The study of the mechanics of hearing organs was hampered by technical limitations, namely the inability to resolve depth.

Recording vibrations in the OHC region in the base of the intact cochlea was impossible before OCT vibrometry. **Chapter 2** reports sound-induced vibrations in cross sections of the OoC at the base of the gerbil cochlea. Vibration maps are constructed by consecutive vibration measurement, separated by 35 μm, while the cochlea is presented with multi-tone wide-band stimuli covering a wide range of frequencies (0-40 kHz) and SPLs (20-90 dB). The cross sections reveal two different vibration modes within the OoC. The BM is sharply tuned, with a non-linear low frequency tail, and a compressive characteristic frequency region. In contrast, the OHCs and the Deiters' cells define a hotspot (HS) of vibrations with distinct mechanical responses. The HS vibrates with greater magnitudes than the BM, is more poorly tuned, the low frequency tail is elevated and compressive, and responses to near-CF stimuli are hyper-compressive. These results do not fit in a conventional view of the cochlear mechanics, where the OHCs drive the BM in a cycle-by-cycle manner. Additionally, measuring the OoC from different orientations indicates the existence of a longitudinal component of motion, which could partially explain the different vibration modes among the HS and the BM.

Chapters 3 and **4** explore the micromechanics of the bushcricket *Mecopoda elongata* hearing organ, the crista acoustica (CA). The superficial location of the CA in the front tibia of the bushcricket makes it well accessible to OCT vibrometry using a range of viewing angles. In **Chapter 3**, we performed simultaneous measurements on the two tympana, and the septum within them. The two tympana move in an antiphasic manner, and the septum between them grossly follows the posterior tympanum. As a result, the CA that are found dorsally to the tracheal wall, are pushed in and out in a frequency-dependent manner. Next, we measured sound-induced vibrations at two distinct structures within the CA, the Dorsal Wall (DW) and the Cap Cells (CC). Mechanotransduction is thought to take place by stretching of the sensory dendrite among these two structures. We report two distinct modes of vibration within the CA,

with the CC tuned at lower frequencies than the DW. The relative motion among the two structures was more sharply tuned than the individual structures, resembling the neural tuning in that respect. There can be different possible geometrical realizations of the different in tuning among the DW and the CC. Namely, different directions of motion can take over the overall structure motion in a frequency-dependent manner. This study points out that one measurement direction is not sufficient to disentangle the different components of motion. In **Chapter 4** we measure vibrations from two different directions on the DW and the CC, using a mirror, utilizing the superficial positioning of the CA. Our results reveal elliptical motion on both the DW and the CC. The CC motion is more tilted and more elliptical. Finally, the relative elliptical motion among the two structures is more sharply tuned than the individual structures.

In **Chapter 5** we measure the OHC motility corner frequency in vivo for the first time in the base of the cochlea. Using OCT vibrometry and narrowband multi-tone stimuli at frequencies up to 10 kHz, we were able to spectrally isolate a rectified component of the OHC motile response, which in turn allowed us to accurately measure the low-pass transfer function of in vivo OHC motility. We report corner frequencies of 2.5-3.1 kHz in the 13-25-kHz region of the cochlear base. We conclude that OHC motility is too sluggish to amplify high-frequency vibrations in a cycle-by-cycle manner. Instead, rectification followed by low-pass filtering is indicative of an automated gain control mechanism.

The OHCs are often thought to amplify vibrations in a cycle-by-cycle manner, and thus, improving the sensitivity of the sensory organ. **Chapter 6** challenges this assumption, extending the findings of **Chapter 5**. Cycle-by-cycle amplification is hampered by sluggishness and rectification in the OHCs. It is shown that, instead of amplifying the incoming acoustic energy, carefully controlled damping is actually useful for the local regulation of sensitivity to prevent overstimulation and avoid damaging levels of vibration evoked by high-intensity stimuli.

Samenvatting

In de gehoororganen van insecten en zoogdieren vindt een mechanische verwerking van geluid plaats. De binnengekomen frequenties worden mechanisch gescheiden en elk op hun eigen plaats in het orgaan verwerkt. In slakkenhuis van zoogdieren wordt bovendien de amplitude van de geluiden gecomprimeerd zodat ze in het beperkte dynamische bereik van de sensorische haarcellen passen. Het onderzoek naar de werking van gehoororganen was tot voor kort gehinderd door technische beperkingen, met name het gebrek aan scherptediepte.

Voor de komst van OCT (opical coherence tomography) was het niet mogelijk om trillingen te meten in het gebied van de buitense haarcellen (outer hair cells; OHC) in een intact slakkenhuis. **Hoofdstuk 2** beschrijft het patroon van akoestisch opgewekte trillingen in de dwarsdoorsnede van het orgaan van Corti in de basale cochleaire winding van de gerbil. Deze tweedimensionele patronen (vibration maps) worden verkregen door het combineren van opeenvolgende trillingsmetingen op een onderlinge afstand van 35 μm. We gebruikten multitonale geluidstimuli met een groot bereik van frequenties (0-40 kHz) en intensiteiten (20-90 dB SPL). De tweedimensionale data vertonen twee verschillende trillingsmodi in het orgaan van Corti. Het basilaire membraan (BM) is scherp frequentie-selectief, lineair in de laagfrequente "staart" en niet-lineair compressief rond de karakteristieke frequentie. De OHC en Deiterse cellen daarentegen vormen een "hotspot" (HS) van trillingen met een afwijkende mechanische respons. De HS trilt met een grotere amplitude dan de BM, heeft een minder scherpe frequentieselectiviteit en verhoogde laagfrequente staart, en vertoont hypercompressie rond de karakteristieke frequentie. Deze waarnemingen passen niet in de gangbare visie op cochleaire mechanica waarin de OHCs het BM fasisch aandrijven. Door de meethoek te variëren werden bovendien sterke aanwijzingen verkregen voor het bestaan van een longitudinale beweginscomponent, hetgeen een gedeeltelijke verklaring opleverde voor het verschil in trillingsmodi tussen BM en HS.

Hoofdstukken 3 en 4 verkennen de micromechanica van het gehoorgaan (crista acustica, CA) in de sabelsprinkhaan Mecopoda elongata. De ligging van de CA dicht onder de oppervlakte van de voorste tibia ligt maakt haar goed bereikbaar voor OCT trillingsmetingen onder onder een waaier van meethoeken. In **Hoofdstuk 3** voerden we gelijktijdige metingen uit aan de twee tympana en het tussengelegen septum. De twee tympani bewegen in antifase, en het septum volgt ruwweg het posterior tympanum. Hierdoor wordt de CA, die dorsaal van de tracheawand ligt, op

een frequentie-afhankelijke wijze naar binnen en buiten geduwd. Vervolgens maten we akoestisch opgewekte trillingen in twee verschillende structuren binnen de CA, de dorsale wand (DW) en de cap cell (CC). Mechanotransductie wordt verondersteld te berusten op het spannen van de sensorische dendriet tussen deze twee structuren. We namen verschillende trillingsmodi waar binnen de CA, waarbij de CC gevoelig was voor lagere frequenties dan de DW. De relatieve beweging van de twee structuren vertoonde een scherpere frequentieselectieviteit dan elk van de individuele structuren, en heeft dat gemeen met de neurale respons. Verschillende meetkundige scenario's zouden de waargenomen verschillen in frequentieselectiviteit kunnen verklaren. Met name kan de dominante bewegingsrichting afhangen van de frequentie. Uit dit werk concluderen we dat meting onder een enkele hoek niet volstaat om de verschillende bewegingsrichtingen te onderscheiden. In **Hoofdstuk 4** meten we trillingen in de DW en CC vanuit twee verschillende richtingen met behulp van een spiegel, hierbij geholpen door de oppervlakkige ligging van de CA. We vonden een ellipsvormige beweging, zowel in de DW als de CC. De beweging in de CC was meer gekanteld en meer ellipsvormig. De ellipsvormige relatieve beweging tussen de twee structuren tenslotte, vertoonde een scherpere frequentieslectiviteit dan elk der structuren.

In **Hoofdstuk 5** maten we de afsnijfrequentie van OHC electromotility (door de membraanpotentiaal geïnduceerde lengteverandering van OHC). Dit zijn de eerste in vivo metingen van deze afsnijfrequentie. Met behulp van OCT trillingsmetingen en smalbandige stimuli tot aan 10 kHz isoleerden we een gelijkgerichte electromotility component uit de respons, die we vervolgens gebruikten voor een nauwkeurige bepaling van de frequentie-overdracht van de electromotility. We vonden afsnijfrequenties van 2.5 tot 3.1 kHz in de basale winding in de gerbil cochlea met karakteristieke frequenties tussen 13 en 25 kHz. We concluderen dat OHC electromotility te traag is om hoogfrequente trillingen fasisch te versterken. Als alternatief merken we op dat de combinatie van gelijkrichting en een laagdoorlaat filter duidt op een automatische sterkteregeling.

Het wordt vaak aangenomen dat OHCs trillingen fasisch versterken en daarmee de gevoeligheid van het gehoororgaan verbeteren. Deze aanname wordt in **Hoofdstuk 6** kritsch ontleed bij wijze van uitbreiding van **Hoofdstuk 5**. Fasische versterking wordt belemmerd door de traagheid van OHCs en hun gelijkrichtende werking. We tonen aan dat, i.p.v. een mechanische versterking van de binnenkomende akoestische energie, nauwkeurig aangestuurde demping juist nuttig is voor de regulering van de gevoeligheid ter preventie van overstimulatie en schadelijke trillingsniveaus bij harde

geluiden.

PhD Portfolio

Education and Experience:

2017-2022 PhD student at Erasmus MC, Dept. of Neuroscience, Rotterdam

2013-2017 MSc. "Behaviour: From Neural Mechanisms to Evolution", Bielefeld University, Germany.

2007-2013 Degree of Biology, University of Crete, Greece.

Elective Program: Environmental Biology and Management of Biological Resources

Teaching Experience:

2021-2022 Assisting in the supervision of a neuroscience master student

2017-2021 Assisting with workshops for neuroscience master students

2017-2021 Assisting with workshops for medical students

Courses:

Aug 2019 Biology of the inner ear (MBL, Woods Hole, MA, USA)

May 2018 Neurobiology of Hearing (Salamanca, Spain)

Conference contributions:

2021 Association for research in Otolaryncology MidWinter Meeting (Virtual) - Oral presentation

2020 Association for research in Otolaryncology MidWinter Meeting (San Diego, CA USA) - Poster presentation

2019 Association for research in Otolaryncology MidWinter Meeting (San Diego, CA USA) - Oral presentation

Acknowledgments

I would like to express my deepest gratitude to my supervisor, **Marcel van der Heijden**, as he has been the most generous and supportive mentor I could wish for. Your scientific clarity has been a major source of inspiration. Working with you I grew and matured as a person in many different layers, professional and personal. I know that in the future I will look back and recognize valuable parts of myself that were formed during these years.

I would like to thank **Nigel Cooper**, as he is the one who patiently taught me how to do experiments. Your visits have been a highlight of my time in Rotterdam, and a valuable opportunity to experience what high pace scientific progress looks like. Thank you for your kindness and for your generosity when it comes to sharing your expertise.

Jan Scherberich and **Manuela Nowotny**, thank you for a great collaboration and for guiding me through the beauties of the insect world.

I would like to thank the committee members, **Elisabeth Olson**, **Pim van Dijk** and **Johan Pel** for taking the time to evaluate this thesis and for their helpful feedback.

Dear **Gerard Borst**, my promotor, thank you for your support throughout my PhD, your critical comments and your helpful advice.

Yarmo Mackenbach, **Maurits van der Berg** and **Martijn Sierksma**, your support especially at the early stages of my PhD was precious, and you helped me to have a smooth start in the lab. Dear **Aaron Wong** and **Ursula Stalmann** thank you for sharing your wisdom with me!

The last years would not have been the same without the **LISTEN crew - Lorena, Kseniia, Giuseppe, Jonatan, Navid, Yuvi, Francesca, Maurits, Alek**. We were very lucky to have found each other. I am grateful for the support network that we created, and for all the fun times.

I am very grateful to everyone in the Department of Neuroscience and to **Chris de Zeeuw** for supporting a vibrant and stimulating work environment. **Stephanie Dijkhuizen**, **George Smaragdos**, **Sadaf Soloukey**, **Lorenzo Bina**, **Vincenzo Romano**, **Francois Blot**, you have been great colleagues and I am grateful for our time together. Thank you **Devika Narain** for the career advice! **Aleksandra Badura** thank you for your support.

Elise Buitenhuis, **Elize Haasdijk** and **Mandy Mahmoed** thank you helping

out throughout the years.

Peter Bremen, I will miss your spontaneous visits to the lab, and the great discussions. Thank you for all your help these years. **Kostas Kondylidis** it has been a pleasure to collaborate with you!

My dear **Francesca Fiocchi**, this is a journey we began together. I am honored by your friendship and I want to thank you for being my anchor. **Ana Marchidan** I am very lucky to have you in my life. Thank you for all the emotional support and the much appreciated designer services! **Isabella Zampeta**, our spontaneous laughs when we met at the corridor was a great part of my office routine!

Maria Mitkova, and **Fabian Steinbeck**, your help with the layout was precious. You took a great deal of stress off my shoulders!

Apostolis K., **Foteini C.**, **George M.**, **Foteini G.**, **Danai G.** and **Danai P.**, I am very lucky to have found you in the Netherlands. Thank you for the nice time together.

Michalis, **Paschalia**, **Eirini** and **Aris** I am grateful to have you in my life and I thank you for being there for me. **Martina**, thank you for your help with the cover!

My beloved **Kostis** and **Dafni**, these years of my life have been marked by your presence. I am grateful for the family we created in Mathenesserlaan. This house is exploding with memories!

Finally, this chapter would not have been possible without the support of my family. Thank you **Mom**, **Dad**, **Minas** and **Artemis** for always being there for me. Above all, though, I would like to thank my beloved grandma **Mimo** for being a constant reminder that you should always work towards what you wish. Your unorthodox/orthodox attitude towards life has been the greatest manifestation of woman power. I wish you could attend the PhD defense and celebrate that day with me.

Bibliography

Allen, J. (1990). In *The Mechanics and Biophysics of Hearing, Lecture Notes in Biomathematics (eds Dallos, P., Geisler, C. D., Matthews, J. W., Ruggero, M. A. and Steele, C. R.)* (pp. 324–331).: (Springer Verlag).

Allen, J. (1997). Ohcs shift the excitation pattern via bm tension. *Power (Watts/cm2)*, 10(16), 10–10.

Allen, J. and Fahey, P. (1992). Using acoustic distortion products to measure the cochlear amplifier gain on the basilar membrane. *The Journal of the Acoustical Society of America*, 92(1), 178–188.

Allen, J. B. (1980). Cochlear micromechanics—a physical model of transduction. *The Journal of the Acoustical Society of America*, 68(6), 1660–1670.

Ashmore, J. (2008). Cochlear outer hair cell motility. *Physiological reviews*, 88(1), 173–210.

Ashmore, J. (2011). Pushing the envelope of sound. *Neuron*, 70(6), 1021–1022.

Ashmore, J. (2020). Tonotopy of cochlear hair cell biophysics (excl. mechanotransduction). *Current Opinion in Physiology*.

Ashmore, J. F. and Kolston, P. J. (1994). Hair cell based amplification in the cochlea. *Current opinion in neurobiology*, 4(4), 503–508.

Bangert, M., Kalmring, K., Sickmann, T., Stephen, R., Jatho, M., and Lakes-Harlan, R. (1998). Stimulus transmission in the auditory receptor organs of the foreleg of bushcrickets (tettigoniidae) i. the role of the tympana. *Hearing research*, 115(1-2), 27–38.

Bavi, N., Clark, M. D., Contreras, G. F., Shen, R., Reddy, B. G., Milewski, W., and Perozo, E. (2021). The conformational cycle of prestin underlies outer-hair cell electromotility. *Nature*, 600(7889), 553–558.

Bell, J. S. (2004). *Speakable and unspeakable in quantum mechanics: Collected papers on quantum philosophy*. Cambridge university press.

Beurg, M., Evans, M. G., Hackney, C. M., and Fettiplace, R. (2006). A large-conductance calcium-selective mechanotransducer channel in mammalian cochlear hair cells. *Journal of Neuroscience*, 26(43), 10992–11000.

Beurg, M., Goldring, A. C., Ricci, A. J., and Fettiplace, R. (2016). Development and localization of reverse-polarity mechanotransducer channels in cochlear hair cells. *Proceedings of the National Academy of Sciences*, 113(24), 6767–6772.

Brass, D. and Kemp, D. (1993). Analyses of Mössbauer mechanical measurements indicate that the cochlea is mechanically active. *The Journal of the Acoustical Society of America*, 93(3), 1502–1515.

Brownell, W. (1983). Observations on a motile response in isolated outer hair cells. *Mechanisms of hearing*.

Brownell, W. E., Bader, C. R., Bertrand, D., and De Ribaupierre, Y. (1985). Evoked mechanical responses of isolated cochlear outer hair cells. *Science*, 227(4683), 194–196.

Bushnell, D. M. (1990). *Viscous drag reduction in boundary layers*, volume 123. AIAA.

Chen, F. and Nuttall, A. L. (2009). Comment on "Measuring power production in the mammalian cochlea"[curr. biol. 17, 1340 (2007)]. *The Journal of the Acoustical Society of America*, 125(1), 11–14.

Chen, F., Zha, D., Fridberger, A., Zheng, J., Choudhury, N., Jacques, S. L., Wang, R. K., Shi, X., and Nuttall, A. L. (2011). A differentially amplified motion in the ear for near-threshold sound detection. *Nature Neuroscience*, 14(6), 770–774.

Choma, M. A., Izatt, S. D., Wessells, R. J., Bodmer, R., and Izatt, J. A. (2006). In vivo imaging of the adult drosophila melanogaster heart with real-time optical coherence tomography. *Circulation*, 114(2), e35–e36.

Cody, A. and Russell, I. (1985). Outer hair cells in the mammalian cochlea and noise-induced hearing loss. *Nature*, 315(6021), 662–665.

Cody, A. and Russell, I. (1987). The response of hair cells in the basal turn of the guinea-pig cochlea to tones. *The Journal of physiology*, 383(1), 551–569.

Cooper, N. and Dong, W. (2003). Baseline position shifts and mechanical compression in the apical turns of the cochlea. In *Biophysics of the Cochlea: from Molecules to Models* (pp. 261–270). World Scientific.

Cooper, N. P. (2004). Compression in the peripheral auditory system. In *Compression: From cochlea to cochlear implants (eds Bacon, S., Fay, R. R. and Popper, An. N.)*, volume 17 (pp. 18–61). Springer.

Cooper, N. P. and Rhode, W. (1997). Mechanical responses to two-tone distortion products in the apical and basal turns of the mammalian cochlea. *Journal of neurophysiology*, 78(1), 261–270.

Cooper, N. P. and Rhode, W. S. (1992). Basilar membrane mechanics in the hook region of cat and guinea-pig cochleae: sharp tuning and nonlinearity in the absence of baseline position shifts. *Hearing research*, 63(1-2), 163–190.

Cooper, N. P. and Rhode, W. S. (1995). Nonlinear mechanics at the apex of the guinea-pig cochlea. *Hearing research*, 82(2), 225–243.

Cooper, N. P. and van der Heijden, M. (2016). Dynamics of cochlear nonlinearity. In *Physiology, Psychoacoustics and Cognition in Normal and Impaired Hearing* (pp. 267–273). Springer, Cham.

Cooper, N. P. and van der Heijden, M. (2018). Spatial profiles of sound-evoked vibration in the gerbil cochlea. In *To the Ear and Back Again: Advances in Auditory Biophysics, Proc. 13th Mechanics of Hearing Workshop (eds Bergevin, C. and Puria, S)*, number 1 (pp. 080001).: AIP Publishing LLC.

Cooper, N. P., Vavakou, A., and van der Heijden, M. (2018). Vibration hotspots reveal longitudinal funneling of sound-evoked motion in the mammalian cochlea. *Nature communications*, 9(1), 1–12.

Dallos, P. (1984). Some electrical circuit properties of the organ of corti. ii. analysis including reactive elements. *Hearing research*, 14(3), 281–291.

Dallos, P. (1985). Response characteristics of mammalian cochlear hair cells. *Journal of Neuroscience*, 5(6), 1591–1608.

Dallos, P. (1986). Neurobiology of cochlear inner and outer hair cells: intracellular recordings. *Hearing research*, 22(1-3), 185–198.

Dallos, P. and Cheatham, M. A. (1976). Production of cochlear potentials by inner and outer hair cells. *The Journal of the Acoustical Society of America*, 60(2), 510–512.

Dallos, P. and Evans, B. N. (1995). High-frequency outer hair cell motility: corrections and addendum. *Science*, 268(5216), 1420–1421.

Dannhof, B., Roth, B., and Bruns, V. (1991). Length of hair cells as a measure of frequency representation in the mammalian inner ear? *Naturwissenschaften*, 78(12), 570–573.

Davis, H. (1983). An active process in cochlear mechanics. *Hearing research*, 9(1), 79–90.

De Boer, E. (1983). No sharpening? a challenge for cochlear mechanics. *The Journal of the Acoustical Society of America*, 73(2), 567–573.

De Boer, E. and Nuttall, A. L. (2000). The mechanical waveform of the basilar membrane. II. from data to models—and back. *The Journal of the Acoustical Society of America*, 107(3), 1487–1496.

De Vries, H. (1948). Brownian movement and hearing. *Physica*, 14(1), 48–60.

Dewey, J. B., Altoè, A., Shera, C. A., Applegate, B. E., and Oghalai, J. S. (2021). Cochlear outer hair cell electromotility enhances organ of Corti motion on a cycle-by-cycle basis at high frequencies in vivo. *Proceedings of the National Academy of Sciences*, 118(43), e2025206118.

Dewey, J. B., Applegate, B. E., and Oghalai, J. S. (2019). Amplification and suppression of traveling waves along the mouse organ of corti: Evidence for spatial variation in the longitudinal coupling of outer hair cell-generated forces. *Journal of Neuroscience*, 39(10), 1805–1816.

Dong, W. and Olson, E. S. (2009). In vivo impedance of the gerbil cochlear partition at auditory frequencies. *Biophysical journal*, 97(5), 1233–1243.

Dong, W. and Olson, E. S. (2013). Detection of cochlear amplification and its activation. *Biophysical journal*, 105(4), 1067–1078.

Dong, W., Xia, A., Raphael, P. D., Puria, S., Applegate, B., and Oghalai, J. S. (2018). Organ of corti vibration within the intact gerbil cochlea measured by volumetric optical coherence tomography and vibrometry. *Journal of neurophysiology*, 120(6), 2847–2857.

Edge, R., Evans, B., Pearce, M., Richter, C.-P., Hu, X., and Dallos, P. (1998). Morphology of the unfixed cochlea. *Hearing research*, 124(1-2), 1–16.

Emadi, G., Richter, C.-P., and Dallos, P. (2004). Stiffness of the gerbil basilar membrane: radial and longitudinal variations. *Journal of neurophysiology*, 91(1), 474–488.

Fallah, E., Strimbu, C. E., and Olson, E. S. (2019). Nonlinearity and amplification in cochlear responses to single and multi-tone stimuli. *Hearing research*, 377, 271–281.

Frank, G., Hemmert, W., and Gummer, A. W. (1999). Limiting dynamics of high-frequency electromechanical transduction of outer hair cells. *Proceedings of the National Academy of Sciences*, 96(8), 4420–4425.

French, A. S. (1988). Transduction mechanisms of mechanosensilla. *Annual review of entomology*, 33, 39–58.

Gao, S. S., Raphael, P. D., Wang, R., Park, J., Xia, A., Applegate, B. E., and Oghalai, J. S. (2013). In vivo vibrometry inside the apex of the mouse cochlea using spectral domain optical coherence tomography. *Biomedical optics express*, 4(2), 230–240.

Gao, S. S., Wang, R., Raphael, P. D., Moayedi, Y., Groves, A. K., Zuo, J., Applegate, B. E., and Oghalai, J. S. (2014). Vibration of the organ of corti within the cochlear apex in mice. *Journal of neurophysiology*, 112(5), 1192–1204.

Geisler, C. D. and Sang, C. (1995). A cochlear model using feed-forward outer-hair-cell forces. *Hearing research*, 86(1-2), 132–146.

Gibian, G. and Kim, D. (1982). Cochlear microphonic evidence for mechanical propagation of distortion products (f2- f1) and (2f1- f2). *Hearing research*, 6(1), 35–59.

Goblick Jr, T. J. and Pfeiffer, R. R. (1969). Time-domain measurements of cochlear nonlinearities using combination click stimuli. *The Journal of the Acoustical Society of America*, 46(4B), 924–938.

Gopfert, M. C., Briegel, H., and Robert, D. (1999). Mosquito hearing: sound-induced antennal vibrations in male and female aedes aegypti. *Journal of Experimental Biology*, 202(20), 2727–2738.

Graff, K. (1991). Wave motion in elastic solids. (Dover Publications).

Grant, G. (1999). Gustaf retzius and camillo golgi. *Journal of the History of the Neurosciences*, 8(2), 151–163.

Greenwood, D. D. (1996). Comparing octaves, frequency ranges, and cochlear-map curvature across species. *Hearing research*, 94(1-2), 157–162.

Guinan, J. J. (2012). How are inner hair cells stimulated? evidence for multiple mechanical drives. *Hearing research*, 292(1-2), 35–50.

He, D. Z. and Dallos, P. (1999). Somatic stiffness of cochlear outer hair cells is voltage-dependent. *Proceedings of the National Academy of Sciences*, 96(14), 8223–8228.

He, W., Kemp, D., and Ren, T. (2018). Timing of the reticular lamina and basilar membrane vibration in living gerbil cochleae. *eLife*, 7, 1–17.

He, W. and Ren, T. (2021). The origin of mechanical harmonic distortion within the organ of corti in living gerbil cochleae. *Communications biology*, 4(1), 1–11.

Heinrich, R., Jatho, M., and Kalmring, K. (1993). Acoustic transmission characteristics of the tympanal tracheae of bushcrickets (tettigoniidae). ii: comparative studies of the tracheae of seven species. *The Journal of the Acoustical Society of America*, 93(6), 3481–3489.

Hoffmann, E. and Jatho, M. (1995). The acoustic trachea of tettigoniids as an exponential horn: theoretical calculations and bioacoustical measurements. *The Journal of the Acoustical Society of America*, 98(4), 1845–1851.

Housley, G. D. and Ashmore, J. F. (1992). Ionic currents of outer hair cells isolated from the guinea-pig cochlea. *The Journal of Physiology*, 448(1), 73–98.

Huang, G. and Santos-Sacchi, J. (1993). Mapping the distribution of the outer hair cell motility voltage sensor by electrical amputation. *Biophysical Journal*, 65(5), 2228–2236.

Hummel, J., Kössl, M., and Nowotny, M. (2011). Sound-induced tympanal membrane motion in bushcrickets and its relationship to sensory output. *Journal of Experimental Biology*, 214(21), 3596–3604.

Hummel, J., Kössl, M., and Nowotny, M. (2017). Morphological basis for a tonotopic design of an insect ear. *Journal of Comparative Neurology*, 525(10), 2443–2455.

Hummel, J., Schöneich, S., Kössl, M., Scherberich, J., Hedwig, B., Prinz, S., and Nowotny, M. (2016). Gating of acoustic transducer channels is shaped by biomechanical filter processes. *Journal of Neuroscience*, 36(8), 2377–2382.

Hummel, J., Wolf, K., Kössl, M., and Nowotny, M. (2014). Processing of simple and complex acoustic signals in a tonotopically organized ear. *Proceedings of the Royal Society B: Biological Sciences*, 281(1796), 20141872.

Jabeen, T., Holt, J. C., Becker, J. R., and Nam, J.-H. (2020). Active outer hair cell motility can suppress vibrations in the organ of corti. *bioRxiv*.

Johnson, S. L., Beurg, M., Marcotti, W., and Fettiplace, R. (2011). Prestin-driven cochlear amplification is not limited by the outer hair cell membrane time constant. *Neuron*, 70(6), 1143–1154.

Johnstone, J. R., Alder, V. A., Johnstone, B. M., Robertson, D., and Yates, G. K. (1979). Cochlear action potential threshold and single unit thresholds. *The Journal of the Acoustical Society of America*, 65(1), 254–257.

Jonsson, T., Montealegre-Z, F., Soulsbury, C. D., Robson Brown, K. A., and Robert, D. (2016). Auditory mechanics in a bush-cricket: direct evidence of dual sound inputs in the pressure difference receiver. *Journal of the Royal Society Interface*, 13(122), 20160560.

Joris, P. X., Bergevin, C., Kalluri, R., Mc Laughlin, M., Michelet, P., van der Heijden, M., and Shera, C. A. (2011). Frequency selectivity in old-world monkeys corroborates sharp cochlear tuning in humans. *Proceedings of the National Academy of Sciences*, 108(42), 17516–17520.

Kale, S. S. and Olson, E. S. (2015). Intracochlear scala media pressure measurement: implications for models of cochlear mechanics. *Biophysical journal*, 109(12), 2678–2688.

Karavitaki, K. D. and Mountain, D. C. (2007). Imaging electrically evoked micromechanical motion within the organ of corti of the excised gerbil cochlea. *Biophysical journal*, 92(9), 3294–3316.

Kemp, D. T. (1978). Stimulated acoustic emissions from within the human auditory system. *The Journal of the Acoustical Society of America*, 64(5), 1386–1391.

Kemp, D. T. (1979). Evidence of mechanical nonlinearity and frequency selective wave amplification in the cochlea. *Archives of oto-rhino-laryngology*, 224(1), 37–45.

Kiang, N. Y.-S. (1965). *Discharge patterns of single fibers in the cat's auditory nerve.* Technical report, MASSACHUSETTS INST OF TECH CAMBRIDGE RESEARCH LAB OF ELECTRONICS.

Kim, D. (1980). An active cochlear model with negative damping in the partition: comparison with rhodes ante-and postmortem observation. *Psychophysiological, Physiological and Behavioural Studies in Hearing*, (pp. 7–14).

Kim, D. (1986). Active and nonlinear cochlear biomechanics and the role of outer-hair-cell subsystem in the mammalian auditory system. *Hearing research*, 22(1-3), 105–114.

Kim, D., Molnar, C., and Matthews, J. (1980). Cochlear mechanics: Nonlinear behavior in two-tone responses as reflected in cochlear-nerve-fiber responses and in ear-canal sound pressure. *The Journal of the Acoustical Society of America*, 67(5), 1704–1721.

Kössl, M. and Russell, I. J. (1992). The phase and magnitude of hair cell receptor potentials and frequency tuning in the guinea pig cochlea. *Journal of Neuroscience*, 12(5), 1575–1586.

Kössl, M. and Vater, M. (1995). Cochlear structure and function in bats. In *Hearing by bats* (pp. 191–234). Springer.

Lee, H. Y., Raphael, P. D., Park, J., Ellerbee, A. K., Applegate, B. E., and Oghalai, J. S. (2015). Noninvasive in vivo imaging reveals differences between tectorial membrane and basilar membrane traveling waves in the mouse cochlea. *Proceedings of the National Academy of Sciences*, 112(10), 3128–3133.

Lee, H. Y., Raphael, P. D., Xia, A., Kim, J., Grillet, N., Applegate, B. E., Bowden, A. K., and Oghalai, J. S. (2016). Two-dimensional cochlear micromechanics measured in vivo demonstrate radial tuning within the mouse organ of corti. *Journal of Neuroscience*, 36(31), 8160–8173.

LePage, E. L. (1987). The application of a capacitive probe technique for direct observation of electromechanical processes in the guinea pig cochlea. *The Journal of the Acoustical Society of America*, 82(1), 126–138.

Lewis, D. (1974). The physiology of the tettigoniid ear: Ii. the response characteristics of the ear to differential inputs: Lesion and blocking experiments. *Journal of Experimental Biology*, 60(3), 839–851.

Liang, X., Madrid, J., Gärtner, R., Verbavatz, J.-M., Schiklenk, C., Wilsch-Bräuninger, M., Bogdanova, A., Stenger, F., Voigt, A., and Howard, J. (2013). A nompc-dependent membrane-microtubule connector is a candidate for the gating spring in fly mechanoreceptors. *Current Biology*, 23(9), 755–763.

Liberman, M. C., Gao, J., He, D. Z., Wu, X., Jia, S., and Zuo, J. (2002). Prestin is required for electromotility of the outer hair cell and for the cochlear amplifier. *Nature*, 419(6904), 300–304.

Liberman, M. C. and Klang, N. Y. (1984). Single-neuron labeling and chronic cochlear pathology. iv. stereocilia damage and alterations in rate-and phase-level functions. *Hearing research*, 16(1), 75–90.

Lighthill, J. (1978). *Waves in Fluids Cambridge University Press Cambridge*. Cambridge University Press.

Lighthill, J. (1981). Energy flow in the cochlea. *Journal of fluid mechanics*, 106, 149–213.

Lighthill, J. (1992). Acoustic streaming in the ear itself. *Journal of Fluid Mechanics*, 239, 551–606.

Lim, D. J. (1980). Cochlear anatomy related to cochlear micromechanics. A review. *The Journal of the Acoustical Society of America*, 67(5), 1686–1695.

Lin, Y., Kalmring, K., Jatho, M., Sickmann, T., and Rössler, W. (1993). Auditory receptor organs in the forelegs of gampsocleis gratiosa (tettigoniidae): morphology and function of the organs in comparison to the frequency parameters of the conspecific song. *Journal of Experimental Zoology*, 267(4), 377–388.

Lukashkin, A. N., Walling, M. N., and Russell, I. J. (2007). Power amplification in the mammalian cochlea. *Current biology*, 17(15), 1340–1344.

Mammano, F. and Ashmore, J. (1996). Differential expression of outer hair cell potassium currents in the isolated cochlea of the guinea-pig. *The Journal of Physiology*, 496(3), 639–646.

Mammano, F. and Ashmore, J. F. (1993). Reverse transduction measured in the isolated cochlea by laser Michelson interferometry. *Nature*, 365(6449), 838–841.

Marquardt, T. (2018). Illustrations of Lighthill's 1992 equations for the two-dimensional fluid motion and associated viscous dissipation within the cochlea. In *In To the Ear and Back Again: Advances in Auditory Biophysics, Proc. 13th Mechanics of Hearing Workshop(eds Bergevin, C. & Puria, S) Conference Proceedings*, number 1 (pp. 150001).: AIP Publishing LLC.

Martin, G. K., Stagner, B. B., Jassir, D., Telischi, F. F., and Lonsbury-Martin, B. L. (1999). Suppression and enhancement of distortion-product otoacoustic emissions by interference tones above f2. I. Basic findings in rabbits. *Hearing research*, 136(1-2), 105–123.

Meenderink, S. and van der Heijden, M. (2010). Reverse cochlear propagation in the intact cochlea of the gerbil: Evidence for slow traveling waves. j neurophysiol 103: 1448-1455, 2010. *Journal of neurophysiology*, 103(5).

Meenderink, S. W. and van der Heijden, M. (2011). Distortion product otoacoustic emissions evoked by tone complexes. *Journal of the Association for Research in Otolaryngology*, 12(1), 29–44.

Mhatre, N., Dewey, J. B., Quiñones, P. M., Mason, A., Applegate, B. E., and Oghalai, J. S. (2021). Reconstruction of sound driven, actively amplified and spontaneous motions within the tree cricket auditory organ. *bioRxiv*.

Michelsen, A. and Larsen, O. N. (1978). Biophysics of the ensiferan ear. *Journal of comparative physiology*, 123(3), 193–203.

Michelsen, A., Rohrseitz, K., Heller, K.-G., and Stumpner, A. (1994). A new biophysical method to determine the gain of the acoustic trachea in bushcrickets. *Journal of Comparative Physiology A*, 175(2), 145–151.

Mistrík, P., Mullaley, C., Mammano, F., and Ashmore, J. (2009). Three-dimensional current flow in a large-scale model of the cochlea and the mechanism of amplification of sound. *Journal of The Royal Society Interface*, 6(32), 279–291.

Montealegre-Z, F., Jonsson, T., Robson-Brown, K. A., Postles, M., and Robert, D. (2012). Convergent evolution between insect and mammalian audition. *Science*, 338(6109), 968–971.

Montealegre-Z, F. and Robert, D. (2015). Biomechanics of hearing in katydids. *Journal of Comparative Physiology A*, 201(1), 5–18.

Müller, M. (1996). The cochlear place-frequency map of the adult and developing mongolian gerbil. *Hearing research*, 94(1-2), 148–156.

Narayan, S. S., Temchin, A. N., Recio, A., and Ruggero, M. A. (1998). Frequency tuning of basilar membrane and auditory nerve fibers in the same cochleae. *Science*, 282(5395), 1882–1884.

Neely, S. T. (1981). Finite difference solution of a two-dimensional mathematical model of the cochlea. *The Journal of the Acoustical Society of America*, 69(5), 1386–1393.

Neely, S. T. and Kim, D. (1986). A model for active elements in cochlear biomechanics. *The journal of the acoustical society of America*, 79(5), 1472–1480.

Neely, S. T. and Kim, D. O. (1983). An active cochlear model showing sharp tuning and high sensitivity. *Hearing research*, 9(2), 123–130.

Nioi, M., Napoli, P. E., Mayerson, S. M., Fossarello, M., and d'Aloja, E. (2019). Optical coherence tomography in forensic sciences: a review of the literature. *Forensic Science, Medicine and Pathology*, 15(3), 445–452.

Nobili, R. and Mammano, F. (1996). Biophysics of the cochlea ii: Stationary nonlinear phenomenology. *The Journal of the Acoustical Society of America*, 99(4), 2244–2255.

Nuttall, A. and Dolan, D. (1993). Intermodulation distortion (f 2- f 1) in inner hair cell and basilar membrane responses. *The Journal of the Acoustical Society of America*, 93(4), 2061–2068.

Ohlemiller, K. K. and Echteler, S. M. (1990). Functional correlates of characteristic frequency in single cochlear nerve fibers of the mongolian gerbil. *Journal of Comparative Physiology A*, 167(3), 329–338.

Oldfield, B. (1982). Tonotopic organisation of auditory receptors in tettigoniidae (orthoptera: Ensifera). *Journal of comparative physiology*, 147(4), 461–469.

Olson, E. and Mountain, D. (1994). Mapping the cochlear partition's stiffness to its cellular architecture. *The Journal of the Acoustical Society of America*, 95(1), 395–400.

Olson, E. S. (2001). Intracochlear pressure measurements related to cochlear tuning. *The Journal of the Acoustical Society of America*, 110(1), 349–367.

Olson, E. S. and Nowotny, M. (2019). Experimental and theoretical explorations of traveling waves and tuning in the bushcricket ear. *Biophysical journal*, 116(1), 165–177.

Olson, E. S. and Strimbu, C. E. (2020). Cochlear mechanics: new insights from vibrometry and optical coherence tomography. *Current Opinion in Physiology*, 18, 56–62. Physiology of Mammalian Hearing.

Palghat Udayashankar, A., Kössl, M., and Nowotny, M. (2012). Tonotopically arranged traveling waves in the miniature hearing organ of bushcrickets. *PLoS One*, 7(2), e31008.

Palghat Udayashankar, A., Kössl, M., and Nowotny, M. (2014). Lateralization of travelling wave response in the hearing organ of bushcrickets. *PLoS One*, 9(1), e86090.

Pappa, A. K., Hutson, K. A., Scott, W. C., Wilson, J. D., Fox, K. E., Masood, M. M., Giardina, C. K., Pulver, S. H., Grana, G. D., Askew, C., et al. (2019). Hair cell and neural contributions to the cochlear summating potential. *Journal of neurophysiology*, 121(6), 2163–2180.

Patuzzi, R. and Robertson, D. (1988). Tuning in the mammalian cochlea. *Physiological reviews*, 68(4), 1009–1082.

Patuzzi, R. B., Yates, G. K., and Johnstone, B. M. (1989). Changes in cochlear microphonic and neural sensitivity produced by acoustic trauma. *Hearing research*, 39(1-2), 189–202.

Prosen, C. A., Petersen, M. R., Moody, D. B., and Stebbins, W. C. (1978). Auditory thresholds and kanamycin-induced hearing loss in the guinea pig assessed by a positive reinforcement procedure. *The Journal of the Acoustical Society of America*, 63(2), 559–566.

Rabbitt, R. D. (2020). The cochlear outer hair cell speed paradox. *Proceedings of the National Academy of Sciences*, 117(36), 21880–21888.

Ramamoorthy, S., Deo, N. V., and Grosh, K. (2007). A mechano-electro-acoustical model for the cochlea: response to acoustic stimuli. *The Journal of the Acoustical Society of America*, 121(5), 2758–2773.

Ramamoorthy, S., Zha, D., Chen, F., Jacques, S. L., Wang, R., Choudhury, N., Nuttall, A. L., and Fridberger, A. (2014). Filtering of acoustic signals within the hearing organ. *Journal of Neuroscience*, 34(27), 9051–9058.

Recio-Spinoso, A. and Oghalai, J. S. (2017). Mechanical tuning and amplification within the apex of the guinea pig cochlea. *The Journal of physiology*, 595(13), 4549–4561.

Recio-Spinoso, A. and Oghalai, J. S. (2018a). Differences between mechanical and neural tuning at the apex of the intact guinea pig cochlea. In *AIP Conference Proceedings*, number 1 (pp. 020002).: AIP Publishing LLC.

Recio-Spinoso, A. and Oghalai, J. S. (2018b). Unusual mechanical processing of sounds at the apex of the guinea pig cochlea. *Hearing research*, 370, 84–93.

Ren, T. (2002). Longitudinal pattern of basilar membrane vibration in the sensitive cochlea. *Proceedings of the National Academy of Sciences*, 99(26), 17101–17106.

Ren, T. and He, W. (2018). Reticular lamina and basilar membrane vibrations in the basal turn of gerbil and mouse cochleae. In *To the Ear and Back Again: Advances in Auditory Biophysics, Proc. 13th Mechanics of Hearing Workshop (eds Bergevin, C. and Puria, S)*, volume 1965 (pp. 020005).: AIP Publishing LLC.

Ren, T. and He, W. (2020). Two-tone distortion in reticular lamina vibration of the living cochlea. *Communications Biology*, 3(1), 1–8.

Ren, T., He, W., and Barr-Gillespie, P. G. (2016a). Reverse transduction measured in the living cochlea by low-coherence heterodyne interferometry. *Nature communications*, 7(1), 10282.

Ren, T., He, W., and Gillespie, P. G. (2011a). Measurement of cochlear power gain in the sensitive gerbil ear. *Nature communications*, 2(1), 1–7.

Ren, T., He, W., and Kemp, D. (2016b). Reticular lamina and basilar membrane vibrations in living mouse cochleae. *Proceedings of the National Academy of Sciences*, 113(35), 9910–9915.

Ren, T., He, W., and Porsov, E. (2011b). Localization of the cochlear amplifier in living sensitive ears. *PLoS One*, 6(5), e20149.

Rhode, W. S. (1971). Observations of the vibration of the basilar membrane in squirrel monkeys using the Mössbauer technique. *The Journal of the Acoustical Society of America*, 49, 1218–1231.

Rhode, W. S. (1978). Some observations on cochlear mechanics. *The Journal of the Acoustical Society of America*, 64(1), 158–176.

Rhode, W. S. and Cooper, N. P. (1996). Nonlinear mechanics in the apical turn of the chinchilla cochlea in vivo. *Aud. Neurosci*, 3, 101–121.

Richter, C.-P. and Dallos, P. (2003). In *The Biophysics of the Cochlea: Molecules to Models (ed. Gummer, A. W.)* (pp. 278–284).: World Scientific.

Robles, L. and Ruggero, M. A. (2001). Mechanics of the mammalian cochlea. *Physiological reviews*, 81(3), 1305–1352.

Rose, J. E., Hind, J. E., Anderson, D. J., and Brugge, J. F. (1971). Some effects of stimulus intensity on response of auditory nerve fibers in the squirrel monkey. *Journal of Neurophysiology*, 34(4), 685–699.

Ruggero, M. A. and Rich, N. C. (1983). Chinchilla auditory-nerve responses to low-frequency tones. *The Journal of the Acoustical Society of America*, 73(6), 2096–2108.

Russell, I. and Sellick, P. (1978). Intracellular studies of hair cells in the mammalian cochlea. *The Journal of Physiology*, 284(1), 261–290.

Ryan, A. (1976). Hearing sensitivity of the mongolian gerbil, m erionesunguiculatis. *The Journal of the Acoustical Society of America*, 59(5), 1222–1226.

Ryan, A. and Dallos, P. (1975). Effect of absence of cochlear outer hair cells on behavioural auditory threshold. *Nature*, 253(5486), 44.

Rybalchenko, V. and Santos-Sacchi, J. (2003). Cl- flux through a non-selective, stretch-sensitive conductance influences the outer hair cell motor of the guinea-pig. *The Journal of physiology*, 547(3), 873–891.

Sachs, M. B. and Abbas, P. J. (1974). Rate versus level functions for auditory-nerve fibers in cats: tone-burst stimuli. *The Journal of the Acoustical Society of America*, 56(6), 1835–1847.

Santos-Sacchi, J. (1989). Asymmetry in voltage-dependent movements of isolated outer hair cells from the organ of corti. *Journal of Neuroscience*, 9(8), 2954–2962.

Santos-Sacchi, J. and Dilger, J. (1988). Whole cell currents and mechanical responses of isolated outer hair cells. *Hearing research*, 35(2-3), 143–150.

Santos-Sacchi, J., Navaratnam, D., and Tan, W. J. (2021). State dependent effects on the frequency response of prestin's real and imaginary components of nonlinear capacitance. *Scientific Reports*, 11(1), 1–15.

Santos-Sacchi, J. and Tan, W. (2018). The frequency response of outer hair cell voltage-dependent motility is limited by kinetics of prestin. *Journal of Neuroscience*, 38(24), 5495–5506.

Sarria-S, F. A., Chivers, B. D., Soulsbury, C. D., and Montealegre-Z, F. (2017). Non-invasive biophysical measurement of travelling waves in the insect inner ear. *Royal Society open science*, 4(5), 170171.

Scherer, M. P. and Gummer, A. W. (2004). Impedance analysis of the organ of corti with magnetically actuated probes. *Biophysical Journal*, 87(2), 1378–1391.

Schroeder, M. (1969). Relation between critical bands in hearing and the phase characteristics of cubic difference tones. *The Journal of the Acoustical Society of America*, 46(6B), 1488–1492.

Schumacher, R. (1975). Scanning-electron-microscope description of the tibial tympanal organ of the tettigonioidea (orthoptera, ensifera). *Zeitschrift für Morphologie der Tiere*, 81(3), 209–219.

Sellick, P. M., Patuzzi, R., and Johnstone, B. M. (1982). Measurement of basilar membrane motion in the guinea pig using the Mössbauer technique. *The journal of the acoustical society of America*, 72(1), 131–141.

Shera, C. A. (2007). Laser amplification with a twist: traveling-wave propagation and gain functions from throughout the cochlea. *The Journal of the Acoustical Society of America*, 122(5), 2738–2758.

Siebert, W. M. (1974). Ranke revisited—a simple short-wave cochlear model. *The Journal of the Acoustical Society of America*, 56(2), 594–600.

Slepecky, N. B. (1996). Structure of the mammalian cochlea. In *The cochlea* (pp. 44–129). Springer.

Soons, J. A. M., Ricci, A. J., Steele, C. R., and Puria, S. (2015). Cytoarchitecture of the mouse organ of corti from base to apex, determined using in situ two-photon imaging. *Journal of the Association for Research in Otolaryngology*, 16(1), 47–66.

Spicer, S. S. and Schulte, B. A. (1994). Differences along the place-frequency map in the structure of supporting cells in the gerbil cochlea. *Hearing research*, 79(1-2), 161–177.

Spoendlin, H. (1969). Innervation patterns in the organ of corti of the cat. *Acta oto-laryngologica*, 67(2-6), 239–254.

Spoendlin, H. (1972). Innervation densities of the cochlea. *Acta oto-laryngologica*, 73(2-6), 235–248.

Steele, C. R. and Taber, L. A. (1979a). Comparison of wkb and finite difference calculations for a two-dimensional cochlear model. *The Journal of the Acoustical Society of America*, 65(4), 1001–1006.

Steele, C. R. and Taber, L. A. (1979b). Comparison of wkb calculations and experimental results for three-dimensional cochlear models. *The Journal of the Acoustical Society of America*, 65(4), 1007–1018.

Strauß, J., Lehmann, G. U., Lehmann, A. W., and Lakes-Harlan, R. (2012). Spatial organization of tettigoniid auditory receptors: insights from neuronal tracing. *Journal of Morphology*, 273(11), 1280–1290.

Strimbu, C. E. and Olson, E. S. (2021). Salicylate-induced changes in organ of corti vibrations. *Hearing research*, (pp. 108389).

Strimbu, C. E., Wang, Y., and Olson, E. S. (2020). Manipulation of the endocochlear potential reveals two distinct types of cochlear nonlinearity. *Biophysical Journal*, 119(10), 2087–2101.

Takumida, M., Harada, Y., Wersäll, J., and Bagger-Sjöbäck, D. (1988). The glycocalyx of inner ear sensory and supporting cells. *Acta Oto-Laryngologica*, 105(sup458), 84–89.

ter Kuile, E. (1900). Die Uebertragung der Energie von der Grundmembran auf die Haarzellen. *Archiv für die gesamte Physiologie des Menschen und der Tiere*, 79(3), 146–157.

van der Heijden, M. (2005). Cochlear gain control. *The Journal of the Acoustical Society of America*, 117(3), 1223–1233.

van der Heijden, M. (2014). Frequency selectivity without resonance in a fluid waveguide. *Proceedings of the National Academy of Sciences*, 111(40), 14548–14552.

van der Heijden, M. and Cooper, N. P. (2018). Wave propagation in the mammalian cochlea. In *In To the Ear and Back Again: Advances in Auditory Biophysics, Proc. 13th Mechanics of Hearing Workshop(eds Bergevin, C. & Puria, S) Conference Proceedings*, number 1 (pp. 080002).: AIP Publishing LLC.

van der Heijden, M. and Joris, P. X. (2003). Cochlear phase and amplitude retrieved from the auditory nerve at arbitrary frequencies. *Journal of Neuroscience*, 23(27), 9194–9198.

van der Heijden, M. and Versteegh, C. P. C. (2015a). Energy flux in the cochlea: evidence against power amplification of the traveling wave. *Journal of the Association for Research in Otolaryngology*, 16(5), 581–597.

van der Heijden, M. and Versteegh, C. P. C. (2015b). Questioning cochlear amplification. In *Mechanics of Hearing: From Protein to Perception (eds Karavitaki, K Domenica and Corey, David P) AIP Conference Proceedings*, volume 1703 (pp. 010003).: AIP Publishing LLC.

Vater, M. and Kössl, M. (2011). Comparative aspects of cochlear functional organization in mammals. *Hearing research*, 273(1-2), 89–99.

Vavakou, A., Cooper, N. P., and van der Heijden, M. (2019). The frequency limit of outer hair cell motility measured in vivo. *eLife*, 8, 1–18.

Vavakou, A., Scherberich, J., Nowotny, M., and van der Heijden, M. (2021). Tuned vibration modes in a miniature hearing organ: Insights from the bushcricket. *Proceedings of the National Academy of Sciences*, 118(39).

Veitch, D., Celiker, E., Aldridge, S., Pulver, C., Soulsbury, C. D., Jonsson, T., Woodrow, C., and Montealegre-Z, F. (2021). A narrow ear canal reduces sound velocity to create additional acoustic inputs in a microscale insect ear. *Proceedings of the National Academy of Sciences*, 118(10).

Versteegh, C. P. and van der Heijden, M. (2013). The spatial buildup of compression and suppression in the mammalian cochlea. *Journal of the Association for Research in Otolaryngology*, 14(4), 523–545.

Versteegh, C. P. C. and van der Heijden, M. (2012). Basilar membrane responses to tones and tone complexes: nonlinear effects of stimulus intensity. *Journal of the Association for Research in Otolaryngology*, 13(6), 785–798.

Victor, J. D. (1979). Nonlinear systems analysis: comparison of white noise and sum of sinusoids in a biological system. *Proceedings of the National Academy of Sciences*, 76(2), 996–998.

Videler, J. J. (1993). *Fish swimming*, volume 10. Springer Science & Business Media.

von Békésy, G. (1960). *Experiments in hearing*. McGraw-Hill.

Wang, Y., Fallah, E., and Olson, E. S. (2019). Adaptation of cochlear amplification to low endocochlear potential. *Biophysical journal*, 116(9), 1769–1786.

Wang, Y., Steele, C. R., and Puria, S. (2016). Cochlear outer-hair-cell power generation and viscous fluid loss. *Scientific reports*, 6(1), 1–14.

WHO (2021). *World Report on Hearing, WORLD HEALTH ORGANISATION*. https://www.who.int/teams/noncommunicable-diseases/sensory-functions-disability-and-rehabilitation/highlighting-priorities-for-ear-and-hearing-care.

Yack, J. E. (2004). The structure and function of auditory chordotonal organs in insects. *Microscopy research and technique*, 63(6), 315–337.

Zetes, D. E., Tolomeo, J. A., and Holley, M. C. (2012). Structure and mechanics of supporting cells in the guinea pig organ of corti. *PLoS One*, 7(11), e49338.

Zheng, J., Shen, W., He, D. Z., Long, K. B., Madison, L. D., and Dallos, P. (2000). Prestin is the motor protein of cochlear outer hair cells. *Nature*, 405(6783), 149.

Zwicker, E. (1955). Der ungewöhnliche amplitudengang der nichtlinearen verzerrungen des ohres. *Acta Acustica united with Acustica*, 5(1), 67–74.

Zwicker, E. (1979a). Different behaviour of quadratic and cubic difference tones. *Hearing Research*, 1(4), 283–292.

Zwicker, E. (1979b). A model describing nonlinearities in hearing by active processes with saturation at 40 db. *Biological Cybernetics*, 35(4), 243–250.

Zwislocki, J. (1946). Über die mechanische Klanganalyse des Ohrs [On sound analysis in the ear]. *Experientia*, 2(10), 415–417.